

AN INVESTIGATION INTO THE ACCURACY OF SURFACE TEMPERATURE RETRIEVALS FROM THE AATSR

Thesis submitted for the degree of
Doctor of Philosophy
at the University of Leicester

by

Elizabeth J. Noyes
Earth Observation Science Group
Department of Physics and Astronomy
University of Leicester

December 2005

UMI Number: U209980

All rights reserved

INFORMATION TO ALL USERS

The quality of this reproduction is dependent upon the quality of the copy submitted.

In the unlikely event that the author did not send a complete manuscript and there are missing pages, these will be noted. Also, if material had to be removed, a note will indicate the deletion.



UMI U209980

Published by ProQuest LLC 2013. Copyright in the Dissertation held by the Author.
Microform Edition © ProQuest LLC.

All rights reserved. This work is protected against
unauthorized copying under Title 17, United States Code.



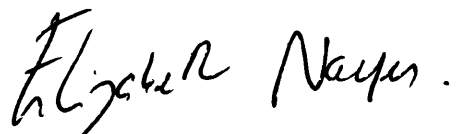
ProQuest LLC
789 East Eisenhower Parkway
P.O. Box 1346
Ann Arbor, MI 48106-1346

© Elizabeth J. Noyes, April 11, 2006

This thesis is copyright material and no quotation from it may be published without proper acknowledgement.

Declaration

I hereby declare that no part of this thesis has been previously submitted to this or any other University as part of the requirement for a higher degree. The work described herein was conducted by the undersigned except for contributions from colleagues as acknowledged in the text.

A handwritten signature in black ink, reading "Elizabeth Noyes." The signature is written in a cursive style with a large initial 'E' and a period at the end.

Elizabeth J. Noyes

April 11, 2006

AN INVESTIGATION INTO THE ACCURACY OF SURFACE TEMPERATURE RETRIEVALS FROM THE AATSR

Elizabeth J. Noyes

ABSTRACT

This thesis investigates the accuracy of operational sea surface temperature (SST) and land surface temperature (LST) data from the Advanced Along-Track Scanning Radiometer (AATSR). The study includes some of the first in situ validation results for these data sets, and forms an integral part of the overall AATSR validation programme. In addition, a comprehensive sensitivity study of the response of these retrievals to changes in atmospheric and surface conditions is also presented as an aid to interpreting validation results.

AATSR SSTs recorded during 2003 have been validated over the Caribbean sea, using in situ observations of SST from the Marine-Atmosphere Emitted Radiance Interferometer (M-AERI). This validation experiment, which extends over a full year, is the most extensive yet performed for any of the ATSR instruments (ATSR-1, ATSR-2 and AATSR) using in situ SSTs derived from radiometric measurements. These data also provide a first opportunity to study seasonal biases using observations of this type. The results demonstrate that clear-sky SSTs obtained using the unique dual-viewing geometry of the AATSR agree with the in situ data to within 0.3 K. Nadir-only retrievals performed using three channels also provide SSTs that approach this accuracy, but the split-window retrievals are found to be warm-biased by ~ 0.6 K. When tropospheric dust aerosol is present, the accuracy of the retrieved SSTs is reduced, with the nadir-view SSTs becoming cold biased and the dual-view SSTs, warm biased.

For the first time, the potential for validation of LST over heterogeneous land sites is also explored. Two methodologies are presented for upscaling point in situ LSTs to the 1-km spatial scale of the AATSR, together with initial validation results over a field site in Morocco, which suggest that the AATSR LSTs are warm-biased by at least 0.6 K over this site. The findings of this study suggest that validation over heterogeneous sites is possible for situations where the variation of LST is characterised by several in situ point observations of LST.

PUBLICATIONS

Journal Articles

Corlett G. K., Barton, I. J., Donlon, C. J., Edwards, M.C., Good, S. A., Horrocks, L. A., Llewellyn-Jones, D. T., Merchant, C. J., Minnett, P. J., Nightingale, T. J., Noyes, E. J., OCarroll, A. G., Remedios, J. J., Robinson, I. S, Saunders, R. W. & Watts, J. G. (2005), The accuracy of SST retrievals from AATSR: an initial assessment through geophysical validation against in situ radiometers, buoys and other SST data sets, *Advances in Space Research*, in press.

Good, S.A., Corlett, G. K., Noyes, E. J., Remedios, J. J. & Llewellyn-Jones, D. T. (2005) Evidence of cloud contamination in AATSR sea surface temperature data over the Caribbean, *Remote Sensing of Environment*, submitted.

Noyes, E. J., Minnett, P. J., Remedios, J. J., Corlett, G. K., Good, S. A. & Llewellyn-Jones, D. T. (2005) The accuracy of the AATSR sea surface temperatures in the Caribbean, *Remote Sensing of Environment*, **101**, 38-51.

Noyes, E. J., Sória, G., Sobrino, J. A., Remedios, J. J., Llewellyn-Jones, D. T. & Corlett, G. K. (2005), AATSR land surface temperature product algorithm verification over a WATERMED site, *Advances in Space Research*, in press.

Conference Proceedings

Noyes, E. J., Minnett, P. J., Corlett, G. K., Good, S. A., Remedios, J. J., Mannering, B., Edwards, M. C. & Llewellyn-Jones, D. T. (2004), Validation of the AATSR gridded sea surface temperature product with in situ measurements from the M-AERI, *Proceedings of the Envisat Symposium, Salzburg, Austria*, September 2004

Noyes, E. J., Minnett, P. J., Remedios, J. J., Mannering, B., Corlett, G. K., Edwards, M. C. & Llewellyn-Jones, D. T. (2003), Validation of the AATSR L2 GSST product with in situ measurements from the M-AERI, *Proceedings of the MAVT Workshop, Frascati, Italy*, October 2003

Noyes, E. J., Remedios, J. J., Llewellyn-Jones, D. T. & Edwards, M. C. (2002), Comparison of Meteosat-7 and (A)ATSR data over land: a sensitivity analysis, *Proceedings of Recent Advances in Quantitative Remote*, Valencia, Spain, September 2002

Noyes, E. J., Sória, G., Sobrino, J. A., Remedios, J. J., Llewellyn-Jones, D. T. & Corlett, G. K. (2004), The WATERMED project: validation of the AATSR land surface temperature product with in situ measurements, *Proceedings of the Envisat Symposium*, Salzburg, Austria, September 2004

ACKNOWLEDGEMENTS

A big thank you must go to my supervisors Dr. John Remedios and Prof. David Llewellyn-Jones, without whom I would not have embarked upon this project. Thank you David for persuading me not to do the MSc five years ago, you were right, the PhD was definitely worth it! I also owe enormous thanks to the AATSR post-docs, Dr Gary Corlett and Dr Simon Good (who will also become my husband on 06 May 2006!), for their continued support throughout the past three years - I don't know how I would have managed without you guys, you have been really brilliant (and what fun we had!). I am also very grateful to all the other EOS post-docs over the years, in particular, Dr Marianne Bacon, who worked with me on AATSR validation during the first year of my PhD.

There are many other people who I should also thank for their support during my PhD: Prof. Peter Minnett (RSMAS/MPO, University of Miami, for his help with the M-AERI analysis and general encouragement), Dr Andrew Birks (RAL - the font of all knowledge when it comes to AATSR data processing issues), Prof. Jose Sobrino (University of Valencia - for allowing me to participate in the WATERMED field campaign), Mr Guillem Soria (University of Valencia - co-worker on the WATERMED analysis) and Dr David Smith (RAL - for his help over the field of view work). I would also like to express my gratitude to NERC for funding my work, and ESA for the AATSR data, without which I would not have been able to do this PhD.

This journey has been a difficult one at times, but was made much easier through the friendships that I have made over the past few years. Thanks in particular go to Leigh, Paula, Simon V, Glen, Grant, Dave, Gary and Roland. May we have many more curries! I also owe a great deal to my parents and sisiter, who have been so supportive in this venture. My greatest personal thank you most definitely goes to my fiancé, Simon, who has been an incredible source of support and friendship through thick and thin (and also cooked me all my meals and cleaned the house when I broke my leg in my third year!!!) and who I almost certainly would not have met if I hadn't done this PhD.

Contents

1	Introduction	1
1.1	Rationale for Measurements of SST and LST	1
1.2	Observational Requirements for SST and LST	2
1.3	Satellite Observations of SST and LST	3
1.3.1	Estimation of SST and LST from Infrared Satellite Data	5
1.3.1.1	Radiative Transfer	5
1.3.1.2	SST and LST Retrieval Algorithms	8
1.3.1.3	Sources of Bias in Infrared Satellite SST and LST Retrievals	11
1.3.1.4	Validation of Satellite SST and LST	12
1.4	Summary	15
2	The Along-Track Scanning Radiometer	18
2.1	Heritage of the AATSR instrument	18
2.2	The AATSR Instrument	19
2.2.1	Spectral Channels	23
2.2.2	Instrument Field of View	25
2.2.3	Calibration of Infrared Channels	25
2.2.4	Comparison of AATSR and ATSR-2 BTs	28
2.3	AATSR TOA BTs	29
2.3.1	Processing of Calibration Data	29

2.3.2	Regridding and Geolocation	30
2.3.3	Land and Cloud Flagging	32
2.4	AATSR SSTs and LSTs	33
2.4.1	Sea Surface Temperatures	33
2.4.1.1	Previous Validation of ATSR-1 and -2 SSTs	37
2.4.1.2	The AATSR SST Validation Programme	43
2.4.2	AATSR Land Surface Temperature	43
2.4.2.1	Auxiliary Data	46
2.4.2.2	The AATSR LST Validation Programme	48
2.5	Summary	50
3	The AATSR: A Sensitivity Study	52
3.1	Forward Modelling of AATSR TOA BTs	52
3.1.1	The Oxford Reference Forward Model	52
3.1.2	Model Inputs	54
3.1.2.1	Atmospheric Profiles	54
3.1.2.2	Surface Temperature	56
3.1.2.3	Surface Emissivity	56
3.2	Methodology	60
3.3	Model Results: Surface Temperature	62
3.3.1	Sensitivity of Ocean TOA BTs to SST	62
3.3.2	Sensitivity of Retrieved SSTs to SST	63
3.3.3	Sensitivity of Land TOA BTs to LST	67
3.3.4	Sensitivity of Retrieved LSTs to LST	68
3.4	Model Results: Surface Emissivity	69
3.4.1	Sensitivity of Ocean TOA BTs to Surface Emissivity	69
3.4.2	Sensitivity of Retrieved SSTs to Surface Emissivity	73
3.4.3	Sensitivity of Land TOA BTs to Surface Emissivity	77

3.4.4	Sensitivity of Retrieved LST to Surface Emissivity	79
3.5	Model Results: Atmospheric Water Vapour	80
3.5.1	Height Sensitivity to Atmospheric Water Vapour	80
3.5.2	Sensitivity of Ocean TOA BTs to Atmospheric Water Vapour . .	82
3.5.3	Sensitivity of Retrieved SSTs to Atmospheric Water Vapour . .	85
3.5.4	Sensitivity of Land TOA BTs to Atmospheric Water Vapour . .	87
3.5.5	Sensitivity of Retrieved LSTs to Atmospheric Water Vapour . .	88
3.6	Model Results: Atmospheric Temperature	90
3.6.1	Height Sensitivity to Atmospheric Temperature	90
3.6.2	Sensitivity of Ocean TOA BTs to Atmospheric Temperature . .	90
3.6.3	Sensitivity of Retrieved SSTs to Atmospheric Temperature . .	93
3.6.4	Sensitivity of Land TOA BTs to Atmospheric Temperature . .	94
3.6.5	Sensitivity of Retrieved LSTs to Atmospheric Temperature . .	96
3.7	Model Results: Other Atmospheric Constituents	98
3.7.1	Gaseous Species	98
3.7.2	Aerosols	99
3.7.2.1	Effects of Aerosols on (A)ATSR Thermal Channel BTs	99
3.7.2.2	Effects of Aerosols on (A)ATSR SSTs and LSTs . .	100
3.8	Effects of Radiometric Noise on the AATSR SST/LST Retrievals . . .	103
3.9	Conclusions	104
4	The Accuracy of AATSR SSTs in the Caribbean	108
4.1	In Situ Measurements: The M-AERI	108
4.2	Validation Methodology	110
4.3	Results	111
4.4	Dual-Nadir SST Difference	118
4.4.1	Effect of Filtering Matchups based on Dual-Nadir SST Difference	122
4.4.2	The Effect of Saharan Dust on TOA BTs	127
4.5	Conclusions	132

5	WATERMED Field Campaign	134
5.1	The WATERMED Project	134
5.2	Experimental Procedure: In Situ Measurements	136
5.2.1	Instrumentation	136
5.2.2	Description of Field Site and Basis for Measurements	136
5.2.3	Measurements of At-Surface BTs	139
5.2.4	Downwelling Atmospheric Radiance	142
5.2.5	Surface Emissivity	143
5.3	Results: In Situ Data	146
5.3.1	Surface Emissivity	146
5.3.2	LST and Downwelling Sky Irradiance	149
5.4	Comparison of In Situ LSTs with AATSR data	153
5.4.1	AATSR Data	153
5.4.2	Calculation of In Situ LSTs Over the AATSR Pixels	153
5.4.2.1	Upscaling of In Situ LSTs	154
5.5	Results	158
5.6	Discussion: Sources of Bias	161
5.7	Conclusions	165
6	Conclusions and Future Work	168
6.1	Summary of Conclusions	168
6.2	Recommendations for Future Work	171

List of Figures

1.1	The variation of emissivity over the 1-15 μm range for some natural terrestrial materials. The emissivities were derived from reflectance spectra provided by ASTER Spectral Library (1999).	6
1.2	The variation of transmission with wavelength. Transmissions are shown for mid-latitude and tropical climatologies. Transmission data courtesy of S. A. Good.	7
1.3	Schematic representation of the thermal structure of the uppermost 10 m of the ocean for (a) nighttime and daytime during strong wind conditions and (b) daytime for low windspeeds. For explanation of the SSTs annotated in this diagram, see Section 1.3.1.4. (Figure provided by C. Donlon of the Met. Office; also see Donlon et al. (2002)).	14
2.1	The AATSR Infrared and Visible Radiometer (IVR). Labels show the location of the Focal Plane Assembly (FPA), the cold and hot calibration black bodies (-X BB and +X BB) and the curved Earth view apertures, which are protected by baffles to limit stray radiation from entering the instrument. Figure reproduced from ESA (2002 <i>b</i>).	21
2.2	The AATSR scan geometry showing the forward and nadir views relative to the sub-satellite track. Figure reproduced from ESA (2002 <i>b</i>).	22
2.3	The AATSR scan cycle showing the forward and nadir Earth view apertures, infrared calibration black bodies and visible calibration target. Figure reproduced from ESA (2002 <i>b</i>).	23
2.4	Measured AATSR instrument response curves (a) 0.55 μm , (b) 0.66 μm , (c) 0.87 μm , (d) 1.6 μm , (e) 3.7 μm , (f) 11 μm and (g) 12 μm (data courtesy of D. Smith of RAL).	24

2.5	Measured AATSR IFOVs corresponding to each of the 7 spectral channels of the AATSR (data courtesy of D. Smith of RAL).	26
2.6	The 11 μm channel FOV over the Earth's surface corresponding to the forward view (top row of plots) and nadir view (bottom row of plots), for the centre (pixel number 256) and edges (pixels 0 and 511) of the AATSR swath (data courtesy of D. Smith of RAL). NOTE: different x and y scales have been employed for the nadir and forward FOV maps. .	27
2.7	Illustration of the relationship between geolocation tie points (red crosses, labelled A, B, C and D) and image pixels (black squares). Tie points occur every 32 km in the along-track direction and 25 km in the across-track direction.	31
2.8	Global map showing the distribution of AATSR LST biomes 1-14 (data courtesy of RAL). See Table 2.8 for a description of the biome types. . .	46
2.9	Global map showing the distribution of AATSR LST fractional vegetation data for the month of June (data courtesy of A. Birks of RAL). . . .	47
2.10	Global map showing the distribution of AATSR LST auxiliary precipitable water data for the month of June (data courtesy of A. Birks of RAL). .	48
2.11	Global map showing the distribution of topographic variance flag auxiliary data (data courtesy of A. Birks of RAL).	49
3.1	Variation of AATSR view angle with swath position.	54
3.2	Temperature and water vapour profiles for the MIPAS reference atmospheres (Remedios 1999). 'Mid-lat' describes the temperature and water vapour profiles for both the day and night cases, which are identical for these reference atmospheres.	55
3.3	Variation of the AATSR 11 μm channel emissivity of water with viewing angle. The dotted line corresponds to an emissivity of one. Emissivities determined from refractive indices derived by Bertie & Lan (1996) for pure water.	58
3.4	AATSR split window emissivities for some natural land materials, calculated using reflectance data sourced from ASTER Spectral Library (1999). Line of equality (dashed line) is also shown.	59

3.5	AATSR auxiliary precipitable water variation over the WATERMED field site within biome 12; latitude=31.6563, longitude=-7.6058 (see Chapter 5).	61
3.6	Response of AATSR TOA BTs to changing surface temperature for the MIPAS reference atmospheres. Results are shown for the centre-of-swath scenario over the ocean for the temperature ranges given in Table 3.2.	63
3.7	Response of AATSR SSTs (N2, N3, D2, D3) to changing surface temperature for the MIPAS reference atmospheres. Results are shown for the centre-of-swath scenario over the ocean for the temperature ranges given in Table 3.2. The dotted lines indicate the target ± 0.3 K accuracy of the AATSR SST retrievals.	65
3.8	Response of AATSR LST retrievals to deviating T_S for the MIPAS reference atmospheres. The dotted lines indicate the target ± 2.5 K day time accuracy of the AATSR LSTs, the dotted/dashed line, the target ± 1.0 K night time accuracy, and the dashed line, the line of equality. Results are shown for the centre-of-swath scenario.	68
3.9	Response of AATSR TOA BTs to changing emissivity for the MIPAS reference atmospheres for the centre-of-swath scenario over the ocean. Results shown are for $T_S = T_0$	71
3.10	Response of AATSR D2 and D3 SSTs to changing emissivity in the forward view for the MIPAS reference atmospheres for the centre-of-swath scenario over the ocean. Results shown are for $T_S = T_0 + 2$	74
3.11	Response of AATSR 11 and 12 μm channels to varying fractional vegetation for the MIPAS tropical and mid-latitude atmospheres. Results shown are for the centre of swath for $T_S = T_0$. The reference value of fractional vegetation is 0.5.	78
3.12	Response of AATSR LST to changing fractional vegetation for the MIPAS tropical and mid-latitude reference atmospheres for the centre-of-swath scenario. Results shown are for $T_S = T_0$, where the dotted lines indicate the ± 2.5 K target day time accuracy of the retrievals and the dotted/dashed line, the target ± 1.0 K night time accuracy. The reference value for fractional vegetation is 0.5.	79

3.13	AATSR TOA BT response to change in atmospheric water vapour over the ocean as a function of height. (a) shows the variation of TOA BT where the water vapour is changed by a fixed amount (1897 ppmv - see text for explanation) at each height level for the MIPAS mid-latitude reference atmosphere and (b) shows the variation of TOA BT where the water vapour is changed by 10% at each height level for the MIPAS tropical reference atmosphere. Results are shown for the centre of swath for $T_S = T_0$	81
3.14	AATSR TOA BT response to change in atmospheric water vapour for the MIPAS reference atmospheres over the ocean. % change in water vapour refers to perturbation of the entire profile by that amount. Results are shown for the centre of swath for $T_S = T_0$. NOTE: an expanded scale for the tropical atmosphere has been used.	84
3.15	AATSR SST response to change in atmospheric water vapour for the MIPAS reference atmospheres over the ocean. % change in water vapour refers to perturbation of the entire profile by that amount. Results are shown for the centre of swath for $T_S = T_0$	85
3.16	AATSR LST response to change in atmospheric water vapour for the MIPAS reference atmospheres. % change in water vapour refers to perturbation of the entire profile by that amount. Results shown are for $T_S = T_0$, where the dotted lines indicate the ± 2.5 K target day time accuracy of the retrievals and the dotted/dashed line, the target ± 1.0 K night time accuracy.	89
3.17	AATSR TOA BT response to change in atmospheric temperature over the ocean as a function of height. Atmospheric temperature has been varied by 6.0 K at each height level for the MIPAS mid-latitude reference atmosphere. Results are shown for the centre of swath for $T_S = T_0$	91
3.18	AATSR TOA BT response to change in atmospheric temperature for the MIPAS reference atmospheres over the ocean. % change in temperature refers to perturbation of the entire profile by that amount. Results are shown for the centre of swath for $T_S = T_0$. NOTE: an expanded scale has been used for the tropical atmosphere.	93

3.19	AATSR SST response to change in atmospheric temperature for the MIPAS reference atmospheres over the ocean. % change in temperature refers to perturbation of the entire profile by that amount. Results are shown for the centre of swath for $T_S = T_0$	96
3.20	AATSR LST response to change in atmospheric temperature for the MIPAS reference atmospheres. % change in temperature refers to perturbation of the entire profile by that amount. Results shown are for $T_S = T_0$, where the dotted lines indicate the ± 2.5 K target day time accuracy of the retrievals and the dotted/dashed line, the target ± 1.0 K night time accuracy.	97
4.1	M-AERI viewing geometry. Figure supplied by P. J. Minnet, University of Miami.	109
4.2	Example of an AATSR $11\ \mu\text{m}$ BT image contaminated with cloud (21 August 2003 - orbit 07701). The cloud is represented by the relatively cold BTs (typically < 290 K) in the image. The M-AERI matchups for this orbit is shown by series of black crosses running NW-SE. In this case, the most easterly and two most westerly matchups have been rejected from the analysis due to possible cloud contamination (not identified by the AATSR processor - all these matchups are flagged cloud-free in the operational data).	112
4.3	Geographical location of two-channel (open circles) and three-channel (crosses) M-AERI/AATSR matchups for the 1×1 pixel block size. . . .	113
4.4	Comparisons between AATSR SSTs (y-axis) and in situ SSTs from the M-AERI (x-axis) for (a) nadir two-channel, (b) dual two-channel, (c) nadir three-channel and (d) dual three-channel matchups occurring within ± 60 minutes from the time of the AATSR overpass for the 1×1 pixel block size. Linear regression lines (solid), lines of equality (dashed) and the AATSR ± 0.3 K target accuracy lines (dotted) are also shown. . . .	114
4.5	Distribution of AATSR - M-AERI SST difference for (a) two-channel (daytime) and (b) three-channel (nighttime) matchups occurring within ± 60 minutes from the time of the AATSR overpass for the 1×1 pixel block size. Both nadir- (dotted) and dual-view (dashed) SSTs are shown. . . .	115

4.6	AATSR SST minus in situ SSTs from the M-AERI (y-axis) plotted against the date (in 2003) of the M-AERI SST measurement (x-axis) for (a) nadir-view matchups and (b) dual-view matchups occurring within ± 60 minutes from the time of the AATSR overpass for the 1×1 pixel block size. Two-channel (daytime) matchups are indicated by filled circles and three-channel (nighttime) matchups by filled squares. The AATSR ± 0.3 K target accuracy lines (dotted) are also shown.	119
4.7	Correlation between AATSR dual- minus nadir-view SST difference (D-N) and daytime MODIS aerosol optical depth at 550 nm (both data sets averaged over the month of July) for (a) two-channel (daytime) and (b) three-channel (nighttime) AATSR data. Both the MODIS and AATSR data have been averaged onto a 1 degree resolution grid between 16 - 28° N, and 60 - 88° W. Plots produced by S. A. Good, University of Leicester.	121
4.8	Variation of two- and three- channel D-N and MODIS AOD at 550 nm for the Caribbean region, between 16 - 28° N, and 60 - 88° W, during 2003. Data shown are the mean for each month. The dashed lines indicate the modal D-N for aerosol-free conditions (see Section 4.4.1). Plot produced by S. A. Good, University of Leicester.	122
4.9	Distribution of dual minus nadir SST difference (D-N) for the Caribbean Region (16 to 28 degrees latitude and -88 to -60 degrees longitude) for (a) two-channel 1-km SSTs and (b) three-channel 1-km SSTs for the months January - April and November - December 2003. The plot also shows a Gaussian fit (dashed line) and corresponding mode and standard deviation. The dotted lines indicate the mode and limits of three standard deviations from the mode. Plot produced by S. A. Good, University of Leicester.	124
4.10	Simulated D-N for (a) two-channel and (b) three-channel data, using ECMWF atmospheric data together with (model input) SST data obtained from the M-AERI. The dashed line indicates the upper D-N (aerosol) threshold.	125

4.11	Distribution of differences between AATSR dual-view minus M-AERI SSTs (x-axis) for the 1×1 block for (a) nadir two-channel, (b) dual two-channel, (c) nadir three-channel and (d) dual three-channel matchups. The dotted lines indicate the distribution of all matchups; the solid line for matchups where the dual-nadir SST difference (D-N) is 'normal' (little or no Saharan dust aerosol loading) and the dashed line for matchups where the D-N suggests the presence of Saharan dust aerosol.	126
4.12	Simulated TOA BTs using ECMWF atmospheres plotted against observed AATSR BTs corresponding to daytime matchups for: (a) nadir $11 \mu\text{m}$, (b) forward $11 \mu\text{m}$, (c) nadir $12 \mu\text{m}$ and (d) forward $12 \mu\text{m}$. Lines of equality (dashed) and regression lines (solid) are also shown. TOA BTs corresponding to SSTs where the D-N is 'normal' and abnormally high, are represented by open triangles and squares, respectively.	128
4.13	Simulated TOA BTs using ECMWF atmospheres plotted against observed AATSR BTs corresponding to nighttime matchups for: (a) nadir $3.7 \mu\text{m}$, (b) forward $3.7 \mu\text{m}$, (c) nadir $11 \mu\text{m}$, (d) forward $11 \mu\text{m}$, (e) nadir $12 \mu\text{m}$ and (f) forward $12 \mu\text{m}$. Lines of equality (dashed) and regression lines (solid) are also shown. TOA BTs corresponding to SSTs where the D-N is 'normal' and abnormally high, are represented by open triangles and squares, respectively.	129
5.1	Normalised Differential Vegetation Index (NDVI) map, generated using a Pathfinder Advance Very high Resolution Radiometer (AVHRR) dataset, showing the four WATERMED field sites (black squares). Figure taken from Sobrino et al. (2001).	135
5.2	Landsat ETM+ blue channel image of the WATERMED site. Measurement locations B27 (red), B123 (yellow) and B131 (cyan) are also shown (see text and Table 5.2 for explanation). The white lines indicate the area covered by twelve AATSR pixels considered in this experiment (see Section 5.5). Landsat data courtesy of the WATERMED project.	138
5.3	Photograph of B131 - bare soil with sparse vegetation. Insert courtesy of the Global Change Unit, University of Valencia. Date acquired: 05 March 2003	139
5.4	Photograph of B123 - bare soil with young cultivated wheat. Date acquired: 10 March 2003	141

5.5	Photograph of B27 - cultivated wheat. Date acquired: 11 March 2003 . . .	141
5.6	Collection of radiometric data in field B123 from which surface emissivities are derived using the emissivity box.	144
5.7	Diagrammatic representation of the two-lid box method where the sequence of measurements is carried from left to right. Figure adapted from Rubio et al. (1997).	144
5.8	Calibrated at-surface BTs for measurements coincident with the AATSR daytime overpass on 05 March 2003 over (a) B131 (bare soil - CIMEL Channel 3), (b) B123 (mixed) and (c) B27 (vegetation). The errors for the slopes of each regression line are the one-sigma uncertainty, considering the standard deviation of the measurements.	150
5.9	Correlation between Landsat visible (blue) reflectances and thermal (TIR) channel BTs data. The data have been binned into 0.2% bins for reflectances and 0.4 K bins for TIR BTs.	154
5.10	Landsat ETM+ pixels corresponding location B131 (bare soil) for channel 1 (blue).	156
5.11	Landsat ETM+ pixels corresponding location B123 (mixed) for channel 1 (blue).	156
5.12	Landsat ETM+ pixels corresponding location B27 (vegetation) for channel 1 (blue).	157
5.13	Normalised distribution of Landsat ETM+ channel 1 reflectances for measurement locations B131, B123 and B27. Also shown, are the mean reflectances and corresponding in situ LST for each surface (filled circle, triangle and square) and the relationship obtained between reflectance and LST (dashed line): $y = 261.2 + 5.3x$. The dotted lines correspond to the reflectance range boundaries for each surface, given in Table 5.5.	157
5.14	Example of the upscaling methodologies used in the study for one AATSR pixel over the field site. (a) shows the Landsat channel 1 reflectances for Landsat pixels falling within the nominal 1 km AATSR pixel size, (b) shows the 'retrieved Landsat LSTs' using weighted-mean method, (c) shows the 'retrieved Landsat LSTs' using the regression method and (d) shows the AATSR 11 μm IFOV weighting for this AATSR pixel. . . .	159

5.15	AATSR vs in situ LSTs for 12 pixels over the WATERMED site for (a) in situ LSTs derived using the weighted-mean method, (b) in situ LSTs derived using the weighted-mean method, with additional weighting from the true IFOV of the AATSR applied, (c) in situ LSTs derived using the regression method and (d) in situ LSTs derived using the regression method, with the AATSR IFOV weighting applied. In each graph, matchups represented by open circles correspond to AATSR LSTs that are flagged as having an Envisat blanking pulse associated with the measurements (see Section 5.6 for explanation).	160
5.16	Histogram showing the distribution of Landsat channel 1 reflectances for the twelve AATSR pixels over the WATERMED field site. The blue dotted line shows the vegetation-mixed and the red dotted line, the mixed-bare soil classification boundaries used for the regression method. The green, blue and purple asterisks show the mean Landsat reflectance corresponding to the vegetation, mixed and bare soil surfaces, used in the regression method.	163
5.17	LST difference plotted as a function of (a) proportion of vegetation within each AATSR pixel, as determined by the weighted-mean method and (b) the 11–12 μm BT difference. In each graph, matchups represented by open circles correspond to AATSR LSTs that are flagged as having an Envisat blanking pulse associated with the measurements (see Section 5.6 for explanation).	164

List of Tables

2.1	ATSR spectral channels (adapted from Llewellyn-Jones et al. (2001)). Channels exclusive to ATSR-2 and AATSR are denoted by *.	20
2.2	Summary of AATSR cloud tests. Column ‘Channel’ depicts the channels used in the tests, ‘Day/Night’ whether the test is implemented during the day or night, and column ‘Ocean/Land’, whether the tests are carried out over ocean or land pixels. Tests denoted by * based on methods developed by Saunders & Kriebel (1988) for the AVHRR.	34
2.2	Summary of AATSR cloud tests, continued...	35
2.3	Nadir-view SST coefficients latitude bands.	36
2.4	Current operational AATSR retrieval coefficients for 1-km resolution SSTs for centre and edge-of-swath pixels. Band 0 corresponds to the centre of the swath and band 37 to the edges. Coefficient subscripts indicate channel (3.7, 11, 12) and nadir (n) or forward (f) view data.	38
2.5	Validation results from ATSR-1 and ATSR-2 where the in situ measurements have been obtained using a radiometer. Note, for ATSR-1, the 3.7 μm channel failed on 27 May 1992. Where there is no figure given in the standard deviation columns, it is because there is only one data point available for validation.	40
2.6	Validation results from ATSR-1 and ATSR-2 where the in situ measurements are of bulk SST (BSST). Note, for ATSR-1, the 3.7 μm channel failed on 27 May 1992. Where there is no figure given in the standard deviation columns, it is because there is only one data point available for validation.	41
2.6	Continued...	42
2.7	Operational AATSR LST retrieval coefficients (Prata 2002 <i>b</i>)	45

2.8	AATSR LST biomes derived from Dorman & Sellers (1989). See Figure 2.8 for global distribution of these biomes.	47
2.9	Topographic variance flag definitions	49
3.1	List of absorbing gases in the AATSR thermal channel bandwidths. . . .	55
3.2	Near-surface air temperatures, T_{ns} , corresponding to each model atmosphere. Also shown are the central surface temperatures, T_0 , and range of SSTs/LSTs (T_S) used in this study. No LST ranges are given for the polar atmospheres, as these data have not been included in the land component of the study (see text).	56
3.3	AATSR nadir and forward triple-window channel emissivities used for ocean TOA BT simulations, derived using the refractive indices given by Bertie & Lan (1996). Emissivities corresponding to the centre and edge of swath are shown.	59
3.4	AATSR split window emissivities for some natural land materials, calculated using reflectance data sourced from ASTER Spectral Library (1999).	60
3.5	The BT deficit for $T_S = T_0$ (column A) and the AATSR TOA BT response to a change in T_S of 1.0 K for the MIPAS reference atmospheres over the ocean (column B).	64
3.6	AATSR SST bias for $T_S = T_0$ (column A) and response (column B) to a change in T_S of 1.0 K, for the MIPAS reference atmospheres over the ocean. Also shown are the dual-minus-nadir (D-N) SST differences for each atmospheric scenario.	66
3.7	The BT deficit for $T_S = T_0$ (column A) and the AATSR TOA BT response to a change in T_S of 1.0 K for the MIPAS reference atmospheres over land (column B).	67
3.8	AATSR LST bias for $T_S = T_0$ (column A) and response (column B) to a change in T_S of 1.0 K, for the MIPAS reference atmospheres. Also shown are the minimum and maximum values of precipitable water (PW) corresponding to biome 12, used in the calculations.	69
3.9	AATSR TOA BT response to a change in surface emissivity of 0.001, for the MIPAS reference atmospheres. Results are shown for the centre of swath.	72

3.10	Estimated change in sea surface emissivity corresponding to a change in SST from 301.2 K to 279.0 K, for the AATSR nadir and forward split-window channels, derived using the refractive indices given by (Newman et al. 2005). Emissivities corresponding to the centre and edge of swath are shown.	73
3.11	AATSR SST deficit as a result of a change in surface emissivity, for (i) a decrease in emissivity of 0.006 for all the thermal channels in the forward view (which approximates to the emissivity deficit estimated by Masuda et al. (1988) and Watts et al. (1996) for direct emission from a sea surface roughened by 10 ms^{-1} winds), (ii) the effects of the salinity correction, derived by Friedman (1969) and (iii) a reduction in emissivity consistent with decreasing SST (see Table 3.10 - estimated from the refractive indices provided by Newman et al. (2005), on the AATSR channel emissivities for the MIPAS reference atmospheres). Results are shown for the centre-of swath scenario.	76
3.12	AATSR TOA BT response to change in fractional vegetation of 0.1, for the MIPAS reference atmospheres. Results are shown for the centre-of-swath scenario.	78
3.13	AATSR LST response to change in fractional vegetation of 0.1, for the MIPAS reference atmospheres. Results are shown for the centre of swath.	80
3.14	AATSR TOA BT response to 10% increase in atmospheric water vapour, x , for the MIPAS reference atmospheres over the ocean. The x and x^2 terms of the second-degree polynomials fitted to the data are shown for the centre of swath.	83
3.15	AATSR SST response to 10% increase in atmospheric water vapour, x , for the MIPAS reference atmospheres over the ocean. The x and x^2 terms of the second-degree polynomials fitted to the data are shown for the centre of swath.	86
3.16	AATSR TOA BT response to 10% increase in atmospheric water vapour, x , for the MIPAS reference atmospheres over the land. The x and x^2 terms of the second degree polynomial fitted to the data, are shown for the centre of swath.	88
3.17	AATSR LST response to 10% increase in atmospheric water vapour, x , for the MIPAS reference atmospheres over the land. Results are shown for the centre of the swath.	89

3.18	AATSR TOA BT response to 1% change in atmospheric temperature, x , for the MIPAS reference atmospheres over the ocean. The x and x^2 terms of the second-degree polynomials fitted to the data are shown for the centre of swath.	92
3.19	AATSR SST response to change in atmospheric temperature, x , for the MIPAS reference atmospheres over the ocean. The x and x^2 terms of the second-degree polynomials fitted to the data are shown for the centre of swath.	95
3.20	AATSR TOA BT response to change in atmospheric temperature, x , for the MIPAS reference atmospheres over the land. The x and x^2 terms of the second-degree polynomials fitted to the data are shown for the centre of swath.	97
3.21	AATSR LST response to change in atmospheric temperature, x , for the MIPAS reference atmospheres. The x and x^2 terms of the second-degree polynomials fitted to the data are shown for the centre of swath.	98
3.22	Distribution of aerosol particle size. Reproduced from Hess et al. (1998). σ denotes the width of the lognormal distribution, r_{modN} and r_{modV} the mode by number and the mode by volume and r_{min} and r_{max} , the minimum and maximum radii of the particles.	100
3.23	Simulated BT depressions for different aerosol types. These data have been reproduced from Dundas (1991).	101
3.24	Simulated changes in SST and LST for new volcanic aerosols (Dundas 1991). The tropical AATSR coefficients have been used for the retrievals of SST, and the biome 12 coefficients for the retrievals of LST. The results are applicable to the centre of the AATSR swath.	102
3.25	Standard deviation of the errors in the operational gridded SST retrievals as a result of radiometric noise. Data reproduced from Good (2004). . .	103

4.1	Summary of AATSR/M-AERI matchup statistics for the 1×1 pixel block. Statistics are shown separately for two-channel (day) and three-channel (night) SST retrievals, considering all matchups, and cases where the AATSR dual- minus nadir-view SST (D-N) is ‘normal’ and abnormally high (see Section 4.4.1 for explanation). In the case of ‘all matchups’ for the N2 retrievals, the bias and standard deviation are presented separately for the two distributions (labelled ‘1’ and ‘2’); the mean for the full data set is also given (denoted by *). Bias is defined as AATSR - M-AERI, such that a positive value indicates that AATSR is measuring warm. For each scenario, the proportion of matchups falling within the ± 0.3 K target accuracy is also shown.	116
4.2	Summary of AATSR/M-AERI matchup statistics for the 3×3 pixel block. Statistics are shown separately for two-channel (day) and three-channel (night) SST retrievals, considering all matchups, and cases where the AATSR dual- minus nadir-view SST (D-N) is ‘normal’ and abnormally high (see Section 4.4.1 for explanation). In the case of ‘all matchups’ for the N2 retrievals, the bias and standard deviation are presented separately for the two distributions (labelled ‘1’ and ‘2’); the mean for the full data set is also given (denoted by *). Bias is defined as AATSR - M-AERI, such that a positive value indicates that AATSR is measuring warm. For each scenario, the proportion of matchups falling within the ± 0.3 K target accuracy is also shown.	117
4.3	Statistics of the comparison between the simulated and observed AATSR TOA BTs. The bias (simulated-observed) and standard deviation (StDev) are shown for all data points, data points with D-N below the ‘normal’ threshold and data points with D-N above the ‘normal’ threshold. Δ Bias refers to the additional BT deficit apparent in the observed BTs due to aerosol contamination that is not simulated by the model - this is effectively the mean effect of Saharan dust on the AATSR TOA BTs over the Caribbean.	130
4.4	Change in retrieved SST due to aerosol using the simulation results given in the last column of Table 4.3	132
5.1	Instrumentation used for ground-based radiometric measurements. . . .	137
5.2	Summary description of measurement locations: B131, B123 and B27 .	140

5.3	Summary of in situ emissivity data. Values are absent over bare soil for the RAYTEK and EVEREST instruments due to lack of reliable data. .	147
5.4	Summary of LST calculations over surfaces B131, B123 and B27. The T_i^{sky} coefficients were provided by Guillem S3ria of the University of Valencia.	152
5.5	Landsat Channel 1 reflectance statistics (number of Landsat pixels, mean, standard deviation and range of reflectances, and the % of pixels with reflectances within that range) corresponding to each of the three measurement surface regimes: B131, B123 and B27.	158
5.6	Calculated biases and standard deviations for the comparison of the four sets of derived in situ LSTs with the corresponding AATSR LSTs. Results are shown for all pixels and the eight well-correlated pixels (see Section 5.6).	159
5.7	Calculated biases and standard deviations for the comparison of the four sets of derived in situ LSTs with the corresponding AATSR LSTs. . . .	162

LIST OF ABBREVIATIONS

AATSR	Advanced Along Track Scanning Radiometer
AIRS	Aqua-advanced Infrared Radiation Sounder
AMSR-E	Advance Microwave Scanning Radiometer for Earth observing systems
AOD	Aerosol Optical Depth
ARIES	Airborne Research Interferometer Evaluation System
ASTER	Advanced Spaceborne Thermal Emission and Reflection Radiometer
ATSR-1	Along-Track Scanning Radiometer-1
ATSR-2	Along-Track Scanning Radiometer-2
AVHRR	Advanced Very High Resolution Radiometer
BBU	Black Body electronics Unit
BSST	Bulk Sea Surface Temperature
BT	Brightness Temperature
D2	(A)ATSR dual-view, two-channel surface temperature retrieval
D3	(A)ATSR dual-view, three-channel surface temperature retrieval
DBU	Digital Bus Unit
DEM	Digital Elevation Model
DEU	Digital Electronics Unit
D-N	Dual minus Nadir SST difference
ECMWF	European Centre for Medium Range Weather Forecasts
Envisat	ENVironment SATellite
ERS-1	European Remote Sensing Satellite-1
ERS-2	European Remote Sensing Satellite-2
ESA	European Space Agency
FOV	Field of View
FPA	Focal Plane Assemblies
GHRSSST-PP	GODAE High Resolution Sea Surface Temperature Pilot Project
GODAE	Global Ocean Data Assimilation Experiment
GPS	Global Positioning System
HITRAN	High-resolution TRANsmission molecular absorption database
IEU	Instrument Electronics Unit
IFOV	Instantaneous Field of View
ISAR	Infra-red Autonomous Radiometer
IVR	Infrared and Visible Radiometer

Landsat-ETM	Landsat Enhanced Thematic Mapper
LST	Land Surface Temperature
M-AERI	Marine-Atmosphere Emitted Radiance Interferometer
MIPAS	Michelson Interferometer for Passive Atmospheric Sounding
MODIS	MODderate REsolution Imaging Spectroradiometer
MODTRAN	MODerate spectral resolution atmospheric TRANSmittance algorithm and computer model
N2	(A)ATSR nadir-view, two-channel surface temperature retrieval
N3	(A)ATSR nadir-view, three-channel surface temperature retrieval
NASA	National Aeronautics and Space Administration
NDVI	Normalised Difference Vegetation Index
NE Δ T	Noise Equivalent Δ Temperature
NIST	National Institute of Standards and Technology
NOAA	National Oceanic and Atmospheric Administration
NOC	National Oceanography Centre
NVAP	NASA Water Vapour Project
NWP	Numerical Weather Prediction
PCSU	Power Conditioning and Switching Unit
RAL	Rutherford Appleton Laboratories
RFM	Reference Forward Model
RT	Radiative Transfer
SEVIRI	Spinning Enhanced Infrared and Visible Imager
SISTeR	Scanning Infrared Sea Surface Temperature Radiometer
SSST	Skin Sea Surface Temperature
SST	Sea Surface Temperature
TMI	TRMM Microwave Imager
TOA	Top of Atmosphere
TOGA	Tropical Ocean Global Atmosphere
TOMS	Total Ozone Mapping Spectrometer
TRMM	Tropical Rainfall Measuring Mission
TVF	Topographic Variance Flag
WATERMED	WATER use Efficiency in natural vegetation and agricultural areas by Remote sensing in the MEDiterranean basin
WCRP	World Climate Research Programme

Chapter 1

Introduction

1.1 Rationale for Measurements of SST and LST

The Earth's climate is a complex system that involves interactions between the atmosphere, oceans, land surface, biosphere and cryosphere. One of these interactions is the exchange of long-wave energy between the atmosphere and the surface, which is principally through direct radiation from the surface, or the latent heat associated with evaporation and condensation. As this process, which takes place via the uppermost layer (~ 1 mm) of the Earth's surface, is thermally-driven, measurements of surface temperature are a requirement for many climate-related applications and research studies. Assimilation of observed global sea surface temperature (SST) data, for example, has been shown to reduce errors in models used for operational ocean forecasting (Bell et al. 2000). Due to the close coupling between the atmosphere and the oceans, SST data are also used for monitoring trends possibly associated with global climate change (e.g. Lawrence et al. 2004, Andersen et al. 2002) and large-scale anomalies such as El Niño (e.g. Alexander & Scott 2002, Lawrence et al. 2004). Other ocean phenomena, such as the propagation speed of planetary waves, can also be characterised through observations of SST (e.g. Hill et al. 2000, Challenor et al. 2000).

Although covering a smaller proportion of the Earth's surface, land surface temperature (LST) is also a key parameter required by many earth-system models (e.g. hydrologic models (Rhoads et al. 2001)). In addition, observations of LST have been shown to be useful in agricultural applications, for example, estimating the extent of frosts in orange groves (Caselles & Sobrino 1989). Its sensitivity to surface moisture and vegetation can also be used to detect changes in the biophysical characteristics of land surfaces, such as tendencies towards desertification (e.g. Lambin & Ehrlich 1996, Sobrino & Raissouni

2000). Anomalies in LST have also been observed prior to the occurrence of large earthquakes (Ouzounov & Freund 2004), which may provide a mechanism for their detection before an event.

1.2 Observational Requirements for SST and LST

The accuracy requirements of measurements of surface temperature depend very much on the application for which they are being used. For SST, a latitude-dependent accuracy of between 0.3 - 0.5 K has been specified by the Tropical Ocean Global Atmosphere (TOGA) project of the World Climate Research Programme, or WCRP, (World Meteorological Organization 1985). Accuracies of this order enable the typical SST anomalies of 2 K associated with El Niño, for example, to be resolved. The GODAE (Global Ocean Data Assimilation Experiment) High Resolution Sea Surface Temperature Pilot Project, or GHRSSST-PP, website (<http://ghrsst-pp.metoffice.com>) also provides a useful summary of the requirements of users of SST data for coastal and inland seas, open ocean and ultra high-resolution applications (e.g. for some coastal studies). This document specifies an accuracy of better than 0.3 K for these applications, with higher accuracies (e.g. 0.1 K) required for climate trend analysis.

In terms of the spatial resolution of SST data, requirements vary between 1 km (e.g. for some coastal studies) and 2.5° (e.g. for assimilation into models - see Bell et al. (2000)). Studies involving the identification of climate trends may utilise even coarser-resolution SST data (e.g. 5°-latitude/longitude bins have been used by Casey & Cornillon (2001)); such data sets are also required to be obtained over a minimum of 10 years to ensure that any trends identified are statistically significant (Allen et al. 1994). The temporal specifications for SST data sets also vary between applications. For some coastal and inland sea-related applications, the frequency of observations may be of the order of hours. In other situations, a temporal resolution of weeks is appropriate (e.g. the TOGA project specifies 15 to 30 days (World Meteorological Organization 1985)).

For LST, the requirements are much less well defined. For Numerical Weather Prediction (NWP), for example, the target accuracy for observational data is 0.5 K over 10 km at 30-minute temporal resolution (R. Saunders, Personal Communication). However, an accuracy of 1 K is quoted widely as potentially useful in many applications (e.g. Prata & Cechet 1999, Wan 1999). Due to the strong and variable diurnal cycle of LST, measurements separated by days or even hours are of more limited use. For most applications, such as model evaluation and flux computation (Aires et al. 2004, Jin &

Dickinson 1999), measurements that represent the full diurnal cycle are ideally required (e.g. every few hours at most).

1.3 Satellite Observations of SST and LST

Measurements of surface temperature have been made for many years by collecting in situ data. The earliest SST data, for example, were obtained using a thermometer to measure the temperature of sea water in a bucket drawn from the ocean. The measurement techniques have been refined since those times, and we are now capable of obtaining in situ point observations of SST and LST with an accuracy of 0.1 K, or better, from buoys, ground-based radiometers, ship thermometers and meteorological stations. While these measurements achieve the accuracies discussed in Section 1.2, they are very limited in terms of their spatial coverage. For LST, and SST to a certain extent, these data may also fail to represent what is really going on in terms of the temperature distribution over the Earth's surface at a particular location. LST, for example, can vary by more than 10 K over a few metres (Prata 1994).

Data collected by satellites provide an excellent way to obtain global observations of SST and LST in a relatively short period of time. The latest geostationary satellites, for example Meteosat-8, make measurements every 15 minutes. Polar-orbiting satellites, such as ESA's Envisat, provide global coverage in a matter of days. For LST, satellites really provide the only means of obtaining useful regional or global data due to the extreme spatial variability of this parameter. In the last twenty or thirty years, satellite observations have been used increasingly as a source of SST and LST data. In particular, methods of deriving satellite SST data are well-developed, although there are still inherent problems associated with these data (see Section 1.3.1.3).

Several space-borne sensors have been developed that provide observations of SST and LST. These instruments make measurements of top-of-atmosphere (TOA) radiances, either in the thermal infrared or microwave regions of the electromagnetic spectrum. The radiances are then corrected for the effects of the atmosphere and non-unity of the emissivity of the Earth's surface in order to obtain an estimate of the SST or LST (this will be discussed in detail in Section 1.3.1.1).

Infrared sensors have the distinct advantage over microwave sensors that the signal originating from the Earth will always be stronger at infrared wavelengths. This is due to the nature of the Planck function for Earth temperatures, which peaks in the infrared, and the higher surface emissivity of terrestrial materials at these wavelengths. In addition,

the rate of change of radiance with temperature is lower at microwave wavelengths, thus a higher radiometric resolution is required to obtain the same precision as for an equivalent infrared sensor. As a result of these differences, even the most advanced microwave radiometers cannot provide SSTs or LSTs with the potential accuracy of the infrared radiometers. Measurements made by microwave instruments are of comparably low spatial resolution (e.g. 25-50 km compared with between 60 m and 5 km in the infrared), limited by the size of a microwave receiver. In addition, microwave radiometers can suffer from sidelobe contamination. The main advantage of microwave over infrared radiometry, is that the latter's view of the surface may be obstructed by clouds. Microwaves, on the other hand, are able to penetrate clouds and so provide a more continuous source of SST or LST data.

Examples of current satellite instruments that operate in the infrared include the Advanced Very High Resolution Radiometers (AVHRR - on board the NOAA polar orbiting satellites), the Along-Track Scanning Radiometers (ATSR - on board the polar-orbiting satellites, ERS-1, ERS-2 and Envisat), the MODerate Resolution Imaging Spectroradiometers (MODIS - on board the Terra and Aqua polar-orbiting satellites) and the Spinning Enhanced Infrared and Visible Imager (SEVIRI - on board the Meteosat-8 geostationary satellite). Of these, the ATSR series of instruments, which spans almost 15 years, provides the most accurate radiometric measurements. It is an assessment of the accuracy of the SSTs and LST retrievals from the most recent of the ATSRs, the Advanced ATSR (AATSR), that is the subject of this thesis; Chapter 2 provides a full description of this instrument, and its operational data products.

The AVHRR instruments have also been very successful in their own right, providing observations of SST for more than 20 years, with an estimated accuracy of close to 0.5 K (see Li et al. (2001) and Kearns et al. (2000) for example). More recently, SST and LST data from the the two operational MODIS instruments (on board Terra, launched in 1999, and Aqua, launched in 2002) have also become available. In particular, the MODIS LST product has paved the way for other operational satellite-derived LST data. Accurate observations of LST from satellite data are very difficult to obtain, due to the heterogeneity of land surfaces (this is discussed in more detail in Section 1.3.1.3). Thus the accuracy of these data are usually much lower than for SST (typically 1-3 K). Although limited in number, comparisons with in situ LSTs suggest that the MODIS LSTs are achieving accuracies of better than 1.0 K (Coll et al. 2005, Wan et al. 2004, 2002).

A new operational LST product derived from SEVIRI data has also become available in the last year. While geostationary satellites may not provide the spatial resolution of the polar-orbiters (e.g. 3-5 km compared with better than 1-2 km) due to their higher

satellite orbit (e.g. 35,000 km compared to 800 km), these data have the temporal frequency that is required to capture the diurnal cycle of LST. Arguably, the most useful application of LST derived from extremely accurate polar-orbiting sensors, such as the (A)ATSR, is as a calibration-validation source for LSTs derived from geostationary data. Currently, the geostationary satellites, or indeed any other polar-orbiting sensors, do not provide the radiometric accuracy of the (A)ATSR instruments (e.g. better than 0.1 K for the (A)ATSR compared with 0.25 K, or worse, for SEVIRI's infrared channels). In addition, LST retrieval from geostationary satellites is more challenging due to the higher zenith angles, and therefore increased atmospheric attenuation, at high latitudes. Due to the larger pixel size of geostationary sensors, these observations of LST are more difficult to validate against in situ data (the concept of validation is discussed further in Section 1.3.1.4). The pixel size also limits the use of geostationary LST data for some applications. Data from polar-orbiting sensors, such as the AATSR, have the potential to resolve this problem: some researchers are currently investigating combining LSTs from polar-orbiting and geostationary satellites in order to generate a high-spatial resolution, high-temporal resolution LST data set (e.g. Reutter et al. 1996). Lastly, polar-orbiting satellite LSTs also provide a consistent source of global LST data. To obtain global coverage of LST from geostationary sensors, data from multiple geostationary satellites would be required.

Of microwave radiometers, the TRMM (Tropical Rainfall Measuring Mission) Microwave Imager (TMI) and the Advanced Microwave Scanning Radiometer for Earth observing systems (AMSR-E) are current examples. The target accuracy of the SST data derived from these instruments is between 0.5-0.7 K. As it is thermal infrared observations from the AATSR that are the subject of this thesis, microwave radiometric measurements are not discussed here in any further detail. In light of their spatial resolution and radiometric accuracy, it is clear that the (A)ATSR sensors provide a vital role in the determination of both SST and LST from space.

1.3.1 Estimation of SST and LST from Infrared Satellite Data

1.3.1.1 Radiative Transfer

The measurement made by a satellite sensor is not a direct measurement of the temperature of the Earth's surface. Instead, the sensor measures the radiances at the top of the atmosphere, which depend on the radiant energy emitted by the Earth's surface, and the overlying atmosphere. As the spectral emissivity of the Earth's surface is less than unity

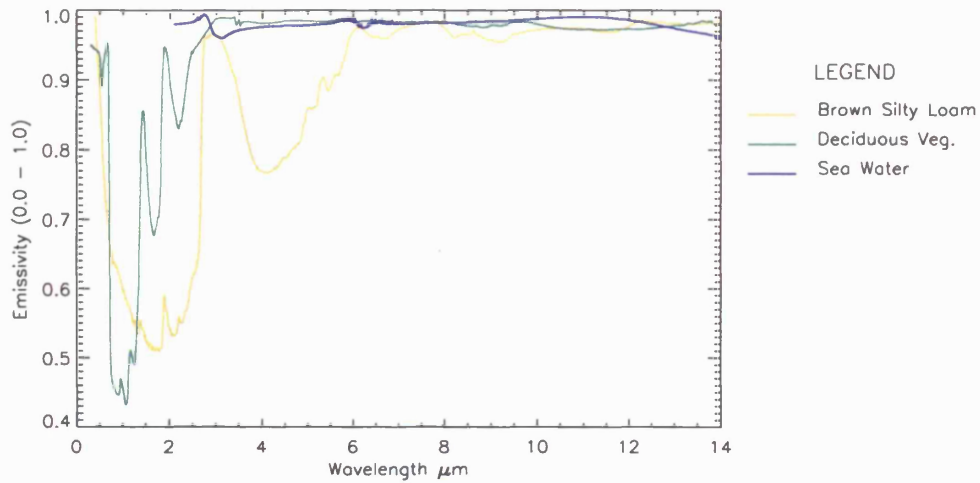


FIGURE 1.1. The variation of emissivity over the 1-15 μm range for some natural terrestrial materials. The emissivities were derived from reflectance spectra provided by ASTER Spectral Library (1999).

(see Figure 1.1 for some examples of terrestrial materials), some of the radiation emitted by the atmosphere is also reflected by the surface of the Earth. The equation which describes this relationship is commonly referred to as the radiative transfer (RT) equation, which can be written in simple terms as:

$$L^{sat} = L_L^{sat} = L_{\uparrow L}^{ground} + L_{\uparrow L}^{atm} + L^{atm.reflected} \quad (1.1)$$

where L^{sat} is the radiance measured by the sensor, and L^{ground} , L^{atm} and $L^{atm.reflected}$ are, respectively, the upwelling radiance emitted by the ground and the atmosphere, and the down-welling radiance emitted by the atmosphere that is reflected by the ground up towards the sensor. L^{sat} is wavelength dependent, as surface emissivity and the effects of the atmosphere also vary with wavelength. For a radiometer with bandwidth $\lambda_1 - \lambda_2$, the measurement is of the integrated radiances over this bandwidth, weighted by the filter function of the instrument. This quantity is sometimes expressed as a TOA brightness temperature (BT), which is equivalent to the temperature of the Planck function that produces the same integrated radiances over the range $\lambda_1 - \lambda_2$. In other words, if the Earth had no atmosphere and the emissivity of the surface was unity, this BT would be the true temperature of the Earth's surface.

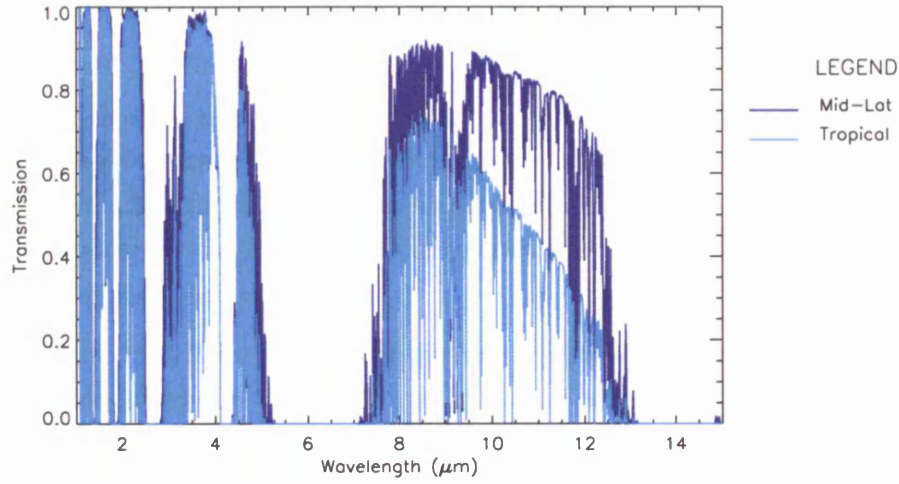


FIGURE 1.2. The variation of transmission with wavelength. Transmissions are shown for mid-latitude and tropical climatologies. Transmission data courtesy of S. A. Good.

As the atmosphere absorbs, as well as emits, radiation, each term of Equation 1.1 is also affected by the transmissivity of the atmosphere (see Figure 1.2). For a radiometer, the right-hand terms can be expressed more specifically as (see Susskind et al. (1984) and Dash et al. (2002) for this version):

$$L_i^{ground} = \int_{\lambda_1}^{\lambda_2} f_i(\lambda) \epsilon(\lambda) B(\lambda, T_s) \tau(\lambda) d\lambda \quad (1.2)$$

$$L_i^{atm} = \int_{\lambda_1}^{\lambda_2} \int_{p=0}^{p_s} f_i(\lambda) B(\lambda, T_p) \frac{d\tau}{dp} d\lambda dp \quad (1.3)$$

$$L_i^{atm.reflected} = \int_{\lambda_1}^{\lambda_2} \int_{\theta=0}^{\frac{\pi}{2}} \int_{\phi=0}^{2\pi} f_i(\lambda) (1 - \epsilon(\lambda)) L^\downarrow(\lambda, \theta, \phi) \tau(\lambda) \sin 2\theta d\lambda d\theta d\phi \quad (1.4)$$

where i is the radiometer channel, f_i is the normalised channel response function (see Chapter 2 for the AATSR), θ is the zenith angle, ϕ is the azimuth angle, λ is wavelength, p is pressure in the atmosphere, p_s is the pressure at the Earth's surface, T_p is the mean temperature of air at pressure level p , $\tau(\lambda)$ is the spectral atmospheric transmissivity,

$\epsilon(\lambda)$ surface spectral emissivity (see Figure 1.1), T_s is surface temperature, $L^\downarrow(\lambda, \theta, \phi)$ is the downwelling atmospheric radiance and B is the Planck function at wavelength λ and temperature T_s or T_p .

In theory, these equations are only valid where the surface is a Lambertian reflector and in thermodynamic equilibrium with the overlying atmosphere. In reality, the behaviour of much of the Earth's surface is between a Lambertian and a specular reflector, and the atmosphere is only in local thermodynamic equilibrium up to approximately 50-70 km in height (Dash et al. 2002).

To minimise the effects of the atmosphere, the bandwidths of space-borne infrared radiometers (designed to provide SST and LST data) are selected to be in the 8-13 μm region, where atmospheric transmission is high (see Figure 1.2). In addition, some radiometers also have spectral channels in the atmospheric window at approximately 3.7 μm . However, as this region of the electromagnetic spectrum is affected by solar radiation, such channels are confined to nighttime observations.

Despite having relatively high atmospheric transmission, atmospheric attenuation is still significant in these 'window' channels, and clear-sky BTs may still be depressed by several K compared to the underlying SST or LST. Most of the attenuation at these wavelengths is due to water vapour absorption, although atmospheric temperature also has an important influence on the measured TOA BTs. In addition, research has shown that both stratospheric and tropospheric aerosols depress infrared radiances (e.g. Dundas 1991, Merchant et al. 1999, Závody et al. 1995, 1994). The role of the atmosphere in infrared radiometry (specifically for the AATSR thermal channels) is discussed further in Chapter 3.

1.3.1.2 SST and LST Retrieval Algorithms

From Section 1.3.1.1, it is apparent that with knowledge of the atmosphere and surface emissivity, one can obtain SST or LST from BTs measured by a radiometer, using Equations 1.1 - 1.4. In practice, as the Earth's atmosphere and surface emissivity are extremely variable, these are not usually well enough known to permit retrievals of SST and LST with the accuracies discussed in Section 1.2.

To overcome the problem of an unknown atmosphere, the multi-channel approach to retrievals of SST and LST has been developed (see for example, Deschamps & Phulpin (1980), McMillin (1984) and Becker & Li (1990)). The method is based on the fact that atmospheric absorption varies with wavelength. By utilising measurements from at least

two different spectral channels, an estimate of the attenuation due to the atmosphere can be obtained. The most common form of the multi-channel method is to use two spectral channels at approximately 11 and 12 μm , known as the split-window channels. This is sometimes supplemented by a third channel at approximately 3.7 μm (triple-window method). In the case of the (A)ATSR instruments, this is further augmented by including data from two viewing angles (discussed further in Chapter 2), which provides further information about the state of the atmosphere (dual-angle method).

Using the split-window method as an example, we have measured radiances corresponding to two channels that provide simultaneous equations, which can be solved for T_s (i.e. SST or LST). The following split-window derivation is taken from McMillin (1984); Deschamps & Phulpin (1980), Prata (2002a) and Becker & Li (1990), for example, provide essentially the same equations.

Considering Equations 1.1-1.2, and an emissivity equal to unity, the BTs measured in two channels at 11 and 12 μm (T_{11} , and T_{12}), respectively, can be expressed as:

$$B_{11}(T_{11}) = B_{11}(T_s)\tau_{11} + (1 - \tau_{11})B_{11}(\overline{T_a}) \quad (1.5)$$

$$B_{12}(T_{12}) = B_{12}(T_s)\tau_{12} + (1 - \tau_{12})B_{12}(\overline{T_a}) \quad (1.6)$$

where the subscripts, 11 and 12 indicate the radiometer channel, and $B_{12}(\overline{T_a})$ is the radiance for mean atmospheric temperature, $\overline{T_a}$, approximated by (McMillin 1984):

$$B_i(\overline{T_a}) = \frac{1}{1 - \tau_i} \int_{p=0}^{p_s} B_i(T_p) d\tau \quad (1.7)$$

Making the assumption that $\overline{T_a}$ is approximately equal between the channels, a first order Taylor approximation, expanding about $\overline{T_a}$, can then be used to derive the following expressions:

$$B_{11}(T_{12}) \simeq B_{11}(\overline{T_a}) + \frac{\partial B_{11}}{\partial B_{12}} [B_{12}(T_{12}) - B_{12}(\overline{T_a})] \quad (1.8)$$

$$B_{11}(T_s) \simeq B_{11}(\overline{T_a}) + \frac{\partial B_{11}}{\partial B_{12}} [B_{12}(T_s) - B_{12}(\overline{T_a})] \quad (1.9)$$

where ∂B_{11} and ∂B_{12} are the changes in radiance at 11 and 12 μm with respect to a given change in temperature. Equations 1.8 and 1.9 can then be substituted into Equation 1.6, which is rearranged to give:

$$B_{11}(\overline{T_a}) = \frac{B_{11}(T_{12}) - \tau_{12}B_{11}(T_s)}{1 - \tau_{12}} \quad (1.10)$$

Equation 1.10 is then equated with Equation 1.5, after rearranging for $B_{11}(\overline{T_a})$. After some manipulation, we obtain:

$$B_{11}(T_s) = B_{11}(T_{11}) + [B_{11}(T_{11}) - B_{11}(T_{12})] \left(\frac{1 - \tau_{11}}{\tau_{11} - \tau_{12}} \right) \quad (1.11)$$

This leads to the generalised split-window algorithm:

$$T_s = a_1 T_{11} + a_2 T_{12} + b \quad (1.12)$$

where b is an offset that corrects for the non-unity of emissivity and other nearly-constant terms, such as CO_2 (Deschamps & Phulpin 1980), and a_1 and a_2 the constants:

$$a_1 = 1 + \left(\frac{1 - \tau_{11}}{\tau_{11} - \tau_{12}} \right) \quad (1.13)$$

$$a_2 = - \left(\frac{1 - \tau_{11}}{\tau_{11} - \tau_{12}} \right) \quad (1.14)$$

These constant terms, or retrieval coefficients, are derived by regressing many TOA BTs against the corresponding SSTs or LSTs to obtain ‘best-fit’ coefficients. The regression data sets may be empirical or theoretical (i.e. simulated TOA BTs using an RT model).

The coefficients for the AVHRR SST retrievals, for example, are derived by regression of many satellite TOA BTs against coincident in situ observations of SST obtained from buoy data (e.g. Li et al. 2001). In contrast, the operational (A)ATSR SST and LST retrieval coefficients are derived theoretically by regressing modelled TOA BTs against the surface temperatures used to simulate those BTs (Závody et al. 1995, Merchant et al. 1999, Prata 2002a). The advantage of this latter approach, is that the retrieved satellite SSTs and LSTs provide observations that are independent of any surface measurements. Further details of SST and LST data derived from the (A)ATSR are given in Chapter 2.

1.3.1.3 Sources of Bias in Infrared Satellite SST and LST Retrievals

As the retrieval coefficients are valid only for the atmospheric conditions from which they are derived, deviations from these conditions may potentially lead to the retrieved SSTs and LSTs being biased from the true values by several tenths of a K (Minnett 1990). The triple-window and multi-angle methods generally achieve better accuracies than the traditional split-window method, as a greater number of observational data are included in the algorithm. This is the subject of Chapter 3 of this thesis, where the differing response to the atmosphere of split-window SSTs and LSTs, and triple and multi-angle SST retrievals from the AATSR, is examined by means of a sensitivity study.

Another source of bias in satellite infrared SST and LST retrievals is surface emissivity. The infrared emissivity of the Earth's oceans is reasonably well known and close to unity. Salinity (e.g. Friedman 1969), windspeed (e.g. Watts et al. 1996, Masuda et al. 1988) and temperature (Newman et al. 2005) have been shown to alter the sea surface emissivity, although estimates of the effects of these phenomena on SST retrievals vary from negligible to a few tenths of a K (depending on the type of retrieval and the study). The infrared emissivity of land, on the other hand, is extremely variable; for example, the AATSR 11 μm channel emissivity of green grass is approximately 0.983, whereas the equivalent typical emissivity of soil is 0.967 (emissivities derived from ASTER Spectral Library (1999)). Some other terrestrial materials (e.g. sand) may have even lower emissivity. The situation is further complicated by the fact that the emissivity of natural land surfaces decreases strongly with viewing angles over $\sim 30^\circ$, where the magnitude of the decrease depends on the surface type (Sobrino & Cuenca 1999). This has severe implications for multi-angle methods of LST retrieval and for observations of LST in regions with high topographic variance. The impact of an inaccurate emissivity correction in an LST retrieval algorithm may lead to biases of several K (Schäädlich et al. 2001). If both emissivity and the atmospheric effects are incorrectly accounted for, the retrieved

LST may be biased from the true value by up to 12 K (Sobrino & Raissouni 2000). In Chapter 3 of this thesis, the impact of changes in emissivity on the AATSR TOA BTs and SST/LST retrievals as a result of these phenomena, are examined.

One of the principal problems associated with satellite SST and LST retrieval is cloud contamination. Unlike microwave radiometers, infrared sensors cannot ‘see through’ cloud. As clouds are generally colder than the underlying surface temperature, the observed TOA BTs will be depressed, where the magnitude of the depression depends on the properties of the cloud and the wavelength of the observations. The reflectivity of clouds at visible wavelengths also differs from that of the surface. Capitalising on these effects, various schemes to detect clouds have been developed utilising data from thermal, visible and near-visible/near-infrared data (e.g. Saunders & Kriebel 1988, Saunders 1986, Ackerman et al. 2002). However, there is much evidence to suggest that, despite these efforts, many clouds still remain undetected in operational satellite data sets (e.g. Jones et al. 1996, Good et al. 2006), and are a major contributor to bias in SST and LST data. As a result, additional screening for cloud, for example by eye, in operational satellite SST and LST data is often required.

1.3.1.4 Validation of Satellite SST and LST

In light of the potential biases introduced into satellite infrared SST and LST retrievals, it is vital that the accuracy of these data is assessed under the full range of expected atmospheric and surface conditions. While theoretical sensitivity studies can be used to investigate and understand biases, it is only through comparison with in situ observations of SST and LST that we can obtain a truly direct assessment of the accuracy of these data. This process is known as ‘validation’. In theory, validation should be an assessment of the atmospheric and emissivity correction. However, as the retrieved SSTs and LSTs are also influenced by errors in the measured satellite TOA BTs, the results of validation experiments are also useful in identifying instrumental problems, such as drift.

Although the concept of validation is a simple one, there are many inherent difficulties in performing such an experiment. Firstly, the in situ measurements are of point LSTs or SSTs (or in the case of a moving ship, for example, the measurements may be integrated along the line of travel), whereas the satellite LSTs or SSTs are representative of larger areas (e.g. 1 km²). As a result, the comparison is not strictly between two equivalent quantities. For SST, this is not usually a particularly troublesome issue, although validation in regions of high temperature gradients, for example, the Bay of Biscay (C. Donlon, personal communication), may be problematic. For LST, on the other hand, up

scaling of point measurements is not well understood, due to the spatial variation of temperature and emissivity. To minimise this problem, validation sites are usually chosen that are homogeneous in terms of these parameters over scales larger than the satellite field of view (FOV); such sites are also topographically flat. However, these sites are very difficult to come by so it is desirable to develop a method of up scaling from in situ point observations of LST to the spatial scale of the satellite. Two such methods are investigated in Chapter 5 within the context of an AATSR LST validation experiment carried out over a heterogeneous field site in Morocco.

Secondly, the in situ measurements are also subject to errors. Current in situ observations of SST are accurate to better than 0.1 K (e.g. Minnett et al. 2001, Parkes et al. 2000, Barton et al. 1995). Uncertainties within in situ LSTs may amount to several tenths of a K or more, when the spatial variability of LST is taken into account. For target accuracies of 0.3 K and 1.0 K for satellite-retrieved SST and LST, respectively, these errors are significant.

Thirdly, the nature of the in situ measurement should be considered carefully in validation experiments. Satellite infrared SSTs and LSTs correspond to the temperature of the top 500 μm or so of the Earth's surface, known as the skin. This skin temperature may be very different from the temperature of the ocean or land below this depth, due to diurnal heating.

The ocean skin effect is well documented (e.g. Minnett 2003, Murray et al. 2000, Schluessel et al. 1990, Donlon & Robinson 1997, Donlon et al. 2002); in particular, Donlon et al. (2002) provide a very clear explanation of this phenomenon. Figure 1.3 shows a schematic representation of the thermal structure of the uppermost 10 m of the ocean for nighttime and daytime during strong winds ($> 10 \text{ ms}^{-1}$), and for daytime for low windspeeds. The diagram shows five definitions of SST:

- SST_{int} - the SST of the infinitely thin layer of ocean at the interface between the ocean and the atmosphere.
- SST_{skin} - the SST of the water below SST_{int} to a depth of approximately 500 μm . This is the SST that infrared satellites observe. The exact depth of SST_{skin} depends on the wavelength of the observations (the variation in SST_{skin} as a function of wavelength is very small - e.g. 0.01K).
- $SST_{subskin}$ - the SST at the bottom of the SST_{skin} layer, which extends to approximately 1 mm depth, known as the subskin SST. This is the SST observed by microwave radiometers.

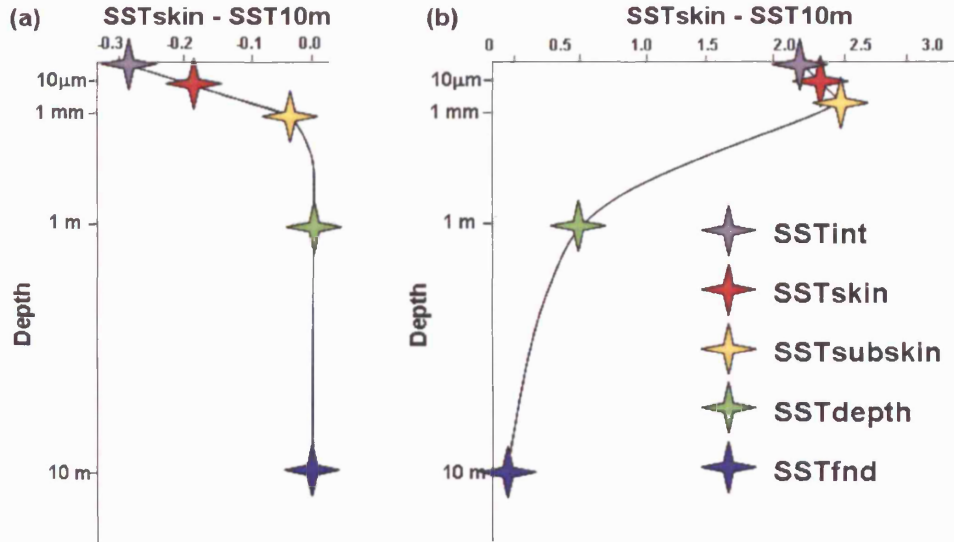


FIGURE 1.3. Schematic representation of the thermal structure of the uppermost 10 m of the ocean for (a) nighttime and daytime during strong wind conditions and (b) daytime for low windspeeds. For explanation of the SSTs annotated in this diagram, see Section 1.3.1.4. (Figure provided by C. Donlon of the Met. Office; also see Donlon et al. (2002)).

- SST_{depth} - the SST between approximately 1 and 10 m depth (sometimes referred to as ‘bulk’ SST, or BSST). This is the SST measured by buoys, for example.
- SST_{fnd} - the foundation SST, where the effects of diurnal heating are negligible.

During the day, under conditions of low wind speed, SST_{skin} is typically several tenths of a K warmer than SST_{bulk} ; in some cases, extremes of up to 2 K have been observed. However, under conditions of high wind speed ($> 10 \text{ ms}^{-1}$), the skin-bulk difference asymptotes to a value of approximately -0.15 as a result of mixing (Donlon et al. 2002). SST_{skin} is approximately 0.2 to 0.3 K cooler at night when solar heating is absent (Minnett 2003, Murray et al. 2000, Donlon et al. 2002).

Thermal stratification of LST also occurs, although the situation is complicated further by the introduction of canopy temperatures, which may also differ from the (soil) skin temperatures. As a result, in situ validation results should be interpreted with care. SSTs and LSTs derived from ground-based radiometric measurements are preferred for validation, as they are also sensitive to the temperature of the skin. However, such data are relatively rare and usually restricted to specific validation experiments (e.g. research

ocean cruises, or instrumented land sites). Data collected by other means, for example, ocean buoys, are still extremely useful for validation, although significant uncertainties can be introduced as a result of the skin-bulk difference; Kearns et al. (2000) estimate that this error is of at least the same order as the error in the satellite SST retrieval. The main advantage of these data is the wider geographical and temporal coverage, which results in a high number of coincident satellite matchups.

Lastly, additional errors may be introduced into the validation data set as a result of spatial and temporal mis-location between the satellite and in situ data. For example, an in situ radiometer making observations of LST may only provide data every few minutes. As the satellite overpass takes only a fraction of a second, there is likely to be a temporal offset between the two observations, during which diurnal warming or cooling may have taken place. This is particularly significant for validation of LST due to its the diurnal cycle. The geolocation (i.e. the latitude and longitude of satellite pixels) of satellite data may also be offset from the true location. For example, the geolocation of MODIS pixels over land is estimated to be accurate to between 100 and 300 m (Z. Wan, personal communication). As a result, it is possible for the incorrect satellite pixels to be used in validation against point observations of SST or LST. The use of homogeneous validation sites can minimise this problem.

Despite these problems, validation is an essential part of developing any satellite product. Ideally, satellite SSTs and LST should be validated at many locations over long periods of time so that any seasonal biases can be identified. This is perhaps even more important for LST, as atmospheric and surface conditions are more extreme over land and obtaining accurate retrievals is more challenging.

1.4 Summary

Global measurements of SST and LST are important for many climate-related studies. For SST, these data are required to an accuracy of 0.3 K or better for many applications. The accuracies desired for LST are between 0.5 K and 1.0 K. User requirements for the spatial resolution of these data may approach 1 km, with a temporal frequency of between hours and weeks, depending on the application. However, for most LST applications, knowledge of the diurnal cycle is required, thus measurements of LST are usually required with a temporal frequency of hours, or even minutes.

Satellite observations provide an excellent way to obtain these data on a global scale over a relatively short period of time (minutes to days). In particular, satellite infrared

radiometry provides the radiometric accuracy and spatial resolution to address the most stringent requirements of data users. However, satellites cannot provide direct measurements of SST or LST. Instead, these parameters are derived from TOA radiances measured by the sensor, which must be corrected for the attenuation of the surface-emitted signal by the atmosphere, and non-unity of the underlying surface emissivity.

A common approach to correct for the effects of the atmosphere is to utilise data from multiple radiometer channels. As atmospheric absorption and scattering is wavelength-dependent, the difference between measurements made in these channels can provide an estimate of the attenuation of the atmosphere. The most frequent approximation of this type of retrieval is known as the split-window method. This method involves using data from two radiometer channels centred in the atmospheric window at wavelengths of around 11 and 12 μm . This multi-channel approach has been developed further in some retrieval schemes by using data from an additional channel at approximately 3.7 μm , and/or data from more than one view of the Earth's surface. In general, these enhanced retrievals provide a better atmospheric correction, and thus a better estimate of the temperature of the ground. Although the multi-channel/view retrieval algorithms are usually expressed as a linear combination of TOA BTs, their physical definition is derived from the RT equation. These coefficients can be derived empirically (i.e. via regression of TOA BTs against in situ observations of SST or LST), or theoretically, using an RT model, and usually contain a correction for surface emissivity.

Operational satellite SST and LST data sets are derived from several satellite-sensors. Of these, the polar-orbiting ATSR series has the potential to provide the most accurate, long-term observations of SST and LST, as it has a radiometric accuracy that is unrivalled by any other existing infrared sensor. In addition, the ATSR retrieval coefficients are derived theoretically, providing SSTs and LSTs that are independent of surface measurements. However, there are several other operational infrared sensors that are providing vital climatological data. In particular, the geostationary Meteosat-8 satellite makes thermal observations of the surface every 15 minutes, providing the temporal resolution required for many LST applications. Although polar-orbiting sensors, such as the (A)ATSR may not provide the temporal coverage required for these applications, they have a higher spatial resolution (e.g. 1 km compared to >3 km for geostationary). Current research is exploring the possibility of producing an LST data set derived from both polar-orbiting and geostationary LST data, which will have the spatial resolution of the former and the temporal resolution of the latter. Such a data set could potentially be of great use to the climate-science community.

There are many sources of bias in satellite SSTs and LSTs. Atmospheric and emis-

sivity effects typically result in biases of several tenths of a K (often more for LST), if not corrected for sufficiently. The challenge of obtaining accurate observations of LST is greater than that for SST due to the heterogeneity of land. These biases may be investigated by means of sensitivity studies. However, the only truly direct assessment of the accuracy of these data is through validation against in situ observations of SST and LST. Validation experiments are a vital part of the development of any satellite SST or LST product. Although a simple concept, there are a number of issues that may compromise the usefulness of the validation experiment, such as in situ measurement errors, the nature of the in situ data and up scaling from point measurements to the spatial scale of the satellite. These issues should be considered together with the results of any validation experiments. Ideally, such experiments should be carried out in many locations over long periods of time, and under the full range of expected atmospheric and surface conditions, in order to characterise any biases.

The purpose of this thesis is to investigate the accuracy of operational retrievals of SST and LST from the AATSR. This is performed through a combination of RT simulations, to identify sources of bias in the operational retrievals, and in situ validation. Although carried out specifically for the AATSR instrument specifications, the results of the RT simulations are applicable to both the ATSR-1 and ATSR-2 instruments, as the design specifications are very similar to those of the AATSR. The validation results presented in this study represent some of the first for the AATSR, and form an integral part of the overall AATSR validation programme.

Chapter 2

The Along-Track Scanning Radiometer

Launched on board ESA's ENVironment SATellite (Envisat) in March 2002, the Advanced Along-Track Scanning Radiometer (AATSR) is the third in a series of instruments with the primary objective of providing global, accurate SST data. Although all three Along-Track Scanning Radiometers (ATSRs) have a common heritage, the instrumental design has undergone several modifications since the launch of the first ATSR (ATSR-1) on board the European Remote Sensing Satellite-1 (ERS-1) in July 1991. The following chapter describes the AATSR instrument, data from which constitutes the focus of this scientific study.

2.1 Heritage of the AATSR instrument

The ATSR-1 was an experimental instrument designed to address the Tropical Ocean Global Atmosphere (TOGA) project of the World Climate Research Programme (WCRP) specification for latitude-dependent accuracy of 0.3 - 0.5 K for observations of SST (World Meteorological Organization 1985). The design of this instrument was based on the multi-channel approach to SST retrieval, described in Chapter 1, that had been developed for the NOAA AVHRR. However, this instrument had a number of novel features that were different from previous instruments of its type. These features included an exceptionally stable on-board calibration system and Stirling-cycle cooled detectors, providing extremely high radiometric accuracy and precision. In addition, the instrument had the ability to make measurements of TOA BT at an angle of approximately 55° from zenith as well as the traditional nadir-view utilised by instruments such as the AVHRR. This design feature allows the same point on the Earth's surface to be viewed through

two different atmospheric path lengths and enables an improved atmospheric correction to be made during the SST retrieval process.

The success of the ATSR-1 instrument led to the launch of the ATSR-2 in April 1995 on board ERS-2. The ATSR-2 had similar specifications to ATSR-1, but with the inclusion of three visible channels at 0.55, 0.66 and 0.87 μm in addition to the near-infrared/infrared channels at 1.6, 3.7, 11 and 12 μm present on the ATSR-1 (Table 2.1). These visible channels were added to extend applications of ATSR data to studies over land (e.g. vegetation indices). The 3.7, 11 and 12 μm channels are used for surface temperature retrieval, with the 1.6 μm channel used predominantly for cloud-clearing. The ATSR-1 continued operations until June 1996, although the 3.7 μm channel failed on 27 May 1992. At the time of writing, the ATSR-2 instrument is still in operation. However, the accuracy of the ATSR-2 geolocation has been compromised since the failure of a gyroscope on board the ERS-2 satellite on 17 January 2001.

The AATSR was launched on board the Envisat satellite in March 2002. The design specifications of this most recent ATSR were based on the previous ATSR missions, with the main difference being the availability of the data in 12-bit digital resolution for all channels over the entire swath throughout the orbit. This is an improvement over the ATSR-2, which employed an optional low-rate mode with 8-bit digitisation, or reduced swath width with 12-bit digitisation, for its visible channels when other ERS-2 payload instruments were active. A number of enhancements have also been made with respect to the processing of AATSR data, compared to ATSR-1/2 data, including the use of a more accurate ellipsoidal, rather than spherical, geometry in the geolocation scheme and the inclusion of a topographic correction to improve the geolocation of land pixels. Together, the ATSR series of instruments have the potential to provide more than 15 years of global SST data with the accuracy and continuity that is required for identifying long-term global climate trends.

2.2 The AATSR Instrument

The AATSR instrument is one of ten instruments on board ESA's Envisat Satellite. The satellite is in a sun-synchronous polar orbit at a nominal height of approximately 800 km above the Earth's surface, resulting in a 35-day repeat cycle. The altitude of Envisat can be altered such that 3- and 168-day repeat cycles can also be employed. However, with a swath width of 512 km, the AATSR is unable to achieve global coverage in the case of the 3-day repeat cycle. Local overpass time was selected to be 10:00/22:00 to

Table 2.1. ATSR spectral channels (adapted from Llewellyn-Jones et al. (2001)).
Channels exclusive to ATSR-2 and AATSR are denoted by *.

Channel	Central Wavelength	Bandwidth	Primary Application
μm	μm	μm	
0.55*	0.555	0.02	Chlorophyll
0.66*	0.659	0.02	Vegetation index
0.87*	0.865	0.02	Vegetation index
1.6	1.61	0.30	Cloud clearing
3.7	3.70	0.30	Sea surface temperature
11	10.85	1.00	Sea surface temperature
12	12.00	1.00	Sea surface temperature

optimise illumination conditions for the optical instruments on board Envisat. Furthermore, this overpass time is some hours from the peak of the diurnal temperature cycle (approximately 3pm, local solar time), thus minimising the occurrence of saturation of the AATSR infrared channels, particularly over land, and the impact of the skin effect on the SST datasets (Chapter 1). This day time overpass time also benefits SST and LST retrievals in that the surface-air temperature difference is not at a maximum; as we shall see in Chapter 3, this affects the biases of the retrievals, particularly for LST, where the surface-air temperature difference may be several K. The following section summarises the main characteristics of the AATSR instrument design and function, based on the description of the AATSR given by ESA (2002*b*) and the ATSR-1 (which has a similar design to the AATSR) given by Mason (1991).

The AATSR instrument consists of three principal components: the Infrared and Visible Radiometer (IVR), the Instrument Electronics Unit (IEU) with the Black Body electronics Unit (BBU) mounted on top, and the Digital Electronics Unit (DEU)/Power Conditioning and Switching Unit (PCSU)/Digital Bus Unit (DBU). The IVR is the actual instrument itself, containing the scan mirrors, calibration sources and detectors, while the other components control the instrument operations (e.g. scan mirror drive control) and data formatting.

Figure 2.1 shows a diagram of the IVR with the main features labeled. Visible and infrared radiation is reflected from the scan mirror onto an off-axis paraboloid mirror, which, in turn, reflects the energy into the visible and infrared Focal Plane Assemblies (FPA). The reflected radiation passes through a single field stop to ensure good spatial

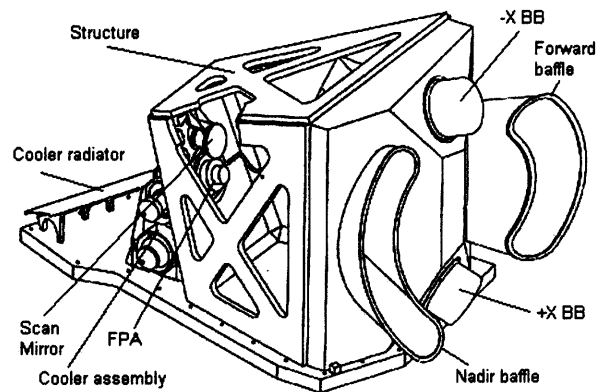


FIGURE 2.1. The AATSR Infrared and Visible Radiometer (IVR). Labels show the location of the Focal Plane Assembly (FPA), the cold and hot calibration black bodies (-X BB and +X BB) and the curved Earth view apertures, which are protected by baffles to limit stray radiation from entering the instrument. Figure reproduced from ESA (2002*b*).

co-registration between the Instantaneous Field Of View (IFOV) of each of the seven channels. Beamsplitters then separate the radiation, which is directed on to the detectors by mirrors or lenses (depending on the channel). The radiative signals are then converted into electrical signals by the detectors. The four infrared detectors are cooled to 80 K by a pair of Stirling cycle coolers, where the heat dissipated by the coolers is radiated into space via a thermal radiator. The visible detectors are maintained at ambient temperature. Once converted to electrical signals in the FPA, the signals are amplified by a signal-preamplifier before being digitised and transmitted back to Earth by other systems on the Envisat satellite.

To achieve the dual-look that is unique to the ATSR instrument design, the scan mirror is rotated through a cone-angle of 46.956° orientated such that the two extreme viewing angles are at true nadir (0.0° - i.e the sub-satellite point) and forward at 46.956° from the true nadir. As the Earth is curved, this forward view makes an angle of approximately 55° with the normal at the Earth's surface (zenith angle), as shown in Figure 2.2. This angle was selected to achieve a balance between increased atmospheric path length to ensure a good atmospheric correction, and an angle that was not so oblique that the dominant contribution to the measured signal would be from the middle atmosphere, thus masking the atmospheric effects in the troposphere (Závodý et al. 1995). In addition, emissivity effects may become more significant for larger viewing angles (Masuda et al. 1988, Watts et al. 1996).

The scan cycle of the AATSR is shown in Figure 2.3. Two infrared calibration black

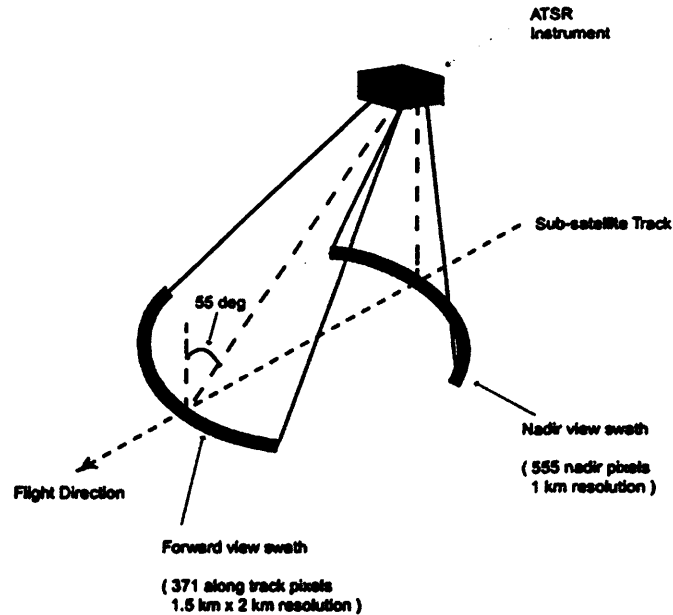


FIGURE 2.2. The AATSR scan geometry showing the forward and nadir views relative to the sub-satellite track. Figure reproduced from ESA (2002b).

bodies and a visible calibration target are viewed each scan along with the data from both the nadir and forward views. The entire scan sequence takes 0.15 seconds, during which time signals for 2000 pixels are integrated. Of these, 974 pixels contain data that correspond to the Earth views or calibration targets, where 555 comprise the nadir view, 371 the forward view and 16 pixels for each of the three calibration targets. The remaining pixels correspond to views of the instrument interior. This pixel integration time results in a nominal pixel size of approximately 1.0 km^2 and $1.5 \text{ km} \times 2 \text{ km}$ at the centre of the nadir and forward views on the Earth's surface, respectively. The nominal pixel size was selected on the basis that at least 500 samples should be cloud-free within a $0.5^\circ \times 0.5^\circ$ cell for adequate noise reduction achieved by averaging over this cell. The requirement also states that at least 20% of pixels within the cell must be cloud free. Considering these requirements, 2500 pixels are required in each cell, giving a sample size of 1 km at nadir (Llewellyn-Jones et al. 2001). During each scan cycle, the sub-satellite point on the Earth's surface moves forward by 1 km. The orbit height and scan angle of the satellite results in a forward-nadir view separation of 1000 km on the ground, which translates into a temporal difference of 150 seconds between the two views for a single point on the Earth's surface.

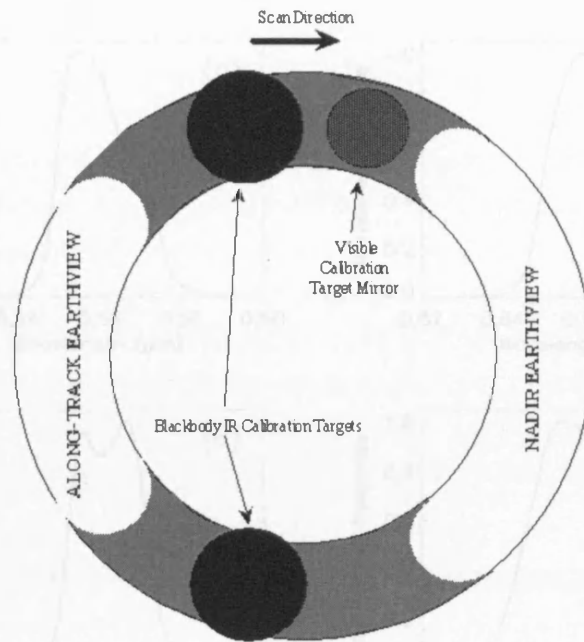


FIGURE 2.3. The AATSR scan cycle showing the forward and nadir Earth view apertures, infrared calibration black bodies and visible calibration target. Figure reproduced from ESA (2002b).

2.2.1 Spectral Channels

The AATSR Infrared Visible Radiometer (IVR) spectral channels are given in Table 2.1. These include the two split window channels at 11 and 12 μm for SST and LST retrieval; a third infrared channel at 3.7 μm is available for triple-window SST retrievals (currently, this channel is not used for LST), although this channel is only used at night as it is affected by solar radiation during the day. The selection of these wavelengths for remote sensing of SST and LST is based on the relative transparency of the atmosphere in these regions of the electromagnetic spectrum, as detailed in Chapter 1. The three visible channels are used for remote sensing of vegetation, and the 1.6 μm channel for cloud-detection. The spectral responses of all seven AATSR channels are shown in Figure 2.4. As the focus of this thesis is SST and LST retrievals from the AATSR, the data products and characteristics of the visible and 1.6 μm channels are not discussed further in any detail.

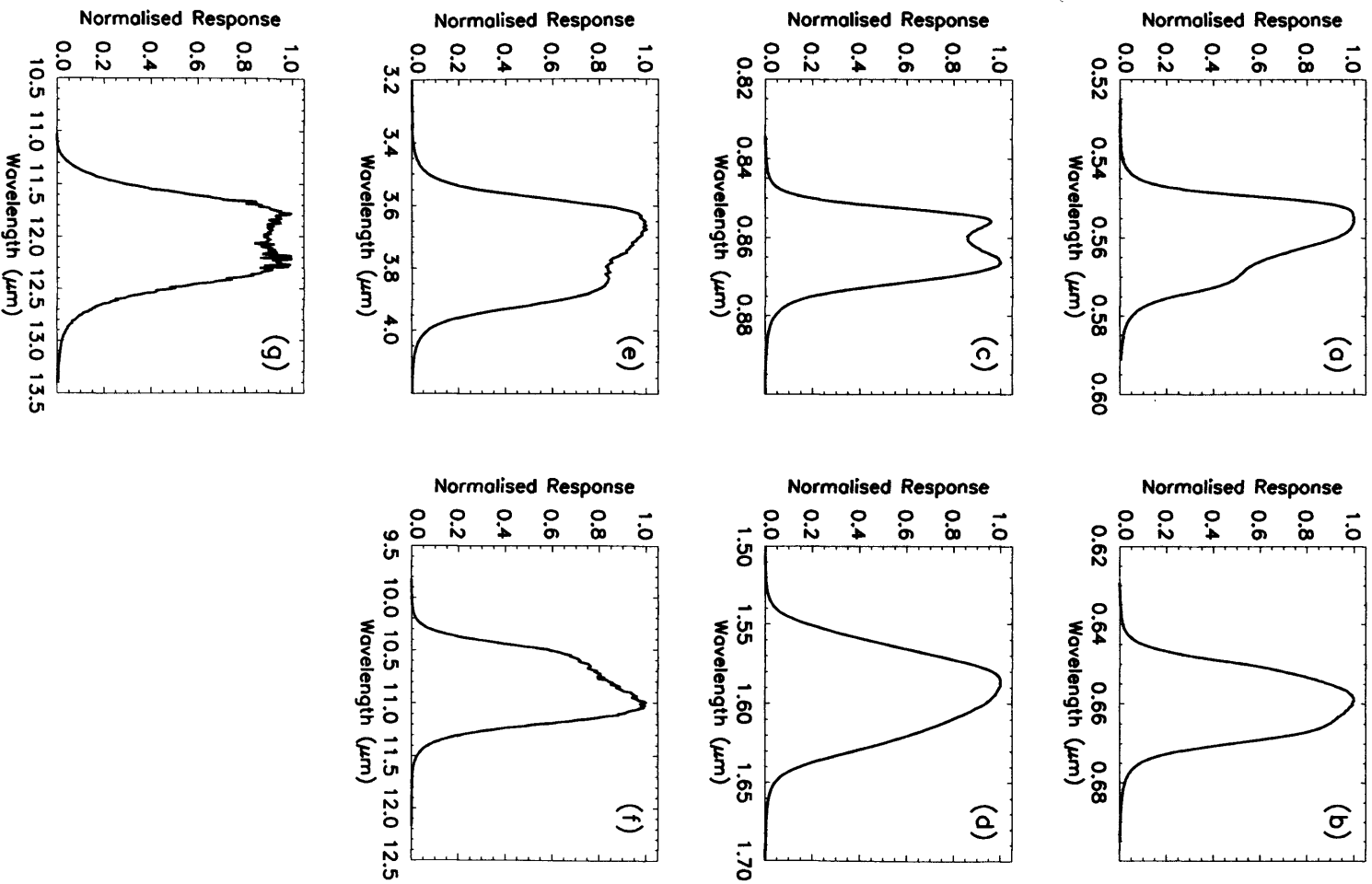


FIGURE 2.4. Measured AATSR instrument response curves (a) 0.55 μm , (b) 0.66 μm , (c) 0.87 μm , (d) 1.6 μm , (e) 3.7 μm , (f) 11 μm and (g) 12 μm (data courtesy of D. Smith of RAL).

2.2.2 Instrument Field of View

Figure 2.5 shows the Instantaneous FOV (IFOV) for each of the AATSR spectral channels. The most noteworthy feature is the spatial variation in sensitivity, particularly for the 11 and 12 μm channels. This can be an important feature to take into account when interpreting measurements made by the instrument, as the tendency is to consider the 1-km data as a simple average over each 1-km grid box. A further complication to consider is the true extent of the FOV when ‘projected’ on the Earth’s surface. Although usually quoted as 1 km, the true FOVs of the AATSR channels actually extend beyond this nominal pixel size. Moreover, as the zenith angle departs from true nadir, the FOV becomes even more extended (this is why the forward view pixel size is usually quoted as 1.5 km \times 2 km), and appears ‘smeared’ in the direction of the scan.

Figure 2.6 shows the 11 μm channel FOV at the centre and edges of the AATSR swath, for both the forward and nadir views. For the centre of the nadir and forward views (i.e. zenith=0° and 55.345°, respectively), the FOV is symmetrical. In the case of the former, the FOV extends to almost 2 km in the across-track direction, although most of the sensitivity is concentrated in the central 1 km. For the forward view, the true FOV covers an area on the ground of more than 2 km \times 2 km. At the edges of the swath, the FOV is angled in the direction of the scan, such that even the nadir-view pixels extend to almost 2 km in the along-track direction.

For most applications, consideration of the true FOVs of the AATSR spectral channels will not be important, particularly if using the spatially-averaged data. However, in some cases this may have a significant bearing on the interpretation of these data; for example, when validating satellite-derived surface temperatures with in situ point measurements in an area where there is significant (relative to the accuracy requirements) variation of temperature on the sub-pixel scale. These effects are investigated further in Chapter 5, where the impact of the true FOV of the AATSR thermal channels is considered over an LST validation site that is heterogeneous in terms of LST on the sub-pixel scale.

2.2.3 Calibration of Infrared Channels

As shown in Figure 2.3, measurements of two high-quality black body targets are made during each scan cycle (i.e. for each row of nadir/forward pixels) to allow near-real-time calibration of AATSR infrared channels during ground processing (Section 2.3). The black bodies are cylindrical cavities with a conical base and lined with non-reflecting

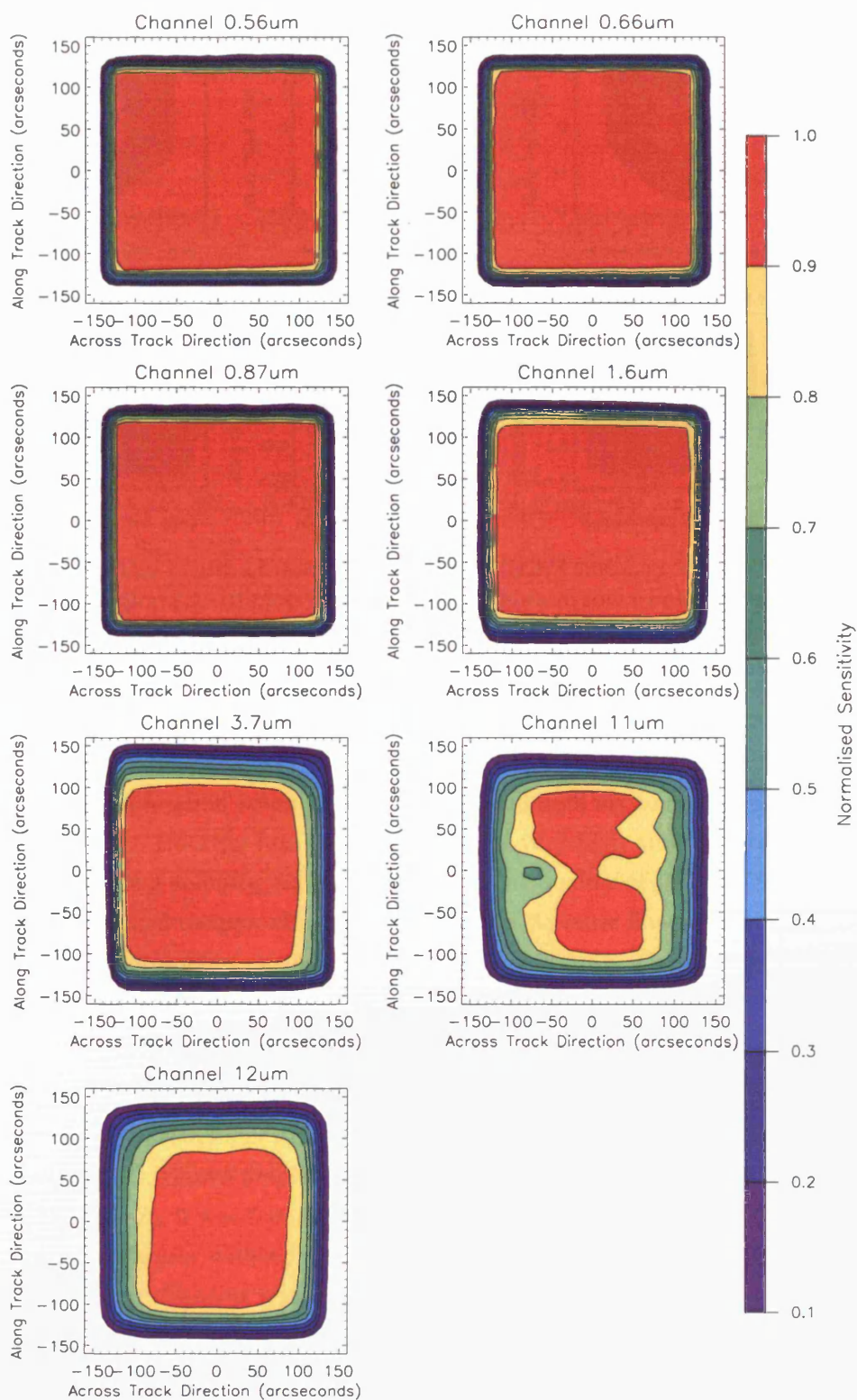


FIGURE 2.5. Measured AATSR IFOVs corresponding to each of the 7 spectral channels of the AATSR (data courtesy of D. Smith of RAL).

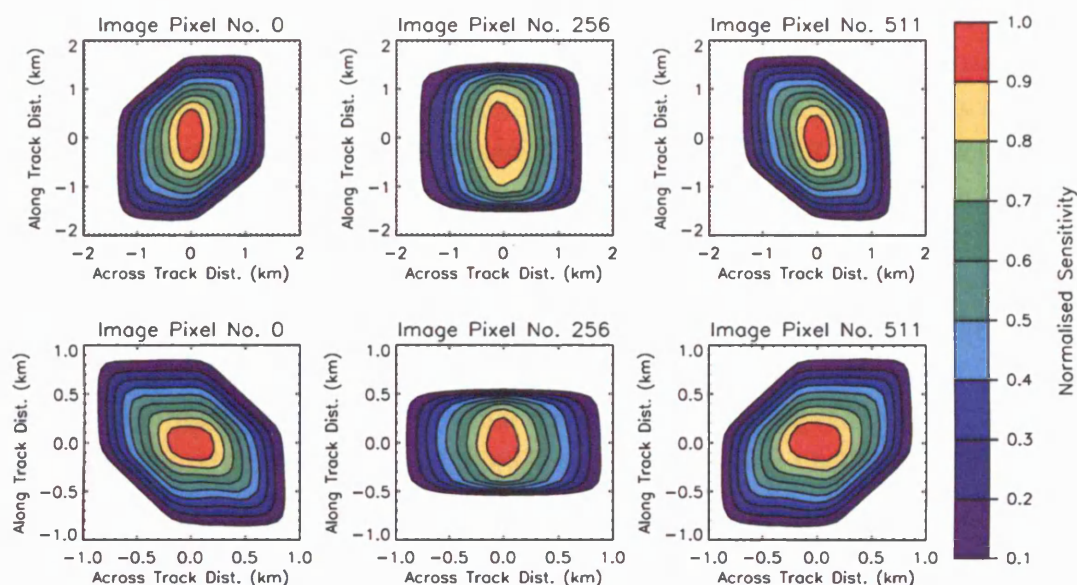


FIGURE 2.6. The $11\ \mu\text{m}$ channel FOV over the Earth's surface corresponding to the forward view (top row of plots) and nadir view (bottom row of plots), for the centre (pixel number 256) and edges (pixels 0 and 511) of the AATSR swath (data courtesy of D. Smith of RAL). NOTE: different x and y scales have been employed for the nadir and forward FOV maps.

coatings. The calibration sources are well insulated with six temperature monitors in each black body. Both cavities are designed to a very high specification in order to achieve exceptional stability, as this is critical to the quality of the AATSR data. One black body is heated to approximately 305 K, while the other floats at the ambient temperature of the fore-optics enclosure (approximately 265 K). These temperatures span the expected range of marine BTs.

Pre-launch calibration of the infrared channels was carried out over a range of target temperatures between 210 and 315 K, using high-accuracy black bodies (overall calibration accuracy $< 0.04\ \text{K}$) that can be traced to international standards. After correction for non-linearity (a known property of the detectors - similar non-linearity was observed for ATSR-1 and -2), it was found that the AATSR-observed BTs were within 50 mK of the target temperatures within the range of 240-315 K. Below 240 K, the deviation of the 11 and $12\ \mu\text{m}$ channels was found to increase up to 0.1 K at 210 K. This result is well within the radiometric accuracy specification of better than 0.1 K for the AATSR infrared channels. Further details of the pre-launch calibration results can be found in Smith et al. (2001).

The in-flight performance of the AATSR is monitored continuously to ensure that this high level of radiometric accuracy is maintained. Variation of the Noise Equivalent Δ Temperature (NE Δ T) over each of the calibration black bodies since the start of the mission indicates a good degree of stability since January 2003, nine months after the launch of the instrument. For the 11 and 12 μm channel, the NE Δ T is approximately 30 mK over both black body targets; for the 3.7 μm channel, where the non-linearity of the planck function is more apparent, the NE Δ T values are approximately 75 mK and 30 mK for the cold and hot targets, respectively. Marked increases in the NE Δ T of the order of 10-20 mK for all three channels over both black bodies have been observed in both May 2003 and May 2004, which corresponds to the peak of the thermal cycle of the Envisat orbit. A similar increase was not observed in May 2005 (see http://aatsr2.ag.rl.ac.uk/data2/aatsr2/EDS-X/MissionTrends/Trends_Plots).

The stability of the black body targets themselves is assessed by performing black-body crossover tests. In brief, this consists of cooling the hot black body target to the ambient temperature of the instrument and heating the cold black body to approximately 305 K. During the respective cooling/heating process, there will be a point when temperatures of the two black bodies will be the same (the cross-over). Radiometric temperatures obtained at this point over both targets can then be compared, with the differences used to ascertain any drift in the black body thermometer calibration or emissivity degradation of the black bodies. Results from the crossover test performed in April 2004 indicate that, relative to each other, the errors in the BTs over the black bodies are less than 10 mK. These results are consistent with the first crossover test carried out during the commissioning phase in April 2002, indicating that there has been no significant degradation in the emissivity or infrared calibration targets or thermometry (Smith 2004).

2.2.4 Comparison of AATSR and ATSR-2 BTs

To quantify the performance of the AATSR against that of the ATSR-2, an intercomparison of BTs and operationally-retrieved SSTs from each instrument has been carried out at Rutherford Appleton Laboratories, UK, using data from six orbits covering one month of the mission. As the AATSR and ATSR-2 are currently operating in tandem mode, with the latter overpassing 30 minutes after the AATSR, the observed differences are an indication of their relative performance.

For the 3.7 and 11 μm channels, these differences were found to be small (26-67 mK). However, it was found that the AATSR 12 μm channel was systematically cooler than the ATSR-2 equivalent by approximately 0.2 K, which cannot be explained by differences

between the pre-launch measured channel spectral responses, noise or diurnal warming (the offset would be apparent in the other channel BTs). Changes in the cloud cover in the FOV and errors due to the geolocation of the ATSR-2 data have also been rejected as possible causes of this disagreement, as these are random and would not cause a systematic bias (Nightingale & Birks 2004). The exact cause of the bias is still unknown, but recent research at RAL suggests that spectral band leakage in the AATSR 12 μm channel could explain the observed cool offset.

2.3 AATSR TOA BTs

The 14 orbits of AATSR data acquired each day are transmitted to one of four ground stations at Kiruna, Fucino, Villafranca and Svalbard. The following section summarises briefly the processing of the infrared data from raw scan pixel counts to gridded BTs; further details can be found in ESA (2002*b*).

After reception, the raw AATSR data are converted into a Level-0 product containing a chronological sequence of records where each record contains a single instrument source packet, representing a single AATSR scan cycle. In general, this data product is not made available to users.

The next stage of processing is conversion of the Level-0 product to the Level-1b product, which contains calibrated, geolocated TOA BTs and reflectances, with complementary cloud and land identification flags. These data are available either at full resolution (1 km) or spatially averaged (10 or 30 arc minute, and 17 km or 50 km).

2.3.1 Processing of Calibration Data

Once the Level-0 source packet data have been unpacked and validated, calibration of the infrared and visible channels is carried out. For the infrared calibration, the gain and offset of each channel are determined by establishing the relationship between the hot and cold blackbody targets and the corresponding AATSR pixel counts. The relationship is resolved by solving simultaneous equations in the form of $y=mx+c$:

$$S_{cold} = GL_{cold} + S_0 \quad (2.1)$$

$$S_{hot} = GL_{hot} + S_0 \quad (2.2)$$

where S_{cold} and S_{hot} are the signals measured over the cold and hot blackbody targets, respectively, G is the channel gain and S_0 , the channel offset. L_{cold} and L_{hot} , are the radiances from the cold and hot blackbody targets, determined from the measured blackbody temperatures on board the IVR for each channel. Look-up tables are used to perform this radiance conversion (as the calibration targets are not perfect blackbodies), with a further correction incorporated to account for the background (fore-optics) temperature. These look-up tables also include a correction for detector non-linearity. Using Equations 2.1 and 2.2, the radiometric gain and offset are calculated, where:

$$G = \frac{S_{hot} - S_{cold}}{L_{hot} - L_{cold}} \quad (2.3)$$

Substituting for G , we obtain an expression for the offset:

$$S_0 = S_{cold} - GL_{cold} \quad (2.4)$$

In practice, the gain and offset are determined from an average of several source packets where the nominal value for each ‘calibration period’ is ten scans. The derived gain and offset values for each calibration period are applied to all Earth-view pixels integrated during the calibration period.

2.3.2 Regridding and Geolocation

The geodetic latitude and longitudes of the scan (instrument) pixels are mapped onto a Cartesian frame of reference through knowledge of the satellite position and angle of the scan mirror. The geodetic latitude and longitudes are then derived from these coordinates. To reduce processing requirements, this is carried out for a subset of tie-point pixels, where a linear interpolation in terms of scan number and scan angle is used to establish the coordinates of the intermediate pixels. This procedure is carried out separately for each of the nadir and forward views.

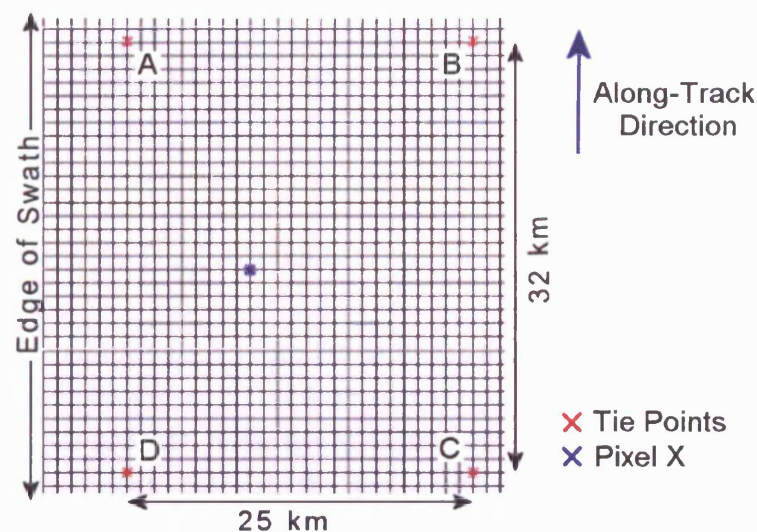


FIGURE 2.7. Illustration of the relationship between geolocation tie points (red crosses, labelled A, B, C and D) and image pixels (black squares). Tie points occur every 32 km in the along-track direction and 25 km in the across-track direction.

The map coordinates of the instrument pixels are used to regrid the pixels onto a rectangular grid, in order to correct for the curved swath of the AATSR and ensure collocation of the nadir and forward views. Any gaps in the image array that result from the regridding process are cosmetically filled with the value of the nearest neighbour pixel. This is particularly common in the forward view, where the pixel size is much larger than that of the nadir. The final product is a 512 km-wide regular grid of image pixels at 1 km spatial resolution.

The associated geolocation information is delivered to the user in the form of latitude and longitude tie points, which occur every 25 km across track and 32 km along track. There are 23 tie points in the across track direction, where the central tie point lies at the centre of the nadir-ground track between image pixels 255 and 256 (pixels number 0-511), and the first and last tie points occur outside the edges of the swath. The tie points correspond to the bottom left hand corner of an image pixel when looking in the along-track direction. Figure 2.7 illustrates the relationship between image pixels and geolocation tie points.

A linear interpolation using three tie points is used to determine the latitude and longitude of each pixel within the 25×32 block of pixels, known as a granule. The latitude and longitude of the bottom left hand corner of a point x within a granule, can be expressed as:

$$lat_x = lat_A + \left(\frac{\delta AB}{AB}\right) \cdot (lat_B - lat_A) + \left(\frac{\delta AD}{AD}\right) \cdot (lat_D - lat_A) \quad (2.5)$$

$$long_x = long_A + \left(\frac{\delta AB}{AB}\right) \cdot (long_B - long_A) + \left(\frac{\delta AD}{AD}\right) \cdot (long_D - long_A) \quad (2.6)$$

where $lat_{(a,b,d,x)}$ and $long_{(a,b,d,x)}$ are the latitudes and longitudes, respectively, of the points in question (see Figure 2.7). δAB and δAD correspond to the distances (from A) along the lines AB and AD, respectively, to the point x . Equations 2.5 and 2.6 can be adjusted easily in order to calculate the geolocation of the centres of the image pixels, by adding 0.5 to the terms δAB and δAD . The geolocation of the tie points is exact with estimated errors in geolocation of the non-tie point pixels, incurred as a result of the interpolation, of < 0.001 degrees (i.e. approximately $\frac{1}{10}$ th of a pixel). This estimate has been obtained by comparing interpolated geolocation information at C with the actual tie point value.

Over land, additional tie point corrections are also derived from a Digital Elevation Model (DEM) to account for topographic variation, which are delivered to the user together with the tie point latitudes and longitudes.

2.3.3 Land and Cloud Flagging

Additional cloud and confidence information is supplied with the Level 1B image and geolocation information. These data include a land flag, derived from an external auxiliary file, and the results of a number of cloud tests that are carried out on the Level 1B BTs during the data processing. These cloud tests are summarised in Table 2.2, with those denoted by * based on methods developed by Saunders & Kriebel (1988) for the AVHRR (see also Závody et al. (2000) for details). The thresholds quoted have been obtained from the current operational auxiliary cloud file, ATS_CL1_AXVIEC20020123_073044_20020101_00000, at the time of writing.

All the cloud tests are carried out separately for the nadir and forward views, with the exception of those that use a combination of data from both views. Tests utilising the $1.6 \mu m$ channel are only implemented during the day as this channel is not available at night. Similarly, tests involving the $3.7 \mu m$ channel are only carried out on night time data. Some of the tests are restricted to ocean pixels as the quantities tested will

be affected by the heterogeneity of land surfaces. For example, the $1.6\ \mu\text{m}$ test is not used over land as the reflectivity in this spectral region is too variable. Similarly, tests involving data from both the nadir and forward views are not implemented over land, as the emissivity in the forward view has a strong dependence on topography and land surface type (Chapter 1).

The tests are carried out in the order in which they are listed below, as some of the tests are only implemented based on the results of previous tests. A pixel is flagged cloudy if any of the tests indicate the presence of cloud.

2.4 AATSR SSTs and LSTs

Level 2 SST and LST products are operationally generated by ESA from the Level 1B TOA BT data described in Section 2.3. This involves converting the TOA BTs directly to SSTs or LSTs by means of pre-determined retrieval coefficients. As for the TOA BT data, these data are available at either full resolution or as spatially averaged data. The final sections of this chapter describe the retrieval algorithms used to produce these data.

2.4.1 Sea Surface Temperatures

The principal objective of the (A)ATSR mission is the provision of accurate, global measurements of SST, with a target absolute uncertainty of $\pm 0.3\ \text{K}$, 1σ . As described in Chapter 1, the retrieval of SST from satellite-measured TOA BTs can be carried out using the split-window methodology, which expresses SST as a linear function of BTs multiplied by retrieval coefficients. The (A)ATSR SST retrieval scheme is based on this approach, where the coefficients are derived theoretically using a RT model and a set of atmospheric profiles. This theoretical methodology is in contrast to that utilised in other SST retrieval schemes, such as the AVHRR, for which coefficients are derived empirically using SST data from buoys. The advantage of the theoretical approach is that the retrievals provide an SST independent of any surface measurements.

Coefficients are derived for four different SST retrievals: a nadir-view, two-channel retrieval (N2), which is the true split window algorithm; a dual-view, two-channel retrieval (D2), which uses data from the split-window channels at $11\ \mu\text{m}$ and $12\ \mu\text{m}$ from both the nadir and forward views; a nadir-view, three-channel retrieval (N3), which uses data from the three thermal channels at 3.7 , 11 and $12\ \mu\text{m}$; and finally, a dual-view,

Table 2.2. Summary of AATSR cloud tests. Column 'Channel' depicts the channels used in the tests, 'Day/Night' whether the test is implemented during the day or night, and column 'Ocean/Land', whether the tests are carried out over ocean or land pixels. Tests denoted by * based on methods developed by Saunders & Kriebel (1988) for the AVHRR.

Test	Channel	Day/Night	Ocean/Land	Description
Gross Cloud	12 μm	Day/Night	Ocean	Works on the principle that cloud is colder than the surface. If the BT of a pixel is lower than a given threshold, the pixel is flagged cloudy. The chosen threshold depends on time of year and geographical location (nadir range: 268.74-283.88 K; forward range=266.83-280.41 K).
Thin Cirrus*	11/12 μm difference	Day/Night	Ocean/Land	BT difference may be large over optically thick cirrus due to emissivity differences at these wavelengths. If the difference is above a threshold, the pixel is flagged cloudy. The chosen threshold depends on view angle and the 11 μm BT (nadir range=0.092-0.609 K; forward range=0.146-0.711 K).
Medium/High Level Cloud*	3.7/12 μm difference	Night	Ocean/Land	If the difference is greater than a given threshold, the pixel is flagged cloudy. The chosen threshold depends on 12 μm BT (nadir range=0.064-1.259 K; forward range=0.142-1.550 K).
Fog/Low Stratus*	3.7/11 μm difference	Night	Ocean/Land	BT difference may be large over fog or low stratus cloud, owing to emissivity differences at these wavelengths. If the difference is above a threshold, the pixel is flagged cloudy. Currently, the threshold for all views and locations is set to 0.1 K.
Spatial Coherence*	11 μm and 11/12 μm difference	Day/Night	Ocean/Land	Pixels contaminated by cloud will have a much higher variability in terms of BT. The standard deviation of a 3 \times 3 pixel block is calculated and if this value is higher than a threshold (0.2 K for ocean pixels, 1.5 K and 1.0 K for day time and night time land pixels, respectively), the pixels are flagged cloudy. Some variability may result from variation of surface temperature (e.g. ocean fronts). To verify that this variation is not due to surface temperature, the average difference between the 11 and 12 μm BTs, which is assumed insensitive to surface temperature variations, is compared to that for neighbouring clear pixels. If the averages differ by less than a 0.1 K, the original 3 \times 3 pixel block is flagged clear.
1.6 μm Histogram	1.6 μm	Day	Ocean	The signal over cloud is high and variable. In a distribution of data from this channel, clear pixels will form a peak at low reflectances. This peak is used to derive a 1.6 μm threshold. For pixels affected by sun-glint, a spatial coherence test (similar to that for the 11 μm channel) is implemented. The test is based on a technique developed by Saunders (1986).

Table 2.2. Summary of AATSR cloud tests, continued...

Test	Channel	Day/Night	Ocean/Land	Description
11/12 μm Nadir/Forward	11 μm nad/fwd 11/12 μm	Day/Night	Ocean	The test is based on differential absorption of atmospheric water vapour in the thermal channels and BT deficit due to water vapour with increasing atmospheric path-length. This relationship may differ from expected in the presence of cloud. The difference between the nadir- and forward-view 11 μm BTs are compared to a modelled nadir-forward BT difference based on the observed difference between the nadir 11 and 12 μm difference. If the discrepancy between the two is greater than a threshold (currently set to 0.15 K), the pixel is flagged cloudy.
11/3.7 μm Nadir/Forward	3.7 μm nad/fwd 11/3.7 μm	Night	Ocean	The basis of this test is as for the 11/12 μm nadir/forward test, but the 3.7 μm channel data are used for the nadir- minus forward-view difference. This is compared to a modelled value based on the 3.7 minus 11 μm BT difference. Currently, the threshold for cloudy pixels is set to 0.075 K.
Infrared Histogram	11/12 μm difference	Day/Night	Ocean	This test is aimed at detection of low stratus clouds, the most likely clouds to have been missed by the previous tests. Firstly, for cloud-free pixels, the 11 and 12 μm BT difference is almost entirely due to absorption due to water vapour as the latter is more affected by this variable. Water vapour is most highly concentrated in the troposphere, thus radiation originating from clouds is not affected by water vapour as much as radiation originating from the ground. Secondly, the emissivity of low clouds is slightly higher in the 12 μm channel than in the 11 μm channel. The combination of these two effects reduces the BT difference, and can therefore be used to identify cloud. One of the conditions of this test is that the variation of atmospheric water vapour is small over an AATSR image of 512 \times 512 pixels. An additional correlation test is also employed to account for situations where there is some atmospheric variability over a scene. For clear pixels, the 11/12 μm BT difference should negatively correlate with the BT in one channel (due to the effects of tropospheric water vapour). For cloudy pixels, the correlation is positive. This test is always applied last and only operates on pixels that have not been flagged cloudy by any of the previous tests.

Table 2.3. Nadir-view SST coefficients latitude bands.

Region Name	Region Centre (°)	Latitude Limits (°)
Tropical	12.5	0-25
Mid-latitude	37.5	25-50
High-latitude	62.5	50-82

three-channel retrieval (D3), which uses data from the three thermal channels from both views. The general expression for (A)ATSR SST can be written as:

$$SST = a_0 + \sum_{i=1}^n a_i T_i \quad (2.7)$$

where n is the number of measurements used, T_i is the BT, obtained from measurement i (from any of the three thermal channels, using either the nadir- or forward-view) and a_0 and a_i are retrieval coefficients. For night time retrievals, N3 and D3 SSTs are calculated, augmented by the N2 and D2 retrievals during the day when data from the $3.7 \mu\text{m}$ channel are not available.

A full description of this scheme, originally developed for the ATSR-1, is given by Závody et al. (1995); similar methodologies have been employed for the ATSR-2 and the AATSR. In summary, TOA BTs are simulated for many atmospheric profiles for SSTs within ± 4 K of the near surface air temperature specified by these profiles. Coefficients are then derived for each of the four SST retrievals via a least-squares fit. For the three-channel SSTs (N3, D3), the coefficients for the $3.7 \mu\text{m}$ channel are weighted more heavily than for the 11 and $12 \mu\text{m}$ channels, as this channel is less affected by atmospheric attenuation. For the same reasons the two-channel retrieval coefficients are weighted in favour of the $11 \mu\text{m}$ channel.

For the AATSR, the coefficients are calculated for 38 across track bands (from the swath centre), as it was not considered practical to calculate coefficients for all pixel viewing angles across the swath. The error, introduced as a result of this band-averaged viewing angle approximation, is considered to be negligible. Coefficients for the dual-view SSTs are not regionally dependent. Conversely, the nadir-view SST are determined for three separate latitude bands, as shown in Table 2.3.

Table 2.4 shows the AATSR coefficients for each of the four SST retrievals corresponding to the centre and edge of swath positions for the 1-km resolution SST retrievals. Similar low-noise coefficients have been derived for the spatially-averaged SSTs.

The temperature and water vapour profiles used to derive the AATSR coefficients have been sourced from a globally representative set of 1290 profiles derived from 1995 ECMWF operational data. Concentrations of the other atmospheric species with absorption bands in the spectral bandwidth of the (A)ATSR channels have been obtained from a number of difference sources, as described by Závody et al. (1995). Tropospheric marine aerosols have been included in the RT model used to generate the retrieval coefficients for all of the ATSR instruments. Stratospheric volcanic aerosols were also introduced into the dual-view retrieval scheme during the latter part of 1999 following the work of Brown et al. (1997) and Merchant et al. (1999), after ATSR-1 validation results indicated that the retrievals were significantly affected by aerosols ejected into the stratosphere by the Mount Pinatubo eruption in 1991 (Donlon & Robinson 1998). At the time of writing, both sets of (A)ATSR nadir-view coefficients have not been made robust to stratospheric aerosols (A. Birks, 2004, personal communication).

In developing the original ATSR-1 coefficients, input sea surface emissivities were calculated for each of the infrared channels for a calm sea using Fresnel's equations, which express emissivity as a function of angle of incidence, and horizontal or vertical polarisations (see Chapter 3). The emissivity spectra were sourced from Hale & Querry (1973). For the AATSR coefficients, the scheme has been updated to include the effects of windspeed on emissivities in the forward view, based on the model proposed by Watts et al. (1996). These effects are discussed further in Chapter 3.

2.4.1.1 Previous Validation of ATSR-1 and -2 SSTs

Several authors have published the results of comparisons between SSTs derived from the ATSR-1 and -2 and in situ measurements. These results are summarised in Tables 2.5 and 2.6, and have been subdivided into comparisons with SSTs derived at depth (e.g. from buoy data, hereafter referred to as Bulk SSTs, or BSSTs), and SSTs derived from at-surface radiometric measurements, respectively.

The validation results indicate that the relative performance differs between the ATSR SST algorithms. These differences, which are investigated further in Chapter 3 with the AATSR, are primarily a result of the differing sensitivities of the SST retrievals to atmospheric conditions. Significantly better results are obtained using the dual-view SSTs, highlighting the advantages of the ATSRs dual-viewing geometry over traditional

Table 2.4. Current operational AATSR retrieval coefficients for 1-km resolution SSTs for centre and edge-of-swath pixels. Band 0 corresponds to the centre of the swath and band 37 to the edges. Coefficient subscripts indicate channel (3.7, 11, 12) and nadir (n) or forward (f) view data.

SST	Region	Swath	Coefficients						
		Band	a_0	$a_{3.7,n}$	$a_{11,n}$	$a_{12,n}$	$a_{3.7,f}$	$a_{11,f}$	$a_{12,f}$
N2	Tropical	0	−0.339206	-	3.42010	−2.42112	-	-	-
		37	−0.562803	-	3.48812	−2.48845	-	-	-
	Mid-lat	0	−1.40941	-	3.42918	−2.42674	-	-	-
		37	−1.74972	-	3.49702	−2.49350	-	-	-
	High-lat	0	4.55286	-	3.18678	−2.17224	-	-	-
		37	−5.18054	-	3.23917	−2.22244	-	-	-
D2	Global	0	2.82873	-	5.42073	−3.07655	-	−3.19957	1.84278
		37	2.29024	-	6.75881	−3.86940	-	−4.55289	2.65270
N3	Tropical	0	0.0410357	1.08097	0.652494	−0.729504	-	-	-
		37	0.0685643	1.09197	0.643431	−0.731267	-	-	-
	Mid-lat	0	1.00331	1.11123	0.581540	−0.691968	-	-	-
		37	1.10945	1.12114	0.573673	−0.694108	-	-	-
	High-lat	0	1.17215	1.13266	0.546548	−0.678972	-	-	-
		37	1.26708	1.14157	0.539633	−0.681018	-	-	-
D3	Global	0	0.697663	2.50940	0.629694	−0.734081	−1.47048	−0.338546	0.401133
		37	0.721492	3.08114	0.805831	−0.907091	−2.05184	−0.504326	0.573038

single-view SST retrieval utilised by sensors such as the AVHRR. In general, the best agreement with the in situ BSSTs is achieved by using the D3 algorithm.

Overall, the ATSR-1 N2, D2 and N3 validation results exhibit a significant negative bias, which is of the order of -0.7, -0.4 and -0.4, respectively. Mutlow et al. (1994) and Barton et al. (1995) also observe a slight negative bias when comparing the D3 SSTs to in situ measurements of BSST. This negative bias has been attributed to aerosol contamination from the Mount Pinatubo eruption that occurred in 1991, which ejected large amounts of aerosol into the stratosphere (Donlon & Robinson 1998, Merchant et al. 1999). The effects of aerosol on the ATSR SST retrievals have been researched by Závody et al. (1994) and Dundas (1991), who find that the dual-view SSTs are less affected by aerosols due to the additional information about the atmosphere gained from using the forward view. In addition, Závody et al. (1994) and Dundas (1991) find that the difference between the equivalent dual- and nadir-view SSTs (hereafter referred to as D-N) moves from being negative to positive under conditions of heavy aerosol loading, thus providing a tracer for aerosol in SST data. This phenomenon, together with the effects of aerosols on SST retrievals from the AATSR, is discussed further in Chapters 3 and 4. For all the ATSR-1 validation results, except for those reported by Barton et al. (1995), the D-N is positive, suggesting the presence of aerosol in the instrument FOV. The results of Barton et al. (1995) are thought to be relatively unaffected by Pinatubo aerosols due to the geographical location of the measurements being away from the area most affected by the eruption plume.

For the ATSR-2 sensor, there are relatively few published validation results. However, for those data that have been collected, in general the biases and standard deviations of the results are smaller than for the earlier ATSR-1, perhaps reflecting improvements to the retrieval algorithms as the mission matured. These data were also obtained after levels of stratospheric aerosols had returned to near-normal after the Pinatubo eruption, and so are less likely to suffer from this type of contamination. This is indicated by the D-N, which is negative for all results. For ATSR-2, biases of 0.27 K, 0.05 K, 0.60 K and 0.05 K are reported by Parkes et al. (2000). However, these results correspond to single data points, so only limited conclusions can be drawn. The results reported by Nightingale & Llewellyn-Jones (2003) are excellent, with a bias for the N3 and D3 algorithm of only a few hundredths of a degree.

Table 2.5. Validation results from ATSR-1 and ATSR-2 where the in situ measurements have been obtained using a radiometer. Note, for ATSR-1, the 3.7 μm channel failed on 27 May 1992. Where there is no figure given in the standard deviation columns, it is because there is only one data point available for validation.

Authors	ATSR	Date MM/YY	Region Data	N2		D2		N3		D3	
				Bias (K)	StDev (K)	Bias (K)	StDev (K)	Bias (K)	StDev (K)	Bias (K)	StDev (K)
Barton et al. (1995)	1 km ¹	09-12/91	16-31° S, 145-168° E	-0.16	0.45	-0.23	0.45	-0.06	0.36	0.20	0.20
Smith et al. (1994)	1 km ¹	11/91	0-15° S, 0-25° W	-2.1	0.26	-0.6	0.25*	-	-	-	-
Thomas et al. (1993)	1 km ¹	10/91- 05/92	Meridional transect	-0.78	0.18	-0.54	0.22	-	-	-	-
Donlon & Robinson (1998)	ASST ¹	09/92	10-22° N, 12-40° W	-0.78	0.22 (RMS)	-0.54	0.18 (RMS)	-	-	-	-
Donlon et al. (1999)	1 km ^{1,a}	03/96	50-51° N, 5-6° W	-1.23	-	-0.57	-	-	-	-	-
Parkes et al. (2000)	1 km ^{1,b}	07-08/96	10-22° N, 12-40° W	0.10	-	-0.18	-	-	-	-	-
Parkes et al. (2000)	1 km ^{2,b}	07-08/96 day/night	10-22° N, 12-40° W	0.27/0.61	-	0.05/0.26	-	0.60	-	0.50	-
Nightingale & Llewellyn- Jones (2003)	1 km ^{2,d}	06-07/02	7-12° S, 58-64° E	-	-	-	-	0.09	0.17	-0.03	0.13

¹ SSTs from ATSR-1

² SSTs from ATSR-2

^a SSTs averaged over measurement transect

^b SSTs averaged 3×3 pixel block. Uses spatially averaged coefficients with localised atmospheric smoothing.

Table 2.6. Validation results from ATSR-1 and ATSR-2 where the in situ measurements are of bulk SST (BSST). Note, for ATSR-1, the 3.7 μm channel failed on 27 May 1992. Where there is no figure given in the standard deviation columns, it is because there is only one data point available for validation.

Authors	ATSR	Date MM/YY	Region Data	N2		D2		N3		D3	
				Bias (K)	StDev (K)	Bias (K)	StDev (K)	Bias (K)	StDev (K)	Bias (K)	StDev (K)
Donlon et al. (2002)	ASST ^{1,a}	08/91- 08/95	Global	-	-	0.07	0.47 (RMS)	-	-	-0.17	0.46 (RMS)
Forrester & Challenor (1995)	1 km ¹	09/91	62-64° N, 3-7° W	-0.41	0.38 (RMS)	-	-	-	-	-	-
Forrester & Challenor (1995)	ASST ¹	09/91	62-64° N, 3-7° W	-0.45	0.45	-	-	-0.66	0.22	-	-
Barton et al. (1995)	1 km ¹	09-12/91	16-31° S, 145-168° E	-0.41	0.36	-0.47	0.31	-0.33	0.22	-0.08	0.32
Thomas et al. (1993)	1 km ¹	10/91- 05/92	Meridional transect	-0.78	0.18	-0.54	0.22	-	-	-	-

Table 2.6. Continued...

Authors	ATSR	Date MM/YY	Region Data	N2		D2		N3		D3	
				Bias (K)	StDev (K)	Bias (K)	StDev (K)	Bias (K)	StDev (K)	Bias (K)	StDev (K)
Harris et al. (1995)	1 km ^{1,b}	02-03/92 day/night	45° N - 50° S	-	-	-0.19/-0.39	0.62/0.39 (RMS)	-	-	-	-
Harris et al. (1995)	ASST ^{1,b}	02-03/92 day/night	45° N - 50° S	-	-	-0.24/-0.45	0.48/0.42 (RMS)	-	-	-	-
Mutlow et al. (1994)	ASST ¹	04-05/92 day/night	70° N - 60° S	-0.58	0.47 (RMS)	-0.36	0.42 (RMS)	-0.46	0.40 (RMS)	-0.03	0.36 (RMS)
Harrison & Jones (1993)	ASST ¹	08/92	50° N-50° S day/night	-	-	-0.4/0.5	-	-	-	-	-
Donlon & Robinson (1998)	ASST ¹	09/92	10-22° N, 12-40° W	-0.81	0.22 (RMS)	-0.57	0.12 (RMS)	-	-	-	-

¹ SSTs from ATSR-1² SSTs from ATSR-2^a ATSR ASSTs averaged over 4 cells^b Uses additional atmospheric smoothing^c SSTs averaged 5×5 pixel block.

2.4.1.2 The AATSR SST Validation Programme

To ensure continuity of the ATSR mission, a similar validation programme has been developed for the AATSR. A number of experiments comprise this programme, which includes validation against the global buoy network (O'Carroll et al. 2005) and SSTs collected from ship-mounted sensors (e.g. Barton & Pearce 2003, Nightingale & Llewellyn-Jones 2003). The result of one of these experiments is presented in Chapter 4 of this thesis. In this chapter, AATSR SSTs recorded during 2003 have been validated over the Caribbean sea, using in situ observations of SST from the Marine-Atmosphere Emitted Radiance Interferometer (M-AERI). This validation experiment, which extends over a full year, is the most extensive yet performed for any of the ATSR instruments using in situ SSTs derived from radiometric measurements. The results also provide a first opportunity to study seasonal biases using in situ observations of this type.

Early data collected from four validation experiments reported by Barton & Pearce (2003) (two data sets), Nightingale & Llewellyn-Jones (2003) and O'Carroll et al. (2005) suggest that the AATSR D3, D2 and N3 retrievals are performing well within the target 0.3 K accuracy. The results for the N2 validation performed by Barton & Pearce (2003) are comparatively poor, with biases of several tenths of a degree (usually AATSR is warm) and high standard deviations (1.27-1.52 K). Results from an additional experiment in the Bay of Biscay, where the in situ SSTs have been obtained from the Infra-red Autonomous Radiometer (ISAR), demonstrate that the D3 SSTs agree with the in situ data to within 0.3 K over this geographical area. The ISAR validation results for D2 also approach this accuracy. However, the N3 and N2 SSTs are biased by -0.37 (standard deviation 0.48 K) and $+0.54$ (standard deviation 0.29 K), respectively, from the in situ data (C. Donlon, personal communication). Overall, these results confirm that the dual-viewing geometry utilised by the (A)ATSR is extremely beneficial in obtaining accurate SSTs, particularly when data from only two channels is available.

2.4.2 AATSR Land Surface Temperature

For the first time in the history of the ATSR mission, an operational product has been developed with the objective of providing global measurements of LST. The following section provides an overview of this product, which became operational on 10 March 2004, based on the detailed description given by Prata (2002a) and references therein.

The target accuracy of the operational LST retrievals is 2.5 K, with better results expected at night (~ 1.0 K) when the effects of differential surface heating (e.g. shad-

owing), are absent. Results of a validation campaign where the prototype version of the product has been compared with in situ LST data is presented in Chapter 5. The product utilises a nadir-only split-window algorithm:

$$LST = a_{f,i,pw} + b_{f,i}(T_{11} - T_{12})^n + (b_{f,i} + c_{f,i})T_{12} \quad (2.8)$$

where $a_{f,i,pw}$, $b_{f,i}$ and $c_{f,i}$ are coefficients that depend on land type class (or biome) i , fractional vegetation cover f and precipitable water pw , and T_{11} and T_{12} are the AATSR BTs in the 11 and 12 μm channels, respectively. At the time of writing, the AATSR product uses 14 different biomes, including one lake class. The auxiliary data i , f and pw depend on geographical location; f and pw are also dependent on season and time of day (the latter is currently operational for lake class only). These auxiliary datasets are discussed later in this section.

The development of multi-window algorithms requires approximations to allow a linear dependence of ST on TOA BTs (Chapter 1). The variable n in Equation 2.8, which allows a small degree of non-linearity and tuning of the algorithm based on validation results, is defined as:

$$n = \frac{1}{\cos \frac{\theta}{m}} \quad (2.9)$$

where m is a variable parameter that controls the dependence on the viewing angle, θ . If m is set to infinity, n tends to unity, and the algorithm becomes linear. The coefficients $a_{f,i,pw}$, $b_{f,i}$ and $c_{f,i}$ are defined as:

$$a_{f,i,pw} = d[\sec \theta - 1]pw + fa_{v,i} + (1 - f)a_{s,i} \quad (2.10)$$

$$b_{f,i} = fb_{v,i} + (1 - f)b_{s,i} \quad (2.11)$$

Table 2.7. Operational AATSR LST retrieval coefficients (Prata 2002b)

Land class	Day/Night	$a_{v,i}$	$a_{s,i}$	$b_{v,i}$	$b_{s,i}$	$c_{v,i}$	$c_{s,i}$
1	Day/Night	0.6907	6.0951	3.8129	4.5637	-2.8456	-3.3617
2	Day/Night	-0.5393	4.6301	3.6472	4.3652	-2.7218	-3.2155
3	Day/Night	-0.6885	4.8786	3.6472	4.3652	-2.7218	-3.2155
4	Day/Night	1.0801	1.0801	3.2972	3.2972	-2.2909	-2.2909
5	Day/Night	0.7804	1.4910	3.2721	3.8117	-2.3374	-2.7233
6	Day/Night	0.9089	0.0348	3.3511	3.9038	-2.3890	-2.7891
7	Day/Night	0.7994	0.7994	3.5088	3.5088	-2.5065	-2.5065
8	Day/Night	1.5662	0.7833	3.1384	3.6560	-2.2419	-2.6121
9	Day/Night	0.8965	0.8965	3.4867	3.4867	-2.4908	-2.4908
10	Day/Night	1.0817	1.0817	3.3039	3.3039	-2.2955	-2.2955
11	Day/Night	0.7075	0.7041	3.7832	3.7832	-2.7868	-2.7868
12	Day/Night	0.8810	0.8810	3.4106	3.4106	-2.4133	-2.4133
13	Day/Night	1.0801	1.0801	3.2972	3.2972	-2.2909	-2.2909
14	Day	-0.0005	-0.0005	2.4225	2.4225	-1.4344	-1.4344
14	Night	-0.3658	-0.3658	2.3823	2.3823	-1.3556	-1.3556

$$c_{f,i} = f c_{v,i} + (1 - f) c_{s,i} \quad (2.12)$$

where d is a second ‘tuning’ parameter that is derived empirically using the results of validation experiments. Currently, the values of m and d are set to 5.0 and 0.4, respectively, in the LST retrieval algorithm (A. Birks, 2004, personal communication). Values for the coefficients $[a, b, c]_{v,i}$ and $[a, b, c]_{s,i}$, given in Table 2.7, are determined for each biome i using simulation datasets to forward model the TOA BTs using a similar methodology to that adopted for the (A)ATSR SST retrieval scheme. These are, in fact, separate regression coefficients for vegetated (subscript v) and bare surfaces (subscript s), respectively, which are weighted according to the value of f (between 0 and 1 by definition). The algorithm becomes independent of f if $[a, b, c]_{v,i} = [a, b, c]_{s,i}$; from Table 2.7 we observe that biomes 4 and 9-14 fall within this category.

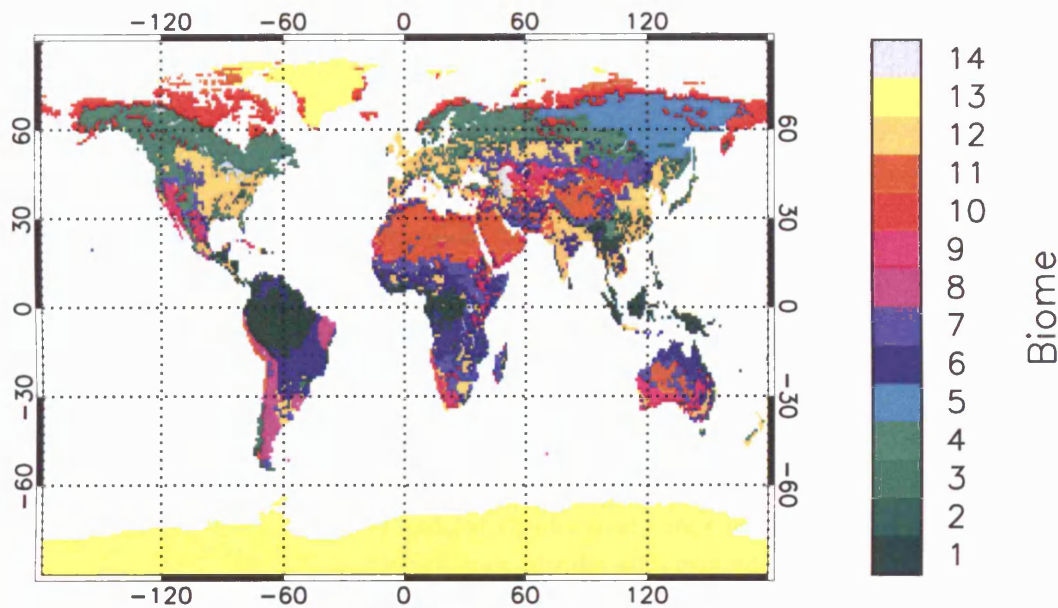


FIGURE 2.8. Global map showing the distribution of AATSR LST biomes 1-14 (data courtesy of RAL). See Table 2.8 for a description of the biome types.

2.4.2.1 Auxiliary Data

Figure 2.8 illustrates the global distribution of the 14 AATSR LST biomes with the corresponding descriptions of each biome given in Table 2.8; the biomes utilised for this product were determined from Dorman & Sellers (1989).

The auxiliary fractional vegetation data are tabulated on a 0.5° grid, with separate global datasets for each month of the year to allow a more realistic estimate of the vegetation proportion in geographical regions where this parameter may be seasonally dependent. These data were derived using a composite of two datasets: monthly vegetation fraction estimates from Dorman & Sellers (1989) for the biomes given in Table 2.8 and International Satellite Land Surface Climatology Project (ISLSCP) Normalised Difference Vegetation Index (NDVI) global composite at $1^\circ \times 1^\circ$ resolution, with the latter being used as an estimate of ‘greenness’. Figure 2.9 shows global data plotted for the month of June.

The auxiliary precipitable water data, also tabulated on a 0.5° grid, with separate global datasets for each month of the year, is based on $2.5^\circ \times 2.5^\circ$ NASA Water Vapour Project (NVAP) climatology. The purpose of these data is to correct for increasing atmospheric absorption with deviation from true nadir (i.e. 0.0°) towards the edges of the

Table 2.8. AATSR LST biomes derived from Dorman & Sellers (1989). See Figure 2.8 for global distribution of these biomes.

Biome Number	Description
1	Broadleaf evergreen trees
2	Broadleaf deciduous trees
3	Broadleaf and needleleaf trees
4	Needleleaf-evergreen trees
5	Needleleaf-deciduous trees
6	Broadleaf trees with groundcover
7	Groundcover
8	Broadleaf shrubs with groundcover
9	Broadleaf shrubs with bare soil
10	Dwarf trees, shrubs with groundcover
11	Bare Soil
12	Broadleaf-deciduous trees with winter wheat
13	Perennial land ice
14	Permanent lakes

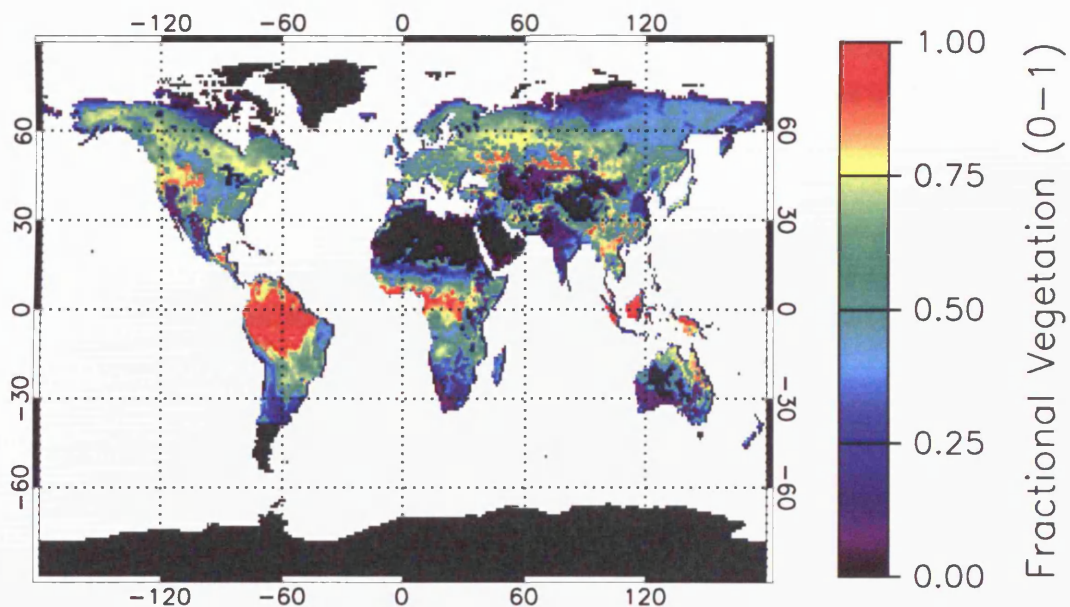


FIGURE 2.9. Global map showing the distribution of AATSR LST fractional vegetation data for the month of June (data courtesy of A. Birks of RAL).

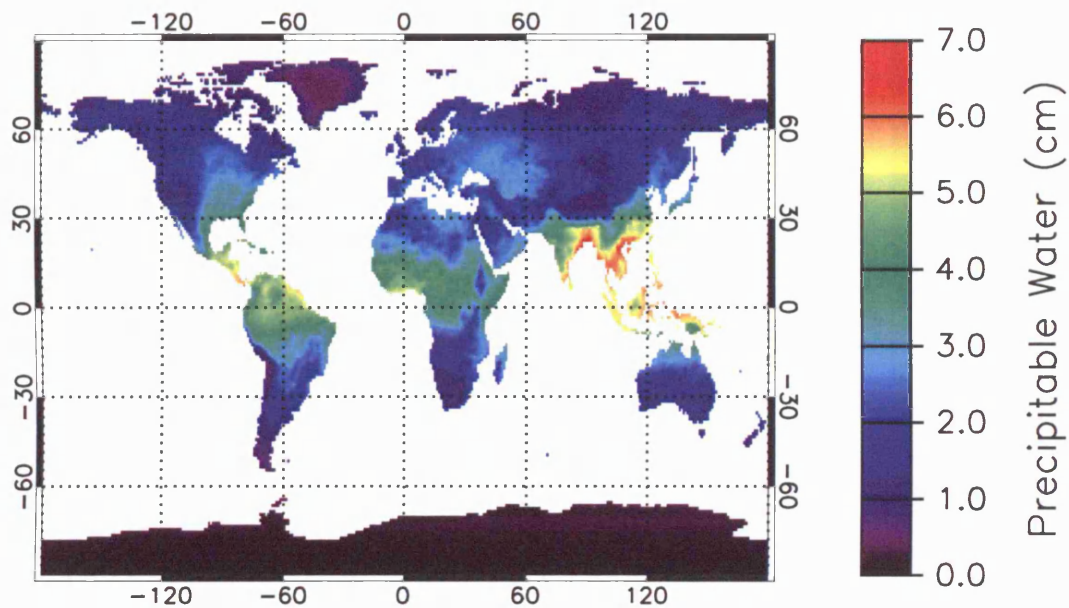


FIGURE 2.10. Global map showing the distribution of AATSR LST auxiliary precipitable water data for the month of June (data courtesy of A. Birks of RAL).

swath. From Equation 2.10, we see that this variable has no effect where $\theta = 0.0^\circ$, i.e. at the centre of the swath. Figure 2.10 shows global data plotted for the month of June.

Additional auxiliary information regarding the confidence of the retrieved LST is presented in the form of a topographic variance flag (TVF) dataset at $0.5^\circ \times 0.5^\circ$ resolution (Figure 2.11), developed using a 30 arc second digital elevation model (DEM). LSTs derived in topographically variable regions may be subject to increased uncertainties, largely due to the dependence of surface emissivity on viewing angle (Chapter 1). Such regions are assigned a low confidence rating, conversely, LSTs derived over topographically uniform regions are assigned a high confidence. Figure 2.11 shows the global variation of TVF; the values of the flags are shown in Table 2.9.

2.4.2.2 The AATSR LST Validation Programme

An AATSR LST validation programme, similar to that for SST validation, has been established. As operational LST retrievals are new to the (A)ATSR mission, there are no previous results for validation of LSTs from ATSR-1 and ATSR-2. A number of experiments comprise this programme. These include validation against LSTs derived from (i) in situ radiometers permanently deployed at designated validation sites, (ii) in situ

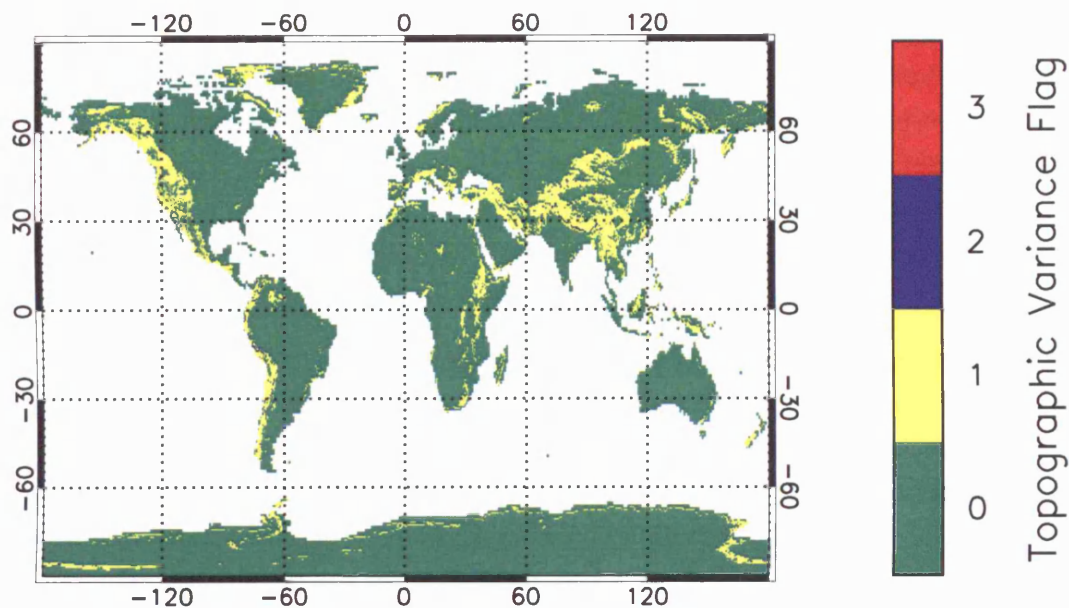


FIGURE 2.11. Global map showing the distribution of topographic variance flag auxiliary data (data courtesy of A. Birks of RAL).

Table 2.9. Topographic variance flag definitions

Flag	Topography	Confidence
0	Extremely flat ground	Very high
1	Some topographic variation	Good
2	Significant topographic variation	Low
3	Extreme topographic variation	None

radiometers, where the measurements have been made during specific validation campaigns and (iii) other LST, or proxy LST, data sets, such as sub-surface LST measurements and near-surface air temperature data. The results of one of these experiments, which falls within category (ii) above, is presented in Chapter 5 of this thesis. This experiment also represents the first attempt at validation of AATSR LSTs over a site that is heterogeneous on the scale of an AATSR pixel.

Results from other validation experiments suggest that the performance of the algorithm varies with geographical location and biome. Coll et al. (2005) obtain a bias (AATSR-in situ) and standard deviation of +3.0 K and 0.9 K, respectively, over an agri-

cultural field site in Spain (biome 6). For the Thangoo validation site in Australia, also of biome 6, a bias and standard deviation of -4.1 and 3.3 K is obtained. Over two other Australian validation sites, Amburla (biome 7) and Uardry (biome 9), better results are obtained. For Amburla, the results yield a bias and standard deviation of -1.1 K and 1.5 K. For Uardry, these figures are calculated to be -0.2 K and 0.9 K (results for all Australian validation sites obtained from F. Prata, personal communication). Excellent results are also obtained over the Lake Tahoe (USA) validation site (biome 14) yield a bias and standard deviation of $+0.05$ K and 0.37 K (S. Hook, personal communication).

The variability and magnitude of the observed biases reflect the difficulties in obtaining accurate observations of LST from satellite data. As discussed in Chapter 1, accurate in situ observations of LST are also much more difficult to obtain due to the spatial and temporal variability of this parameter. The results also highlight the need for an extensive validation, over several sites within each biome, to fully characterise these biases.

2.5 Summary

The AATSR is the third instrument in the ATSR series, designed to provide accurate measurements of the Earth's surface in the visible and infrared region of the electromagnetic spectrum, at approximately 1 km spatial resolution. These measurements are used primarily to infer SST, LST and vegetation indices that can be used in many climatological applications. As the focus of this thesis is ST retrievals from the AATSR, the emphasis of this chapter and subsequent sections is on the measurements made in the infrared.

The AATSR instrument has a number of advantages over other instruments designed for similar applications, such as the AVHRR and MODIS sensors. Its design uses an exceptionally stable on-board calibration system for its infrared channels, which, together with actively cooled detectors, gives extremely high radiometric sensitivity and accuracy. Pre-launch calibration of these infrared channels, at 3.7 , 11 and $12\ \mu\text{m}$, demonstrated accuracies of better than 30 mK. In addition, a conical scanning mechanism enables measurements to be made both at nadir and in the along-track direction at approximately 55° , providing additional information about the intervening atmosphere.

For SSTs derived from AATSR data, four retrievals are performed operationally. These comprise: a three-channel, dual-view retrieval (D3), a two-channel, dual-view retrieval (D2), a three-channel, nadir-view retrieval (N3) and a two-channel, nadir-view retrieval (N2 - the traditional split-window retrieval). The target accuracy of these re-

trievals is ± 0.3 K, 1σ . The two-channel retrieval scheme is only implemented when data from the $3.7 \mu\text{m}$ channel are not available (e.g. during the day, when it is contaminated with solar radiation), as the coefficients are larger and therefore more susceptible to noise. Moreover, previous research and validation results indicate that the three-channel retrievals are superior to their two-channel counterparts. Validation results using ATSR-1 and -2 SSTs indicate that the retrievals have the potential to meet the target 0.3 K accuracy, although biases of the order of several tenths of a degree have been observed in a number of cases.

For LST, an operational retrieval scheme has been developed for the first time during the (A)ATSR mission. The scheme, which became operational in March 2004, utilises a nadir-only, split-window algorithm with a target accuracy of 1.0 K at night, and 2.5 K during the day. Data from the forward view are not included due to the high dependence of land surface emissivity on viewing angle. In addition, the temporal separation between the forward and nadir-view measurements is 150s, during which time significant diurnal heating (of the order of several tenths of a degree) may have occurred.

A comprehensive programme for validation of both SSTs and LSTs derived from AATSR data has been established. This validation programme is vitally important to assess the accuracy of these data, and in the case of SST, to establish continuity with SSTs derived from ATSR-1 and -2. Early validation of SSTs derived from the AATSR data suggest that the D3, D2 and N3 retrievals are performing well within the target 0.3 K accuracy in most cases. Results for the N2 SSTs are biased by several tenths of a degree. Results from LST validation experiments (note the AATSR LST retrieval is also an N2 retrieval) also yield significant biases; which, in some cases, amount to several K.

In Chapter 3, causes of biases in the AATSR retrievals are investigated by means of a simulation study. While this provides insight into the behaviour of the retrievals under various atmospheric and surface conditions, it is only through validation with equivalent in situ data that the true accuracy of the SSTs and LSTs can be assessed. The results of two such validation experiments are presented in Chapters 4 and 5. Both these experiments form an integral part of the overall AATSR validation programme (for SST and LST, respectively) and have been instrumental in improving our understanding of sources of bias in the retrieval algorithms.

Chapter 3

The AATSR: A Sensitivity Study

Previous (A)ATSR validation results (Chapter 2) have shown that the performances of the four SST retrievals, N2, D2, N3 and D3, differ substantially. This is principally due to the differential dependence of the signals in each (A)ATSR thermal channel on atmospheric conditions prevalent at the time of the satellite overpass. As we have seen in Chapter 1, it is this differential dependence that forms the basis of the multi-window approach to SST and LST retrieval that has been adopted for spaceborne sensors, such as the AVHRR and the (A)ATSR, in order to correct for the effects of the atmosphere. In this Chapter, the dependence of the measured AATSR TOA BTs, and retrieved SSTs and LSTs, on varying atmospheric and surface conditions is examined by simulating the TOA signal using an RT model for a given set of surface and atmospheric conditions, and then applying the operational retrieval algorithms to these data.

3.1 Forward Modelling of AATSR TOA BTs

3.1.1 The Oxford Reference Forward Model

Given a set of surface and atmospheric conditions, the TOA signal measured by a spaceborne sensor can be calculated using the RT equation, providing the view angle and instrument response are also known (Chapter 1). The Reference Forward Model (RFM), a line-by-line RT model, developed at the University of Oxford (UK), was employed for this purpose (see www-atm.physics.ox.ac.uk/RFM/). The model is based on GENLN2 (Edwards 1992) and was specifically designed to provide reference spectral calculations for the Michelson Interferometer for Passive Atmospheric Sounding (MIPAS), a high-spectral resolution limb-sounding instrument that is also on board the Envisat satellite.

Although originally designed for limb-sounding simulations, the model can also be run in nadir-sounding mode, where the zenith angle is specified. The model has some limitations, including assuming a plane-parallel atmosphere for nadir sounding mode and ignoring the effects of scattering. Specular reflection at the surface is assumed for downwelling radiance.

The RFM can be operated for any spectral range between 0.001 cm^{-1} and $20,000\text{ cm}^{-1}$ ($10\text{ m} - 0.5\text{ }\mu\text{m}$) at a resolution of 0.0004 to 1.0 cm^{-1} . The input spectral line data for atmospheric species in this work are taken from the HIGH-resolution TRANsmis-sion database (HITRAN) 2000 (Rothman et al. 2003). Due to this high spectral resolution, the RFM was employed for this study in preference to other available RT models commonly used for such purposes, for example, the MODerate spectral resolution at-mospheric TRANSmittance algorithm and computer model (MODTRAN - see Kneizys et al. (1996) for details). Simulations using the RFM have shown that the spectral reso-lution of a RT model is critical in terms of the accuracy of simulated AATSR TOA BTs. For example, by using a spectral resolution of 1 cm^{-1} , which is the highest mode avail-able using MODTRAN, the error on the simulated AATSR TOA BTs is estimated to be of the order of tenths of a K (e.g. $> 0.4\text{ K}$ for the nadir $11\text{ }\mu\text{m}$ channel for a tropical climatology).

Nadir-sounding mode was employed for both the nadir- and forward-view simula-tions in this experiment. The zenith angles were varied according to the AATSR swath position (Figure 3.1), with angles of 0.000° and 55.345° corresponding to the nadir- and forward-views, respectively, at the centre of the swath, and 21.433° and 52.809° , for the swath edges. These view angles were calculated using the expressions derived by Mason (1991) for the orbit height and cone angle of the AATSR (see Chapter 2). For simu-lations over land, only the nadir-view 11 and $12\text{ }\mu\text{m}$ channels were considered as the current AATSR LST algorithm does not utilise data from either the forward view or the $3.7\text{ }\mu\text{m}$ channel. A spectral resolution of 0.01 cm^{-1} over the bandwidths of the AATSR thermal channels (Table 2.1) was used in this study, as this was found to be a reasonable compromise between computational time and accuracy (approximately 0.01 - 0.02 K for BTs).

To simulate the AATSR TOA BTs, the radiances output from the RFM were multi-plied by the AATSR instrument response functions (Figure 2.4) and translated into BTs by comparing the integrated radiances with integrated Planck radiances, also multiplied by the AATSR instrument response functions. The BT is then the equivalent black body temperature that reproduces the integrated AATSR radiances.

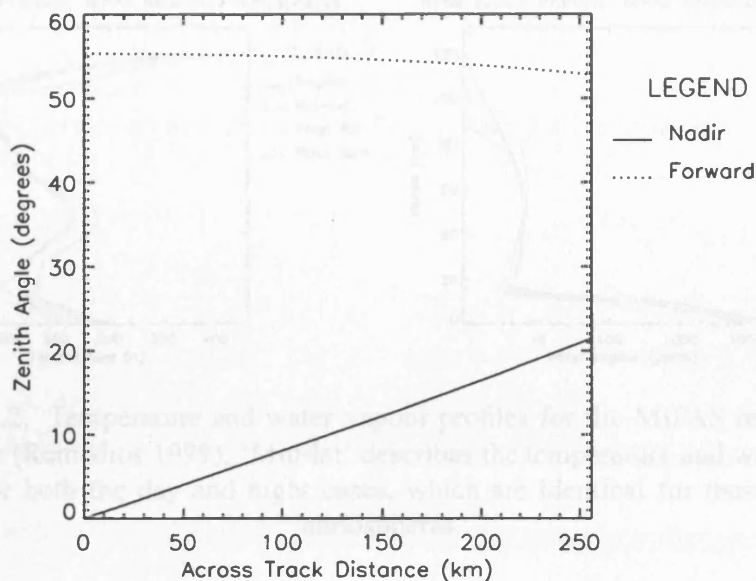


FIGURE 3.1. Variation of AATSR view angle with swath position.

3.1.2 Model Inputs

3.1.2.1 Atmospheric Profiles

Reference atmospheres, specifically designed for use in infrared sounding, for MIPAS-related studies (Remedios 1999), were employed in this experiment. Five atmospheres corresponding to tropical, mid-latitude day/night and polar summer/winter atmospheric conditions are available. These profiles describe the concentrations of 30 atmospheric species, including H_2O , CO_2 and O_3 , between the surface and a height of 120 km with a vertical step size of 1 km. Corresponding pressure and temperature profiles are also provided. Figure 3.2 shows the vertical distribution of temperature and water vapour profiles for the five reference atmospheres; it should be noted that the temperature and water vapour profiles are identical for the mid-latitude day/night reference atmospheres, and are thus represented by a single line in Figure 3.2.

Although water vapour is the principal atmospheric gas with absorption lines over the bandwidth of the AATSR thermal channels, several other gases make a small contribution to the total absorption at these wavelengths (determined from the HITRAN 2000 database). A list of these gases, also included in the model for completeness, is given in Table 3.1. As the concentrations of these species are identical in both the MIPAS mid-

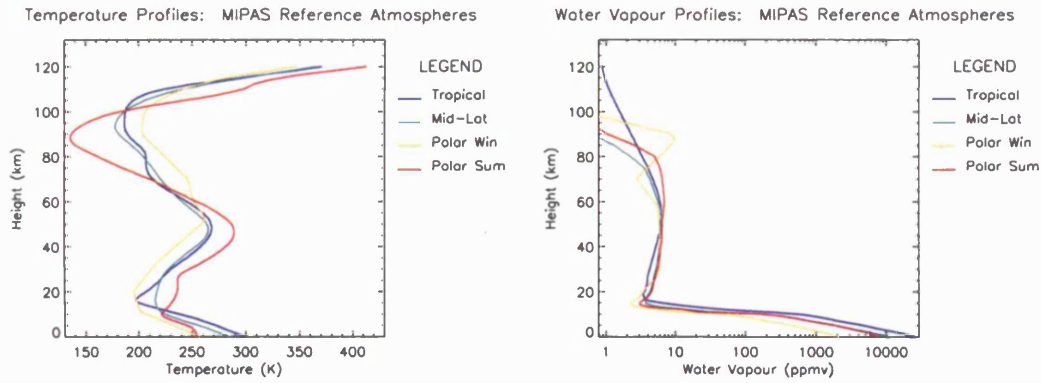


FIGURE 3.2. Temperature and water vapour profiles for the MIPAS reference atmospheres (Remedios 1999). ‘Mid-lat’ describes the temperature and water vapour profiles for both the day and night cases, which are identical for these reference atmospheres.

Table 3.1. List of absorbing gases in the AATSR thermal channel bandwidths.

Channel	Gases
3.7 μm	CO_2 , CO , CH_4 , C_2H_6 , H_2O , N_2 , N_2O , O_3
11 μm	CO_2 , F11, F12, F22, H_2O , HNO_3 , O_3
12 μm	CCl_4 , CO_2 , F11, F12, F22, H_2O , HNO_3 , O_3

latitude day and night atmospheres, all results presented in this study for the mid-latitude climatologies hereafter shall be referred to as ‘mid-latitude’. Continuum absorption for H_2O , CO_2 , O_2 and N_2 was also included in the model calculations.

Only the mid-latitude and tropical atmospheres were included in the land component of this study. The polar atmospheres are not considered, as the study focuses on biome 12 (broadleaf deciduous trees with winter wheat), which extends over much of Europe, N. America, India and China (Figure 2.8). This biome was selected as in situ LST data from a site within this biome have been used to validate the AATSR LSTs in Chapter 5. However, the results for the BT simulations in this chapter are applicable to the other 13 biomes used in the AATSR product; the subsequent LST retrievals are specific to biome 12, as different coefficients are employed for each land type (Chapter 2).

Table 3.2. Near-surface air temperatures, T_{ns} , corresponding to each model atmosphere. Also shown are the central surface temperatures, T_0 , and range of SSTs/LSTs (T_S) used in this study. No LST ranges are given for the polar atmospheres, as these data have not been included in the land component of the study (see text).

Atmosphere	T_{ns} (K)	T_0 (K)	SST Range (K)	LST Range (K)
Tropical	300.93	301.00	299.00-303.00	291.00-311.00
Mid-Latitude	285.15	285.00	283.00-287.00	275.00-295.00
Polar-Summer	254.90	255.00	253.00-257.00	-
Polar-Winter	256.70	257.00	255.00-259.00	-

3.1.2.2 Surface Temperature

T_S data are not explicitly provided in the reference atmosphere profiles, therefore appropriate values must be chosen independently as input into the RT model. As TOA radiances have some dependence on the magnitude of the difference between T_S and the near-surface air temperature (T_{ns}), a range of values for T_S was chosen for each atmospheric profile. To ensure a physically realistic model, the central value, T_0 , within each range of temperatures was selected to be close to the value of T_{ns} specified in the model atmospheres (Table 3.2). For the simulation of TOA BTs over the ocean, an SST range of $T_0 \pm 2$ K was utilised, which is a good approximation for the majority of air-sea temperature differences (e.g. Minnett 1986). For land, the wider range of $T_0 \pm 10$ K was chosen, as LST may differ by several K from the temperature of the near-surface air due to its stronger diurnal temperature range.

3.1.2.3 Surface Emissivity

A number of sources for infrared emissivity of sea water are available. Querry et al. (1977) report measured complex refractive indices of several natural waters, including the Pacific and Atlantic Oceans. Similarly, Friedman (1969) presents measured complex refractive indices of artificial ocean water and distilled water, deriving a small correction for the salinity effects of the former. In this study, the complex refractive indices derived by Bertie & Lan (1996) for pure water at 25°C have been used to estimate the sea surface emissivity for the AATSR thermal channels. Although the effects of salinity are considered by many to be negligible in terms of SST retrieval (e.g. Masuda et al. 1988), this

will be considered in Section 3.4 together with an investigation into the potential effects of windspeed and surface temperature, which are also thought to affect the emissivity of the sea surface.

The equations described by Masuda et al. (1988) have been utilised to derive sea surface emissivity for the AATSR thermal channels in this study, as stated below. Given the zenith angle and the complex refractive indices of a sample corresponding to a given wavelength, the emissivity of that sample at that wavelength can be calculated from:

$$\epsilon(\eta, \theta) = 1 - \rho(\eta, \theta) \quad (3.1)$$

where ϵ is the emissivity at zenith angle θ , and η are the complex refractive indices. ρ is the reflectance, which is calculated according to the equation:

$$\rho(\eta, \theta) = \frac{(|\gamma_{\parallel}|^2 + |\gamma_{\perp}|^2)}{2} \quad (3.2)$$

The variables γ_{\parallel} and γ_{\perp} are obtained using Fresnel's equations:

$$\gamma_{\parallel} = -\frac{(\eta \cos(\theta) - \cos(\theta'))}{(\eta \cos(\theta) + \cos(\theta'))} \quad (3.3)$$

$$\gamma_{\perp} = \frac{(\cos(\theta) - \eta \cos(\theta'))}{(\cos(\theta) + \eta \cos(\theta'))} \quad (3.4)$$

where θ' can be calculated using Snell's law:

$$\sin(\theta') = \frac{1}{\eta} \sin(\theta) \quad (3.5)$$

The emissivity for a given radiometer channel, for example, can then be calculated according to the following equation (e.g. Becker & Li 1990):

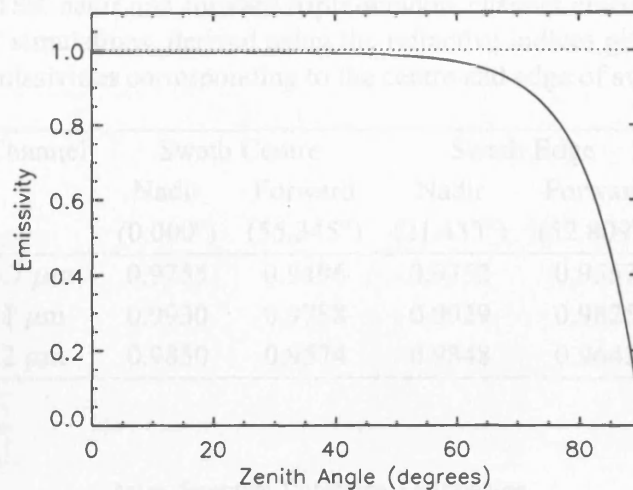


FIGURE 3.3. Variation of the AATSR 11 μm channel emissivity of water with viewing angle. The dotted line corresponds to an emissivity of one. Emissivities determined from refractive indices derived by Bertie & Lan (1996) for pure water.

$$\epsilon_i = \frac{\int f_i(\lambda)\epsilon(\lambda)d\lambda}{\int f_i(\lambda)d\lambda} \quad (3.6)$$

where f is the instrument response curve for channel i , and λ is wavelength. Table 3.3 gives the AATSR thermal channel emissivities of water corresponding to the centre and edge-of swath, calculated using this methodology and the refractive indices of Bertie & Lan (1996). As the emissivity of water diminishes with viewing angles over 30° (Figure 3.3), the forward-view emissivities of the AATSR are always significantly lower than the nadir-view emissivities.

Data from the ASTER Spectral Library (1999), which provides measured laboratory reflectances for almost 2000 natural and man-made materials, were used to obtain suitable land emissivities for input into the RT model. The library contains reflectances corresponding to 58 soil samples, 4 vegetation samples and 12 sandstone samples, for which the AATSR 11 and 12 μm channel emissivities are plotted in Figure 3.4. The corresponding mean and standard deviation of the AATSR split-window channel emissivities, categorised by material type, are shown in Table 3.4. These emissivities are expected broadly to represent the majority of land surfaces on earth. As discussed in Chapter 1, the emissivity of land surfaces may vary with viewing angle. With only

Table 3.3. AATSR nadir and forward triple-window channel emissivities used for ocean TOA BT simulations, derived using the refractive indices given by Bertie & Lan (1996). Emissivities corresponding to the centre and edge of swath are shown.

Channel	Swath Centre		Swath Edge	
	Nadir (0.000°)	Forward (55.345°)	Nadir (21.433°)	Forward (52.809°)
3.7 μm	0.9755	0.9496	0.9752	0.9557
11 μm	0.9930	0.9788	0.9929	0.9825
12 μm	0.9850	0.9574	0.9848	0.9642

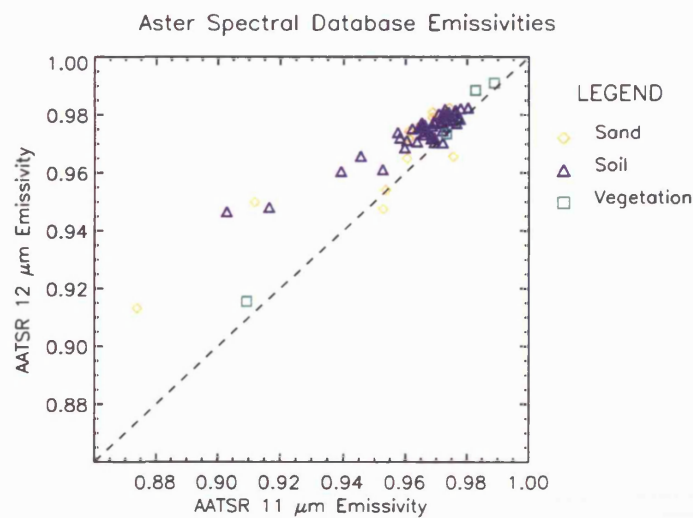


FIGURE 3.4. AATSR split window emissivities for some natural land materials, calculated using reflectance data sourced from ASTER Spectral Library (1999). Line of equality (dashed line) is also shown.

the measured reflectances provided in the ASTER database, it is not possible to derive emissivity as a function of viewing angle from these data. However, the variation with viewing angle is less severe than for water, and is negligible over the range of AATSR nadir viewing angles (e.g. Sobrino & Cuenca 1999). Therefore it is not necessary to consider this effect in this experiment.

From Figure 3.4 and Table 3.4 we observe that, unlike for water, the 11 μm channel emissivities are generally lower than for the 12 μm channel. Most of the materials have an emissivity of approximately 0.97, although a number of the samples have emissivities

Table 3.4. AATSR split window emissivities for some natural land materials, calculated using reflectance data sourced from ASTER Spectral Library (1999).

Material	N Samples	11 μm Channel		12 μm Channel	
		Mean	StDev	Mean	StDev
		K	K	K	K
green vegetation	3	0.9817	0.0079	0.9843	0.0095
dry grass	1	0.9093	-	0.9154	-
soils	58	0.9668	0.0133	0.9750	0.0070
sandstones (all)	12	0.9522	0.0298	0.9633	0.0199
sandstones (0-75 μm)	6	0.9380	0.0379	0.9491	0.0192
sandstones (500-1500 μm)	6	0.9665	0.0051	0.9775	0.0040

that are considerably lower. Green vegetation exhibits the highest emissivity, with similar values obtained for both AATSR channels; this is to be expected, as green vegetation generally shows very little spectral variation over the 8-14 μm waveband, demonstrating near grey-body behaviour (Sutherland 1986). For this study, an average of the emissivities for green vegetation and soils has been adopted, weighted according to the fractional vegetation proportion used in the model.

3.2 Methodology

In the following sections, the sensitivity of the TOA BTs measured by the AATSR thermal channels is examined by perturbing the model inputs for each atmospheric scenario. For example, the sensitivity to changing surface temperature has been assessed by retaining constant surface emissivities and atmospheric data, and varying the surface temperatures input in the RT model within the ranges defined in Section 3.1.2.2. The BT deficit (i.e. how much the TOA BT is depressed compared to the underlying surface temperature) and a response parameter, obtained by fitting either a linear regression line or a polynomial, depending on the variable in question, are then calculated from the modelled BTs.

The sensitivity to surface emissivity, atmospheric water vapour and temperature has also been investigated using this methodology; due to additional dependence of the RT equation on the surface-air temperature difference, these simulations have been carried out for both the central and extreme values of surface temperatures within the ranges de-

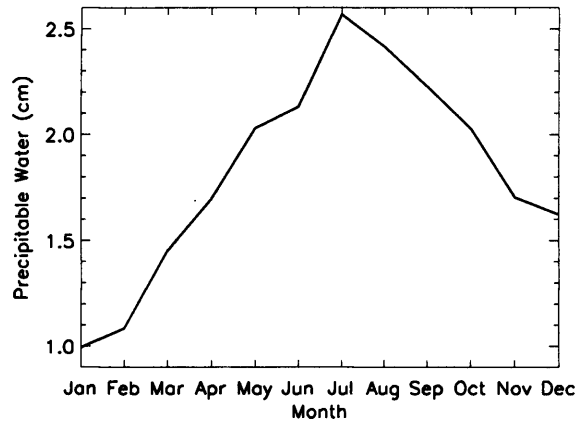


FIGURE 3.5. AATSR auxiliary precipitable water variation over the WATERMED field site within biome 12; latitude=31.6563, longitude=-7.6058 (see Chapter 5).

fined in Section 3.1.2.2. Simulations have been carried out for both the centre and edge-of-swath scenarios, in each case, to characterise the change in sensitivity with across track position. Although the same atmospheric data sets are used for both the land and ocean components of the study, these results are presented separately in light of the different emissivities and surface temperatures used over the ocean and land.

By applying the operational SST and LST retrieval algorithms to the modelled BTs (Chapter 2), the BT responses have been translated into corresponding SST/LST responses. For the LST simulations, two sets of results have been simulated for the edge-of-swath scenario, as the algorithm has some dependence on precipitable water for viewing angles greater than zero (Chapter 2). As precipitable water varies with season and geographical location, the minimum and maximum values corresponding to tropical and mid-latitude regions within biome 12, obtained from the AATSR LST product auxiliary precipitable water data, have been used in the algorithm and applied to the BTs simulated in Section 3.3.3. As an example, Figure 3.5 shows the variation of these data over the WATERMED field site (Chapter 5), which lies within biome 12 .

Although it is the response of the operational retrieval algorithms that are of primary interest in this study, the BT responses for each sensitivity test are also described within the following sections, as these are instrumental in our understanding of the behaviour of the AATSR SSTs/LSTs. Furthermore, these results are useful when considered in conjunction with TOA BTs that have been modelled in order to characterise anomalous matchups from the M-AERI validation campaign (Chapter 4).

3.3 Model Results: Surface Temperature

3.3.1 Sensitivity of Ocean TOA BTs to SST

Figure 3.6 shows the variation of the AATSR TOA BTs with varying T_S at the centre of the AATSR swath. TOA BTs have been simulated for temperatures at intervals of 0.5 K within the range specified in Section 3.1.2.2. The BTs shown in Figure 3.6 are differenced from the BT calculated for $T_S = T_0$ in each case, where T_0 is the reference surface temperature corresponding to each atmosphere given in Table 3.2 (for each climatology, T_0 is very close to the atmospheric temperature at a height of 0 km). The responses of the BTs, obtained by fitting linear regression lines, are given in Table 3.5.

Although the relationship between T_S and the radiance measured by the sensor is non-linear (Section 1.3.1.1), we see from these results that the response is approximately linear over the range of interest. The rate of change of BT with surface temperature for the 3.7 μm channel nadir-view data is similar and close to unity for all atmospheres. Decreased sensitivity to T_S is observed where atmospheric water vapour attenuation is high, with the lowest effect obtained for the 12 μm channel forward view data simulated using the tropical atmosphere. This result is expected as high levels of water vapour in the satellite FOV will attenuate any changes in surface-emitted radiance (Harris et al. 1994); this effect is more profound in the 12 μm channel where attenuation due to water vapour is strongest. In contrast, the highest sensitivity to T_S is observed for the polar winter atmosphere, the driest of the reference atmospheres, where the response of all the channels for both views is very similar.

Also shown in Table 3.5 is the BT deficit, reflecting the difference between the simulated TOA BT and the underlying SST (for $T_S=T_0$). For all scenarios, except for the tropical atmosphere, the BT deficit in the 11 μm channel is the smallest, which is due to the comparatively high emissivity of the sea surface in this channel, compared with that of the 3.7 and 12 μm channels. Results for the tropical atmosphere do not conform as the 11 μm channel BT deficit is dominated by the water vapour attenuation of the surface-emitted signal. Low atmospheric gaseous attenuation also explains the slightly elevated sensitivity of the 11 μm channel for the polar winter atmosphere when compared to that of the 3.7 μm channel.

The results for the edge-of-swath scenario, also shown in Table 3.5, are very similar. Decreased sensitivity together with an increase in the BT deficit is observed in the nadir-view data, which is consistent with the increase in viewing angle. The opposite effects are seen in the forward-view data, as the zenith angle is lower at the edges of the swath

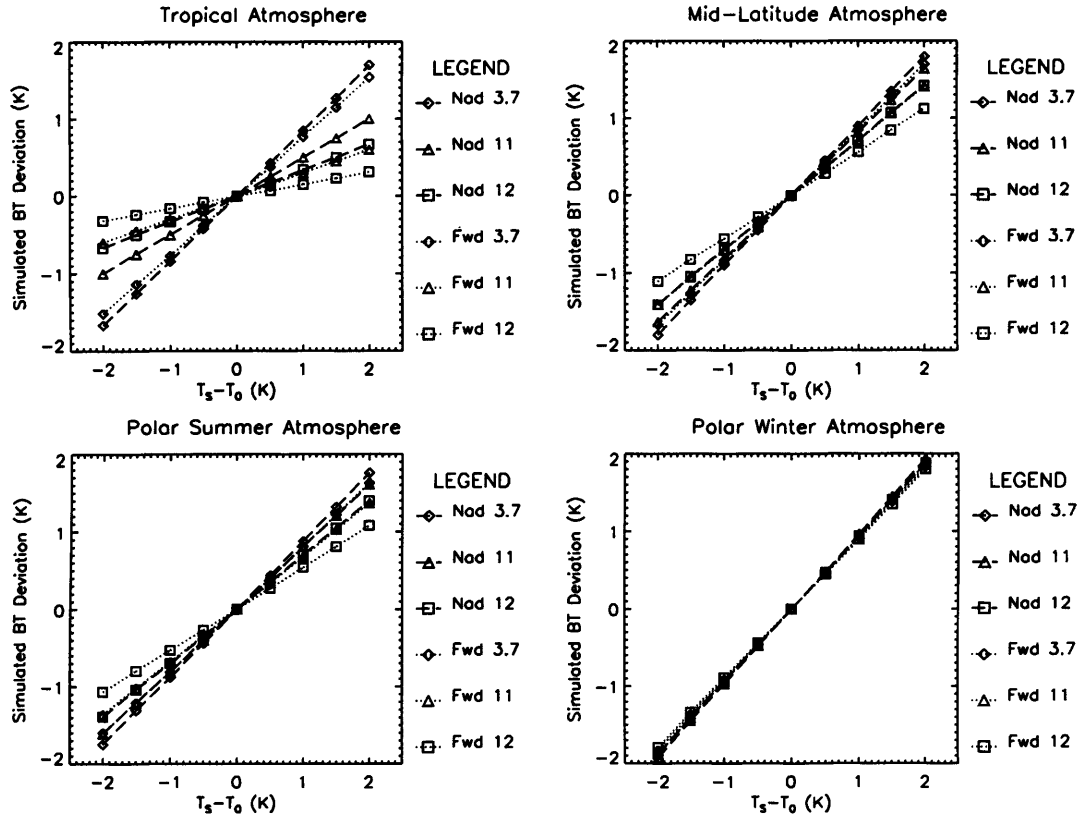


FIGURE 3.6. Response of AATSR TOA BTs to changing surface temperature for the MIPAS reference atmospheres. Results are shown for the centre-of-swath scenario over the ocean for the temperature ranges given in Table 3.2.

than for the centre, thus the atmospheric pathlength is shorter and the surface emissivity higher.

3.3.2 Sensitivity of Retrieved SSTs to SST

Figure 3.7 shows the response of the operational SST algorithms to deviations of T_s from T_0 for the centre-of-swath scenario. The quantities represented by the Y axis refer to the deviation of the retrieved SST from the true value of T_s input into the RT model (i.e. the estimated bias in the retrieval). The calculated SST offsets and responses are given in Table 3.6.

As we might expect, the gradients of the regression lines are all similar and close to unity, with the N2 SSTs exhibiting the strongest deviation from this ideal. Significant offsets (magnitude approximately 0.1 K or greater) are observed for all scenarios, with

Table 3.5. The BT deficit for $T_S = T_0$ (column A) and the AATSR TOA BT response to a change in T_S of 1.0 K for the MIPAS reference atmospheres over the ocean (column B).

Channel	Tropical		Mid-Lat		Polar Win		Polar Sum	
	A	B	A	B	A	B	A	B
	(K)		(K)		(K)		(K)	
CENTRE OF SWATH								
nad 3.7	3.490	0.843	2.290	0.900	1.420	0.950	1.100	0.878
nad 11	5.590	0.500	2.100	0.819	0.860	0.967	0.730	0.806
nad 12	8.450	0.335	3.560	0.707	1.400	0.940	1.230	0.698
fwd 3.7	5.440	0.765	3.770	0.843	2.420	0.918	1.850	0.808
fwd 11	8.500	0.300	3.680	0.705	1.880	0.940	1.360	0.682
fwd 12	11.870	0.157	5.710	0.558	3.110	0.897	2.060	0.537
EDGE OF SWATH								
nad 3.7	3.660	0.834	2.410	0.896	1.480	0.948	1.150	0.870
nad 11	5.900	0.477	2.220	0.807	0.900	0.965	0.760	0.794
nad 12	8.830	0.313	3.720	0.692	1.450	0.940	1.270	0.681
fwd 3.7	5.150	0.778	3.530	0.851	2.250	0.921	1.720	0.819
fwd 11	8.140	0.323	3.430	0.720	1.660	0.943	1.240	0.700
fwd 12	11.470	0.175	5.380	0.578	2.740	0.903	1.910	0.559

the exception of the N3 and D2 retrievals for the tropical and mid-latitude atmospheres, and the dual-view retrievals for the polar summer. The largest-magnitude bias occurs for the N2 retrievals, which demonstrate a warm bias of approximately 0.7 K for both the tropical and mid-latitude atmospheres. This bias becomes negative (approximately -0.4 K) for the polar atmospheres. A warm bias is also observed for the D2 retrievals for the tropical and mid-latitude atmospheres, although the magnitude is significantly lower at 50 mK. This bias also becomes negative for the polar atmospheres: for the polar winter atmosphere, a bias of approximately -0.5 K is obtained for D2; for the polar summer atmosphere, the bias is negligible at approximately -10 mK.

In contrast, small negative biases are observed for both the N3 and D3 retrievals for the tropical and mid-latitude scenarios. This bias becomes positive for the N3 SSTs obtained using the polar atmospheres, where a more substantial offset of several tenths of a degree occurs. The D3 bias remains negative for the polar atmospheres, with a negligible bias of only -1 mK for the polar summer atmosphere. A bias of almost

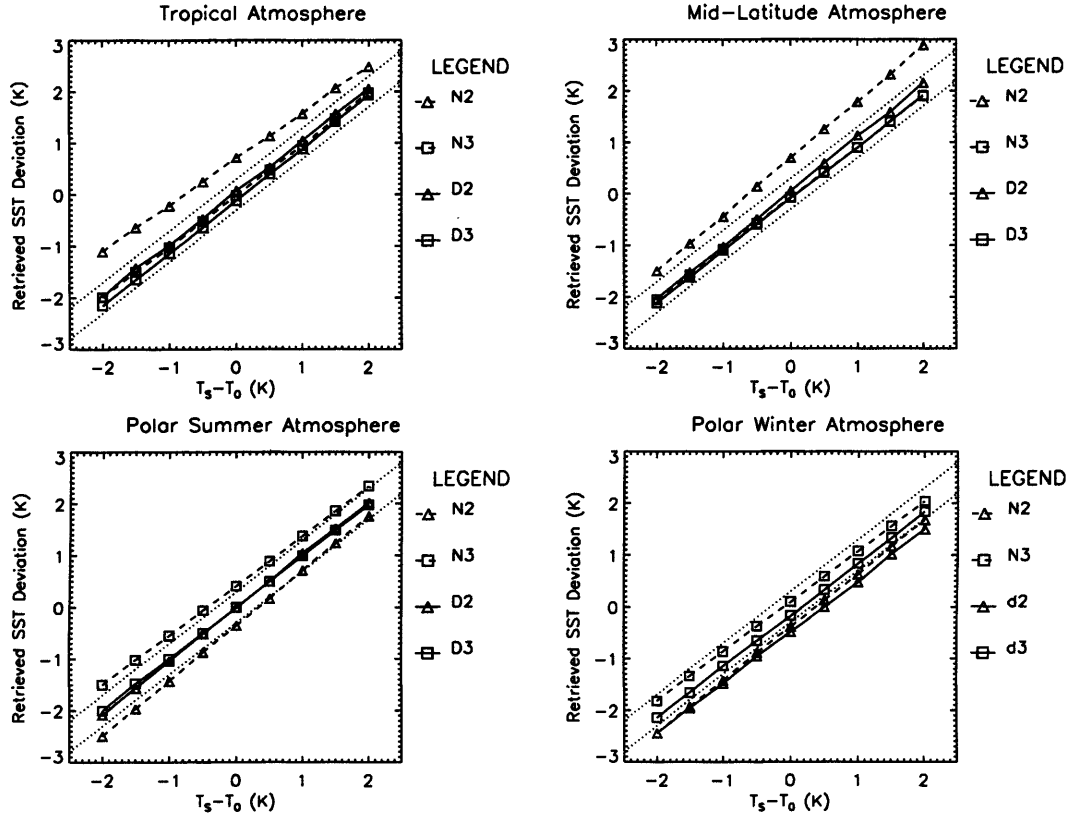


FIGURE 3.7. Response of AATSR SSTs (N2, N3, D2, D3) to changing surface temperature for the MIPAS reference atmospheres. Results are shown for the centre-of-swath scenario over the ocean for the temperature ranges given in Table 3.2. The dotted lines indicate the target ± 0.3 K accuracy of the AATSR SST retrievals.

-0.2 K is observed for the polar winter atmosphere.

Considering all SST retrievals, only the D3 SSTs fall within the ± 0.3 K target accuracy zone for all four reference atmospheres. In theory, the bias for all the SST retrievals should be zero as the model parameters are ideal, and we have not included any atmospheric or surface anomalies. The observed biases may be due to several sources: differences in the RT model, surface emissivity, spectroscopy and/or continuum values used in this study and those used to generate the SST retrieval coefficients, and/or errors in the retrieval coefficients.

Comparing the two-channel (daytime) and three-channel (nighttime) SST retrievals, we find that the nadir SSTs are always higher than their dual-view counterparts, except for the two-channel polar-summer retrievals. This is particularly apparent for the two-channel SSTs, where the dual minus nadir difference (hereafter referred to as D-N) is

Table 3.6. AATSR SST bias for $T_S = T_0$ (column A) and response (column B) to a change in T_S of 1.0 K, for the MIPAS reference atmospheres over the ocean. Also shown are the dual-minus-nadir (D-N) SST differences for each atmospheric scenario.

SST	Tropical		Mid-Lat		Polar Win		Polar Sum	
	A	B	A	B	A	B	A	B
	(K)		(K)		(K)		(K)	
CENTRE OF SWATH								
N2	0.699	0.899	0.691	1.098	-0.382	1.030	-0.358	1.066
N3	-0.017	0.993	-0.079	0.988	0.109	0.966	0.417	0.960
D2	0.050	1.007	0.054	1.050	-0.479	0.986	-0.012	1.029
D3	-0.118	1.021	-0.096	1.005	-0.158	0.994	-0.001	0.994
Dual-Nadir SST Difference								
D2-N2	-0.649	-	-0.637	-	-0.097	-	0.346	-
D3-N3	-0.101	-	-0.017	-	-0.267	-	-0.418	-
EDGE OF SWATH								
N2	0.751	0.881	0.738	1.090	-0.581	1.036	-0.568	1.058
N3	-0.012	0.988	-0.083	0.987	0.126	0.962	0.454	0.959
D2	-0.003	1.000	-0.054	1.038	-0.649	0.980	-0.129	1.029
D3	-0.157	1.009	-0.141	1.001	-0.203	0.997	-0.053	0.989
Dual-Nadir SST Difference								
D2-N2	-0.754	-	-0.792	-	-0.068	-	0.439	
D3-N3	-0.144	-	-0.058	-	-0.329	-	-0.508	

approximately -0.65 K for the tropical and mid-latitude atmospheres. This near-global negative D-N is consistent with values obtained in recent studies of the variation of D-N in observed AATSR data (S. A. Good, 2004, personal communication). Further discussions on the relevance of the D-N are included in Chapter 4.

Results for the edge-of-swath scenario are also shown in Table 3.6. The results are very similar to those for the centre of swath, although there are some noteworthy differences in the biases between the two sets of results of the order of several tenths of a degree. For example, the D3 SSTs have become significantly cooler with changes in bias of approximately -0.05 K. The D2 SSTs are also more negatively biased, with the largest change (-0.17 K) occurring for the polar winter atmosphere.

Table 3.7. The BT deficit for $T_S = T_0$ (column A) and the AATSR TOA BT response to a change in T_S of 1.0 K for the MIPAS reference atmospheres over land (column B).

Channel	Tropical		Mid-Lat	
	A	B	A	B
	(K)		(K)	
CENTRE OF SWATH				
nad 11	5.940	0.492	2.890	0.809
nad 12	8.510	0.333	3.750	0.704
EDGE OF SWATH				
nad 11	6.220	0.468	2.990	0.797
nad 12	8.880	0.310	3.900	0.689

3.3.3 Sensitivity of Land TOA BTs to LST

AATSR TOA BTs have been simulated for the mid-latitude and tropical reference atmospheres for surface temperatures within the temperature range given in Table 3.2 at intervals of 1.0 K. The emissivity used in the model corresponds to a fractional vegetation of 0.5 (Section 3.1.2.3).

As for the simulated TOA BTs over the ocean, linear regression lines have been fitted to the data, where the offsets and responses are given in Table 3.7. The numbers are similar to those derived for TOA BTs over ocean, as the BT response to changes in surface temperature is approximately linear over the range of interest. The small differences observed are due to the different emissivities used in the model for land and ocean surfaces.

Again, the results for the edge of swath are similar, with an increase in the BT deficit and slightly decreased sensitivity observed (approximately 0.02 and 0.01 for the tropical and mid-latitude atmospheres, respectively). This change in BT deficit and sensitivity is consistent with the increase in atmospheric path length as we move away from the centre of the nadir ground track.

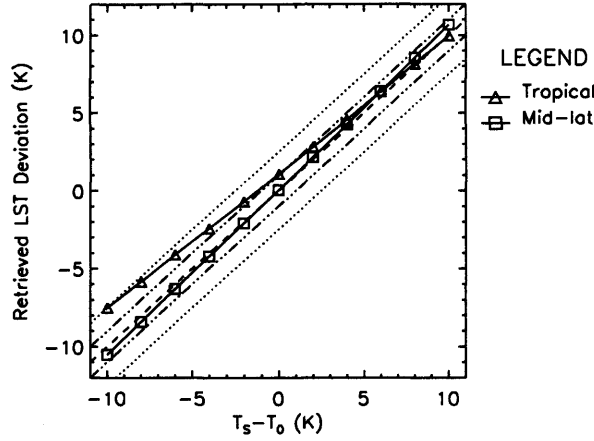


FIGURE 3.8. Response of AATSR LST retrievals to deviating T_s for the MIPAS reference atmospheres. The dotted lines indicate the target ± 2.5 K day time accuracy of the AATSR LSTs, the dotted/dashed line, the target ± 1.0 K night time accuracy, and the dashed line, the line of equality. Results are shown for the centre-of-swath scenario.

3.3.4 Sensitivity of Retrieved LSTs to LST

Figure 3.8 shows the response of the operational LST algorithm for biome 12 for pixels at the centre of the AATSR swath. The quantities represented by the Y axis refer to the deviation of the retrieved LST from the true value of T_s input into the RT model (i.e. the estimated bias in the retrieval). The calculated LST offsets and linear responses are given in Table 3.8. The results for the mid-latitude atmosphere are near-ideal, where we obtain 0.05 K and 1.06 for the bias and response, respectively. For the tropical atmosphere, the results are comparatively poor, with the bias of 1.13 K and a response of 0.88. As the surface - near-surface air temperature difference can vary by several K over land, the non-unity of this response will result in a highly changeable bias. For example, at night, when the surface - near-surface air temperature difference might be 0 K, the tropical LST might be warm biased by approximately 1.13 K. However, during the day, when the surface - near-surface air temperature difference may approach 10 K, the retrieved LST is expected to be cold-biased from the true LST by only a few hundredths of a K.

From the results given in Table 3.8, we find that the LST response for the edge of the swath is very similar to that for the centre-of-swath, particularly in the case of the mid-latitude climatology. However, the observed biases have increased by approximately 0.2 K for the maximum value of precipitable water. This suggests that the magnitude of the precipitable water correction, which is weighted by the parameter, d , in the LST

Table 3.8. AATSR LST bias for $T_S = T_0$ (column A) and response (column B) to a change in T_S of 1.0 K, for the MIPAS reference atmospheres. Also shown are the minimum and maximum values of precipitable water (PW) corresponding to biome 12, used in the calculations.

Min/Max PW	Tropical			Mid-Lat		
	PW	A	B	PW	A	B
	(cm)	(K)		(cm)	(K)	
CENTRE OF SWATH						
—	0.000	1.126	0.875	0.000	0.050	1.060
EDGE OF SWATH						
Min	0.587	1.128	0.853	0.178	0.085	1.057
Max	6.764	1.312	0.853	5.646	0.248	1.057

retrieval algorithm, is too high in this instance. It should be noted that for the edge-of-swath scenario, no difference in response is observed by varying the value of precipitable water used in the LST retrievals, as this is just a constant term in the algorithm (Section 2.4.2).

3.4 Model Results: Surface Emissivity

3.4.1 Sensitivity of Ocean TOA BTs to Surface Emissivity

To investigate the sensitivity of the AATSR BTs over the ocean to surface emissivity, the emissivity has been perturbed from those values defined in Table 3.3 by ± 0.006 at increments of 0.002. Although the range is not critical as TOA BT varies linearly with surface emissivity (see Section 1.3.1.1), this range was chosen as it encompasses most of the expected variation of sea surface emissivity as a result of varying salinity and windspeed. These effects are discussed further below, together with the implications of the temperature dependence of emissivity, which has recently been investigated by Newman et al. (2005).

Figure 3.9 shows the response of the AATSR TOA BTs over the ocean at the centre-of-swath, for $T_S = T_0$; the BTs shown in the plot are differenced from the BT obtained for an emissivity deviation of zero in each case. The weak non-linearity observed in

the modelled data is a result of the precision of the calculated RFM TOA BTs. The calculated response parameters, obtained by fitting a linear regression line to the data, are given in Table 3.9. Most notably, the forward-view BTs exhibit a lower response to changes in emissivity than their nadir-view counterparts, with the lowest response observed for the tropical atmosphere. As stated in Section 3.3, this is to be expected, as we would expect to see a lower response where the effects of water vapour are greatest. Conversely, the results for the drier atmospheres exhibit a higher sensitivity to changes in surface emissivity, with the most significant response observed for the polar winter atmosphere.

The results for the $3.7\ \mu\text{m}$ channel demonstrate little variation, varying between 0.012 and 0.021 K per 0.001 change in emissivity, considering all scenarios for both the forward and nadir view. This sensitivity is consistently less than for both the 11 and $12\ \mu\text{m}$ channels, which vary typically between 0.024 and 0.064 K per 0.001 change in emissivity for all scenarios, except for the tropical climatology. This overall lower sensitivity in the $3.7\ \mu\text{m}$ channel can be explained by considering the nature of the Planck function: for a given change in temperature, the change in flux at $3.7\ \mu\text{m}$ is much larger than at 11 and $12\ \mu\text{m}$. Therefore, for a given change in flux, for example, as a result of a change in emissivity of 0.001, at all wavelengths, the equivalent temperature change (which is really our BT) is much smaller at $3.7\ \mu\text{m}$ than at 11 and $12\ \mu\text{m}$. Results for the tropical atmosphere do not conform, as the sensitivity of the 11 and $12\ \mu\text{m}$ channels is affected strongly by the high amounts of water vapour in the satellite FOV.

These results can be put into context by considering factors that are known to affect sea surface emissivity, namely windspeed, salinity and SST. Masuda et al. (1988) and Watts et al. (1996) estimate a decrease in emissivity in the forward view of approximately 0.006 for the effects of direct emission from a roughened sea surface in the presence of windspeeds of around $10\ \text{ms}^{-1}$ (typical windspeeds over the ocean are in the range of $3\text{--}12\ \text{ms}^{-1}$). However, it should be noted that Watts et al. (1996) estimate the actual emissivity deficit to be much smaller under conditions of high windspeed, when the emissivity-enhancing effects of surface-emitted surface-reflected radiation are also taken into account. In this instance, radiation emitted from a roughened sea surface at high zenith angles may then be reflected by an inclined facet into the satellite field of view, increasing the effective emissivity. More recently, experimental observations in the Pacific Ocean of the dependence of infrared emissivity on windspeed, reported by Hanafin & Minnett (2005), suggest that the effects are much smaller than the models predict. In fact, the results of Hanafin & Minnett (2005) imply no change in sea water emissivity at 9 and $11\ \mu\text{m}$ for a zenith angle of 40° for windspeeds between 3 and $13\ \text{ms}^{-1}$, and a mean

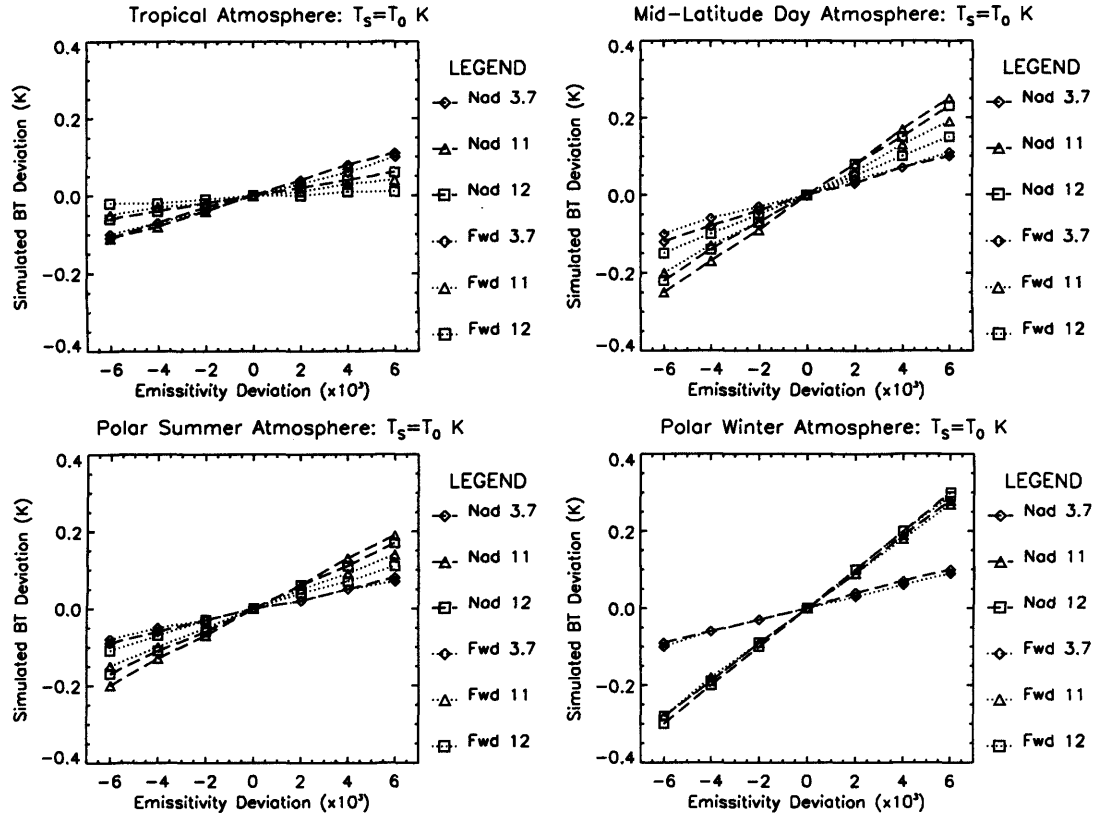


FIGURE 3.9. Response of AATSR TOA BTs to changing emissivity for the MIPAS reference atmospheres for the centre-of-swath scenario over the ocean. Results shown are for $T_S = T_0$.

increase in sea water emissivity of 0.004 at 55° from zenith for an increase in windspeed from 0 to 13 ms^{-1} . The effect of increasing windspeed on nadir-view emissivities is estimated to be negligible.

Sea water has a slightly lower emissivity than pure water in the 3.7 and $11 \mu\text{m}$ channels, but a slightly higher emissivity in the $12 \mu\text{m}$ channel. For example, if the salinity correction derived by Friedman (1969) is applied to the Bertie & Lan (1996) refractive indices, changes in emissivity are -0.0007, -0.0004 and +0.0006, for the nadir-view 3.7, 11 and $12 \mu\text{m}$ channels, respectively. Similar results are obtained by comparing the calculated emissivities for sea water and tap water from the ASTER Spectral Library (1999). The effects in the forward view are slightly larger, with the largest magnitude difference of 0.0017 observed for the $12 \mu\text{m}$ channel. The results of Querry et al. (1977) suggest that the emissivity of the sea may be even more extreme when compared to the data of Bertie & Lan (1996), for example, a difference of +0.007 observed for the forward-view

Table 3.9. AATSR TOA BT response to a change in surface emissivity of 0.001, for the MIPAS reference atmospheres. Results are shown for the centre of swath.

Channel	$T_S - T_0$ K	Tropical (K)	Mid-Lat (K)	Polar Win (K)	Polar Sum (K)
nad 3.7	-2	0.018	0.018	0.016	0.013
nad 3.7	0	0.018	0.018	0.016	0.014
nad 3.7	+2	0.019	0.021	0.017	0.015
nad 11	-2	0.018	0.041	0.046	0.032
nad 11	0	0.019	0.042	0.047	0.032
nad 11	+2	0.019	0.059	0.048	0.033
nad 12	-2	0.010	0.036	0.049	0.027
nad 12	0	0.010	0.037	0.050	0.028
nad 12	+2	0.012	0.064	0.051	0.029
fwd 3.7	-2	0.016	0.017	0.016	0.012
fwd 3.7	0	0.017	0.017	0.016	0.012
fwd 3.7	+2	0.017	0.017	0.016	0.013
fwd 11	-2	0.007	0.032	0.045	0.023
fwd 11	0	0.007	0.033	0.046	0.024
fwd 11	+2	0.009	0.033	0.046	0.025
fwd 12	-2	0.003	0.024	0.047	0.017
fwd 12	0	0.003	0.025	0.048	0.018
fwd 12	+2	0.003	0.026	0.049	0.019

12 μm channel for the Atlantic Ocean water sample used in the study.

While the effects of windspeed and salinity have been under investigation for several years, recent work carried out by Newman et al. (2005) has identified some dependence of sea surface emissivity on SST. In this study, which used a combination of retrieved emissivities determined over a real and artificial ocean using the Airborne Research Interferometer Evaluation System (ARIES), the authors observe a marked decrease in emissivity with decreasing SST over much of the thermal infrared. In particular, they note a strong feature between 760 and 830 cm^{-1} , which coincides with much of the bandwidth of the AATSR 12 μm channel (approximately 800-870 cm^{-1}), obtaining a spread of 0.008 over a temperature range of 27 K. Relatively little effect is observed over the bandwidth of the 11 μm channel (approximately 881-966 cm^{-1}). Using the tabulated complex refractive indices of Newman et al. (2005), which have been derived at temperatures of 279.0 K and 301.2 K, the estimated change in emissivity for the AATSR 11

Table 3.10. Estimated change in sea surface emissivity corresponding to a change in SST from 301.2 K to 279.0 K, for the AATSR nadir and forward split-window channels, derived using the refractive indices given by (Newman et al. 2005). Emissivities corresponding to the centre and edge of swath are shown.

Channel	Swath Centre		Swath Edge	
	Nadir (0.000°)	Forward (55.345°)	Nadir (21.433°)	Forward (52.809°)
11 μm	−0.0005	−0.0013	−0.0005	−0.0011
12 μm	−0.0033	−0.0050	−0.0035	−0.0053

and 12 μm channels between these temperatures is given in Table 3.10. Results for the AATSR 3.7 μm channel are not shown, as the complex refractive indices given by Newman et al. (2005) are restricted to the 770-1230 cm^{-1} (approximately 8-13 μm) range.

The results given in Table 3.9 demonstrate that factors such as salinity, windspeed and temperature could potentially alter the measured TOA BT by several tenths of a degree, particularly for the drier atmospheres. From the general RT equation (Section 1.3.1.1), an increase in TOA BT response with increasing SST is anticipated. Although of negligible magnitude, this is reflected in the results in Table 3.9. Virtually identical results are obtained for the edge-of-swath scenario, with a maximum difference in the BT response observed to be 0.002 K per 0.001 change in emissivity.

3.4.2 Sensitivity of Retrieved SSTs to Surface Emissivity

Figure 3.10 shows the variation of the four AATSR SSTs, N2, N3, D2 and D3 with decreasing emissivity in the forward view, consistent with increasing windspeed. The quantities represented by the Y axis refer to the deviation of the retrieved SST from the true value of T_S input into the RT model (i.e. the estimated bias in the retrieval). Although the gradients of the N2 and N3 SSTs are zero (the nadir-view emissivities are unchanged), these SSTs are included on the graphs for comparison.

The gradient of the D3 SSTs is observed to be much lower than that of the D2 SSTs due to the inclusion of data from 3.7 μm channel, which, as we have seen from Section 3.4.1, is much less sensitive to changes in surface emissivity. The exception is the tropical atmosphere, where this difference in sensitivity is masked by the high concentration of water vapour. Overall, the decrease in the forward-view emissivity has the effect of

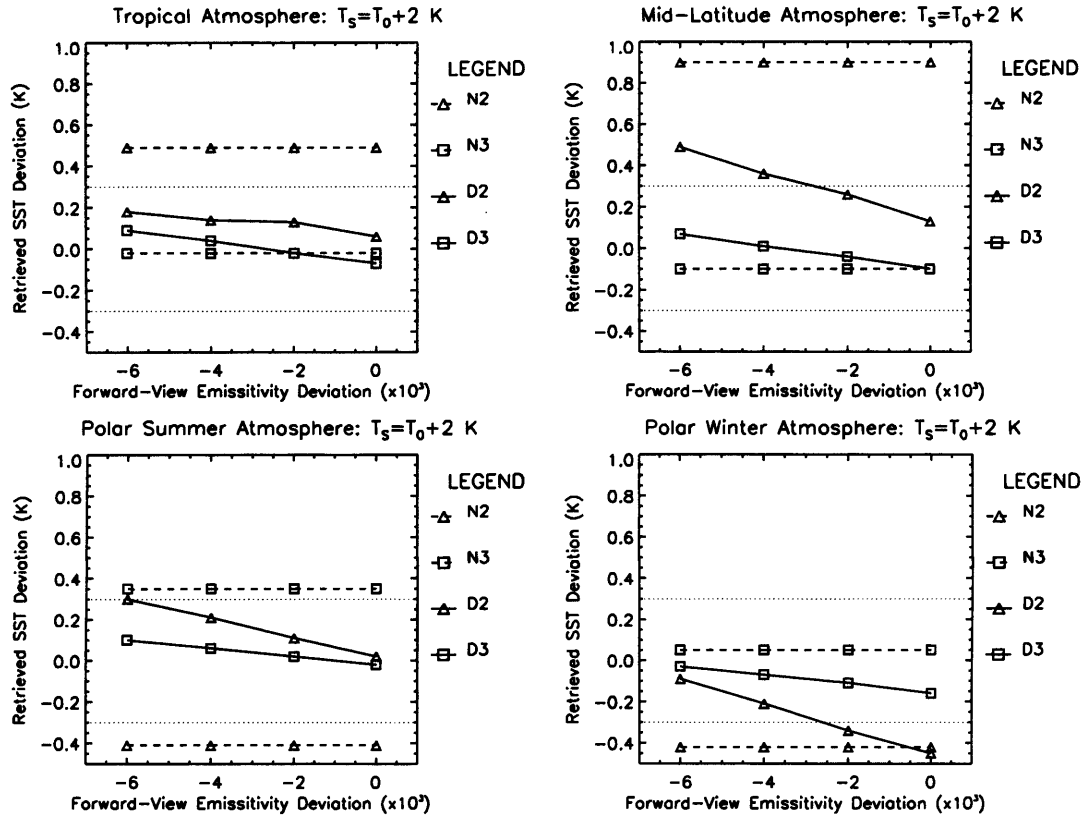


FIGURE 3.10. Response of AATSR D2 and D3 SSTs to changing emissivity in the forward view for the MIPAS reference atmospheres for the centre-of-swath scenario over the ocean. Results shown are for $T_s = T_0 + 2$.

increasing the dual-view SSTs, which is consistent with the findings of Harris et al. (1994) for the ATSR-1 instrument, which has very similar specifications to that of the AATSR. This increase in SST is due to the weighting of the coefficients. For the dual-view coefficients, the weighting of the forward-view $11 \mu\text{m}$ and forward-view $3.7 \mu\text{m}$ BTs are strongly negative for the two- and three-channel SST retrievals, respectively. Thus if these BTs are depressed, the resulting SSTs are higher.

The change in the forward-view emissivity has a significant effect on the relationship between the four SSTs. For the tropical and mid-latitude atmospheres, the N2 SSTs are consistently higher than the D2 SSTs, although the difference decreases with decreasing emissivity in the forward view. For the three-channel SSTs, the dual-view SST becomes increasingly higher than the nadir-view SST with decreasing emissivity in the forward-view. For the polar atmospheres, the N3, D2 and D3 SSTs approach the same value with decreasing emissivity in the forward view.

Table 3.11 shows the simulated changes in SST corresponding to each MIPAS reference atmosphere, with respect to (i) a decrease in emissivity of 0.006 for all the AATSR thermal channels in the forward view (which approximates to the emissivity deficit estimated by Masuda et al. (1988) and Watts et al. (1996) for direct emission from a sea surface roughened by 10 ms^{-1} winds), (ii) the effects of the salinity correction for pure-water emissivity, derived by Friedman (1969), and (iii) a reduction in the AATSR channel emissivities consistent with that expected for decreasing SST (see Table 3.10). In the case of (iii), results for the three-channel retrievals (N3, D3) are omitted, since Newman et al. (2005) only present results for the long-wave infrared.

The results in Table 3.11 indicate that increasing windspeed and decreasing surface temperature have the potential effect of increasing the AATSR SSTs. This is in contrast to increasing salinity, which has the overall effect of decreasing the SSTs in most cases (the exception being the polar winter atmosphere). As stated previously, whether the retrieved SST increases or decreases depends on the change in BT and the weighting of the retrieval coefficients; for example, a decrease in the $12 \mu\text{m}$ channel will actually result in an *increase* in the retrieved N2 SST, as the coefficient for this channel is negative.

From the results presented in Table 3.11, it is clear that the potential effects of windspeed and the temperature dependence of emissivity could lead to errors in the retrieved SSTs of the order of a few tenths of a degree, particularly where the atmosphere is relatively transparent. For salinity, the effects are less significant, with virtually negligible changes in SST observed for almost all scenarios, with the exception of the mid-latitude and polar-winter N2 retrievals, which exhibit changes of more than 0.1 K.

Similar results are obtained for the edge-of-swath nadir-view SSTs, which is largely due to the fact that the increase in the magnitude of the coefficients with increasing distance from the swath centre is only small (see Table 2.4). This is not the case for the dual-view coefficients, and the observed change in SST is typically 50% higher. These findings suggest that the effects of salinity should be considered negligible for the N3, D2 and D3 SSTs, with potentially significant errors introduced into the N2 retrievals over mid- to high-latitudes. The effects of windspeed on sea surface emissivity are still under debate. However, these results strongly suggest that if increasing windspeed does cause significant change in the forward-view emissivities, this could be a large source of error in the AATSR SST retrievals at mid- and high-latitudes.

Table 3.11. AATSR SST deficit as a result of a change in surface emissivity, for (i) a decrease in emissivity of 0.006 for all the thermal channels in the forward view (which approximates to the emissivity deficit estimated by Masuda et al. (1988) and Watts et al. (1996) for direct emission from a sea surface roughened by 10 ms^{-1} winds), (ii) the effects of the salinity correction, derived by Friedman (1969) and (iii) a reduction in emissivity consistent with decreasing SST (see Table 3.10 - estimated from the refractive indices provided by Newman et al. (2005), on the AATSR channel emissivities for the MIPAS reference atmospheres). Results are shown for the centre-of swath scenario.

Channel	$T_S - T_0$ K	Tropical			Mid-Lat			Polar Win			Polar Sum		
		(K)			(K)			(K)			(K)		
		(i)	(ii)	(iii)	(i)	(ii)	(iii)	(i)	(ii)	(iii)	(i)	(ii)	(iii)
N2	-2	0.00	-0.04	0.05	0.00	-0.11	0.22	0.00	-0.12	0.28	0.00	-0.08	0.14
N2	0	0.00	-0.04	0.05	0.00	-0.11	0.22	0.00	-0.13	0.28	0.00	-0.08	0.15
N2	2	0.00	-0.04	0.06	0.00	-0.17	0.41	0.00	-0.13	0.29	0.00	-0.08	0.16
N3	-2	0.00	-0.02	—	0.00	-0.04	—	0.00	-0.04	—	0.00	-0.03	—
N3	0	0.00	-0.02	—	0.00	-0.04	—	0.00	-0.04	—	0.00	-0.03	—
N3	2	0.00	-0.02	—	0.00	-0.06	—	0.00	-0.04	—	0.00	-0.03	—
D2	-2	0.10	-0.03	0.05	0.35	0.00	0.15	0.34	0.07	0.10	0.25	-0.01	0.11
D2	0	0.10	-0.03	0.05	0.36	0.00	0.15	0.35	0.07	0.10	0.26	0.00	0.12
D2	2	0.14	-0.03	0.07	0.35	-0.08	0.37	0.34	0.07	0.10	0.27	0.00	0.12
D3	-2	0.15	-0.01	—	0.16	-0.01	—	0.12	0.01	—	0.11	-0.01	—
D3	0	0.16	-0.01	—	0.16	-0.01	—	0.12	0.01	—	0.11	-0.01	—
D3	2	0.16	-0.01	—	0.15	-0.03	—	0.12	0.00	—	0.12	-0.01	—

3.4.3 Sensitivity of Land TOA BTs to Surface Emissivity

We have seen from Sections 3.4.1 and 3.4.2 that sea surface emissivity can have a substantial effect on the observed TOA BTs and retrieved SSTs. Over land, the situation is very much more complicated not only because emissivity may depend on viewing angle, but also due to the variety of land surface materials that may be present in the satellite FOV (Chapter 1). Apart from variations in emissivity occurring as a result of topographical variation influencing the true zenith angle of the satellite measurements, the effect of the former is considered negligible for the AATSR nadir viewing angle range (Sobrino & Cuenca 1999).

A simplified model has been adopted in this instance to attempt to quantify the effects of changing surface emissivity, as a result of changing land surface composition, on the nadir AATSR TOA 11 and 12 μm BTs. AATSR TOA BTs have been simulated for the mid-latitude and tropical reference atmospheres for the given range of surface temperatures. Emissivity has been determined for a fractional vegetation range between 0 and 1, in incremental steps of 0.25, using the vegetation and soil emissivities obtained in Section 3.1.2.3. It should be noted that the BT responses per unit of emissivity given in Table 3.9 are actually valid over both the land and the sea (for the given surface emissivities and surface-air temperature differences), as TOA BT varies linearly with surface emissivity (Section 1.3.1.1). However, the response per unit change in emissivity is slightly higher over the oceans due to the higher emissivity of the sea, when compared to that of a typical land surface. These numbers may be translated into the TOA BT response per unit of fractional vegetation, f , using the following equation:

$$\frac{dT_i(f)}{df} = 100 \cdot \frac{\Delta\epsilon}{\Delta f} \cdot \frac{dT_i(\epsilon)}{d\epsilon} \quad (3.7)$$

where $\Delta\epsilon$ is defined as:

$$\Delta\epsilon = \epsilon_{i,veg} - \epsilon_{i,soil} \quad (3.8)$$

and $\Delta f = 1.0$. $dT_i(f)/df$ is the change in BT of channel i for a change in fractional vegetation (units of 0.1), $\Delta T_i(\epsilon)$ is the change in channel BT for an emissivity change (i.e. the values given in Table 3.9 - units of 0.001), and $\epsilon_{i,veg}$ and $\epsilon_{i,soil}$ are the channel emissivities of vegetation and soil, respectively. Figure 3.11 shows the BT response for

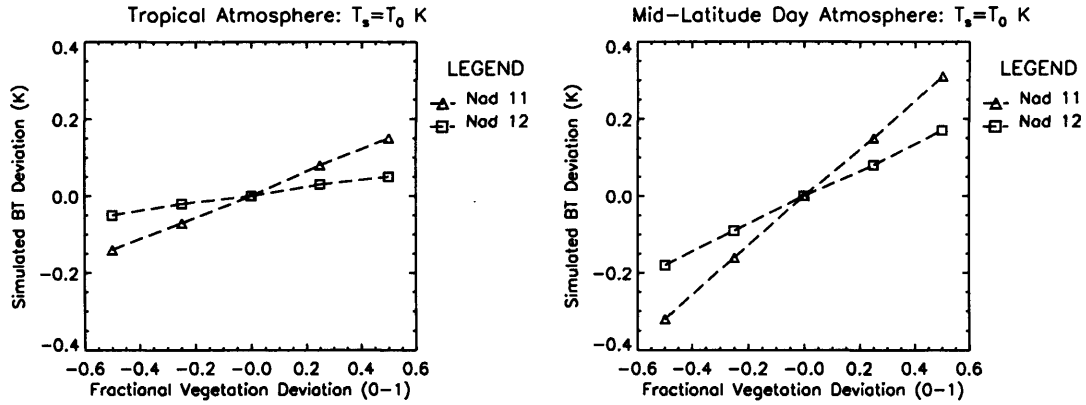


FIGURE 3.11. Response of AATSR 11 and 12 μm channels to varying fractional vegetation for the MIPAS tropical and mid-latitude atmospheres. Results shown are for the centre of swath for $T_s = T_0$. The reference value of fractional vegetation is 0.5.

Table 3.12. AATSR TOA BT response to change in fractional vegetation of 0.1, for the MIPAS reference atmospheres. Results are shown for the centre-of-swath scenario.

Channel	$T_s - T_0$ (K)	Tropical (K)	Mid-Lat (K)
nad 11	-10	0.022	0.056
nad 11	0	0.029	0.063
nad 11	+10	0.035	0.071
nad 12	-10	0.008	0.030
nad 12	0	0.010	0.035
nad 12	+10	0.013	0.040

$T_s = T_0$, where the BTs shown in the plot are differenced from the BT calculated for a deviation in fractional vegetation of zero in each case. The results for the full range of surface-air temperature differences are given in Table 3.12.

Both the 11 and 12 μm channels for both reference atmospheres show an increase in BT with fractional vegetation; this is expected as the emissivity of vegetation is generally higher than that of soil. Similar conclusions, to those for BTs over the oceans, are drawn from the results: i) the response of the BTs for the tropical atmosphere is lower than that for the mid-latitude atmosphere, ii) the 12 μm channel has a lower response than the 11 μm channel, and iii) an increase in sensitivity is observed with increasing surface-air

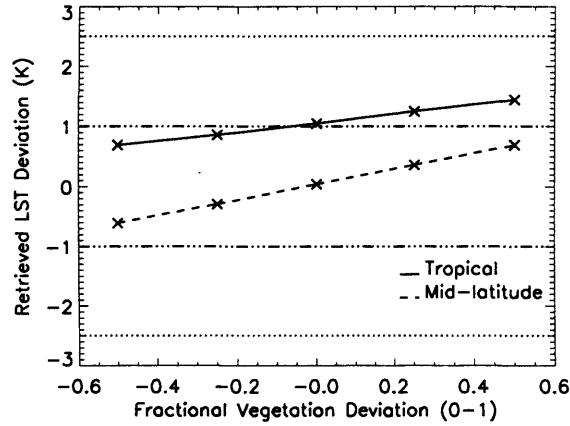


FIGURE 3.12. Response of AATSR LST to changing fractional vegetation for the MIPAS tropical and mid-latitude reference atmospheres for the centre-of-swath scenario. Results shown are for $T_S = T_0$, where the dotted lines indicate the ± 2.5 K target day time accuracy of the retrievals and the dotted/dashed line, the target ± 1.0 K night time accuracy. The reference value for fractional vegetation is 0.5.

temperature difference.

Results for the edge of the swath are not significantly different from those for the centre of the swath, with a maximum difference of 0.003 K per 0.1 fractional vegetation observed between the centre- and edge-of-swath scenarios.

3.4.4 Sensitivity of Retrieved LST to Surface Emissivity

Figure 3.12 shows the response of the AATSR LST to changes in fractional vegetation for both the tropical and mid-latitude reference atmospheres for $T_S = T_0$. The quantities represented by the Y axis refer to the deviation of the retrieved LST from the true value of T_S input into the RT model (i.e. the estimated bias in the retrieval). The response for all LST-air temperature ranges are given in Table 3.13.

As anticipated from the results presented in Table 3.12, the response of the LSTs increases with increasing LST-air temperature difference, with significantly higher sensitivity observed for the mid-latitude atmosphere than for the tropical atmosphere. The results suggest that errors of the order of several tenths of a degree may be introduced into the LST retrieval where an inappropriate surface emissivity is assumed in the retrieval algorithm. This effect will be amplified where the surface-air temperature difference is large and positive (e.g. typical of much of the globe during the day). For several of the

Table 3.13. AATSR LST response to change in fractional vegetation of 0.1, for the MIPAS reference atmospheres. Results are shown for the centre of swath.

LST	$T_S - T_0$ (K)	Tropical (K)	Mid-Lat (K)
N2	-5	0.055	0.119
N2	0	0.076	0.145
N2	+5	0.087	0.138

LST product biomes, this problem is overcome to some extent by the inclusion of the fractional vegetation term in the retrieval algorithm (see Chapter 2). However, as the algorithm for biome 12 is actually independent of this parameter, a constant value for surface emissivity is effectively assumed for locations within this biome.

Again, the results for the edge of the swath are almost identical to those given in Table 3.12, differing by only a few thousandths of a K. As we have seen previously, the response is slightly reduced due to the increase in atmospheric pathlength in the nadir view.

3.5 Model Results: Atmospheric Water Vapour

3.5.1 Height Sensitivity to Atmospheric Water Vapour

Sections 3.5.2 - 3.5.5 describe the results of experiments investigating the sensitivity of the AATSR TOA BTs and retrieved SST/LSTs to changes in the total column water vapour. However, the TOA BTs are also sensitive to the height of the water vapour in the atmosphere. This height-dependent sensitivity is described here, using results obtained from the mid-latitude and tropical MIPAS reference atmosphere over the ocean as an example.

Due to the highly variable concentration of water vapour with height in the atmosphere, this experiment utilises two methodologies. Firstly, the concentration of water vapour has been varied by a fixed amount at each height level (1 km intervals) and secondly, by a percentage at each height level. For the first methodology, the water vapour was varied by 1897 ppmv, which is the largest possible absolute concentration by which the profile below 6 km can be varied, without generating negative concentrations (1897

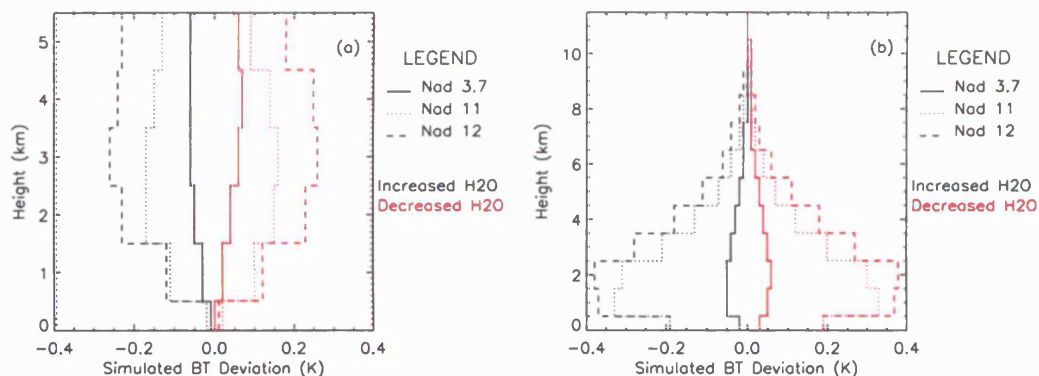


FIGURE 3.13. AATSR TOA BT response to change in atmospheric water vapour over the ocean as a function of height. (a) shows the variation of TOA BT where the water vapour is changed by a fixed amount (1897 ppmv - see text for explanation) at each height level for the MIPAS mid-latitude reference atmosphere and (b) shows the variation of TOA BT where the water vapour is changed by 10% at each height level for the MIPAS tropical reference atmosphere. Results are shown for the centre of swath for $T_S = T_0$.

ppmv is the concentration of water vapour at 5 km). The second method was included due to the fact that the concentration of water vapour becomes very small above about 6 km, and little change in BT is observed for fixed changes in the concentration of water vapour of this magnitude, thus only limited results can be obtained. However, interpretation of the results using the second method may be subjective as water vapour varies strongly with height (see Figure 3.2).

From the results shown in Figure 3.13, it is clear that each channel has a different sensitivity to water vapour. Both sets of results (Figure 3.13a and b) indicate that the influence of the near-surface water vapour concentration on the TOA BTs is secondary to the concentration within the middle- and upper-troposphere. This result is in agreement with the conclusions of Minnett (1986), who finds that water vapour below a pressure level of 850 mbar (approximately 1 km height) has a much smaller effect on the observed TOA BT than water vapour above this pressure level over the AVHRR/2 split-window channels, which operate over similar bandwidths to those of the AATSR. Figure 3.13a suggests that the water vapour concentration between heights of 1.5 and 4.5 km has the strongest effect on the TOA BTs; the results in Figure 3.13b are misleading with respect to this point as water vapour decreases sharply with height in the troposphere, thus the absolute concentration of a percentage change is obviously larger nearer the surface. However, Figure 3.13b does suggest that the effect of water vapour is negligible above

~10 km. This is also the conclusion of Barton (2004) who has derived water vapour weighting functions for each of the ATSR-2 infrared channels, which are close to zero above a height of 8 km.

3.5.2 Sensitivity of Ocean TOA BTs to Atmospheric Water Vapour

The sensitivity of the AATSR TOA BTs to changing total column water vapour has been examined in this study by perturbing the water vapour profiles in the MIPAS reference atmospheres between -50 and $+50\%$, at intervals of 10% , at all height levels. A 50% limit was chosen as this was considered a reasonable approximation of the change in water vapour for the reference atmospheres based on the companion one-sigma profiles. Although perhaps conservative for mid/upper tropospheric water vapour concentration, which may differ by more than 100% , the near surface water vapour one-sigma deviation is of the order of $20\text{-}30\%$. As previously, BTs have been simulated for a range of $T_S - T_0$ between -2 and $+2$ K.

From Figure 3.14, which shows results for the centre-of-swath scenario for $T_S = T_0$, we observe that the response is almost linear over the range of interest, particularly for the tropical climatology. Note that the BTs shown in this plot are differenced from the BT obtained for the unperturbed atmospheric water vapour profile in each case. To obtain a measure of the response of the BTs, second-degree polynomials have been fitted to the data, where the x and x^2 terms are given in Table 3.14. The intercomparison of results for the different atmospheres may be subjective, as the water vapour is varied by a percentage of the profile in question and not by an absolute amount.

For all profiles, with the exception of the polar summer atmosphere, the TOA BTs always decrease with increasing water vapour. The results for the polar atmospheres demonstrate low sensitivity to water vapour, with a change in BT of only approximately 0.3 K for a 50% change in total column water vapour. The increase in the 11 and $12\ \mu\text{m}$ TOA BTs using the polar summer atmosphere where $T_S = T_0 - 2$ K, can be attributed to the fact that a significant proportion of the thermal radiation measured by the sensor is emitted from the water vapour molecules themselves where the SST used in the model is at its lowest (i.e. 253 K). This is a particularly interesting observation, as the shape of the water vapour profiles for the mid-latitude and polar summer atmospheres are very similar in the troposphere (Figure 3.2), where the effects of the atmosphere on the AATSR channels are more profound.

Results for tropical and mid-latitude atmospheres vary significantly between the different channels, and for the nadir and forward views. For both atmospheres, the nadir

Table 3.14. AATSR TOA BT response to 10% increase in atmospheric water vapour, x , for the MIPAS reference atmospheres over the ocean. The x and x^2 terms of the second-degree polynomials fitted to the data are shown for the centre of swath.

Channel	$T_S - T_0$ (K)	Tropical		Mid-Lat		Polar Win		Polar Sum	
		x	x^2	x	x^2	x	x^2	x	x^2
nad 3.7	-2	-0.118	0.002	-0.053	0.001	-0.013	0.000	-0.007	0.000
nad 3.7	0	-0.136	0.002	-0.063	0.001	-0.016	0.000	-0.018	0.000
nad 3.7	2	-0.153	0.002	-0.073	0.001	-0.020	0.000	-0.030	0.000
nad 11	-2	-0.535	-0.013	-0.132	-0.005	-0.013	0.000	0.019	0.000
nad 11	0	-0.650	-0.011	-0.182	-0.006	-0.019	-0.001	-0.039	-0.002
nad 11	2	-0.765	-0.010	-0.232	-0.008	-0.024	-0.001	-0.096	-0.003
nad 12	-2	-0.687	-0.010	-0.195	-0.005	-0.025	0.000	0.034	-0.001
nad 12	0	-0.804	-0.005	-0.263	-0.006	-0.035	-0.001	-0.044	-0.002
nad 12	2	-0.921	0.000	-0.331	-0.007	-0.045	-0.001	-0.121	-0.004
fwd 3.7	-2	-0.155	0.003	-0.073	0.001	-0.019	0.000	-0.008	0.000
fwd 3.7	0	-0.179	0.003	-0.088	0.002	-0.025	0.000	-0.024	0.000
fwd 3.7	2	-0.202	0.004	-0.102	0.002	-0.030	0.000	-0.039	0.001
fwd 11	-2	-0.722	-0.014	-0.172	-0.008	-0.017	-0.001	0.057	-0.002
fwd 11	0	-0.844	-0.007	-0.247	-0.009	-0.026	-0.001	-0.027	-0.004
fwd 11	2	-0.967	-0.001	-0.321	-0.010	-0.035	-0.001	-0.111	-0.005
fwd 12	-2	-0.860	-0.009	-0.210	-0.012	-0.020	0.000	0.106	-0.009
fwd 12	0	-0.960	0.001	-0.300	-0.012	-0.037	-0.001	0.005	-0.008
fwd 12	2	-1.061	0.011	-0.390	-0.012	-0.053	-0.001	-0.097	-0.008

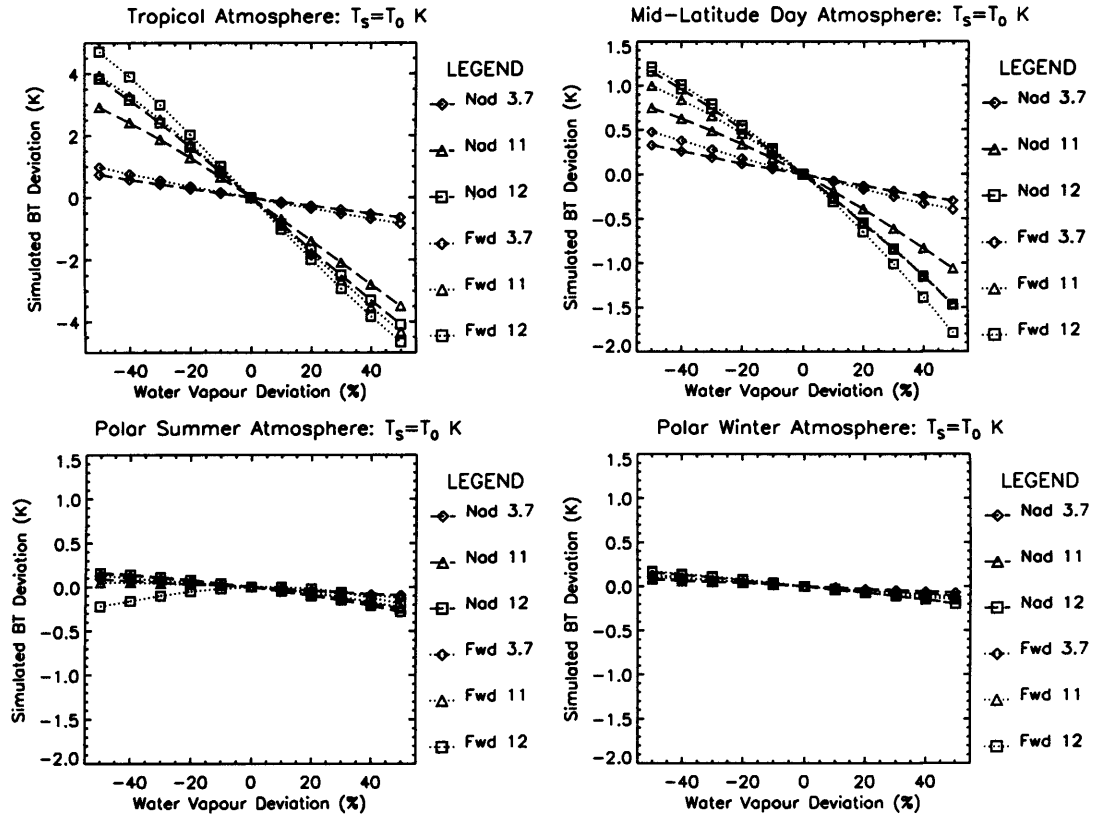


FIGURE 3.14. AATSR TOA BT response to change in atmospheric water vapour for the MIPAS reference atmospheres over the ocean. % change in water vapour refers to perturbation of the entire profile by that amount. Results are shown for the centre of swath for $T_S = T_0$. NOTE: an expanded scale for the tropical atmosphere has been used.

3.7 μm channel demonstrates the lowest response, with the forward 12 μm channel the highest, results which are consistent with the findings of other researchers, such as Barton (2004). A higher response is observed for the 12 μm channel as the attenuation due to water vapour is stronger in this region; with the longer atmospheric pathlength, these effects are exaggerated further in the forward view. An overall increase in sensitivity is observed with increasing surface-air temperature difference, where the polynomial coefficients become more negative.

The results for the edge-of-swath do not vary significantly (a few hundredths or thousandths of a K) from those given in Table 3.14, with a small increase in the nadir-view x term due to the longer atmospheric pathlength (and thus more water vapour in the AATSR FOV); the small value of x^2 remains virtually unchanged for all scenarios.

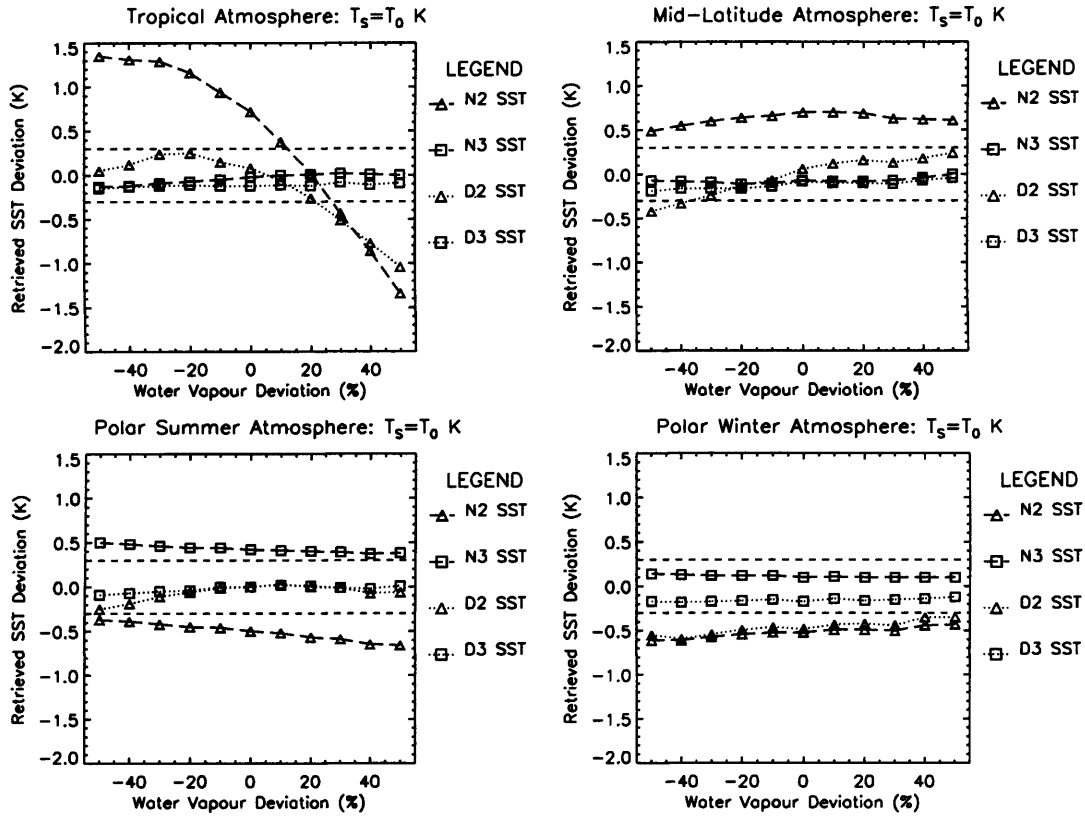


FIGURE 3.15. AATSR SST response to change in atmospheric water vapour for the MIPAS reference atmospheres over the ocean. % change in water vapour refers to perturbation of the entire profile by that amount. Results are shown for the centre of swath for $T_S = T_0$.

3.5.3 Sensitivity of Retrieved SSTs to Atmospheric Water Vapour

The variation of the four AATSR SST retrievals with % change in column water vapour for $T_S = T_0$ is shown in Figure 3.15. The quantities represented by the Y axis refer to the deviation of the retrieved SST from the true value of T_S input into the RT model (i.e. the estimated bias in the retrieval). Table 3.15 shows the x and x^2 coefficients of second-degree polynomials fitted to the SST data for the full range of SST-air temperature differences employed in the study.

The most notable feature of these data is the stability of the three-channel retrievals when compared to their two-channel counterparts for the tropical and mid-latitude atmospheres. This highlights clearly the benefits of including the $3.7 \mu\text{m}$ channel in the SST algorithm for these latitudes. The advantages of utilising the dual-view feature of the AATSR are also very apparent when comparing the D2 and N2 retrievals; the for-

Table 3.15. AATSR SST response to 10% increase in atmospheric water vapour, x , for the MIPAS reference atmospheres over the ocean. The x and x^2 terms of the second-degree polynomials fitted to the data are shown for the centre of swath.

Channel	$T_S - T_0$ (K)	Tropical		Mid-Lat		Polar Win		Polar Sum	
		x	x^2	x	x^2	x	x^2	x	x^2
N2	-2	-0.166	-0.019	0.016	-0.003	0.014	0.000	-0.012	0.003
N2	0	-0.274	-0.028	0.010	-0.006	0.017	0.000	-0.030	-0.001
N2	+2	-0.389	-0.034	0.001	-0.009	0.022	0.000	-0.043	-0.003
N3	-2	0.024	0.001	0.000	0.002	-0.005	0.000	-0.020	0.001
N3	0	0.016	-0.002	0.006	0.002	-0.004	0.000	-0.012	0.001
N3	+2	0.007	-0.004	0.012	0.002	-0.005	0.000	-0.004	0.001
D2	-2	-0.062	-0.010	0.047	-0.005	0.025	0.000	0.011	-0.006
D2	0	-0.114	-0.023	0.066	-0.006	0.022	0.000	0.017	-0.007
D2	+2	-0.178	-0.031	0.067	-0.007	0.022	0.001	0.028	-0.006
D3	-2	-0.003	0.002	0.010	-0.001	0.003	0.000	0.006	-0.002
D3	0	0.004	0.000	0.013	0.000	0.004	0.000	0.009	-0.002
D3	+2	0.009	-0.001	0.014	0.000	0.005	0.000	0.010	-0.001

mer provides a significantly more stable SST under the test conditions. The results for the polar atmospheres reflect the stability of the BTs with changing total column water vapour over the ranges of interest (Section 3.5.2).

An interesting feature in these data is the relationship between the dual and nadir SSTs. In Section 3.3.2, we saw how the D-N was negative for all scenarios with the exception of the two-channel polar summer SSTs. However, this relationship becomes increasingly positive for the tropical atmosphere two-channel SSTs (N2, D2) with increasing water vapour. The magnitude of the D-N also varies with water vapour loading for all other scenarios. For example, the two-channel D-N becomes more positive for the polar summer atmosphere with increasing water vapour. As seen in Section 3.5.2, we see a general increase in sensitivity with increasing SST-air temperature difference for most scenarios.

The edge of swath results are not significantly different (of the order of thousandths of a K) for almost all scenarios. The exception is the sensitivity of the tropical N2 SSTs, which differ by a few hundredths of a degree.

3.5.4 Sensitivity of Land TOA BTs to Atmospheric Water Vapour

Using the same methodology as that adopted in Section 3.5.2, the sensitivity of the AATSR TOA BTs to atmospheric water vapour over land has been investigated. Table 3.16 shows the response of the nadir 11 and 12 μm , where the results exhibit similar characteristics to those observed for the ocean TOA BT simulations - a general increase in sensitivity is observed with increasing surface-air temperature difference and the effects of attenuation due to water vapour are much more profound on the 12 μm channel. However, the magnitude of the responses are slightly reduced due to the lower emissivity of the land surface than that of the ocean. The results also highlight the role of the surface-air temperature difference. For example, increasing the amount of water vapour in the atmosphere by just 10% depresses the observed BT by 1.4 K in the 12 μm channel for $T_S - T_0 = +10$ K, compared to just 0.8 K for $T_S - T_0 = 0$ K. This is an important factor to consider over land, where the surface-air temperature difference may be several K.

Results for the edge of swath share the same characteristics as those for the ocean nadir TOA BT simulations, with increases in the magnitude of the x term of the polynomial of the order of a few hundredths of a degree. Again, the x^2 terms remain largely unchanged.

Table 3.16. AATSR TOA BT response to 10% increase in atmospheric water vapour, x , for the MIPAS reference atmospheres over the land. The x and x^2 terms of the second degree polynomial fitted to the data, are shown for the centre of swath.

Channel	$T_S - T_0$ (K)	Tropical		Mid-Lat	
		x	x^2	x	x^2
nad 11	-10	0.000	-0.025	0.121	0.001
nad 11	0	-0.573	-0.016	-0.137	-0.005
nad 11	+10	-1.142	-0.010	-0.381	-0.013
nad 12	-10	-0.210	-0.032	0.096	-0.002
nad 12	0	-0.784	-0.007	-0.246	-0.006
nad 12	+10	-1.366	0.016	-0.578	-0.012

3.5.5 Sensitivity of Retrieved LSTs to Atmospheric Water Vapour

Figure 3.16 shows the response of the AATSR LST retrieval for the tropical and mid-latitude atmospheres as a function of varying atmospheric water vapour. The quantities represented by the Y axis refer to the deviation of the retrieved LST from the true value of T_S input into the RT model (i.e. the estimated bias in the retrieval). Notably, all the LST retrievals are well within the target ± 2.5 K day time accuracy, and most are within the target ± 1.0 K night time accuracy of the product for both atmospheres for the water vapour range used for this study. The parabolic shape of the response for the tropical atmosphere bears significant resemblance to the AATSR SST N2 retrieval, which is also a split-window algorithm. However, unlike the SST N2 retrievals, the response for the mid-latitude atmosphere appears linear. Although the simulated TOA BTs decrease in magnitude with increasing water vapour, the retrieved LSTs can increase. This is due an increasing difference between the 11 and 12 μm channels, the latter of which decreases at a faster rate than the former. The effect therefore increases the retrieved LST as a result of the negative sign of the 12 μm channel coefficient.

Table 3.17 gives the x and x^2 coefficients of second-degree polynomials fitted to the data. As suggested by the results in Section 3.5.4, the figures indicate that the response of the AATSR LSTs has a strong dependence on surface-air temperature difference. In this instance, an increase in response with increasing surface-air temperature difference is observed for the tropical atmosphere, with the opposite results obtained for the mid-latitude atmosphere.

The results for the edge of the AATSR swath demonstrate a slight increase in re-

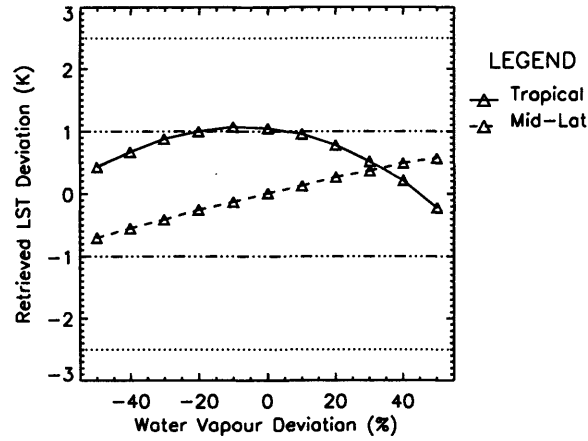


FIGURE 3.16. AATSR LST response to change in atmospheric water vapour for the MIPAS reference atmospheres. % change in water vapour refers to perturbation of the entire profile by that amount. Results shown are for $T_S = T_0$, where the dotted lines indicate the ± 2.5 K target day time accuracy of the retrievals and the dotted/dashed line, the target ± 1.0 K night time accuracy.

Table 3.17. AATSR LST response to 10% increase in atmospheric water vapour, x , for the MIPAS reference atmospheres over the land. Results are shown for the centre of the swath.

Channel	$T_S - T_0$ (K)	Tropical		Mid-Lat	
		x	x^2	x	x^2
N2	-10	0.506	-0.008	0.008	0.008
N2	0	-0.061	-0.038	0.129	-0.003
N2	+10	-0.599	-0.073	0.095	-0.015

sponse with respect to the centre of the swath, with changes in both the x and x^2 coefficients of the order of hundredths of a degree. This culminates in changes in LST which may amount to several tenths of a degree. Using the tropical atmosphere results for $T_S - T_0 = 0$ K as an example, increasing the atmospheric water vapour by 50% causes a change in the retrieved LST of -1.26 and -1.48 K, for the centre and edge-of-swath, respectively, with respect to the bias observed for the nominal water vapour profile (i.e. 0% deviation in water vapour), given in Table 3.8.

3.6 Model Results: Atmospheric Temperature

3.6.1 Height Sensitivity to Atmospheric Temperature

Sections 3.6.2 - 3.6.5 describe the results of experiments investigating the sensitivity of the AATSR TOA BTs and retrieved SST/LSTs to changes in the atmospheric temperature. However, the TOA BTs are also sensitive to the vertical distribution of temperatures in the atmosphere. This height-dependent sensitivity is described here, using results obtained the mid-latitude MIPAS reference atmosphere over the ocean as an example.

Figure 3.17 shows the sensitivity of the TOA BTs to atmospheric temperature as a function of height, where the temperature has been perturbed at each height level by 6.0 K (6.0 K is within the one-sigma variation limit for the mid-latitude MIPAS reference atmosphere). As for the water vapour, the sensitivity is highest to the temperature in the lower to middle troposphere, with little sensitivity observed above a height of about 7 km. However, the greatest sensitivity to atmospheric temperature is between 1-2 km, which is at lower elevation than that for water vapour, which peaks between 2-4 km. Again, these results are similar to those of Minnett (1986), who finds that the AVHRR/2 split window BTs are more sensitive to temperature changes in the atmosphere at heights below approximately 850 mbar (~ 2 km). As for water vapour, the individual AATSR channels show quite different sensitivities to atmospheric temperature. These differences will be explored further below.

3.6.2 Sensitivity of Ocean TOA BTs to Atmospheric Temperature

Using the same methodology to that adopted in Section 3.5.2, the sensitivity to atmospheric temperature has been examined by perturbing the temperature at each height level within the reference atmospheres between -2% and $+2\%$, in increments of 0.5% . The 2% limits were chosen by examination of the one-sigma reference atmosphere profiles. As for the water vapour sensitivity study, the intercomparison of results for the different atmospheres may be subjective, as the temperature is varied by a percentage of the profile in question and not an absolute amount.

From the results shown in Figure 3.18, we observe that the response is almost linear over the range of interest. Note that the BTs shown in this plot are differenced from the BT obtained for the unperturbed atmospheric temperature profile in each case. The data have several features in common with those produced for varying water vapour: the forward-view BTs are more sensitive to atmospheric temperature than their nadir-view

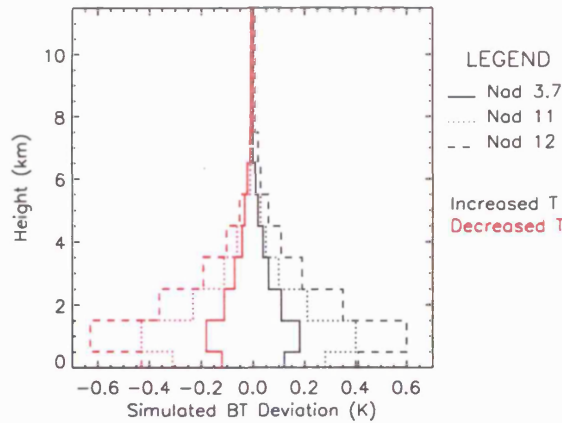


FIGURE 3.17. AATSR TOA BT response to change in atmospheric temperature over the ocean as a function of height. Atmospheric temperature has been varied by 6.0 K at each height level for the MIPAS mid-latitude reference atmosphere. Results are shown for the centre of swath for $T_S = T_0$.

counterparts and 12 μm channel has a higher response than the 11 and 3.7 μm channels, with the latter demonstrating the lowest response. For the polar winter atmosphere, the data have a very low gradient, with similar results obtained for all channels. For all scenarios, the BTs increase with respect to increasing atmospheric temperature.

Table 3.18 shows the x and x^2 coefficients for the second degree polynomials fitted to the data. As we have seen previously, the surface-air temperature difference has considerable effect on the sensitivity of the TOA BTs. For both the nadir and forward 3.7 μm channel BTs, the response appears to diminish with increasing surface-air temperature difference. The opposite effect is observed for the 11 and 12 μm channels, with the exception of the polar winter atmosphere, where small decreases occur for these channels. These coincide with instances where the atmosphere is most transparent, and can be attributed to the signal emanating from the underlying surface dominating the signal measured by the sensor.

Results for the edge of swath demonstrate a small increase in sensitivity for the nadir-view BTs and a small decrease in sensitivity in the forward view, consistent with the increase and decrease in the atmospheric pathlengths, respectively. For the x^2 term of the polynomials, these changes are negligible; for the x term the changes are of the order of hundredths of a degree for all atmospheres, with results for the polar atmosphere exhibiting the smallest change.

Table 3.18. AATSR TOA BT response to 1% change in atmospheric temperature, x , for the MIPAS reference atmospheres over the ocean. The x and x^2 terms of the second-degree polynomials fitted to the data are shown for the centre of swath.

Channel	$T_S - T_0$ (K)	Tropical		Mid-Lat		Polar Winter		Polar Summer	
		x	x^2	x	x^2	x	x^2	x	x^2
nad 3.7	-2	0.47	0.02	0.28	0.01	0.12	0.01	0.33	0.02
nad 3.7	0	0.45	0.02	0.27	0.01	0.11	0.01	0.30	0.01
nad 3.7	+2	0.43	0.02	0.25	0.01	0.11	0.01	0.28	0.01
nad 11	-2	1.61	-0.06	0.52	-0.02	0.07	0.00	0.49	-0.02
nad 11	0	1.64	-0.06	0.53	-0.02	0.07	0.00	0.49	-0.02
nad 11	+2	1.67	-0.06	0.54	-0.02	0.07	0.00	0.50	-0.02
nad 12	-2	2.09	-0.06	0.81	-0.02	0.13	0.00	0.74	-0.02
nad 12	0	2.13	-0.07	0.82	-0.02	0.12	0.00	0.75	-0.02
nad 12	+2	2.16	-0.07	0.83	-0.02	0.12	0.00	0.77	-0.02
fwd 3.7	-2	0.69	0.02	0.44	0.02	0.21	0.01	0.50	0.02
fwd 3.7	0	0.66	0.02	0.41	0.02	0.19	0.01	0.47	0.02
fwd 3.7	+2	0.63	0.02	0.39	0.02	0.18	0.01	0.43	0.02
fwd 11	-2	2.24	-0.07	0.83	-0.03	0.13	0.00	0.78	-0.03
fwd 11	0	2.27	-0.07	0.85	-0.03	0.12	0.00	0.79	-0.03
fwd 11	+2	2.31	-0.07	0.86	-0.03	0.12	0.00	0.80	-0.03
fwd 12	-2	2.65	-0.06	1.20	-0.04	0.21	0.00	1.11	-0.03
fwd 12	0	2.68	-0.06	1.22	-0.04	0.20	0.00	1.13	-0.04
fwd 12	+2	2.71	-0.06	1.23	-0.04	0.20	0.00	1.15	-0.04

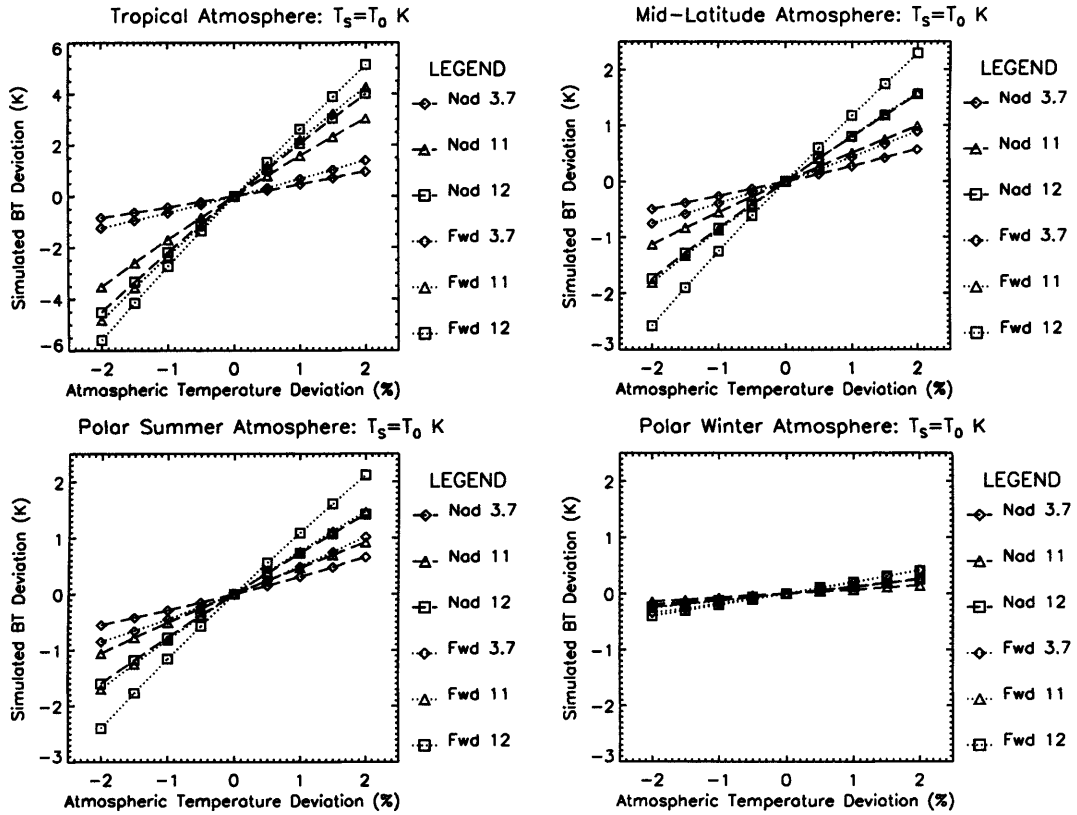


FIGURE 3.18. AATSR TOA BT response to change in atmospheric temperature for the MIPAS reference atmospheres over the ocean. % change in temperature refers to perturbation of the entire profile by that amount. Results are shown for the centre of swath for $T_s = T_0$. NOTE: an expanded scale has been used for the tropical atmosphere.

3.6.3 Sensitivity of Retrieved SSTs to Atmospheric Temperature

Figure 3.19 shows the response of the four AATSR SST retrievals, N2, N3, D2 and D3, as a function of atmospheric temperature. The quantities represented by the Y axis refer to the deviation of the retrieved SST from the true value of T_s input into the RT model (i.e. the estimated bias in the retrieval). As for the water vapour sensitivity study, the inclusion of data from the $3.7 \mu\text{m}$ channel and/or data from the forward view in the retrieval clearly improves the stability of the SSTs. For the tropical and mid-latitude atmospheres, the N2 retrieval is affected strongly by the change in atmospheric temperature, such that changes of more than 1.5 K are evident in the case of the former for the study conditions. Interestingly, the N2 SSTs increase with increasing atmospheric temperature for the tropical atmosphere, whilst the opposite effect occurs for the mid-latitude retrievals.

This difference is, at least in part, due to the fact that the N2 coefficients are dependent on latitude, thus different coefficients are used for each atmosphere. The weighting of the coefficients, together with the rate of change of the difference between the 11 and 12 μm BTs with respect to the increase in the 11 μm BT with atmospheric temperature, determines whether the retrieved SST increases or decreases. Notably, the three other SST retrievals all remain within the target 0.3 K accuracy zone for both the tropical and mid-latitude atmospheres. Results for the polar atmospheres show a high degree of stability, but are subject to strong biases, as discussed in Section 3.3.2.

As for the response for deviation of atmospheric water vapour, the D-N also appears to be affected by the change in atmospheric temperature. Considering the tropical two-channel retrievals as an example, the relationship becomes increasingly negative as the temperature of the atmosphere increases, such that for an overall 2% rise in temperature, the D-N is almost -1.5 K. For the opposite extreme, the D-N approaches +0.5 K for a decrease in atmospheric temperature of 2%. Contrary to the results for varying water vapour presented in Section 3.5.3, the three-channel D-N appears to be quite sensitive to changes in atmospheric temperature. Using the tropical atmosphere as an example, the D-N decreases from approximately -0.1 K to almost -0.3 K for an 2% increase in atmospheric temperature. Similarly, a change in the three-channel D-N of approximately -0.2 K is observed for the mid-latitude and polar atmospheres when the temperature of the atmosphere is increased by 2%.

Table 3.19 shows the x and x^2 coefficients of the polynomials fitted to the results for all SST-air temperature differences. The response of the SSTs demonstrates a small dependence on the surface-air temperature difference, with changes of only a few hundredths of a K in all cases.

For the edge of the swath, a decrease in sensitivity is observed for the N2 and N3 SSTs. Conversely, a slight increase is observed for the dual-view SSTs in all cases, with the exception of the tropical D3 retrieval. These differences between the centre and edge of the swath are small, and of the order of hundredths of a degree.

3.6.4 Sensitivity of Land TOA BTs to Atmospheric Temperature

Table 3.20 shows the x and x^2 coefficients for the second degree polynomials fitted to the simulated TOA BTs over land for the tropical and mid-latitude reference atmospheres. The results are very similar to the simulated ocean TOA BTs, with a small reduction in the sensitivity due to the differences in the ocean and land emissivities used in the

Table 3.19. AATSR SST response to change in atmospheric temperature, x , for the MIPAS reference atmospheres over the ocean. The x and x^2 terms of the second-degree polynomials fitted to the data are shown for the centre of swath.

Channel	$T_S - T_0$ (K)	Tropical		Mid-Lat		Polar Winter		Polar Summer	
		x	x^2	x	x^2	x	x^2	x	x^2
N2	-2	0.442	-0.054	-0.160	0.000	-0.039	-0.002	-0.066	-0.007
N2	0	0.464	-0.053	-0.157	-0.007	-0.036	-0.002	-0.065	-0.006
N2	+2	0.481	-0.055	-0.159	-0.002	-0.025	0.000	-0.060	0.000
N3	-2	0.031	0.025	0.052	0.018	0.096	0.005	0.130	0.024
N3	0	0.004	0.025	0.034	0.016	0.087	0.007	0.099	0.024
N3	+2	-0.026	0.023	0.014	0.016	0.081	0.005	0.066	0.021
D2	-2	0.013	-0.018	-0.131	0.007	-0.015	0.001	-0.093	0.000
D2	0	0.027	-0.014	-0.120	-0.007	-0.009	-0.003	-0.098	0.003
D2	+2	0.009	-0.022	-0.123	0.009	0.006	0.007	-0.085	0.007
D3	-2	-0.055	0.020	-0.008	0.002	0.001	-0.002	0.022	0.008
D3	0	-0.068	0.022	-0.004	0.002	0.001	0.003	0.009	0.006
D3	+2	-0.087	0.019	-0.009	0.002	0.010	0.000	-0.005	0.005

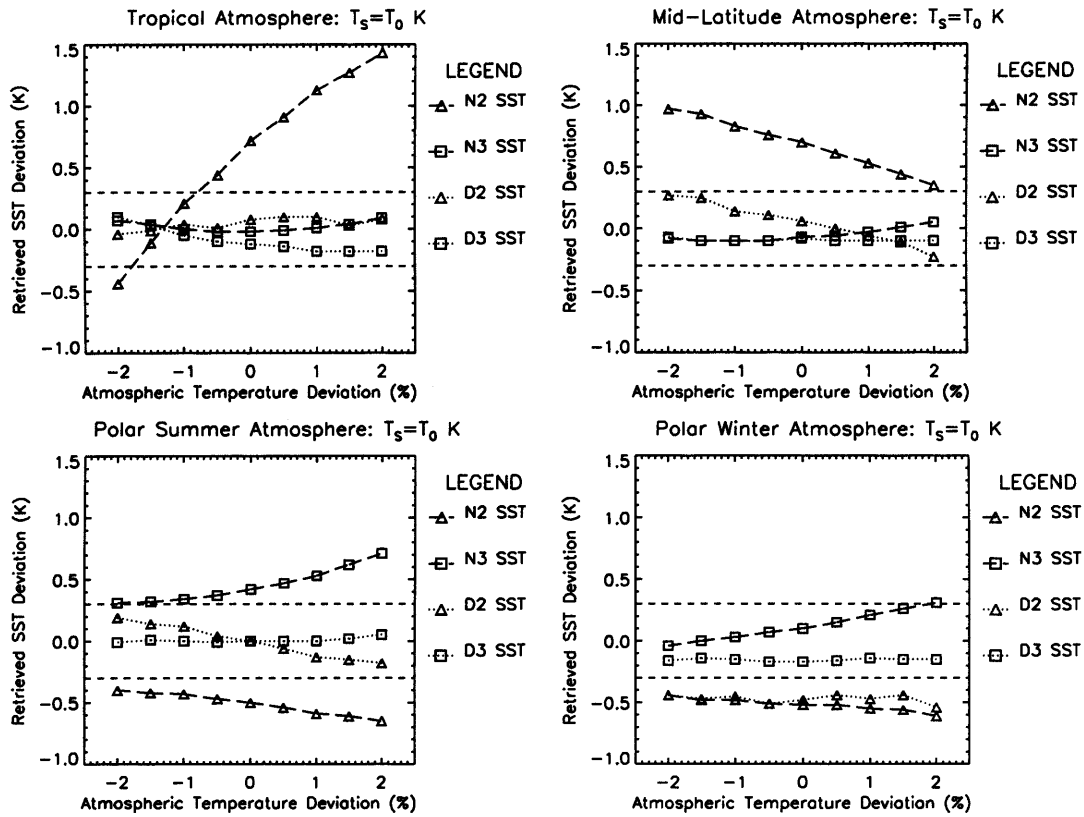


FIGURE 3.19. AATSR SST response to change in atmospheric temperature for the MIPAS reference atmospheres over the ocean. % change in temperature refers to perturbation of the entire profile by that amount. Results are shown for the centre of swath for $T_s = T_0$.

model. As for the model results over the ocean, a small increase in sensitivity of the order of hundredths of a degree is observed for the edge-of-swath results.

3.6.5 Sensitivity of Retrieved LSTs to Atmospheric Temperature

Figure 3.20 shows the response of the AATSR LST retrieval to atmospheric temperature, for biome 12. The quantities represented by the Y axis refer to the deviation of the retrieved LST from the true value of T_s input into the RT model (i.e. the estimated bias in the retrieval). As for atmospheric water vapour, the response of the retrieval is very different for the tropical and mid-latitude atmospheres, with the former showing an overall increase in LST with increasing atmospheric temperature, and the latter a decrease. This relationship is very similar to that observed for the N2 SST in Section 3.6.3. As for water vapour, both curves fall well within the 2.5 K target accuracy zone.

Table 3.20. AATSR TOA BT response to change in atmospheric temperature, x , for the MIPAS reference atmospheres over the land. The x and x^2 terms of the second-degree polynomials fitted to the data are shown for the centre of swath.

Channel	$T_S - T_0$ (K)	Tropical		Mid-Lat	
		x	x^2	x	x^2
nad 11	-10	1.483	-0.057	0.495	-0.014
nad 11	0	1.629	-0.061	0.526	-0.017
nad 11	+10	1.778	-0.067	0.561	-0.020
nad 12	-5	1.960	-0.061	0.776	-0.021
nad 12	0	2.124	-0.066	0.821	-0.021
nad 12	+10	2.293	-0.067	0.868	-0.025

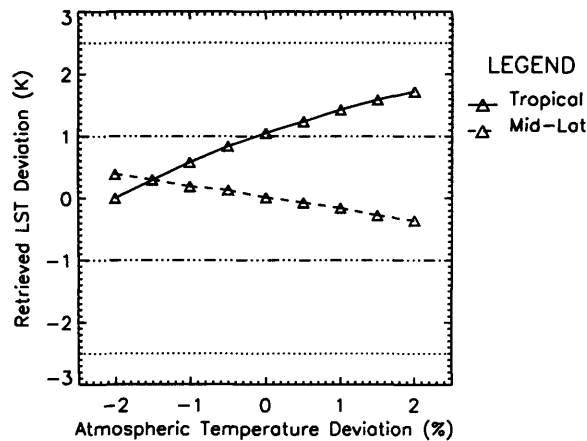


FIGURE 3.20. AATSR LST response to change in atmospheric temperature for the MIPAS reference atmospheres. % change in temperature refers to perturbation of the entire profile by that amount. Results shown are for $T_S = T_0$, where the dotted lines indicate the ± 2.5 K target day time accuracy of the retrievals and the dotted/dashed line, the target ± 1.0 K night time accuracy.

The mid-latitude LSTs retrievals also fall within the target 1.0 K night time accuracy; for high atmospheric temperatures, the tropical LST retrievals are warm-biased by more than 1.0 K.

Table 3.21 shows the response for each surface-air temperature difference used within the study. A general increase in sensitivity is observed with increasing surface-air temperature difference for both the tropical and mid-latitude atmospheres, although in the

Table 3.21. AATSR LST response to change in atmospheric temperature, x , for the MIPAS reference atmospheres. The x and x^2 terms of the second-degree polynomials fitted to the data are shown for the centre of swath.

Channel	$T_S - T_0$ (K)	Tropical		Mid-Lat	
		x	x^2	x	x^2
N2	-10	0.327	-0.046	-0.184	-0.004
N2	0	0.429	-0.048	-0.188	-0.002
N2	+10	0.528	-0.060	-0.183	-0.008

case of the latter, the increase is negligible (thousandths of a K). As for the N2 SST retrievals, the change in sensitivity of the LST retrievals with surface-air temperature difference is higher for the tropical atmosphere than for the mid-latitude. However, while this change is still negligible for tropical SST because of the relatively small range of surface-air temperature differences, the equivalent increases are significant (tenths of a K) over land due to the wide range of surface-air temperature differences.

For the edge of the swath, the sensitivity is slightly enhanced for the tropical atmosphere and diminished for the mid-latitude atmosphere. As for the SSTs, the differences are of the order of a few hundredths of a degree.

3.7 Model Results: Other Atmospheric Constituents

3.7.1 Gaseous Species

In addition to water vapour, a number of other gases have absorption and emission lines within the bandwidths of the AATSR thermal channels, the most important being carbon dioxide. Závody et al. (1995) estimate that by using a mixing ratio of 330 ppmv for CO₂ compared to a mixing ratio of 355 ppmv, the effect on the ATSR-1 TOA BTs is an overestimate in the forward-view BTs of between 0.03-0.06 K. The figure of 330 ppmv is appropriate to the 1970s; the larger concentration of CO₂ is more appropriate for 1991, when the study of Závody et al. (1995) was carried out. They estimate the corresponding nadir-view BT excess to be approximately half this amount, with the largest effect occurring in the 3.7 μm channel due to a strong absorption band at approximately 4.3 μm .

CO₂ levels in the MIPAS reference atmospheres used in this study are the same for all profiles. For the troposphere, the concentration is given as 368.5 ppmv, decreasing

by less than 6 ppmv up to about 70 km. Above this height, the values decline more rapidly to approximately 5 ppmv at 120 km. The companion minimum and maximum profiles only deviate from these values by about 1.5% in the troposphere, where most of the sensitivity of the AATSR thermal channels lies. Even by deviating the profiles by an extreme 5%, the maximum change in BT is only found to be 0.02 K for the forward-view. This figure is slightly lower than the results obtained by Závody et al. (1995), and is probably due to the different radiative transfer models, updated spectroscopy (this study uses the HITRAN 2000 database) and different test atmospheres used in the studies.

Changing the concentration of the other atmospheric species that contribute to the signal measured by the AATSR thermal channels (see Table 3.1), is found to have almost no effect on the simulated BTs. A quantitative discussion of the sensitivity to these atmospheric species has therefore not been included in this work.

3.7.2 Aerosols

3.7.2.1 Effects of Aerosols on (A)ATSR Thermal Channel BTs

The effects of atmospheric aerosol on satellite measurements has become a hot topic in recent years. The general term ‘aerosol’ may refer to a variety of airborne particles with radii ranging between 0.0001 μm and 100 μm . There are several types of aerosols: primary aerosols, emitted directly into the atmosphere as a result of natural and anthropogenic processes, which include sea salt, mineral dust and soot, and secondary aerosols, formed by gas to particle conversion processes, which include sulphate aerosols from volcanic, biological and anthropogenic sources. Aerosols may occur in both the troposphere and the stratosphere, where the latter tend to be more homogeneous in terms of composition, and spatial and temporal distribution. Aerosols both absorb and scatter radiation, where the type of scattering depends on the size of the particle and the wavelength in question. Where the particle size is less than $\sim 1/10$ th of the wavelength, the scattering is predominantly Rayleigh scattering; for larger particles, Mie scattering occurs.

Limited information is available on the effects of aerosols in the thermal infrared, with the majority of the research being carried out in the visible region of the electromagnetic spectrum. For the thermal channels of the (A)ATSR, soot, sea salt, volcanic and transported mineral dust are considered to be the most important. Table 3.22 shows the particle size distribution for these aerosols, as reported by Hess et al. (1998).

Table 3.22. Distribution of aerosol particle size. Reproduced from Hess et al. (1998). σ denotes the width of the lognormal distribution, r_{modN} and r_{modV} the mode by number and the mode by volume and r_{min} and r_{max} , the minimum and maximum radii of the particles.

Aerosol	σ	r_{modN}	r_{modV}	r_{min}	r_{max}
	(μm)	(μm)	(μm)	(μm)	(μm)
Soot	2.00	0.0118	0.05	0.005	20.0
Sea salt (accumulated)	2.03	0.209	0.94	0.005	20.0
Sea salt (coagulated)	2.03	1.75	7.90	0.005	60.0
Mineral (transported)	2.20	0.50	3.00	0.02	5.0
Sulphate droplets	2.03	0.0695	0.31	0.005	20.0

Previous studies have shown that these aerosols depress the signal in the thermal infrared. For example, Pierangelo et al. (2004) have used the results of Hess et al. (1998) for transported mineral dust to simulate the effects on the BTs measured by the Aqua-Advanced Infrared Radiation Sounder (AIRS). For the (A)ATSR thermal channel wavelengths, they find that the effects are highest at $11 \mu\text{m}$ and lowest at $3.7 \mu\text{m}$. The same conclusions are reported by Dundas (1991), who has simulated the effects of desert and volcanic aerosols on the ATSR-1/2 BTs (Table 3.23). Although these data have been simulated for the ATSR-1/2 instrument specifications, these will be comparable to the BT deficits for the AATSR (within $\sim 0.1 \text{ K}$), as the differences between the filter functions are only small (Nightingale & Birks 2004).

Závody et al. (1995) also simulate deficits in the ATSR-1 BTs in the presence of marine aerosols, which they found to be largest in the $3.7 \mu\text{m}$ channel. For a change in visibility from 100 km to 23 km, they simulate a decrease in the TOA BT that ranges between -0.577 K and -0.690 K for the $3.7 \mu\text{m}$ channel, compared with -0.150 K to -0.226 K , and -0.127 K to -0.233 K for the 11 and $12 \mu\text{m}$ channels, respectively. As seen with the water vapour and atmospheric temperature sensitivity analyses carried out in this study, Závody et al. (1995) also found the effects to be more pronounced with increasing surface-air temperature difference.

3.7.2.2 Effects of Aerosols on (A)ATSR SSTs and LSTs

Since aerosols affect observed thermal channel BTs, it might be expected that aerosol effects are also present in the corresponding retrieved SSTs and LSTs. Indeed, aerosols

Table 3.23. Simulated BT depressions for different aerosol types. These data have been reproduced from Dundas (1991).

View	Nadir			Forward		
Wavelength (μm)	3.7	11	12	3.7	11	12
	(K)	(K)	(K)	(K)	(K)	(K)
New volcanic ¹	0.53	0.83	0.60	0.91	1.43	1.04
Old volcanic ¹	0.41	0.83	0.64	0.71	1.43	1.10
Background volcanic ¹	0.48	0.83	0.52	0.84	1.43	0.88
Desert ¹	0.51	0.83	0.80	0.90	1.43	1.37
New volcanic ²	0.40	0.62	0.45	0.69	1.07	0.78

¹ results normalised to produce same BT deficit at 11 μm in each view

² true simulated BT depressions for tropical atmosphere at the centre of the swath

have been observed to affect SSTs retrieved from the thermal infrared satellite observations in a number of studies. For example, Vazquez-Cuervo et al. (2004) report effects of aerosols on AVHRR and ATSR-2 SSTs. Diaz et al. (2001) have noted deficits of as much as 1.74 K in the AVHRR Pathfinder SST dataset, which coincide with high values of aerosol optical depth inferred using data from the Total Ozone Mapping Spectrometer (TOMS). Donlon & Robinson (1998) attribute biases in SSTs retrieved from ATSR-1 data to aerosol ejected into the stratosphere during the Mount Pinatubo eruption in 1991. As a result, the (A)ATSR dual-view SST retrievals have been made robust to stratospheric aerosol (see Chapter 2). Little information is available on the effects of aerosol on LST retrieval. However, based on the results obtained within this study for other atmospheric constituents, we can infer that the effects are probably similar to the effects observed for the N2 SST retrievals.

Calculated depressions in the TOA BTs can be translated to errors in the retrieved surface temperatures by applying the SST/LST retrieval coefficients given in Chapter 2. The BT deficits given in Table 3.23 are multiplied by the coefficient for each channel (excluding the a_0 term, which is just an offset that cancels out). Table 3.24 shows the calculated change in bias (from the clear-sky, non-aerosol biases shown in Tables 3.6 and 3.8), using the results of Dundas (1991) for new volcanic aerosols: these have not been normalised at 11 μm . The SST retrieval coefficients have not been applied to the simulated BT depressions for old and background volcanic, and desert aerosols, as these

Table 3.24. Simulated changes in SST and LST for new volcanic aerosols (Dundas 1991). The tropical AATSR coefficients have been used for the retrievals of SST, and the biome 12 coefficients for the retrievals of LST. The results are applicable to the centre of the AATSR swath.

Aerosol Type	SST N2 (K)	SST N3 (K)	SST D2 (K)	SST D3 (K)	LST N2 (K)
New volcanic	-1.02	-0.50	0.02	0.01	-1.02

results have been normalised for the nadir and forward views separately at $11\ \mu\text{m}$. The tropical coefficients corresponding to the centre of the swath have been used for the SST retrieval, which are consistent with the simulation conditions. For the LST retrieval, the coefficients corresponding to biome 12 have been applied to the simulated BTs.

The results in Table 3.24 demonstrate that the net effect of new volcanic aerosol is a decrease in the nadir SSTs. As anticipated, the results for the LST N2 retrieval are comparable to the SST N2 retrieval. The dual-view SSTs are essentially unchanged, with only a very small increase in the dual-view SSTs; this result is expected, as the retrieval coefficients used here should be robust to stratospheric aerosols (see Chapter 2). If we consider the biases calculated for each SST retrieval in Section 3.3, this results in an overall bias of $-0.32\ \text{K}$, $-0.52\ \text{K}$, 0.07 and $-0.12\ \text{K}$, for N2, N3, D2 and D3, respectively, for new volcanic aerosol. What is most interesting about these results, is that the dual SSTs are now warmer than their nadir counterparts and the D-N has moved from being negative for clear-sky, non-aerosol conditions to positive ($\sim 0.4\ \text{K}$ in for both two- and three-channel SSTs), in the presence of aerosol.

This result is consistent with the findings of Závody et al. (1994) and Dundas (1991), and more recently others working in the AATSR field, who have used D-N as a tracer for the transport of mineral dust from the Saharan desert across the Atlantic the Indian Oceans (S. A. Good, 2005, personal communication). This latter study has also included radiative transfer simulations of the effects of dust aerosols on AATSR SSTs; the preliminary results also indicate a decrease in the nadir-view SSTs together with an increase in the dual-view SSTs, which appears to be of larger magnitude than simulated using the results of Dundas (1991) for new volcanic aerosol. This behaviour of the dual-view SSTs might be construed as counter intuitive. However, although aerosols will depress both the nadir and forward TOA BTs, it is the relative weighting of the dual-view retrieval coefficients that can result in an increase in the calculated SST - a similar effect has been noted (by Merchant & Harris (1999)) for dual-view SSTs contaminated with

Table 3.25. Standard deviation of the errors in the operational gridded SST retrievals as a result of radiometric noise. Data reproduced from Good (2004).

Location	SST N2 (K)	SST N3 (K)	SST D2 (K)	SST D3 (K)
Tropics, centre of swath	0.042	0.015	0.072	0.031
Tropics, edge of swath	0.043	0.015	0.094	0.040
Poles, centre of swath	0.039	0.014	0.073	0.031
Poles, edge of swath	0.039	0.014	0.094	0.040

clouds. These findings suggest that, while the current dual-view AATSR SST coefficients are sufficiently robust to stratospheric volcanic aerosols, the SSTs may still be biased in the presence of desert aerosols. The effects of desert aerosols on the current AATSR SST retrievals will be investigated further in Chapter 4 within the context of a validation experiment over the Caribbean sea.

3.8 Effects of Radiometric Noise on the AATSR SST/LST Retrievals

In addition to the surface and atmospheric characteristics in the satellite FOV, radiometric noise in the AATSR thermal channels will affect the retrievals of SST and LST. For the AATSR, the $NE\Delta T$ is approximately 30 mK for the infrared channels (slightly higher for the 3.7 μm channel at colder temperatures - see Chapter 2). However, because the retrieval coefficients are greater than unity in several cases, the resulting error on the SST/LST retrievals may be larger than this figure.

A study to investigate these effects has been carried out by Good (2004), a summary of which is given here. A random number generator was used to create a gaussian distribution of errors with a standard deviation of 0.01 K (chosen to ensure greater than 99% of the BT errors are within 0.03 K). The operational gridded SST retrieval coefficients were then applied to these errors for 100,000 such simulations. The results of the study are summarised in Table 3.25.

The N2 and D2 retrievals have much wider distributions due to the magnitude of the coefficients being much higher than unity (Chapter 2); in the case of the D2 distribution, the extremes of SST deviations are as high as 0.2 K. These results demonstrate that for

the majority of SSTs, the estimated uncertainty as a result of radiometric noise will be less than 0.1 K.

Good (2004) show that these results improve further when the effects of operational smoothing of the atmospheric correction are taken into consideration. Operationally, the retrieved SSTs are smoothed by calculating the mean difference between the retrieved cloud-free SSTs and the corresponding 11 μm BTs over a 3×3 block of pixels, and then adding that difference on to the central 11 μm BT. This procedure smoothes the atmospheric correction applied to the retrieved SSTs. The effect of the averaging is to reduce the overall noise, resulting in a narrowing of the distributions. In this case, the standard deviation of the D2 SSTs reduces to approximately 0.03 K (maximum 0.1 K) where the 3×3 block is completely cloud-free. For the other SST retrievals, the standard deviations fall to approximately 0.017 K for N2, 0.011 K for N3 and 0.015 K for D3.

In conclusion, the random noise present in the AATSR channels may be significant (~ 0.1 K) for all SST retrievals where no operational smoothing has been performed (e.g. due to cloud-cover), with the exception of perhaps the N3 SSTs. Where operational smoothing has been implemented, the effect of the noise on the SST retrievals is diminished and becomes negligible in all cases where the entire 3×3 pixel block is cloud free. For the operational LST retrievals, it is anticipated that the results will be identical to those obtained for the SST N2 retrievals, although the implications are much less, considering the accuracy requirements of these data.

3.9 Conclusions

A detailed sensitivity study has been carried out investigating the effects of surface temperature and emissivity, and atmospheric water vapour and temperature on the AATSR thermal channel BTs. These results have been translated into the effects on the retrieved 1 km SSTs and LSTs, using the operational algorithms and coefficients detailed in Chapter 2. The effects of other atmospheric constituents, such as carbon dioxide and aerosol, and the effects of random noise in the AATSR thermal channels, have also been discussed quantitatively.

The results of this study demonstrate that the four operational SST retrievals (D3, N3, D2, N2) have very different sensitivities to surface and atmospheric conditions. This is a direct result of the differing responses of each of the AATSR channels to these parameters, and the weighting of the retrieval coefficients.

As one would expect, the response of the SST retrievals to a change in the true SST is close to unity in all cases, except for that of the N2 retrievals. However, all the retrievals, except perhaps D2 and N3 are subject to significant biases for the tropical and mid-latitude atmospheres. For D3, this bias ranges between -0.10 and -0.16 K. For N2, the bias is between $+0.70$ and $+0.75$ K. In comparison, the D2 and N3 retrievals are biased by approximately 50-80 mK for these atmospheres. The results for the polar atmospheres are erratic and of the order of several tenths of a K for all scenarios except for the dual-view polar summer retrievals. The observed biases, for all retrievals, may be due to several sources: differences in the RT model, surface emissivity, spectroscopy and/or continuum values used in this study and those used to generate the SST retrieval coefficients, and/or errors in the weighting of the retrieval coefficients.

Both the D3 and N3 retrievals provide the most consistently accurate results allowing for changing surface emissivity, atmospheric water vapour and temperature. This is due to the inclusion of the $3.7\text{ }\mu\text{m}$ channel in the retrieval, which is the least sensitive of the thermal channels to these parameters. Both retrievals deviate by approximately 0.1-0.2 K for a change in total column water vapour of 50% for all atmospheric scenarios. Similar results are obtained for the tropical and mid-latitude atmospheres, and for D3 with the polar atmospheres, for a deviation in atmospheric temperature of up to 2%. The N3 polar retrievals do not perform so well for changes in atmospheric temperature and may reflect a problem with the weighting of the retrieval coefficients at high latitudes.

For the two-channel SSTs (N2 and D2), the sensitivity of the retrievals to atmospheric water vapour and temperature is very high, as both the 11 and $12\text{ }\mu\text{m}$ channels are affected strongly by the atmosphere. However, the benefits of including data from the forward view are very apparent, particularly when considering the extremes of the tropical atmosphere simulations. For example, an increase in total column water vapour of 50% results in a decrease in the retrieved N2 SST of approximately 2.1 K, but only 1.3 K in the corresponding D2 SSTs. The two-channel retrievals also demonstrate a higher sensitivity to changing surface emissivity than do the three-channel retrievals (the $3.7\text{ }\mu\text{m}$ channel is much less sensitive to surface emissivity than the longer wavelength thermal channels). Except for the effects of windspeed on sea surface emissivity, which are thought to be negligible for nadir viewing angles, the N2 retrievals are more sensitive than the corresponding D2 retrievals to emissivity changes that may occur as a result of varying salinity and SST. The results of this study suggest that biases in the two-channel retrievals of up to 0.3 K may occur as a result of assuming a constant emissivity for the sea surface in the current operational retrieval coefficients. For the tropical atmosphere, the effects of changing surface emissivity are negligible.

The AATSR TOA BTs show negligible dependence on other atmospheric gaseous species. Aerosol, on the other hand, can depress the observed BTs by several tenths of a degree, causing biases in the retrieved SSTs of a similar magnitude. The net effect is found to be a decrease in the nadir SSTs and a small increase in the dual-view SSTs, resulting in the dual-view SSTs being warmer than their nadir-view equivalents. This is a particularly interesting result, as the dual-nadir SST difference (D-N) is found to be largely negative for most simulated clear-sky, non-aerosol scenarios, although extremes of atmospheric temperature and water vapour may also cause the D-N to become positive.

The response of the retrieved LSTs for biome 12, strongly resembles that of the N2 retrievals, as both algorithms use only the nadir split window channels. Considering the relative performance of the four operational SST algorithms to changing emissivity, atmospheric water vapour and temperature, the results of this study suggest strongly that the performance of the operational LST algorithm could be improved by using data from the forward view and/or the $3.7\ \mu\text{m}$ channel. The current LST algorithm has a strong dependence on surface emissivity, increasing by almost 2.0 K for an unaccounted change in fractional vegetation of zero to one for the mid-latitude atmosphere scenario. The dependence is less severe for the wetter tropical atmosphere, where changes in the surface emissivity are more attenuated by the overlying atmosphere. At present, the operational retrieval coefficients for biome 12 do not take into account any annual variation in surface emissivity. The results of this study suggest that the current algorithm could be improved by incorporating some dependence on fractional vegetation as a proxy for the emissivity, as is practice for the majority of the other land biomes. With such a strong variation in emissivity over land, the use of the $3.7\ \mu\text{m}$ channel, which is much less sensitive to this parameter, could offer further improvements to the algorithm for dealing with this problem.

The results of this sensitivity study also suggest that the performance of the LST algorithm is compromised by using the same retrieval coefficients for different latitudes. The algorithm for biome 12 demonstrates the ideal near-zero bias and a response of 1.0 for a change in the true LST, for the mid-latitude climatology. However, for the tropical atmosphere, a bias of approximately 1.0 K and a response of 0.9 is observed. The biases at the edge-of-swath, in conditions of high water vapour, are also found to differ from those at the centre by approximately 0.2 K, suggesting that algorithm may not be correcting sufficiently for the increased path length as the view angle departs from true nadir.

All the SST and LST retrievals are found to be affected by the surface-air temperature

difference; in most cases, an increased surface-air temperature difference results in an increase in sensitivity. Any increases in sensitivity will culminate in a much wider range in the bias of the retrievals, with respect to changing water vapour, emissivity, etc. This has particularly strong implications for LST retrieval, as the surface temperature may differ by several degrees from the near-surface air temperature. These results suggest that current LST algorithm would benefit from utilising separate coefficients for day and night, as recommended by Prata (2002a), to reduce these biases.

It is estimated that random noise in the AATSR thermal channels will result in a typical error of less than 0.1 K in the retrieved SSTs and LSTs, with the largest error occurring for the D2 retrievals. For SSTs or LSTs that have undergone operational atmospheric smoothing, this error will be reduced to only a few hundredths of a K. This demonstrates the potential of the AATSR retrievals to obtain the high accuracy and precision required for the climatological applications for which they were intended.

The results presented in this chapter provide a basis for understanding the relative behaviour of the SST and LST retrievals under different surface and atmospheric conditions. Such understanding can aid interpretation of the results of comparisons between the operational SST/LST retrievals and other SST/LST data sets, such as in situ data collected during validation experiments. Chapters 4 and 5 describe two such validation experiments (SST and LST, respectively), where the results of this chapter have been used as an aid to identify or exclude sources of bias in the results.

Chapter 4

The Accuracy of AATSR SSTs in the Caribbean

The results of the sensitivity analysis presented in Chapter 3 can provide us with an invaluable insight into both the relative and absolute performance of the operational SST algorithms. However, as these investigations are theoretical, only a comparison of the satellite SSTs with equivalent in situ data can provide a true assessment of the accuracy of the product.

This chapter focuses on the results of a comparison between 1 km-resolution SSTs derived from the AATSR and co-located in situ measurements obtained from the Marine-Atmospheric Emitted Radiance Interferometer, or M-AERI (Minnett et al. 2001), over the Caribbean Sea during 2003. The M-AERI, which is permanently deployed on board the Explorer of the Seas that sails continuously around the Caribbean, provides an unprecedented opportunity to perform a long-term validation of AATSR SSTs over this area. Furthermore, the atmospheric conditions in this area are challenging in terms of satellite retrieval of SST since this region is affected by high atmospheric water vapour and aerosol (e.g. Carlson & Prospero 1972), providing a stringent test of the performance of the (A)ATSR instrument and the accuracy of the SST retrieval methodology.

4.1 In Situ Measurements: The M-AERI

The M-AERI is a sea-going Fourier-transform interferometric infrared spectroradiometer that provides the means to make precise measurements of SST_{skin} (better than 0.1 K accuracy). The instrument measures interferograms in the time domain that are trans-

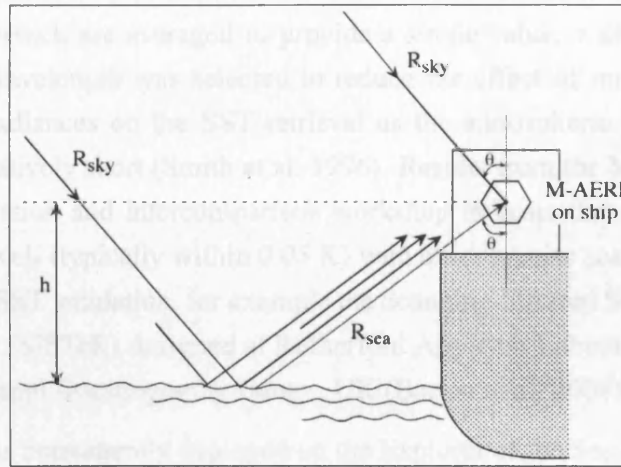


FIGURE 4.1. M-AERI viewing geometry. Figure supplied by P. J. Minnett, University of Miami.

formed into spectra between 3 and 18 μm wavelength with a resolution of approximately 0.5 cm^{-1} . The half angle of the beam width is 1.3° . The M-AERI is internally calibrated using two black-bodies (at temperatures of 60°C and ambient), which are traceable to the National Institute of Standards and Technology (NIST); the residual uncertainties are less than 0.05 K (Minnett et al. 2001), based on laboratory measurements of a NIST-designed calibration target (Fowler 1995) characterised by the NIST Transfer Standard Radiometer TXR (Rice & Johnson 1998, Rice et al. 2004).

The viewing geometry of the M-AERI is shown in Figure 4.1. A measurement of the sea surface emission (R_{sea}) is made at an angle θ from the nadir, with a further measurement made at θ from zenith, to correct for the effects of downwelling sky irradiance (R_{sky}). A measurement is also made at zenith for atmospheric profile retrievals. The correction for the effects of the atmosphere between the instrument and the sea surface is achieved by a parameterisation, previously derived using radiative transfer simulations, dependent on air temperature, humidity, height of the instrument above sea level (h) and θ (Smith et al. 1996). When the measurements are being made in the presence of Saharan dust (see Section 4.4), the uncorrected effects of the aerosols between the height of the M-AERI and the sea surface is estimated to be less than 0.005 K .

A number of independent interferograms are averaged over a predetermined time interval in order to improve the signal to noise ratio. Typically, this time period is set to 90 seconds; for a ship travelling at 22 knots (11 ms^{-1}) this is equivalent to 1.0 km. This measurement sequence is bracketed by the black body calibration. The entire se-

quence takes approximately 11 minutes. The SST itself is derived from 10 spectral points around $7.7\ \mu\text{m}$, which are averaged to provide a single value, with an associated uncertainty. This wavelength was selected to reduce the effect of imperfectly corrected reflected cloud radiances on the SST retrieval as the atmospheric path length at this wavelength is relatively short (Smith et al. 1996). Results from the Miami2001 infrared radiometer calibration and intercomparison workshop indicate that the M-AERI compares extremely well (typically within 0.05 K) with other precise sea-borne radiometers used for satellite SST validation, for example the Scanning Infrared Sea-surface Temperature Radiometer (SISTeR) designed at Rutherford Appleton Laboratories, UK, and the ISAR of the National Oceanography Centre, UK (Barton et al. 2004).

An M-AERI is permanently deployed on the Explorer of the Seas cruise ship, which sails around the Caribbean Sea. The ship has two cruise tracks, the western and eastern cruise tracks, each of which takes one week to complete. On the Explorer of the Seas, the instrument is secured at a height of approximately 39 m above sea level and θ is set to 55° to view beyond the ship's bow wave. The location of the resulting SSTs is determined using the Global Positioning System (GPS) data stream. Gaps in this near-continuous SST dataset are usually due to the mirror being put into 'safe-mode' when the M-AERI's onboard rain sensor detects water droplets close to the M-AERI aperture.

In this study, SSTs have been excluded where the standard deviation of the 10 SSTs (obtained from 10 spectral points around $7.7\ \mu\text{m}$), averaged to obtain the in situ SSTs, is above 0.1 K. This is similar to the threshold of 0.09 K employed by Kearns et al. (2000). Possible reasons for high values that justify the exclusion of such data points, include: temperature transients inside the instruments caused by sunlight entering the aperture, either directly or reflected off the sea surface; temperature transients in the black bodies (e.g. caused by wind entering the aperture); interference from the ship's radios; and increase in strays from scattering elements on the scan mirror (e.g. salt crystals from spray).

4.2 Validation Methodology

Comparisons between M-AERI and AATSR SSTs were made between co-located measurements for 1×1 and 3×3 blocks of AATSR pixels, centred on the pixel containing the latitude and longitude of an M-AERI SST (determined at the mid-point of the sea-viewing measurement). Validation using the 3×3 block was carried out as a secondary experiment in order to verify that potential sources of errors linked to the movement

of the ship (e.g. spatial variation of SST) and AATSR geolocation (particularly in the forward view) were not affecting the results. In this instance, an average value was calculated where at least three valid SSTs occurred within the pixel block. All spatially-coincident matchups occurring within 60 minutes of the AATSR overpass were included in the analysis, which is within the temporal criteria recommended by Minnett (1991).

Undetected cloud-contamination is a major contributor to bias errors in SSTs derived from infrared radiometer data (e.g. Jones et al. 1996). In this study, SSTs were rejected where either the nadir- or forward-view pixels were flagged as cloudy, as defined by the operational AATSR cloud screening algorithms (see Section 2.3.3). Additional cloud screening was carried out by eye, to ensure that only clear-sky pixels were included in the final data set. This was performed by examining the AATSR BT and SST scenes corresponding to each matchup deemed cloud free by the operational processor for signs of potential cloud (e.g. unrealistic ‘streaks’ of abnormally cold BTs or matchups surrounded by several cloud-flagged pixels - see Figure 4.2 for an example). Pixels occurring within 3 km of land or within 6 pixels of the edges of the swath were also excluded from the analysis, the former largely because of potential geolocation errors (particularly in the forward view) and the latter because unrealistic or absent values in the pixels at the extreme margins of the swath were found to occur frequently (possibly as a result of process of regridding the curved swath of the AATSR onto a regular 1-km grid).

No auxiliary windspeed data have been included in this analysis (for example, to screen out data obtained during periods of high windspeed). Although some authors have suggested that windspeed may affect the emissivity of sea water at high zenith angles (e.g. $>50^\circ$), the results presented in Chapter 3 have demonstrated that any effects on the AATSR data will be very small at tropical latitudes due to high levels of water vapour. Furthermore, Hanafin & Minnett (2005) have demonstrated that at-sea measurements of the wind-speed dependence of the surface emissivity is smaller than predicted previously, for example, using the models of Watts et al. (1996) and Masuda et al. (1988).

4.3 Results

Of the 384 coincident M-AERI and AATSR (1×1) measurements, 201 were rejected after cloud screening (approximately 20 of these 201 data points were as a result of the visual inspection of the imagery). A further 84 matchups were discarded on the basis of the standard deviation of the M-AERI SST being above 0.1 K. Of the remainder, 25 of the AATSR SSTs were obtained during the day (using the two-channel SST algorithm)

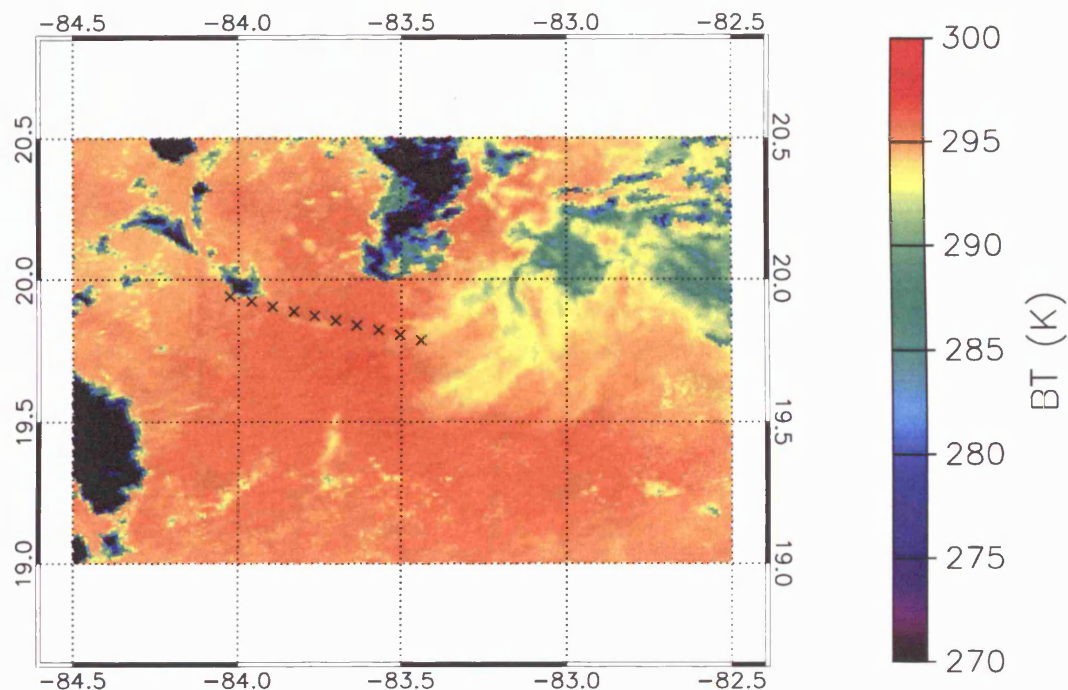


FIGURE 4.2. Example of an AATSR $11\ \mu\text{m}$ BT image contaminated with cloud (21 August 2003 - orbit 07701). The cloud is represented by the relatively cold BTs (typically $<290\ \text{K}$) in the image. The M-AERI matchups for this orbit is shown by series of black crosses running NW-SE. In this case, the most easterly and two most westerly matchups have been rejected from the analysis due to possible cloud contamination (not identified by the AATSR processor - all these matchups are flagged cloud-free in the operational data).

and 74 during the night (using the three-channel AATSR SST algorithm); the locations of these matchups are shown in Figure 4.3.

Figure 4.4 shows both the AATSR nadir and dual-view SSTs comparisons with M-AERI data for these data points. From these data, we observe that the correlation is high (> 0.9) and the slope is very close to unity for the D2, N3 and D3 retrievals. The performance of the N2 SSTs is comparatively poor, with a correlation of only 0.41 and a slope of 0.86. Figure 4.5 shows the distribution of AATSR minus M-AERI SST differences for both daytime and nighttime, two- and three-channel matchups. These data show the distribution of nighttime data is approximately Gaussian, with bias and standard deviation of 0.10 K and 0.27 K, respectively, for N3 SSTs, and 0.06 K and 0.28 K for D3 SSTs (see Table 4.1). These results are extremely encouraging and suggest that the three-channel

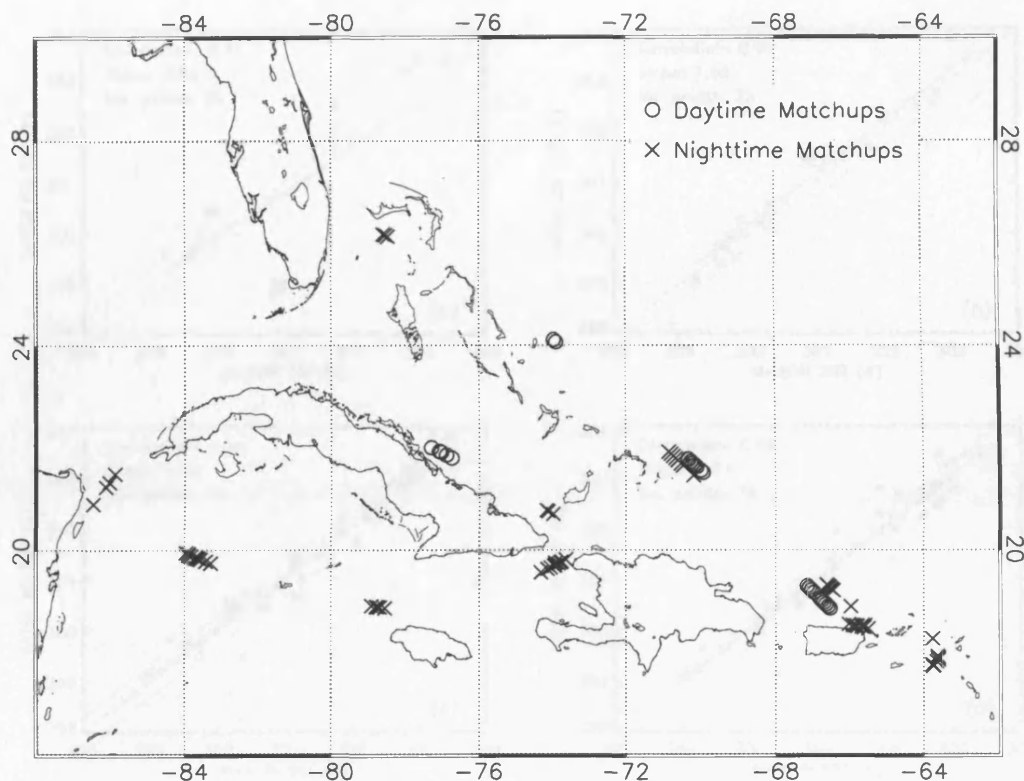


FIGURE 4.3. Geographical location of two-channel (open circles) and three-channel (crosses) M-AERI/AATSR matchups for the 1×1 pixel block size.

nighttime AATSR SST retrievals are of very high quality over the Caribbean region, although the apparent bias in the N3 retrievals is of some concern.

The distribution of the two-channel daytime SSTs is much more difficult to interpret as the distributions are not obviously Gaussian, which may, of course, be an artefact of the limited number of data points. This is particularly apparent in the case of the N2 SSTs, which has a strong peak at approximately -2 K in addition to the main distribution that occurs between -0.5 K and 1.5 K. Interestingly, this negatively-biased distribution is due to seven matchups that occur from the same two-hour temporal window on 30 June 2003 (Orbit 06956). These matchups, together with one matchup occurring on 12 October 2003, are also responsible for the secondary peak that occurs at approximately $+0.6$ K in the D2 distribution. For the D2 SSTs, the bias and standard deviation of the distribution are calculated to be 0.16 K and 0.38 K, respectively, which suggests that considering all 25 daytime matchups, the AATSR D2 SST retrieval is performing below specification over this geographical region. In this instance, an overall bias and standard

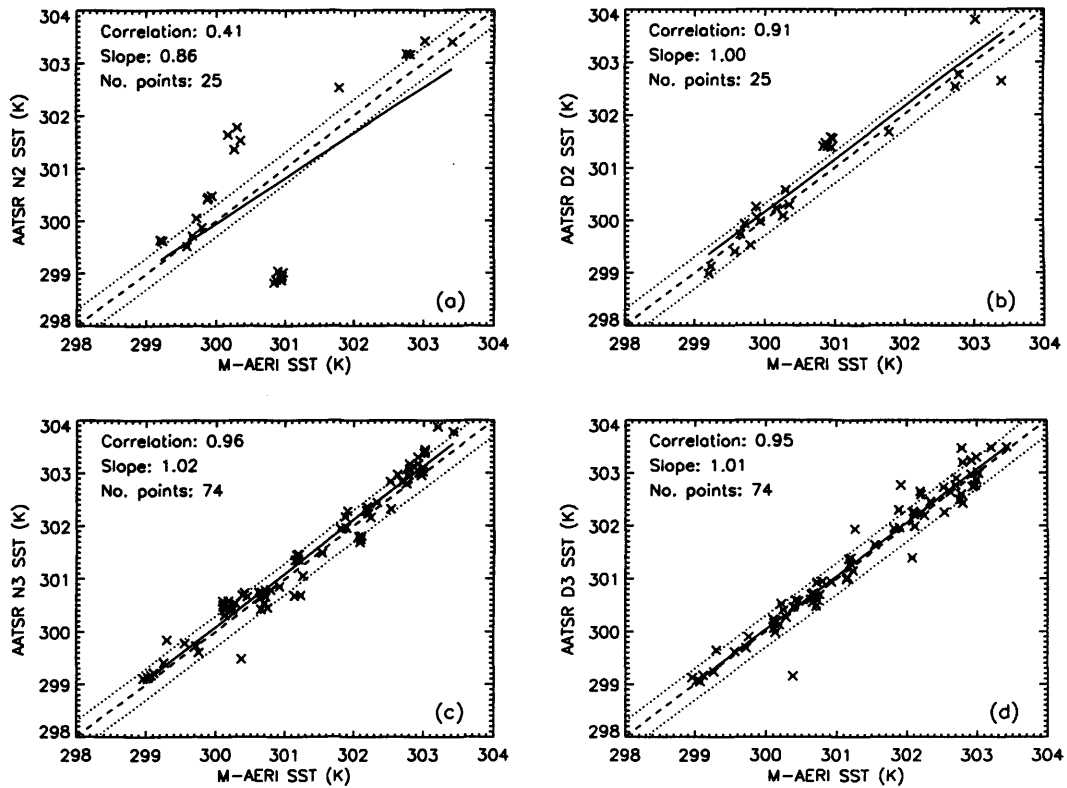


FIGURE 4.4. Comparisons between AATSR SSTs (y-axis) and in situ SSTs from the M-AERI (x-axis) for (a) nadir two-channel, (b) dual two-channel, (c) nadir three-channel and (d) dual three-channel matchups occurring within ± 60 minutes from the time of the AATSR overpass for the 1×1 pixel block size. Linear regression lines (solid), lines of equality (dashed) and the AATSR ± 0.3 K target accuracy lines (dotted) are also shown.

deviation calculation for the N2 retrievals is probably inappropriate due to the apparent multi-modal distribution of data. Considering the two principal distributions separately, a bias and standard deviation of 0.56 K and 0.47 K, respectively, are obtained for the main distribution (18 data points) and -1.98 K and 0.07 K for the second distribution (7 data points). The overall mean of these data is calculated to be -0.15 K.

The outlying data points may be due to residual cloud contamination, which should always be considered as a possible source of error when using satellite data to obtain measurements of SST. Although the presence of cloud in the instrument FOV may depress the observed TOA BTs, the resulting AATSR SST may be positively or negatively biased due to the weighting of the retrieval coefficients and the varying effect of various cloud types on the radiances at different wavelengths (Merchant & Harris 1999). How-

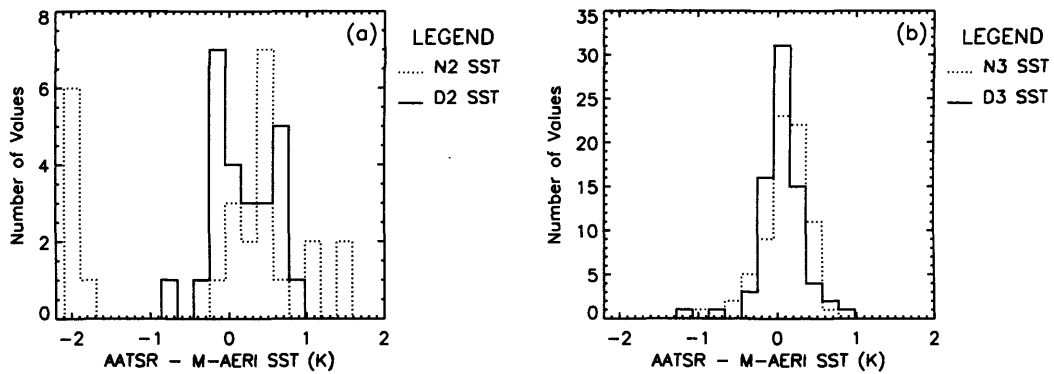


FIGURE 4.5. Distribution of AATSR - M-AERI SST difference for (a) two-channel (daytime) and (b) three-channel (nighttime) matchups occurring within ± 60 minutes from the time of the AATSR overpass for the 1×1 pixel block size. Both nadir- (dotted) and dual-view (dashed) SSTs are shown.

ever, as the data have been screened for cloud by eye, in addition to the operational cloud detection algorithms, it is more likely that the observed outliers are a result of another source of error. An alternative source will be explored in Section 4.4.

The results for the 3×3 block (Table 4.2) closely mirror those for the 1×1 block. When considering all matchups, no major differences in the statistics are found, except for the increase in the number of matchups. This suggests that no additional errors are introduced into the validation dataset as a result of any spatial variation of SST, the movement of the ship and any errors in the AATSR geolocation.

Analysis of the results for both the 1×1 and 3×3 blocks show that the accuracy of the AATSR SSTs with respect to the in situ SSTs exhibits no correlation with (i) SST, (ii) heterogeneity of the surrounding SST (assessed by calculating the standard deviation of the corresponding 3×3 pixel block), (iii) latitude of matchup (iv) longitude of matchup (v) temporal offset from the time of the AATSR overpass and (vi) the swath position of the AATSR pixel. However, these results are limited by the number of data points available and the small magnitude of these effects (e.g. the range of SSTs is only a few K). The lack of correlation with the latter two points is consistent with the findings of Donlon & Robinson (1998), although it should be noted that they were validating the ATSR-1 spatially averaged product (generated by applying SST retrieval coefficients to cloud-free TOA BTs averaged over 10 arcminute cells).

Overall, the N2 SSTs compare least well with the in situ measurements. By using the additional data from the forward view during the day (D2 SSTs), when the $3.7 \mu\text{m}$

Table 4.1. Summary of AATSR/M-AERI matchup statistics for the 1×1 pixel block. Statistics are shown separately for two-channel (day) and three-channel (night) SST retrievals, considering all matchups, and cases where the AATSR dual- minus nadir-view SST (D-N) is ‘normal’ and abnormally high (see Section 4.4.1 for explanation). In the case of ‘all matchups’ for the N2 retrievals, the bias and standard deviation are presented separately for the two distributions (labelled ‘1’ and ‘2’); the mean for the full data set is also given (denoted by *). Bias is defined as AATSR - M-AERI, such that a positive value indicates that AATSR is measuring warm.

For each scenario, the proportion of matchups falling within the ± 0.3 K target accuracy is also shown.

Matchups	No. Matchups	Nadir			Dual		
		Bias (K)	StDev (K)	% within ± 0.3 K.	Bias (K)	StDev (K)	% within ± 0.3 K.
all matchups 2ch	25	-0.15*	-	16.0	0.16	0.38	60.0
all matchups 2ch (1)	18	0.56	0.47	22.2	-	-	-
all matchups 2ch (2)	7	-1.98	0.07	0.0	-	-	-
all matchups 3ch	74	0.10	0.27	68.9	0.06	0.28	81.1
‘normal’ D-N 2ch	17	0.57	0.48	23.5	-0.05	0.26	88.2
‘normal’ D-N 3ch	65	0.14	0.24	72.3	0.02	0.25	84.6
high D-N 2ch	8	-1.68	0.85	0.0	0.60	0.10	0.0
high D-N 3ch	9	-0.16	0.31	44.4	0.32	0.36	55.6

Table 4.2. Summary of AATSR/M-AERI matchup statistics for the 3×3 pixel block. Statistics are shown separately for two-channel (day) and three-channel (night) SST retrievals, considering all matchups, and cases where the AATSR dual- minus nadir-view SST (D-N) is ‘normal’ and abnormally high (see Section 4.4.1 for explanation). In the case of ‘all matchups’ for the N2 retrievals, the bias and standard deviation are presented separately for the two distributions (labelled ‘1’ and ‘2’); the mean for the full data set is also given (denoted by *). Bias is defined as AATSR - M-AERI, such that a positive value indicates that AATSR is measuring warm.

For each scenario, the proportion of matchups falling within the ± 0.3 K target accuracy is also shown.

Matchups	No. Matchups	Nadir			No. Matchups	Dual		
		Bias (K)	StDev (K)	% within ± 0.3 K.		Bias (K)	StDev (K)	% within ± 0.3 K.
all matchups 2ch	32	-0.17*	-	15.6	0.16	0.36	62.5	
all matchups 2ch (1)	23	0.53	0.43	21.7	-	-	-	
all matchups 2ch (2)	9	-1.96	0.07	0.0	-	-	-	
all matchups 3ch	84	0.07	0.27	66.7	0.04	0.26	81.0	
‘normal’ D-N 2ch	22	0.54	0.44	22.7	-0.04	0.21	90.9	
‘normal’ D-N 3ch	71	0.13	0.22	70.4	0.01	0.23	87.3	
high D-N 2ch	10	-1.73	0.75	0.0	0.62	0.10	0.0	
high D-N 3ch	13	-0.23	0.32	46.2	0.24	0.34	46.2	

channel is not available, the quality of the SSTs, in terms of both bias and standard deviation, is significantly improved. This highlights clearly the advantages of using a sensor with dual-viewing capabilities to obtain a better atmospheric correction when retrieving SSTs. The results presented suggest that the most accurate SSTs are obtained when the $3.7\ \mu\text{m}$ channel data are used, with similar results achieved using both the nadir- and dual-view data, although the former exhibits a significant warm bias. However, it should be noted that these results are specific to the Caribbean and may not be representative of the global performance of the AATSR SST retrieval algorithms.

4.4 Dual-Nadir SST Difference

Figure 4.6 shows the AATSR/M-AERI SST difference plotted as a function of date, where the points are coloured according to the corresponding D-N (dual minus nadir SST difference - see Chapter 3).

From this figure, it can be seen that AATSR SSTs showing comparatively poor agreement with co-located M-AERI SSTs (e.g. $> 0.3\ \text{K}$) occur throughout the year, and are not confined to one particular season. Excluding cloud contamination (Section 4.3), a possible explanation for non-zero bias errors stems from the regional nature of this study. Through the choice of the distribution of atmospheric profiles used in the radiative transfer simulations, the coefficients for the AATSR atmospheric correction algorithm are optimised for the global range of atmospheric variability, and applications of the algorithm to correct a limited subset of atmospheric conditions could potentially lead to bias errors of several tenths of a degree in a particular location (Minnett 1990).

A likely explanation, however, concerns the effect of mineral dust aerosols, which may also affect satellite SST retrievals (e.g. Vazquez-Cuervo et al. 2004). The effects of aerosols on (A)ATSR data have been explored within Section 3.7.2.2 of this thesis, where it was shown that the nadir-view SSTs are depressed and the dual-view SSTs, if anything, increase under these conditions. This relative behaviour of the SST retrievals results in an increase in the D-N.

As noted in Section 3.7.2.2, this effect has been observed in real (A)ATSR data, where the D-N has been used to track the transport of Saharan dust across the Atlantic (Dundas 1991). This well-documented natural phenomenon occurs throughout the year, transporting mineral aerosol particles from North West Africa as far as the Eastern United States and the Caribbean (e.g. Carlson & Prospero 1972). The concentration of Saharan dust generally peaks in the Northern Hemisphere summer months, but can vary on

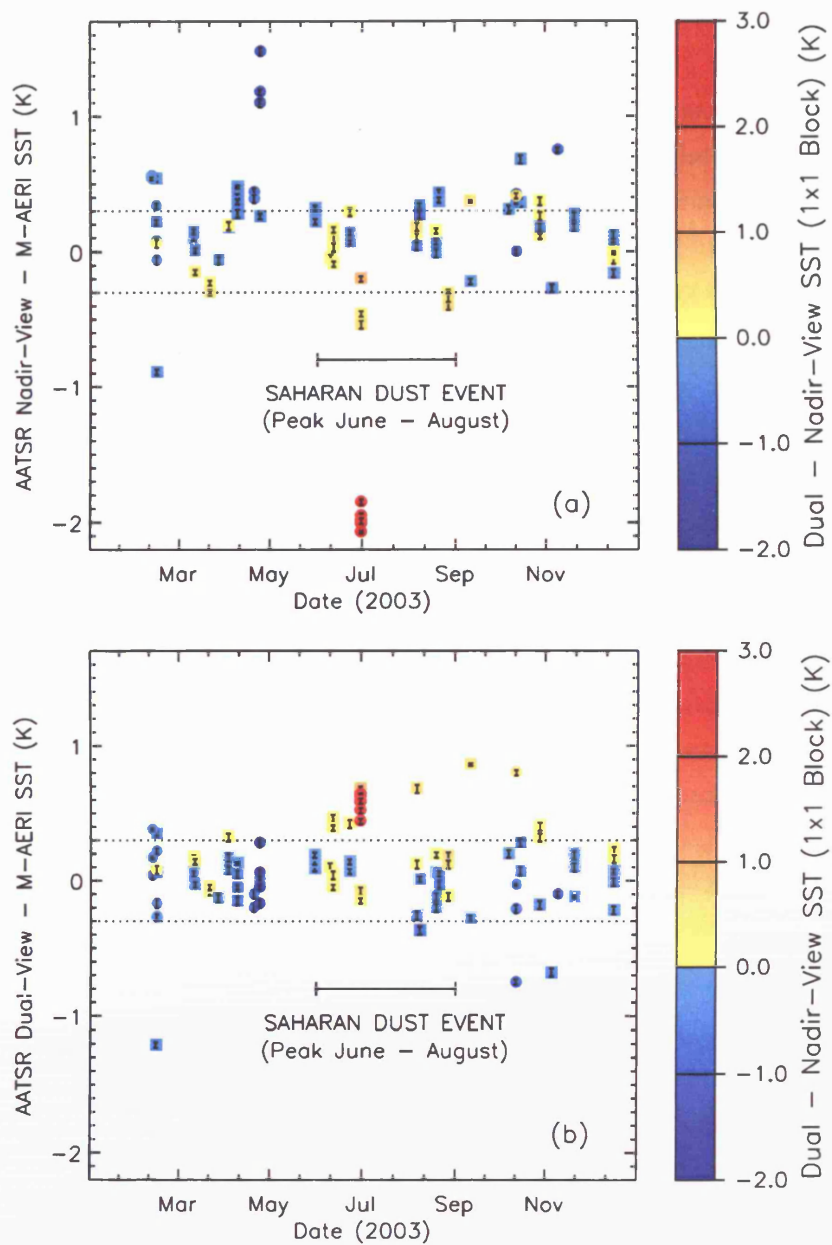


FIGURE 4.6. AATSR SST minus in situ SSTs from the M-AERI (y-axis) plotted against the date (in 2003) of the M-AERI SST measurement (x-axis) for (a) nadir-view matchups and (b) dual-view matchups occurring within ± 60 minutes from the time of the AATSR overpass for the 1×1 pixel block size. Two-channel (daytime) matchups are indicated by filled circles and three-channel (nighttime) matchups by filled squares. The AATSR ± 0.3 K target accuracy lines (dotted) are also shown.

the scale of days, as events are typically sporadic and plume transport has a strong meteorological dependence (e.g. Arimoto et al. 1995). Saharan dust aerosol particles are relative large (e.g. several μm) and transported in the troposphere, typically at heights of 1.5 - 4.5 km (Prospero & Carlson 1972, Dunion & Veldon 2003). The transport of the dust can also be associated with unusually high atmospheric temperature and low relative humidity, which have been traced as far as the Caribbean (Carlson & Prospero 1972). Therefore, the effects on (A)ATSR SSTs may be two-fold: the direct effect of the dust on infrared measurements, due to strong absorption features in the 11 and 12 μm channels (e.g. Dundas 1991) and the additional effects of the accompanying extreme atmospheric conditions.

To investigate the effects of the aerosol phenomenon on AATSR data over the Caribbean, variations of D-N with aerosol optical depth (AOD) derived from MODIS observations at 550 nm (see Kaufman & Tanré (1998) for further details) have been examined. A global analysis of this relationship is currently being conducted at the University of Leicester (S. A. Good, personal communication). The data shown in Figure 4.7 is for the month of July 2003, which is at the peak of Saharan dust transport. From this plot, we see that these two data sets are well correlated for both day (two-channel D-N) and night (three-channel D-N) AATSR data, where the gradients reflect the differing sensitivities of the AATSR SST algorithms to aerosol. The apparent lower sensitivity of the three-channel (nighttime) D-N is due to the fact that the retrieval is dominated by the 3.7 μm channel, which is less affected by desert aerosol than the 11 and 12 μm channels (Dundas 1991). Some degree of scatter is observed, which may, at least in part, be a result of different types of aerosol and varying height distribution having different effects on the satellite SSTs.

The monthly averages of D-N and MODIS AOD over the Caribbean, shown in Figure 4.8, also suggest a relationship between these two parameters. The primary feature in all three data sets is the maximum that occurs in July 2003, which corresponds to the peak of the Saharan dust transport. Other features can be attributed to the effects resulting from differences between the times of observation (the AATSR three-channel data are obtained at night, whilst the AATSR two-channel and MODIS data are obtained during the day), the limited coverage of the AATSR swath, and variability of atmospheric water vapour and temperature.

From Figure 4.6, we see that a number of positively-biased outliers are characterised by a high positive D-N, with the largest number of these data occurring through June - August 2003, consistent with the peak of the observations of the Saharan dust event as noted previously. The comparatively poor agreement between the AATSR and M-AERI

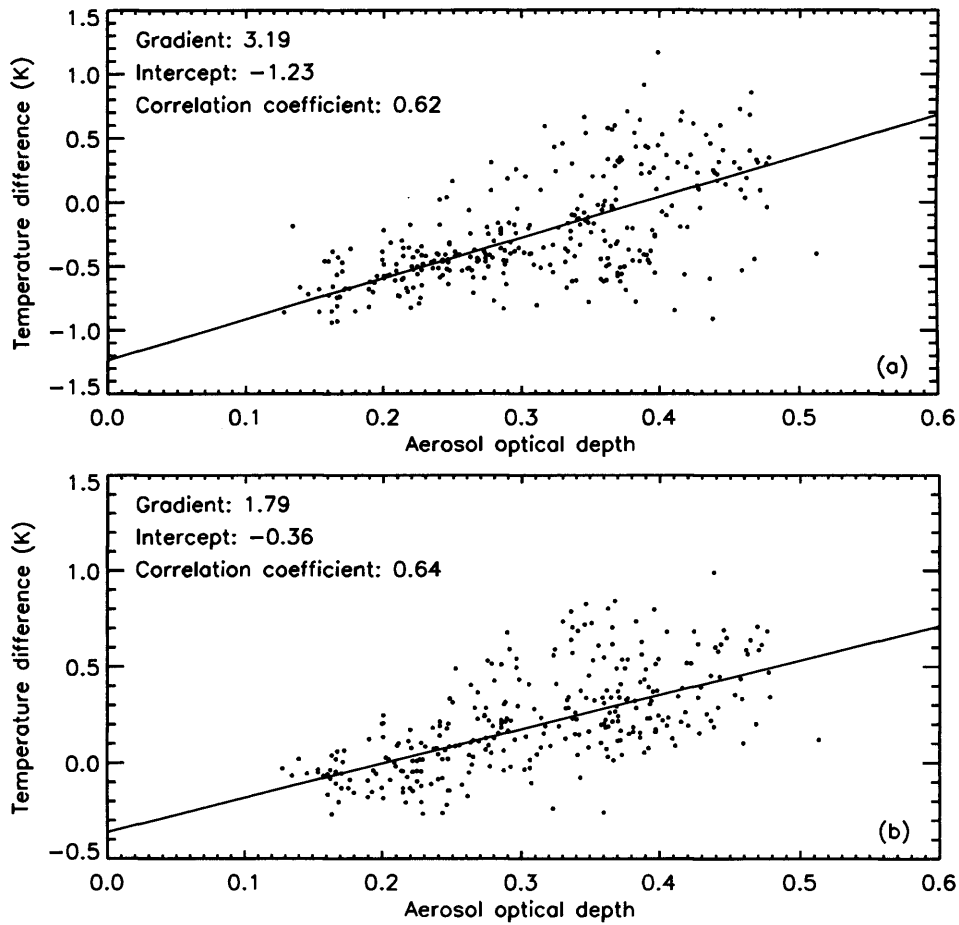


FIGURE 4.7. Correlation between AATSR dual- minus nadir-view SST difference (D-N) and daytime MODIS aerosol optical depth at 550 nm (both data sets averaged over the month of July) for (a) two-channel (daytime) and (b) three-channel (night-time) AATSR data. Both the MODIS and AATSR data have been averaged onto a 1 degree resolution grid between 16 - 28° N, and 60 - 88° W. Plots produced by S. A. Good, University of Leicester.

SSTs for these matchups suggests that the AATSR may not be correcting accurately for the atmosphere under these conditions. The variable nature of Saharan dust concentrations, even during the peak months, may explain the variability in the M-AERI AATSR SST comparisons and the occurrence of some matchups with low D-N at that time.

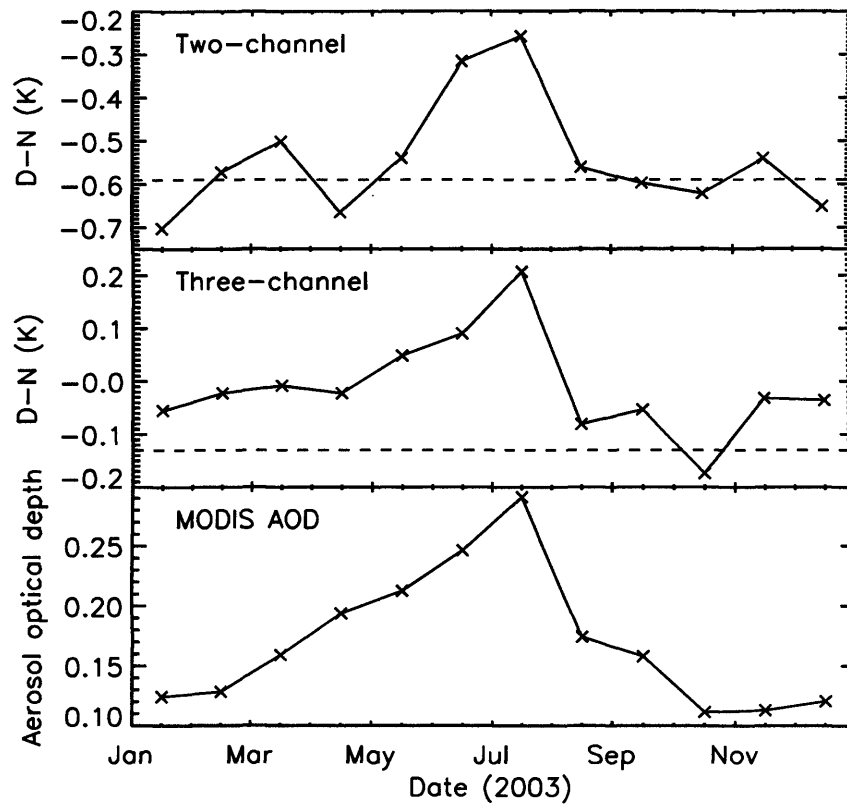


FIGURE 4.8. Variation of two- and three- channel D-N and MODIS AOD at 550 nm for the Caribbean region, between 16 - 28° N, and 60 - 88° W, during 2003. Data shown are the mean for each month. The dashed lines indicate the modal D-N for aerosol-free conditions (see Section 4.4.1). Plot produced by S. A. Good, University of Leicester.

4.4.1 Effect of Filtering Matchups based on Dual-Nadir SST Difference

In order to separate the effects of aerosol, separate threshold D-N values for both two- and three-channel SSTs for ‘normal’ conditions have been determined by considering the distribution of D-N for months relatively unaffected by Saharan dust aerosol. The AATSR 1 km SST data over the Caribbean region from January to April, and November and December 2003 have been plotted as a histogram showing the distribution of D-N in Figure 4.9. Unlike the two-channel histogram, the three-channel D-N distribution is asymmetrical with a positive ‘tail’, a feature that is not seen in the two-channel (daytime data). Interestingly, this ‘tail’ also does not appear in the equivalent plots for the AATSR spatially averaged data (not shown), suggesting that it is not related to the 3.7 μm chan-

nel. The most likely cause of these anomalous data points is undetected cloud, as the effects of individual cloudy pixels are likely to be less significant in the spatially averaged data as a result of the averaging process (Good et al. 2006). For the two-channel (daytime) retrieval, data from a designated cloud-screening channel at $1.6 \mu\text{m}$ are employed that are not available at night, possibly explaining the absence of this ‘tail’ in these data.

The differences in mode and standard deviation are principally due to the differential dependence of the four AATSR SST retrievals on atmospheric water vapour and temperature. Considering limits of three standard deviations (99.7% of the data) around the mode of the Gaussian curve fitted to the data, upper D-N thresholds of $+0.25 \text{ K}$ and $+0.26$ for two- and three-channel SSTs, respectively, are obtained (S. A. Good, 2005, personal communication). For matchups with D-Ns above the given thresholds, it is considered likely that these data are affected by Saharan dust aerosol. The mode of the Gaussian curves, -0.59 K and -0.13 K for two- and three-channel D-N, respectively, agree well with the expected D-N of -0.75 K and -0.14 K for an aerosol-free tropical atmosphere, simulated in Chapter 3.

To exclude the possibility that matchups with high, positive D-N are caused by the atmospheric state (excluding the effects of aerosols), NWP data and a radiative transfer model have been used to simulate the AATSR TOA BTs. The modelled BTs are then converted into SST using the operational, gridded retrieval coefficients (Chapter 2). As no aerosol is included in the model, these simulated D-Ns should reflect the range expected for an aerosol-free atmosphere.

The model used in this study was the Oxford RFM, which was described in Chapter 3 of this thesis. For the input surface parameters, SSTs from the M-AERI have been used, with the sea surface emissivities corresponding to the AATSR thermal channels given in Table 3.3. For the atmospheric data, profiles from 1.125° gridded European Centre for Medium-Range Weather Forecasts (ECMWF 1995) have been employed, using a weighted average (by distance) of the four profiles geographically and temporally closest to the location of each M-AERI SST. Concentrations for atmospheric species other than water vapour, which are provided by ECMWF, were obtained from the tropical atmospheric profile given by Remedios (1999) (see Chapter 3).

AATSR TOA BTs have been simulated for all 183 cloud-free coincident AATSR and M-AERI measurements. The M-AERI SSTs with standard deviation above 0.10 K have been included in the simulations, as the exercise is theoretical and the accuracy of the in situ SSTs is not critical. The two-channel SSTs have also been derived for the nighttime overpasses in order to increase the number of D-N data points for these retrievals. An

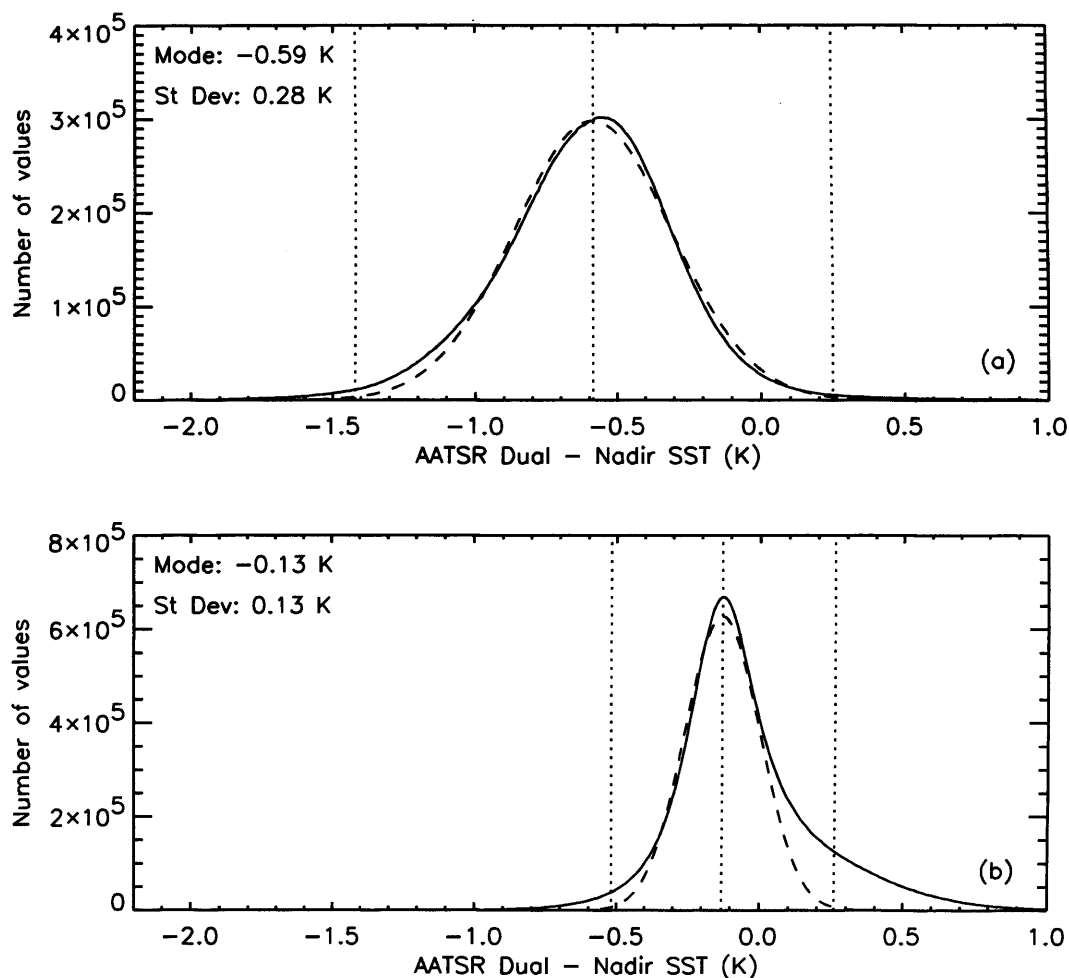


FIGURE 4.9. Distribution of dual minus nadir SST difference (D-N) for the Caribbean Region (16 to 28 degrees latitude and -88 to -60 degrees longitude) for (a) two-channel 1-km SSTs and (b) three-channel 1-km SSTs for the months January - April and November - December 2003. The plot also shows a Gaussian fit (dashed line) and corresponding mode and standard deviation. The dotted lines indicate the mode and limits of three standard deviations from the mode. Plot produced by S. A. Good, University of Leicester.

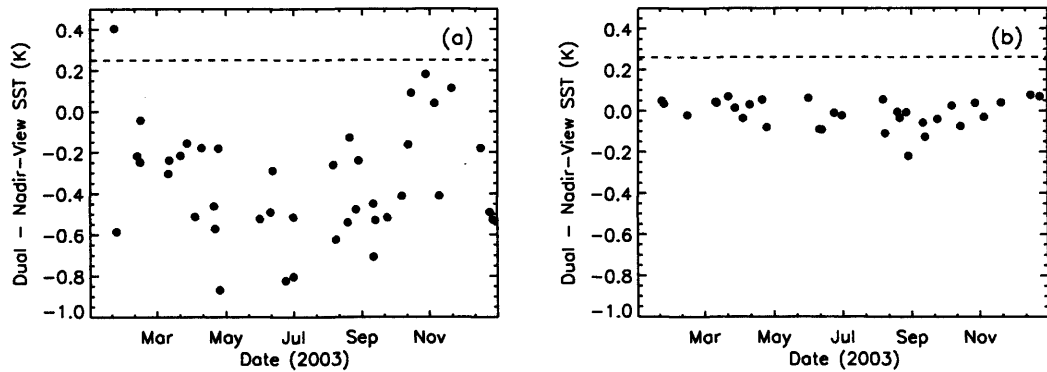


FIGURE 4.10. Simulated D-N for (a) two-channel and (b) three-channel data, using ECMWF atmospheric data together with (model input) SST data obtained from the M-AERI. The dashed line indicates the upper D-N (aerosol) threshold.

average value of the D-N for all matchups within an orbit has been used, as there is almost no variation in the D-N for matchups originating from the same orbit due to the coarse spatial resolution of the ECMWF atmospheric data.

Figure 4.10 shows the variation of simulated D-N as a function of date. From the results, a bias and standard deviation of -0.34 K and 0.28 K, respectively, are calculated for the two-channel D-N, and -0.01 K and 0.06 K for the three-channel D-N. These numbers are comparable to the mode and standard deviation obtained for the D-N data plotted in Figure 4.9, with the differences arising from the fact that we are only considering a small subset of the data in this instance. In contrast to the D-Ns shown in Figure 4.8, no seasonal cycle is evident in the data. With the exception of one matchup in the two-channel D-N results (Figure 4.10), all the simulated D-Ns fall below the aerosol thresholds (indicated by the dashed lines in the plots). This suggests that the cause of the high D-Ns in our validation data set is unlikely to be due to atmospheric water vapour and/or temperature.

Figure 4.11 shows the histograms of the AATSR minus M-AERI SST differences for (a) N2, (b) D2, (c) N3 and (b) D3 matchups, for all data, and as classified by the magnitude of the D-N. The secondary peaks centred about -2 K and $+0.6$ K in the N2 and D2 distributions, respectively, correspond to matchups with D-Ns > 0.25 K. For the three-channel matchups, no obvious separation is observed, although the small positive tail in the D3 distribution and some of the more negatively-biased matchups in the N3 distribution can be explained by matchups with D-Ns > 0.26 K.

The statistics for the ‘filtered’ 1×1 matchup distributions are given in Table 4.1. In

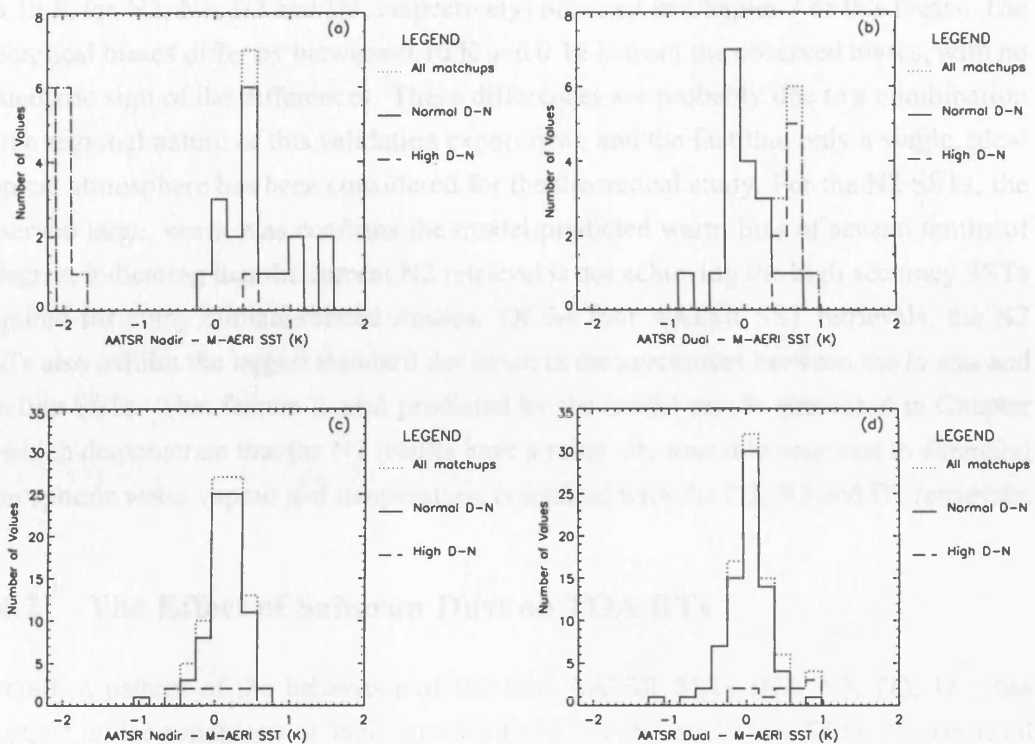


FIGURE 4.11. Distribution of differences between AATSR dual-view minus M-AERI SSTs (x-axis) for the 1×1 block for (a) nadir two-channel, (b) dual two-channel, (c) nadir three-channel and (d) dual three-channel matchups. The dotted lines indicate the distribution of all matchups; the solid line for matchups where the dual-nadir SST difference (D-N) is 'normal' (little or no Saharan dust aerosol loading) and the dashed line for matchups where the D-N suggests the presence of Saharan dust aerosol.

the case of the D2 matchups, the bias and standard deviation of the distributions with $D-N < 0.25$ are -0.05 K and 0.26 K. For the high D-N distribution, these figures are 0.60 K and 0.10 K. For the N2 matchups the bias and standard deviation are $+0.57$ K and 0.48 K for $D-N < 0.25$, and -1.68 K and 0.85 K for matchups with D-N greater than this threshold.

For the D3 SSTs, the bias and standard deviation are $+0.02$ K and 0.25 K, respectively, for $D-N < 0.26$, and $+0.32$ K and 0.36 K for the high D-N distribution. For N3, the bias and standard deviation are $+0.14$ K and 0.24 K for $D-N < 0.26$, and -0.16 K and 0.31 K for high D-N.

The non-aerosol, clear-sky SST biases obtained in this experiment are comparable

with the theoretical biases for the tropical atmosphere (+0.70 K, −0.02 K, +0.05 K and −0.12 K for N2, N3, D2 and D3, respectively) obtained in Chapter 3 of this thesis. The theoretical biases differ by between 0.10 K and 0.16 K from the observed biases, with no systematic sign of the differences. These differences are probably due to a combination of the regional nature of this validation experiment, and the fact that only a single, ideal tropical atmosphere has been considered for the theoretical study. For the N2 SSTs, the observed large, warm bias confirms the model-predicted warm bias of several tenths of a degree, indicating that the current N2 retrieval is not achieving the high accuracy SSTs required for many climate-related studies. Of the four AATSR SST retrievals, the N2 SSTs also exhibit the largest standard deviation in the agreement between the *in situ* and satellite SSTs. This feature is also predicted by the model results presented in Chapter 3, which demonstrate that the N2 results have a relatively unstable response to changing atmospheric water vapour and temperature, compared with the D2, N3 and D3 retrievals.

4.4.2 The Effect of Saharan Dust on TOA BTs

Overall, a pattern of the behaviour of the four AATSR SSTs (N2, N3, D2, D3) has emerged under conditions of high positive D-N. For the dual-view SSTs, the retrieval algorithms appear to be overcompensating for the effects of the atmosphere and the resulting SST is too warm. For the nadir-view SSTs, the effect is the opposite, resulting in an overall increase in the D-N. These observations are consistent with the model predictions discussed in Chapter 3.

Through radiative transfer modelling, it is also possible to obtain an estimate of the effects on the TOA BTs corresponding to the AATSR SSTs used in this study. To do this, the AATSR TOA BTs simulated in Section 4.4.1 have been compared to the corresponding observed AATSR TOA BTs for each valid SST matchup. The comparisons have then been classified into those matchups where the retrieved D-N is below the thresholds calculated in Section 4.4.1, and those matchups where the D-N is high. As the modelled BTs assume an aerosol-free atmosphere, the relative agreement between the modelled and observed BTs, for the situations with low and high D-N, should provide us with an estimate of the effect of any aerosol on the BTs corresponding to matchups with high D-N.

In this case, matchups where the standard deviation of the M-AERI SST is above 0.10 K have been excluded (unlike in Section 4.4.1), as this experiment involves comparing the modelled data with real data, thus the accuracy of the M-AERI SSTs is important. Figures 4.12 and 4.13 show the results for the daytime and nighttime BT data, respec-

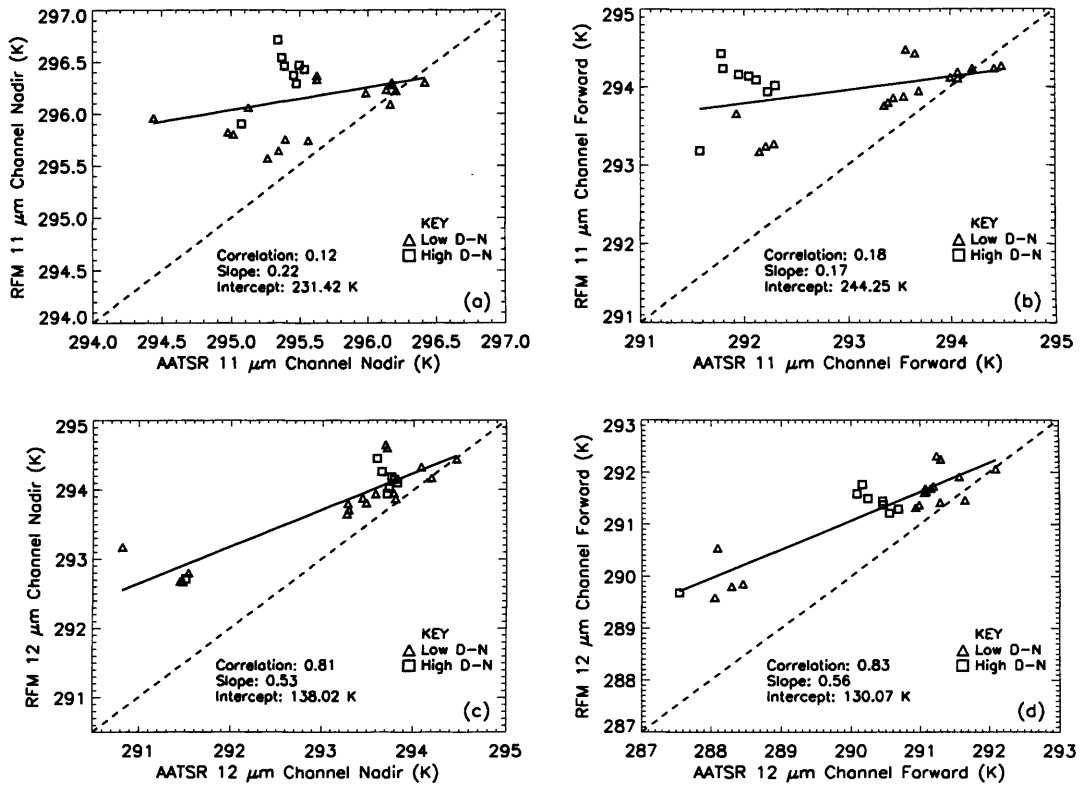


FIGURE 4.12. Simulated TOA BTs using ECMWF atmospheres plotted against observed AATSR BTs corresponding to daytime matchups for: (a) nadir 11 μm , (b) forward 11 μm , (c) nadir 12 μm and (d) forward 12 μm . Lines of equality (dashed) and regression lines (solid) are also shown. TOA BTs corresponding to SSTs where the D-N is 'normal' and abnormally high, are represented by open triangles and squares, respectively.

tively. Table 4.3 gives the calculated biases and standard deviations of the differences between the simulated and observed BTs.

Considering all the data, the best agreement between any of the comparisons is obtained for the nadir 3.7 μm channel, with a bias and standard deviation of -0.07 K and 0.24 K, respectively. Results for the forward 3.7 μm BTs also show good agreement (bias and standard deviation of -0.02 and 0.34 K). The results for the 11 and 12 μm channels are comparatively poor, where the mean difference between the modelled and observed BTs ranges between 0.2 K and 0.98 K and the standard deviations, between 0.47 K and 0.94 K. Overall, the results for the forward-view simulations are significantly worse than those for the nadir view. The daytime simulations also appear to show relatively poor agreement with the observed AATSR BTs with respect to the nighttime comparisons.

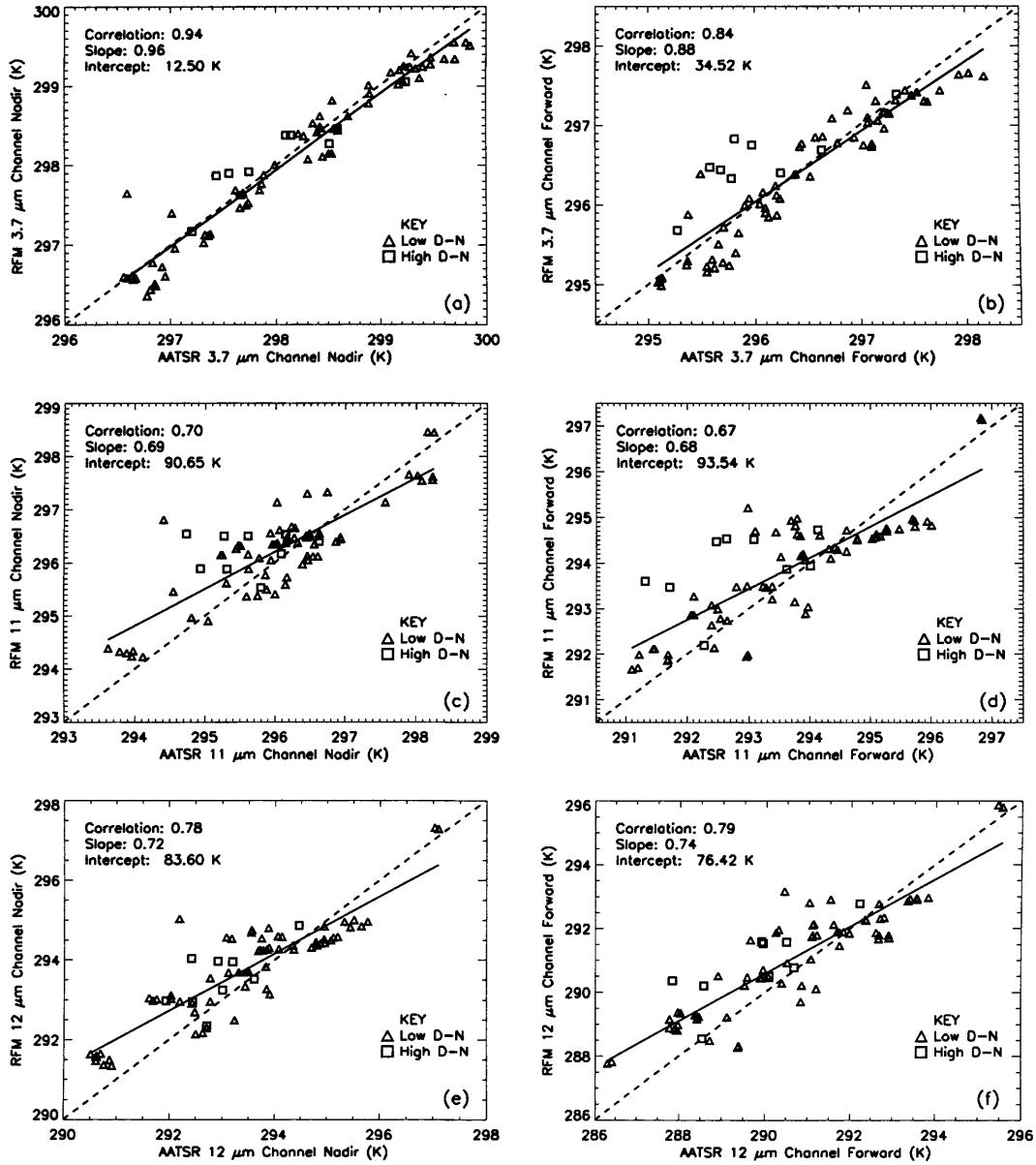


FIGURE 4.13. Simulated TOA BTs using ECMWF atmospheres plotted against observed AATSR BTs corresponding to nighttime matchups for: (a) nadir 3.7 μm , (b) forward 3.7 μm , (c) nadir 11 μm , (d) forward 11 μm , (e) nadir 12 μm and (f) forward 12 μm . Lines of equality (dashed) and regression lines (solid) are also shown. TOA BTs corresponding to SSTs where the D-N is 'normal' and abnormally high, are represented by open triangles and squares, respectively.

Table 4.3. Statistics of the comparison between the simulated and observed AATSR TOA BTs. The bias (simulated-observed) and standard deviation (StDev) are shown for all data points, data points with D-N below the ‘normal’ threshold and data points with D-N above the ‘normal’ threshold. Δ Bias refers to the additional BT deficit apparent in the observed BTs due to aerosol contamination that is not simulated by the model - this is effectively the mean effect of Saharan dust on the AATSR TOA BTs over the Caribbean.

Day/Ngt	Channel (μm)	Nad / Fwd	All Data Points		Low D-N		High D-N		Δ Bias
			Bias (K)	StDev (K)	Bias (K)	StDev (K)	Bias (K)	StDev (K)	(K)
day	11	nad	0.60	0.47	0.41	0.44	1.00	0.19	−0.59
day	12	nad	0.60	0.54	0.63	0.61	0.53	0.34	0.10
day	11	fwd	0.98	0.88	0.48	0.52	2.05	0.37	−1.57
day	12	fwd	0.90	0.65	0.75	0.67	1.21	0.52	−0.46
ngt	37	nad	−0.07	0.24	−0.09	0.23	0.10	0.26	−0.18
ngt	11	nad	0.20	0.58	0.14	0.55	0.59	0.69	−0.45
ngt	12	nad	0.33	0.72	0.30	0.73	0.57	0.61	−0.27
ngt	37	fwd	−0.02	0.34	−0.09	0.26	0.51	0.37	−0.60
ngt	11	fwd	0.24	0.81	0.12	0.72	1.11	0.94	−1.00
ngt	12	fwd	0.45	0.93	0.36	0.92	1.06	0.85	−0.70

However, this is an artefact of the limited number of data points (and the scales used in the plots), a high proportion of which are aerosol-affected.

The disagreement between the simulated and modelled BTs is almost entirely due to inaccuracies within the atmospheric profiles used in the simulations. The uncertainties in the M-AERI SSTs data are very small ($\ll 0.1$ K, although this is the accuracy of the point measurement, so over 1 km^2 , the spatial variation of SST may increase this error); simulations for a tropical atmosphere carried out in Chapter 3 suggest that for this level of uncertainty, the corresponding error in the simulated BTs will be much less than 0.1 K and will be most apparent in the results for the $3.7 \mu\text{m}$ channel. Similarly, uncertainties in the sea surface emissivity will result in errors in the simulated BTs of this magnitude, at worst, because of the high levels of atmospheric water vapour attenuating changes in the signal originating from the surface. Errors in the atmospheric profiles, namely atmospheric water vapour, temperature and aerosol, will manifest themselves predominantly in the 11 and $12 \mu\text{m}$ channel BTs, and more so in the forward view. As

the overall disagreement between the simulated and observed BTs is worse for the 12 μm channel, and generally in the forward view compared to the nadir view, we can conclude that the water vapour and temperature profiles are probably not a completely accurate representation of the state of the atmosphere at the time of the AATSR overpasses. The overall high bias in the simulated BTs, compared with the observed BTs in the 11 and 12 μm channels, suggests that the transmission in the model atmospheres is too high. This could be caused by the water vapour profiles being too dry, for example.

Considering the BT comparisons corresponding to SST matchups where the D-N is high (i.e. where there is aerosol contamination), we find that the model BTs are generally warmer-biased with respect to the AATSR observations than the model BTs corresponding to situations with low D-N. Referencing these biases to those obtained for matchups with low D-N, we obtain the estimation of the effect on the TOA BTs due to aerosol. These figures are given in the last column of Table 4.3. Except for the daytime 12 μm results, the changes are negative (i.e. aerosols are depressing the observed BTs). The 11 μm channel appears to be the most affected by the Saharan dust aerosol, with the 3.7 μm channel being the least affected. This agrees with the results of Závody et al. (1994) and Dundas (1991), discussed in Chapter 3.

The relative magnitude of these depressions also supports the conclusion that the matchups with high D-N are indeed contaminated by aerosols. Of all the factors that have a significant effect on the AATSR thermal channels (surface temperature, emissivity, water vapour, atmospheric temperature and aerosol), the results presented in Chapter 3 have shown that only aerosol affects the 11 μm channel more than the 3.7 μm or 12 μm channels.

The BT deficits due to aerosol, shown in Table 4.3, can be translated into changes in SST by applying the operational coefficients, as was performed in Section 3.7.2.2 for the results of Dundas (1991). Table 4.4 shows the estimated changes in SST using these data. Not surprisingly, these data agree quite well with the observed SST biases of -1.68 K, -0.16 K, $+0.60$ K and $+0.32$ K, for the N2, N3, D2 and D3 retrievals, respectively. The differing results between the day and night two-channel retrievals are probably an artefact of the limited number of data available for the daytime overpasses. Nevertheless, these results show clearly that, for the relative channel/view BT depressions caused in the presence of aerosol, the nadir-view SSTs will decrease and the dual-view SSTs will increase.

Table 4.4. Change in retrieved SST due to aerosol using the simulation results given in the last column of Table 4.3

SST	Day (K)	Night (K)
N2	-2.28	-0.89
N3	-	-0.29
D2	+0.64	+0.29
D3	-	+0.39

4.5 Conclusions

Accurate in situ measurements of SST have been obtained from the M-AERI, deployed on the Explorer of the Seas cruise ship in the Caribbean Sea, and used to validate the AATSR 1 km gridded SST retrievals during the year 2003.

Daytime and nighttime comparisons were considered separately as the AATSR SST retrieval algorithm includes data from the 3.7 μm channel at night. The final validation dataset consisted of 25 daytime and 74 nighttime cloud-free matchups, with AATSR SSTs obtained from both nadir-only and dual-view measurements. Comparisons were made between the SST obtained from the M-AERI and the closest, single AATSR pixel to that geographical location within an hour of the Envisat overpasses; similar results are obtained using an SST averaged over a 3×3 pixel block centred on this pixel.

From these data, the biases (AATSR minus M-AERI SST) and standard deviations are calculated to be 0.06 K and 0.28 K for the three-channel (nighttime) dual-view SSTs (D3), 0.10 K and 0.27 K for the three-channel (nighttime) nadir-view SSTs (N3), and 0.16 K and 0.38 K for the two-channel (daytime), dual-view SSTs (D2). For the two-channel, nadir-view (N2) SSTs, calculation of an overall bias and standard deviation is inappropriate as the distribution is multi-modal. The mean of these data is -0.15 K.

The secondary distributions in the two-channel SSTs can be attributed to situations influenced by Saharan dust aerosol, which causes a warm bias in the dual-view SSTs and a cold bias in the nadir-view SSTs. The effect is observed to be less profound for the three-channel retrievals; this is due to the fact that the retrieval is dominated by the 3.7 μm channel, which is not as sensitive to desert aerosol as the 11 and 12 μm channels. In addition, the three-channel retrieval is less sensitive to the radiative effects of the anomalously dry Saharan air layer that often accompanies the dust outflows across

the Atlantic. As discussed both here, and in Chapter 3, this warming/cooling of the retrieved SSTs causes the difference between the dual- and nadir-view SSTs (D-N) to increase. Upper threshold D-N values for ‘normal’ conditions have been derived from AATSR observations of SST over the Caribbean. These values are +0.25 K and +0.26 K for two- (daytime) and three-channel (nighttime) SSTs, respectively.

By classifying the matchups using these D-N threshold values, this study has provided empirical evidence that the AATSR dual-view SSTs retrievals are providing an extremely high-quality SST when the D-N is below these thresholds over this geographical area. Under these conditions, the bias and standard deviation are 0.02 K and 0.25 K for D3, and -0.05 K and 0.26 K for D2. For matchups with D-N above the thresholds, the bias and standard deviation are observed to be 0.32 K and 0.36 K for D3, and 0.60 K and 0.10 K for D2.

For the N3 retrievals the bias and standard deviation for matchups with low D-N are calculated to be 0.14 K and 0.24 K, compared with -0.16 K and 0.31 K, for pixels with $D-N > 0.25$ K. Although it appears that the N3 SST retrievals are actually performing best in terms of bias for higher D-N, this may be an artefact of the conditions prevalent in the Caribbean region, with the presence of Saharan dust simply causing a change in bias of -0.30 from the ‘normal’ conditions. For the N2 matchups, figures of 0.57 K and 0.48 K for the bias and standard deviation for matchups with low D-N are obtained, and -1.68 K and 0.85 K for matchups with high D-N.

The effect of Saharan dust aerosol on the AATSR BTs has also been verified experimentally in this study, by comparing TOA BTs simulated using a radiative transfer model (without aerosol) with the observed data. The results agree well with the simulations carried out by other researchers at the wavelengths of the AATSR thermal channels, and demonstrate that the $11\text{ }\mu\text{m}$ channel is most affected by dust aerosol. The $3.7\text{ }\mu\text{m}$ channel is the least-affected AATSR channel.

The results of this study have provided experimental evidence of some of the conclusions presented in Chapter 3, such as the advantages of using a dual-viewing sensor like the AATSR, over the traditional linear-scan sensors to obtain accurate measurements of SST that can be used for climatological studies. The benefits of including the $3.7\text{ }\mu\text{m}$ channel in the retrievals is also apparent in these observational results, as the three-channel retrievals have been shown to provide a very stable SST under varying atmospheric conditions.

Chapter 5

The WATERMED Field Campaign

As for SST validation, the results of the sensitivity analysis presented in Chapter 3 can provide us with an extremely useful insight into the performance of the operational LST algorithm. However, as we saw in Chapter 4, only validation using equivalent in situ data will yield a true assessment of the accuracy of the retrievals under real atmospheric/surface conditions. An experiment to assess the accuracy of the AATSR LST product was carried out over a field site in Morocco in March 2003. LSTs retrieved from AATSR observations have been compared with in situ LST data, derived from at-surface BTs and emissivity data obtained over the site. This experiment was carried out in conjunction with a group of researchers from the University of Valencia, Spain. These data were collected as part of the WATERMED (WATER use Efficiency in natural vegetation and agricultural areas by Remote sensing in the MEDiterranean basin) project. This chapter will focus on the measurement techniques employed during the campaign, the derivation of LST from ground-based radiometric measurements coincident with satellite overpasses, and finally, the results of the comparison between these results and LSTs obtained from the AATSR LST product (Chapter 2).

5.1 The WATERMED Project

The WATERMED project is a multi-institutional venture funded by the European Union (INCO-med projects) and coordinated by Dr. Jose Sobrino, of the Global Change Unit, University of Valencia, Spain. The principal objective of the project is to analyse water use efficiency in the Mediterranean basin region by means of simulation models, for which the inputs are estimated using a combination of multi-spectral and multi-spatial

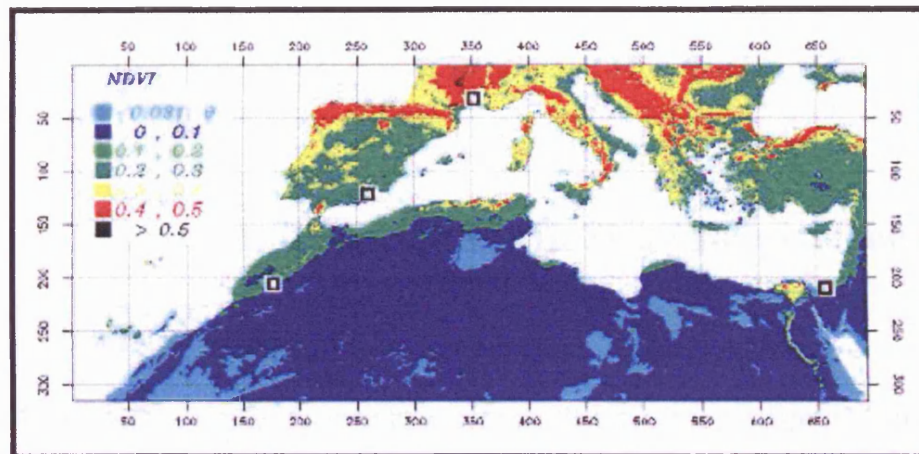


FIGURE 5.1. Normalised Differential Vegetation Index (NDVI) map, generated using a Pathfinder Advance Very high Resolution Radiometer (AVHRR) dataset, showing the four WATERMED field sites (black squares). Figure taken from Sobrino et al. (2001).

satellite data from a variety of sensors, in situ and historic data sets. Four field sites, (Figure 5.1) were selected as suitable locations to carry out preliminary studies (validation of algorithms, etc) at a local scale, before eventually up-scaling to a regional level; these sites are: the Guadalentin basin in SE Spain, the Tensift Al Haouz region of Morocco, the lower Rhone valley in SE France (Alpilles-RESeDA test site), and the northern region of the Sinai Peninsula in Egypt (Sobrino et al. 2001). As part of the project, an intensive series of field measurements was carried out at the beginning of 2003, at the WATERMED field site near Marrakech, Morocco (the most Eastern location WATERMED field site in Figure 5.1). Several different groups of researchers participated in the campaign, each focusing on a particular component of the fieldwork depending on their expertise. Areas of study included: evapotranspiration, Leaf Area Index (LAI), and LST, with measurements of the latter being carried out by a combined group from the Universities of Leicester and Valencia between 04 - 16 March 2003.

The principal objective of this element of the WATERMED campaign was to obtain ground-based radiometric measurements in the thermal infrared over the site in order to validate LSTs obtained using data from the AATSR (including LSTs derived using the operational algorithm), the Landsat Enhanced Thematic Mapper + (ETM+) and the MODIS sensors. This chapter focuses on the results of the validation of the operational AATSR LST algorithm. In addition, measurements of surface emissivity (required for LST retrieval), the variation in apparent emissivity with zenith angle of observation,

and the thermal inertia of the soil at the site were made. Instruments to measure water vapour, optical aerosol thickness and total column ozone were also deployed on the roof of a farmhouse near the centre of the site, by members of the Solar Radiation Unit from the University of Valencia.

5.2 Experimental Procedure: In Situ Measurements

5.2.1 Instrumentation

Table 5.1 shows the instrumentation used for this element of the campaign. Three precision radiometers (CIMEL, EVEREST and RAYTEK MID radiometers, denoted by * in Table 5.1), were used for measurements of at-surface BT (including those used to derive emissivity). Calibration of the radiometers was carried out in two stages: an initial laboratory calibration of the instruments was carried out experimentally prior to the field campaign by making a series of measurements of a black body at known temperatures and inferring a relationship between the signal output by the radiometers and that from the black body. This known relationship is then used to correct for any instrumental bias in subsequent readings made by the radiometers. Secondary calibration of all three radiometers was also carried out at the WATERMED field site during the campaign itself, using the portable EVEREST black body calibration source (Table 5.1), where readings were made at the start and end of each set of in situ measurements.

5.2.2 Description of Field Site and Basis for Measurements

The WATERMED field site is located in a large, relatively flat, irrigated agricultural area in the Marrakech region of Morocco, where the principal crops grown are wheat, alfalfa, barley and olives. GPS readings made during the campaign indicate the site to be at approximately 600 m above sea level. The field site is composed almost entirely of rectangular fields that are typically 400 x 100 m in size, where the majority of the fields contain wheat at various different stages of cultivation. A significant proportion of the area is also reserved for animal grazing, where this latter classification of ground type can generally be considered as bare soil with sparse vegetation (<10%). The soil type over the site is predominantly clay-rich, with a deep red-brown colour indicative of high iron content. Small loose, quartz-rich rocks were found at all measurement locations, and were particularly evident in areas of bare soil with sparse vegetation where they contributed to approximately 1% of the surface material. Although the main land

Table 5.1. Instrumentation used for ground-based radiometric measurements.

Instrument	Spectral Bands (range/ μm)	BT Scale Range (K)	Resolution (K)	Accuracy (K)	Field of View (°)
CIMEL CE 312 Radiometer ^{1,*}	1) 8.0-13.0 2) 11.5-12.5 3) 10.5-11.5 4) 8.2-9.2	193.15 - 323.15	1) 8×10^{-3} 2) 50×10^{-3} 3) 50×10^{-3} 4) 50×10^{-3}	± 0.1	10
EVEREST 3000.4ZLC Radiometer ^{2,*}	8.0-14.0	193.15 - 373.15	0.1	± 0.5	4
RAYTEK Thermalert MID Radiometer ^{3,*}	8.0-14.0	233.15 - 873.15	0.1	± 0.5	20
RAYTEK ST6 Radiometer ³	8.0-14.0	241.15 - 773.15	0.1	± 1.0	8
EVEREST 1000 Calibration Black Body ²	N/A	273.15 - 333.15	0.1	± 0.3	N/A

¹ Information obtained from CIMEL Electronique (2001)

² Information obtained from <http://www.everestinterscience.com/>

³ Information obtained from G. Sória (personal communication)

* Instruments used for at-surface BT measurements.

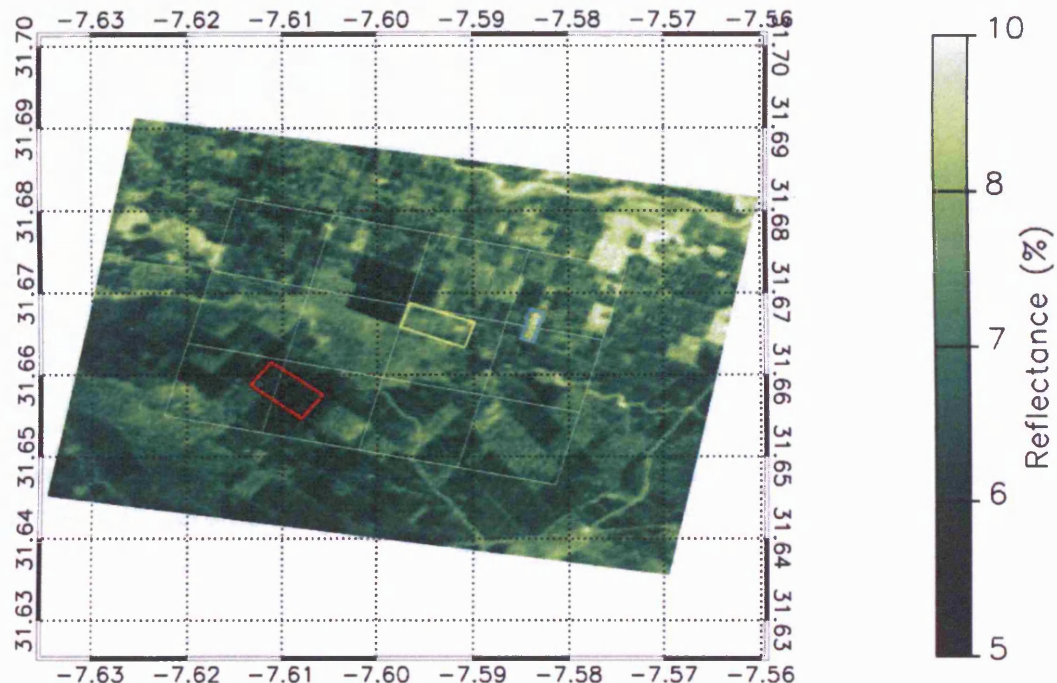


FIGURE 5.2. Landsat ETM+ blue channel image of the WATERMED site. Measurement locations B27 (red), B123 (yellow) and B131 (cyan) are also shown (see text and Table 5.2 for explanation). The white lines indicate the area covered by twelve AATSR pixels considered in this experiment (see Section 5.5). Landsat data courtesy of the WATERMED project.

cover type is wheat, adjacent fields may be at different stages within the growth cycle, where the proportion of vegetation may range between 30-100%. As a result, the area is heterogeneous, in terms of land cover type, on the scale of an AATSR pixel (1x1 km). Figure 5.2, a LANDSAT ETM+ blue channel image of the site obtained during the field campaign, shows the visible heterogeneity of the site. This Landsat channel is useful for distinguishing between soil and vegetation, and shows clearly the ‘patchwork’ of fields over the site, where darker colours represent areas with high proportion of vegetation.

In light of the heterogeneous nature of the site on the scale of a satellite pixel, the approach adopted for the campaign was to make radiometric measurements over the principal surface types, with in situ values of LST (and emissivity) derived for each measurement location. These LSTs could then be upscaled to the resolution of the 1 km satellite pixels (see Section 5.4.2 for a detailed description of this methodology). Limited by

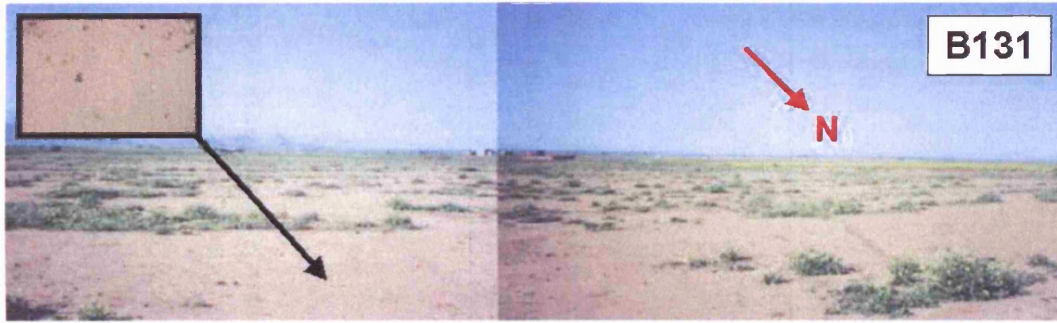


FIGURE 5.3. Photograph of B131 - bare soil with sparse vegetation. Insert courtesy of the Global Change Unit, University of Valencia. Date acquired: 05 March 2003

the number of precise radiometers available, three surface types, which were considered most representative of the site as a whole, were selected for the experiment. These surface types were categorised as: bare soil with sparse vegetation, young wheat crop (with a mixture of bare soil vegetation) and fully-grown wheat crop (fully vegetated). Table 5.2 summarises the characteristics of the three measurement locations, hereafter referred to as B131, B123 and B27, respectively, within the WATERMED field site that were selected for this experiment. The geographical location of the three measurement surfaces within the WATERMED site is indicated on Figure 5.2; photographs of the surfaces are also given in Figures 5.3, 5.4 and 5.5.

5.2.3 Measurements of At-Surface BTs

As we have seen in Chapter 1, the BT measured by a sensor channel at any height above the Earth's surface can be described by Equations 1.1-1.4. For measurements made at the surface of the earth, the effects of the intervening atmosphere are generally ignored and RT equation can be redefined in terms of T_s to give:

$$B_i(T_s) = \frac{B_i(T_i) - (1 - \epsilon_i)L_i^\downarrow}{\epsilon_i} \quad (5.1)$$

where B_i is the Planck function for channel i , ϵ_i is the channel emissivity of the Earth's surface and L_i^\downarrow is the down-welling radiance emitted by the atmosphere reflected off the Earth's surface. From Equation 5.1 it can be seen that to retrieve LSTs (T_s) from the BTs measured by a radiometer at the Earth's surface, the downwelling atmospheric radiance

Table 5.2. Summary description of measurement locations: B131, B123 and B27

Location	Surface Description	Radiometer	Measurement Interval (m)	Measurement Transects
B131 (bare soil)	<p>>90% bare soil with sparse wild vegetation typically 0.01-0.5 m high.</p> <p>One field adjacent to dirt road on three sides. Fourth side adjacent to a field of young cultivated wheat</p>	CIMEL	5-10	Two lines of measurements in the shape of a lower-case 't' at the North end of the field
B123 (mixed)	<p>20-30% young cultivated wheat typically 0.1 m high</p> <p>6 fields (adjacent by long sides). Fields separated by a low, rubbly bare soil mound 5-10 m wide with <30% wild vegetation</p>	EVEREST	10	Two lines of measurements running parallel with the short axes of the 6 fields
B27 (vegetation)	<p>90%+ mature cultivated wheat typically 0.4-0.5 m high</p> <p>6 fields (adjacent by long sides). Fields separated by a low, rubbly bare soil mound 5-10 m wide with <30% wild vegetation</p>	RAYTEK MID	10	As for B123

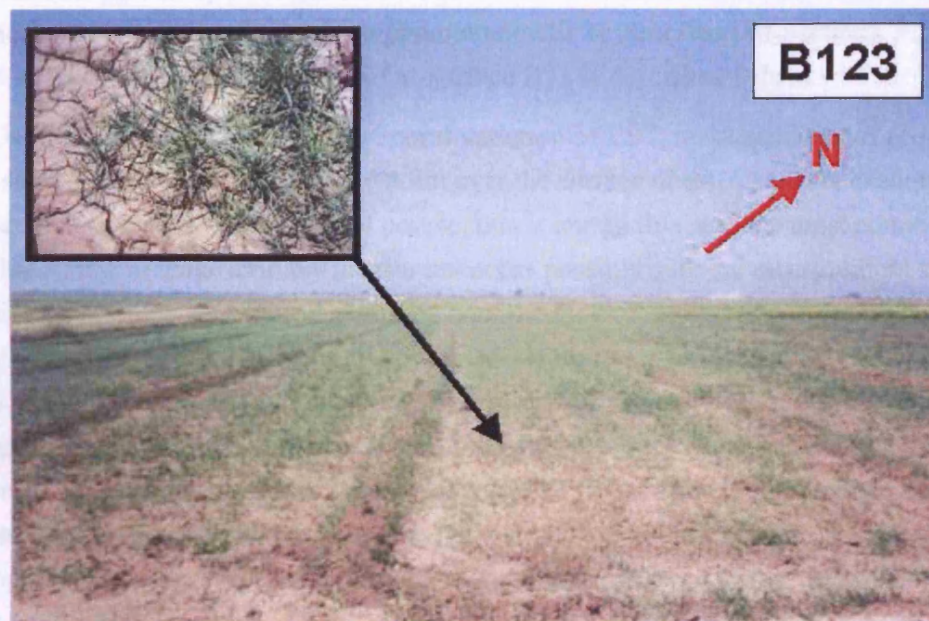


FIGURE 5.4. Photograph of B123 - bare soil with young cultivated wheat. Date acquired: 10 March 2003



FIGURE 5.5. Photograph of B27 - cultivated wheat. Date acquired: 11 March 2003

and surface emissivity over the bandwidth of the channel i must also be known. The methodologies used to obtain these parameters will be described in Sections 5.2.4 and 5.2.5, respectively; the acquisition of at-surface BTs is described below.

Due to the strong spatial and temporal variation of LST, measurements of at-surface BTs should ideally be made at every point over the surface of interest at the exact time of the satellite overpass. Practically, of course, this is impossible, and the most common approximation is to make as many measurements as possible over the measurement surface within a reasonable time period, centred about the time of the satellite overpass (e.g Coll et al. 2005). For this experiment, the time period adopted was 30 minutes (± 15 minutes from the time of the satellite overpass), where measurements were made every 5-10 m along marked transects (Table 5.2). No fixed supports for the radiometers were used: the readings were made by holding the sensor vertically at arms length, and pointing the aperture towards the surface in question. Care was taken not to make measurements over the operator's shadow or feet, or any other abnormal feature of this surface, such as the transect marker.

5.2.4 Downwelling Atmospheric Radiance

An stimulation of the downwelling sky irradiance is required to perform corrections for this variable when calculating LST from at-surface BT data (Equation 5.1), due to the non-unity of the surface emissivity. This is commonly obtained by making a radiometric measurement whilst the radiometer is pointing at the sky. For clear skies, a measurement made at 53° from zenith is an approximation for the hemispherical downward sky irradiance (K. Y. Kondratyev 1969). In this experiment, sky measurements T_i^{sky} , were made at zenith and then converted to L_i^\downarrow using the following relationship:

$$L_i^\downarrow \approx aB(T_i^{sky}) \quad (5.2)$$

where a is a correctional coefficient to account for the fact that the measurement of T_i^{sky} was made at zenith and not 53° from zenith, and B is the planck function. The value of this coefficient depends on the sensor bandwidth and the atmospheric conditions prevalent at the time of the measurement; typical values are between 1.32-1.59 in the 11.5-12.5 μm bandwidth and 1.47-1.68 in the 10.5-11.5 μm bandwidth (C. Coll & R. Niclos, personal communication). In practise, this value has a very small effect on the retrieved LST as the emissivity of the Earth's surface is close to unity. Nevertheless,

coefficients appropriate for the radiometers used in this experiment and the atmospheric conditions at the WATERMED site have been used in this study for completeness (see Table 5.4).

Making regular measurements of T_i^{sky} is especially important if the sky is not perfectly homogeneous (e.g. if there are small amounts of very thin cirrus cloud present). During the WATERMED campaign, measurements of downwelling sky irradiance were made at the beginning and end of each measurement period and at the inter-field boundaries along the marked transects in B27 and B123. For B131, additional measurements were made at the end of each marked transect line. In this instance, the measurements were also used to indicate when an inter-field boundary had been crossed, or the direction of the marked transect had changed, as these readings should be markedly lower than those made over the land surface (e.g. typically 218 K).

5.2.5 Surface Emissivity

Values of surface emissivity were obtained using the two-lid box method, where a number of locations in B27, B123 and B26 (a barley field to the South of B27) were selected that typically represented each of the three surface types, such that an average value for each surface type could be determined. A summary of the method, based on a publication by Rubio et al. (1997) and references therein, is given below; a full description and background can also be found in Sobrino & Caselles (1993).

The method utilises a cuboid-shaped box (Figure 5.6) with open ends, where the four walls of the box are lined with highly polished aluminium with an emissivity as close to zero as possible. The box has two lids: i) a cold reflective lid, made from the same material as the sides of the box, and ii) a hot 'black-body lid', where the emissivity should be close to unity. Both lids have apertures at the centre just large enough to enable a reading to be made inside the box using a radiometer: a series of three measurements are made as described below (also illustrated in Figure 5.7):

1. The box is placed over the surface to be measured with the cold lid and left for a few minutes to allow the temperature of the measurement surface and aluminium sides to stabilise.
2. Using a radiometer that operates over same bandwidth as the required emissivity value, a measurement (M1) is made through the aperture (Figure 5.7)



FIGURE 5.6. Collection of radiometric data in field B123 from which surface emissivities are derived using the emissivity box.

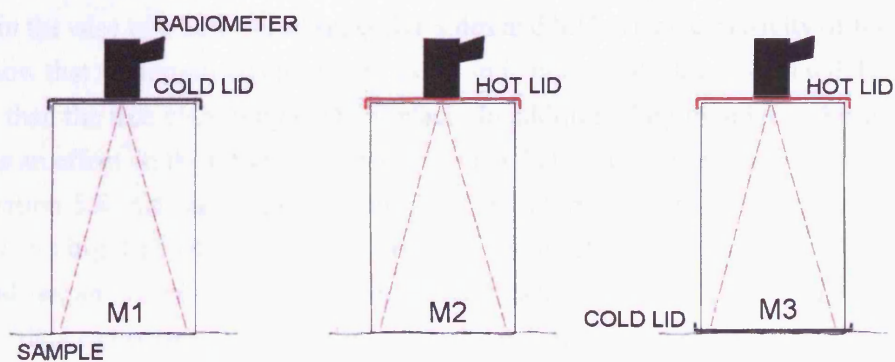


FIGURE 5.7. Diagrammatic representation of the two-lid box method where the sequence of measurements is carried from left to right. Figure adapted from Rubio et al. (1997).

3. The cold lid is replaced by the heated lid, and a second radiometric measurement (M2) is made. This step should be carried out as quickly as possible to avoid increasing the temperature of the sample significantly as a result of the heated lid.
4. The cold lid is then placed over the base of the box (with the heated lid still in place) and a third measurement (M3) is made.

The equation used for determining surface emissivity using the box method is based on the radiative transfer equation. In this case, Equation 5.1 is rearranged for ϵ_i to give:

$$\epsilon_i = \frac{L_i^\downarrow - B_i(T_i)}{L_i^\downarrow - B_i(T_s)} \quad (5.3)$$

which can be redefined in the context of the experiment to be:

$$\epsilon_i = \frac{M3 - M2}{M3 - M1} \quad (5.4)$$

In reality, this equation is only valid for a box whose sides and reflective lid are perfect reflectors (i.e. $\epsilon = 0$), and where the heated lid is a perfect black body (i.e. $\epsilon = 1$) (Conaway & van Bavel 1967, Dana 1969). For example, Rubio et al. (1997) have shown that for a surface emissivity of 0.907, the measured emissivity can be as low as 0.898 in the case of a box whose reflective sides and lid have an emissivity of 0.03. They also show that the measured emissivity using an imperfect black-body lid will be slightly higher than the true emissivity of the surface. In addition, they found that the size of the box has an effect on the retrieved emissivity such that a correction factor must be applied to Equation 5.4 that takes into account both the interior composition and geometry of the box. As highlighted in Chapter 3, accurate values of emissivity are required for LST retrieval, as an error of 0.01 in the emissivity used to retrieve LST from radiometric satellite data can typically result in errors in the retrieved LST of around 0.4 K. Equation 5.4 can therefore be rewritten more practically in terms of radiometric temperature, with the aforementioned correction factor as (G. Sória, personal communication):

$$\epsilon_i = \frac{(T_{bb})^a - (T_{sbb})^a}{(T_{bb})^a - (T_{scc})^a} \quad (5.5)$$

where T_{bb} is the radiometric temperature of the black body cover; $T_{s_{bb}}$ is the radiometric temperature of the ground surface in the box with the hot black body cover; $T_{s_{cc}}$ is the radiometric temperature of the ground surface in the box with the cold cover and a is the correction factor which must be determined for each individual box.

For this field campaign, our measurement procedure deviated slightly from that described above. The black-body lid was heated to 95°C using a generator and three measurement cycles were performed at each location in order to obtain an average value, with the heated lid at three different temperatures as the lid cooled. All three precise radiometers (Table 5.1) were used during the experiment to achieve a broad spectrum of measurements. Measurement 3 (M3) was obtained using the RAYTEK ST6 Radiometer to take an average measurement of the temperature of the black-body lid without using the box itself. This was largely due to the fact that the measurements were being repeated three times at each location and the downward pressure that would have been exerted by the cold lid on the measurement sample may have changed the nature of the surface (e.g. by compressing the vegetation), thus affecting the results.

5.3 Results: In Situ Data

5.3.1 Surface Emissivity

A total of 63 emissivity data points were collected at 21 different locations over the WATERMED field site, which can be classified broadly into the three land surface classes: bare soil (i.e. <10% vegetation), mixed vegetation and bare soil (i.e. ~30-70% bare soil) and vegetation (i.e. <10% bare soil). Calibration and conversion to emissivity for each of the 63 measurements (Equation 5.5), was carried out by the team from the University of Valencia.

From Equation 5.5, we see that the accuracy of the box method is largely dependent upon being able to determine accurately the temperature of the hot black body lid. By heating the black body lid to very high temperatures, this accuracy becomes much less critical. During the experiment, it was found that the radiometric temperature of the lid varied by several degrees over the surface, generating errors not only in determining an accurate 'hot-lid' temperature (M3 - Section 5.2.5), but also by irradiating the ground heterogeneously. Unfortunately, these errors are impossible to quantify, as the experimental procedure must be carried out very quickly (Section 5.2.5) and it is not possible to assess the temperature distribution over the lid. In light of this, emissivity data were

Table 5.3. Summary of in situ emissivity data. Values are absent over bare soil for the RAYTEK and EVEREST instruments due to lack of reliable data.

Surface	Emissivity $\pm \sigma$					
	RAYTEK (8-14 μm)	EVEREST (8-14 μm)	CIMEL1 (8-13 μm)	CIMEL2 (11.5-12.5 μm)	CIMEL3 (10.5-11.5 μm)	CIMEL4 (8.2-9.2 μm)
Bare Soil (B131)	-	-	0.957 ± 0.003	0.979 ± 0.002	0.964 ± 0.003	0.916 ± 0.007
Mixed (B123)	0.953 ± 0.015	0.951 ± 0.002	0.974 ± 0.009	0.979 ± 0.006	0.968 ± 0.008	0.952 ± 0.015
Vegetation (B27)	0.965 ± 0.007	0.976 ± 0.005	0.982 ± 0.004	0.983 ± 0.003	0.975 ± 0.004	0.963 ± 0.007

rejected where the temperature of the black body lid was found to be below 343.15 K, or increased between the first and second measurements at any one location (i.e. the temperature of the black body lid had not stabilised). Measurement locations where the standard deviation of the three measurements made at that location was more than 0.008, were also discarded.

From the remaining measurements, a representative emissivity was calculated for each of the three surface regimes for each instrument. The results, given in Table 5.3, agree well with those published by other researchers and values calculated from the ASTER Spectral Library (1999). For example, Rubio et al. (1997) and Sutherland (1986) report values of 0.957 ± 0.005 and 0.958 ± 0.020 , respectively, for clayey soils in the 8-14 μm waveband, which compares well to the value of 0.957 ± 0.003 obtained over bare soil surfaces for the CIMEL channel 1 in this experiment. Data from the ASTER spectral library for eight specimens that resemble the soil over the WATERMED site have been used to calculate narrow-band emissivities, using the filter functions for the AATSR 12 and 11 μm channels. The emissivities for these channels, which operate over similar wavelengths to the CIMEL channels 2 and 3, yield results of 0.976-0.982 and 0.965-0.976, respectively, which are comparable to the figures of 0.979 ± 0.003 and 0.964 ± 0.003 obtained in this experiment. Snyder et al. (1998) report values of 0.972 and 0.966 over arid bare soil for the MODIS bands 32 and 31, respectively, also comparable to the CIMEL channels 2 and 3, which agree well with the results of this experiment.

Vegetation generally shows very little spectral variation over the 8-14 μm waveband, demonstrating near grey-body behaviour (Sutherland 1986). This characteristic is reflected in the results of this experiment, particularly for the EVEREST and CIMEL channels 1, 2 and 3. Rubio et al. (1997) report a value of 0.976 ± 0.008 in the 8-14 μm waveband for green grass, which may be considered a comparable surface to a field of mature wheat. This figure agrees well with the result obtained using the Everest instrument, but is slightly higher than that obtained for the Raytek, and slightly lower than that obtained for the Cimel channel 1 (8-13 μm). From the ASTER spectral library, figures of 0.989 and 0.983 are obtained for the AATSR 12 and 11 μm channels, respectively, which are slightly higher than those obtained over the WATERMED field site (0.983 ± 0.003 and 0.975 ± 0.004). These differences may, at least in part, be due to i) the differences between the instrumental response curves, ii) some soil contamination in the samples during the field measurement process (the cultivated wheat surfaces are not truly 100% vegetation), as the measurements over the WATERMED site were true in situ measurements and/or iii) the fact that different specimens have been used to obtain these values.

As the emissivity of the soil is lower than that of vegetation, (ii) would have the effect of lowering the overall emissivity of the measurement surface. We see this effect very clearly over B123, where the surface is a mixture of bare soil and wheat, and as expected, the measured emissivities over this surface regime are observed to be between the extremes of bare soil and fully vegetated surfaces.

Overall, the results over B123 (mixed) are much less stable. This is undoubtedly because of the highly variable nature of this surface. B131 (bare soil) and B27 (vegetation) are relatively homogeneous surfaces, a fact that is reflected clearly in the emissivity data collected during this campaign.

5.3.2 LST and Downwelling Sky Irradiance

Coincident measurements of ground-based radiometric temperature were carried out during the day-time overpasses for the AATSR sensor during the campaign, where the satellite overpass times were predicted using the AATSR Overpass Tool (ESA 2002a) at the University of Leicester, prior to the field campaign. Only two day-time AATSR overpasses occurred during the campaign: 05 March 2003 at 10:53 and 08 March at 10:59; of these, only the 05 March 2003 was cloud free. Measurements of radiometric temperature were made simultaneously over all three surface regimes over a 30 minute period, centred about the time of the Envisat overpass, as described in Section 5.2.3. The calibration and conversion of the digital counts/volts output by the radiometers to radiometric temperature was carried out by the team from the University of Valencia.

Figure 5.8 shows the fully-calibrated radiometric data recorded over the measurement locations B131, B123 and B27 over this 30 minute period on 05 March 2003. These data show clearly the different radiometric characteristics of the three surface regimes. As expected, the radiometric temperature over B27 is substantially lower than for either B131 or B123, as the dense wheat plants are actively transpiring and keeping themselves cool. B131, and to a certain extent B27, appear radiometrically quite stable, as indicated by the comparatively low standard deviations of the measurements. In contrast, the measurements over B123 are extremely erratic, which is to be expected as the radiometric temperature depends strongly on the proportion of vegetation within the radiometer IFOV. All the locations show a general increase in temperature with time due to increasing surface temperature as solar heating increases. The mean temperature increases over the 30-minute period are calculated to be 2.64 ± 0.71 K for bare soil (B131 - CIMEL Channel 3), 1.59 ± 1.90 K for mixed (B123) and 3.69 ± 1.33 K for vegetation (B27). Differences in the observed warming between each of these locations is expected due to the differ-

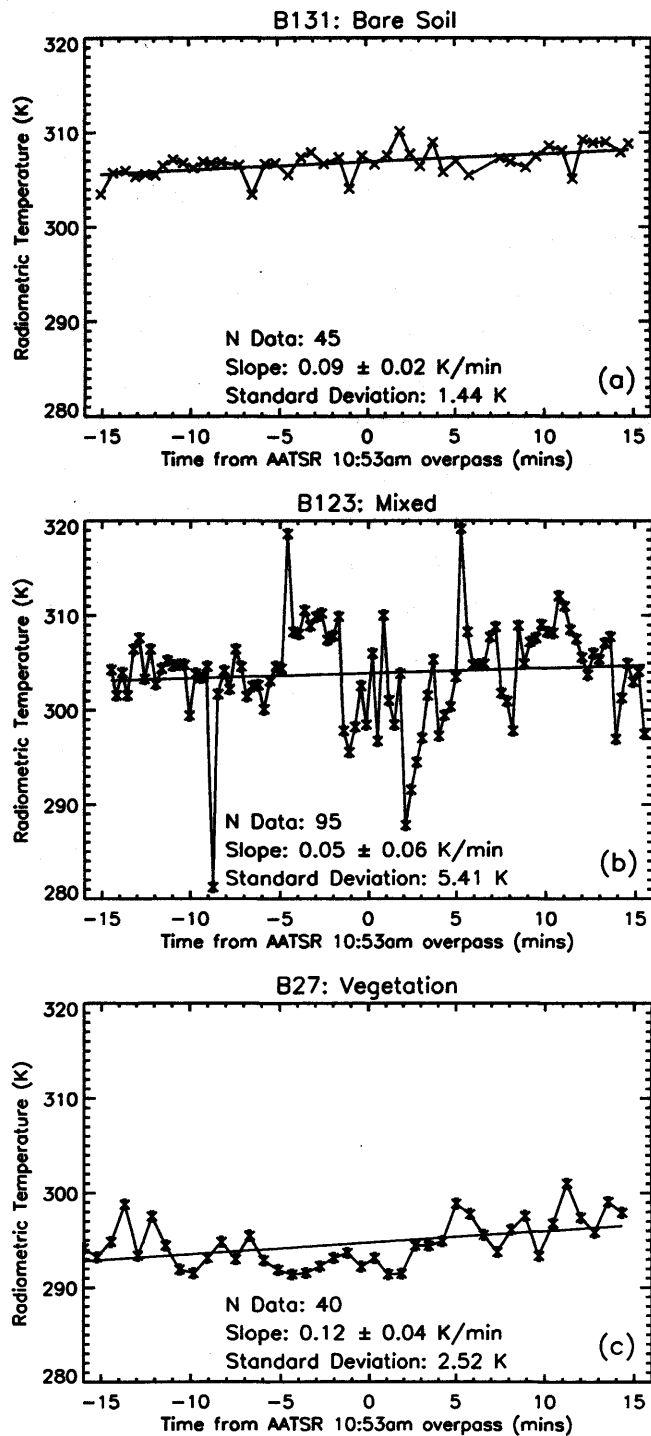


FIGURE 5.8. Calibrated at-surface BTs for measurements coincident with the AATSR daytime overpass on 05 March 2003 over (a) B131 (bare soil - CIMEL Channel 3), (b) B123 (mixed) and (c) B27 (vegetation). The errors for the slopes of each regression line are the one-sigma uncertainty, considering the standard deviation of the measurements.

ent thermal inertia of the surfaces, which depends on a number of properties that differ between each of the measurement surfaces, such as composition, cementation of grains and particle size.

The data shown in Figure 5.8 include measurements made over the inter-field boundaries (<30% vegetation - Section 5.2) in B123 and B27. In the case of the former, the conditions over these inter-field boundaries are very similar to the conditions within the fields in B123 themselves and have therefore been included in the final radiometric dataset. For B27, the conditions over the inter-field boundaries do not resemble the conditions within the B27 fields themselves, and have therefore been excluded from the analysis. Despite this, there appear to be a number of erratic and unrealistic data points within the datasets obtained over B123 and B27 (e.g. a value of <10°C at approximately -10 minutes over B123). In light of this, 1-sigma limits have also been imposed upon the data collected over these surface regimes in the final radiometric datasets in order to stabilise the mean radiometric temperature obtained for these sites. With these 1-sigma limits imposed, an average radiometric temperature for each measurement surface has been determined, and the standard deviations of the final data set are reduced to 2.57 K and 1.24 K, respectively (Table 5.4).

For the measurements of down-welling sky radiance, T_i^{sky} , an average of all measurements made around the overpass time was used (see Table 5.4 for the mean). The down-welling radiometric temperature of the atmosphere was typically 223.15 K (in the 8-14 μm band), which is below the operating range of the RAYTEK instrument. To overcome this problem, the measurements made using the EVEREST were also used in the calculation of LST for the RAYTEK, as the operational bandwidths of the two instruments are the same.

The final in situ LSTs for each surface regime are shown in Table 5.4. These values have been calculated using the *in situ* emissivities described in Section 5.3.1 appropriate for each radiometer and the surface over which it was employed, and averaged radiometric temperature and downwelling sky radiance measurements, as described above. The errors calculated for each of the final LSTs have been calculated from the quadrature sum of the calibration and distribution errors (standard deviation) on each measurement. As for the at-surface BTs corresponding to each measurement surface, the LSTs and their associated uncertainties reflect strongly the proportion of vegetation over the measurement surface, with the LST over B27 being notably cooler than B123 and B131, which have very similar LSTs.

Table 5.4. Summary of LST calculations over surfaces B131, B123 and B27. The T_i^{sky} coefficients were provided by Guillem Soria of the University of Valencia.

Radiometer	Surface	$T_i \pm \sigma$ (K)	$\epsilon_i \pm \sigma$	$T_i^{sky} \pm \sigma$ (K)	T_i^{sky} Coef.	$T_s \pm \sigma$ (K)	$T_s - T_i$ (K)
CIMEL1	Bare Soil (B131)	305.08 ± 1.25	0.957 ± 0.003	215.64 ± 0.96	1.17	307.54 ± 1.29	2.46
CIMEL2	Bare Soil (B131)	307.67 ± 1.48	0.979 ± 0.002	205.62 ± 1.58	1.29	309.02 ± 1.50	1.35
CIMEL3	Bare Soil (B131)	306.83 ± 1.44	0.964 ± 0.003	194.82 ± 1.57	1.50	309.10 ± 1.49	2.27
CIMEL4	Bare Soil (B131)	301.78 ± 1.33	0.916 ± 0.007	222.21 ± 0.99	1.06	306.00 ± 1.05	4.22
EVEREST	Mixed (B123)	304.74 ± 2.57	0.951 ± 0.002	221.55 ± 5.37	1.50	307.25 ± 2.66	2.51
RAYTEK MID	Vegetation (B27)	294.12 ± 1.24	0.965 ± 0.007	221.55 ± 5.37	1.50	295.64 ± 1.37	1.52

5.4 Comparison of In Situ LSTs with AATSR data

5.4.1 AATSR Data

The AATSR LST data used in this study were from the prototype LST product, which was processed from L1B BTs to LST at the Rutherford Appleton Laboratory, UK. The prototype product, which was distributed prior to the production of the operational product for validation purposes only, is essentially the same as the operational product described in Chapter 2. The AATSR LST data used in this experiment were derived from the AATSR overpass that occurred at 10:53 am (GMT) on 05 March 2004.

5.4.2 Calculation of In Situ LSTs Over the AATSR Pixels

As described in Section 5.3.2, LST has been determined over the three principal surface regimes at the Marrakech WATERMED site. Practically, the next stage in the validation process is to determine in situ LSTs that are equivalent to the AATSR LSTs for pixels over the site, using the in situ data. As validation of satellite LSTs is traditionally carried out over homogeneous sites (see Chapter 1), an innovative approach was required for this study in order to derive these data.

To characterise the heterogeneity of the field site, the Landsat ETM+ image from the overpass occurring at 10:52 am on 15 March 2003 was utilised (Figure 5.2). Landsat ETM+ has eight channels, which comprise six visible channels with a spatial resolution of 30 m, one panchromatic band with a spatial resolution of 15 m and one thermal infrared channel with a spatial resolution of 60 m. Unfortunately, the spatial resolution of the thermal Landsat band, which would have been ideal for this task, was found to be too low, with the individual fields (100×400 m) not being resolved very clearly in these data. Instead, data from Landsat channel 1 ($\lambda = 0.45\text{--}0.52 \mu\text{m}$) was used as a proxy for the thermal distribution over the site. This channel was chosen as it covers the blue region of the electromagnetic spectrum, which is very sensitive to the differing reflective properties of soil and vegetation; as we have seen from the in situ measurements over the site, the LSTs demonstrate a dependence on the amount of vegetation in the instrument IFOV. Moreover, regression of the Landsat Thermal Infrared (TIR) channel data with data from the blue channel (rescaled to the spatial resolution of the thermal channel) is sufficiently well correlated (0.49 for some 13446 data points over the field site) to indicate a relationship between these two data sets (Figure 5.9). Although uncorrected for the effects of the atmosphere and surface emissivity, the Landsat BTs can be considered

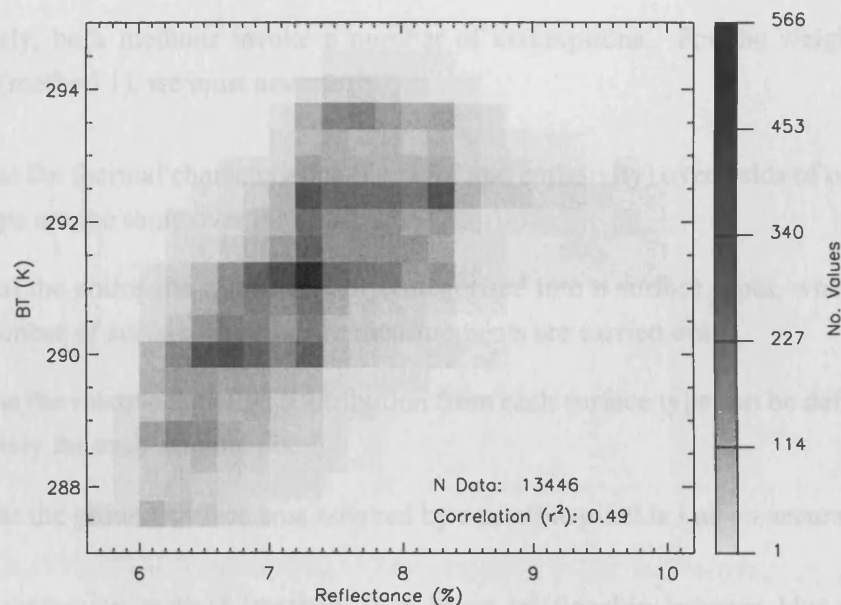


FIGURE 5.9. Correlation between Landsat visible (blue) reflectances and thermal (TIR) channel BTs data. The data have been binned into 0.2% bins for reflectances and 0.4 K bins for TIR BTs.

a proxy for LST on this occasion due to the homogeneity of the site in terms of infrared emissivity (less than 1% - see Table 5.3), and likelihood that the atmosphere does not vary significantly over the 4×3 km site.

5.4.2.1 Upscaling of In Situ LSTs

From Figure 5.2, it is clear that the visible properties in the blue region of the electromagnetic spectrum of the three measurement surfaces are very different. These differences have been exploited in order to determine in situ LSTs on the scale of an AATSR pixel. Two methods of upscaling these data have been utilised in this study. Firstly, the range of blue-visible reflectances over each of the three measurement locations has been identified and used to categorise every Landsat channel 1 pixel over the site as one of these three surface regimes. The proportion of each surface type within the AATSR pixel is then determined, and a simple weighted mean of the corresponding in situ LSTs calculated. Secondly, the mean blue reflectance over each measurement location has been determined and then used to generate an equation describing the relationship between the Landsat visible reflectances and the corresponding LST. Using this equation, an in situ LST can then be determined for each Landsat pixel reflectance; an average of these

LSTs is then calculated for the surface area corresponding to each AATSR pixel.

Clearly, both methods invoke a number of assumptions. For the weighted-mean method (method 1), we must assume:

1. that the thermal characteristics (i.e. LST and emissivity) over fields of one surface type are the same over the entire site,
2. that the entire site can be reliably categorised into n surface types, where n is the number of surface types where measurements are carried out,
3. that the relative radiative contribution from each surface type can be defined accurately for each satellite pixel,
4. that the ground surface area covered by a satellite pixel is known accurately.

For the regression method (method 2), a linear relationship between blue-visible reflectance and LST is assumed.

For both methods, two *in situ* LSTs have been calculated for each AATSR pixel: the first, where the 'retrieved Landsat LSTs' are simply averaged over each 1×1 km AATSR pixel, and the second where the true IFOV of the AATSR (see Chapter 2) has also been taken into account as an additional weighting factor. In this case, the IFOV of the $11 \mu\text{m}$ channel (nadir) is used, but similar values (within 0.1 K for each *in situ* LST equivalent to an AATSR pixel LST) are obtained using the $12 \mu\text{m}$ channel IFOV.

Landsat pixels corresponding to each of the three measurement surfaces (B131, B123, B27) have been extracted from the data and are shown in Figures 5.10- 5.12. Confidence in the geolocation of the Landsat data has been assured by comparing the geolocation of the pixels at the corners of the measurement fields with GPS measurements made during the campaign (within approximately one 30 m Landsat pixel). Figure 5.13 shows the distribution of the blue-visible reflectances over each of the measurement locations. From these data, the three surface regimes - bare soil, mixed and vegetation - have been classified according to the scheme shown in Table 5.5.

For the regression method (method 2), the equation $y = 261.2 + 5.3x$ was obtained, where x is the blue-visible reflectance of a Landsat pixel and y is the corresponding 'retrieved Landsat LST' for that pixel. This equation was derived using the mean reflectance and corresponding *in situ* LST for the measurement surfaces (Figure 5.13); only the data for the bare soil and vegetated surfaces have been used to obtain this relationship, as these provided the most stable *in situ* LST (see Section 5.3.2) and reflectance data sets,

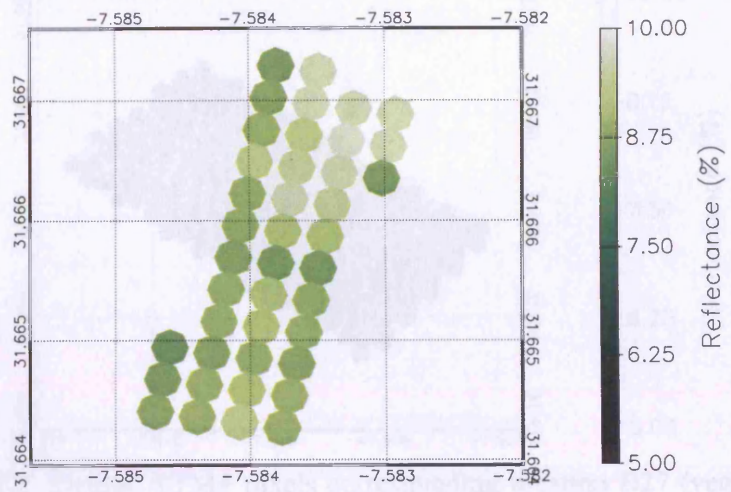


FIGURE 5.10. Landsat ETM+ pixels corresponding location B131 (bare soil) for channel 1 (blue).

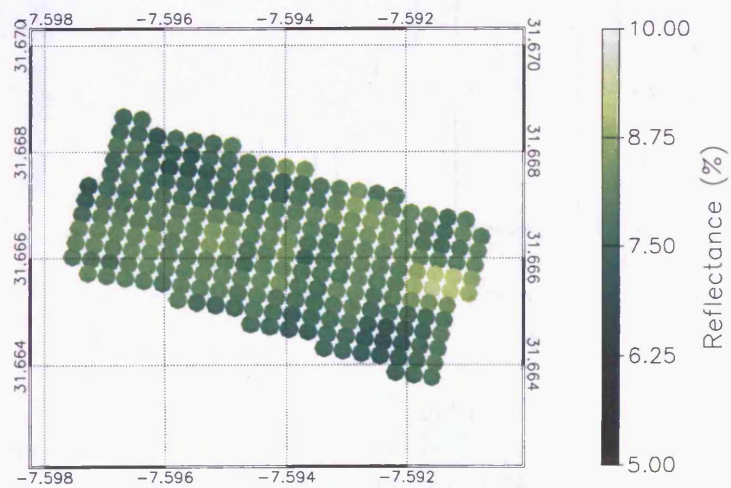


FIGURE 5.11. Landsat ETM+ pixels corresponding location B123 (mixed) for channel 1 (blue).

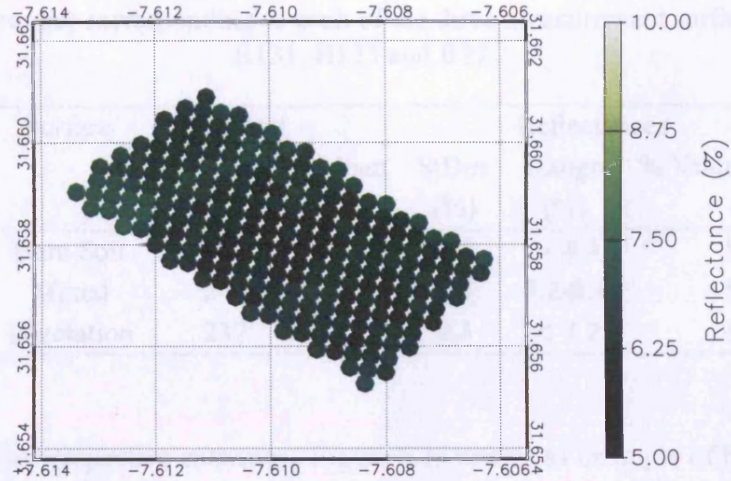


FIGURE 5.12. Landsat ETM+ pixels corresponding location B27 (vegetation) for channel 1 (blue).

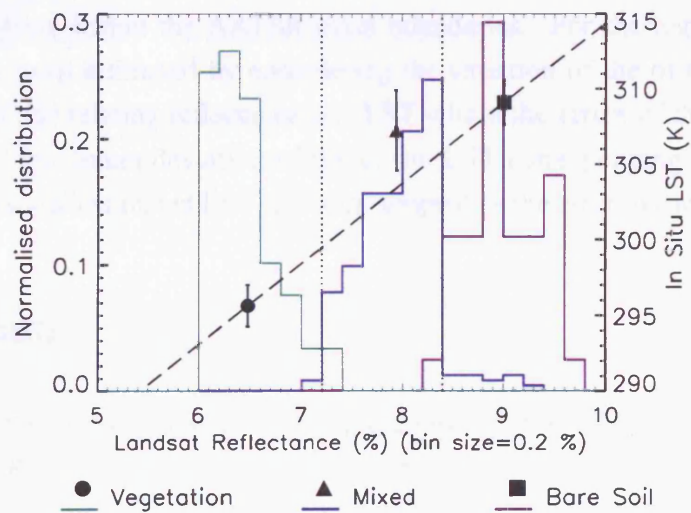


FIGURE 5.13. Normalised distribution of Landsat ETM+ channel 1 reflectances for measurement locations B131, B123 and B27. Also shown, are the mean reflectances and corresponding in situ LST for each surface (filled circle, triangle and square) and the relationship obtained between reflectance and LST (dashed line): $y = 261.2 + 5.3x$. The dotted lines correspond to the reflectance range boundaries for each surface, given in Table 5.5.

Table 5.5. Landsat Channel 1 reflectance statistics (number of Landsat pixels, mean, standard deviation and range of reflectances, and the % of pixels with reflectances within that range) corresponding to each of the three measurement surface regimes: B131, B123 and B27.

Location	Surface	N Landsat	Reflectances			
			Mean	StDev	Range	% Values in Range
			(%)	(%)	(%)	(%)
B131	Bare Soil	41	9.0	0.4	> 8.4	97.6
B123	Mixed	243	7.9	0.4	7.2-8.4	94.2
B27	Vegetation	237	6.5	0.3	< 7.2	96.6

and were at their respective extremes. Figure 5.14 shows as example of both upscaling methods for an AATSR pixel over the WATERMED field site.

Errors for each in situ LST corresponding to an AATSR pixel have been estimated considering the assumptions associated with each methodology listed above. For the weighted-mean method, the error has been calculated from the quadrature sum of the errors on the 'measured' LST for each surface regime, weighted by the proportion of that surface regime within the AATSR pixel boundaries. For the regression method, the errors have been estimated by considering the variation of the of the gradient and intercept of the line relating reflectance and LST within the errors of the 'measured' in situ LSTs. The maximum deviation of the in situ LST corresponding to each AATSR pixel from the actual estimated LST has been adopted as the error in each case.

5.5 Results

Figure 5.15 shows the comparison between the in situ and AATSR LSTs for twelve pixels over the WATERMED site. The nominal 1 km area covered by these pixels is shown in Figure 5.2. The calculated bias and standard deviations corresponding to these data are shown in Table 5.6.

There are a number of similarities between the results for both the weighted mean and regression methods. Both methodologies suggest that the AATSR LSTs are warm biased. Eight (or perhaps nine in the case of the regression method) of the matchups are well correlated ($r^2 = 0.7$ to 0.8); these matchups are shown by filled circles in Figure 5.15. The remaining three or four pixels, shown by open circles in Figure 5.15, are comparative

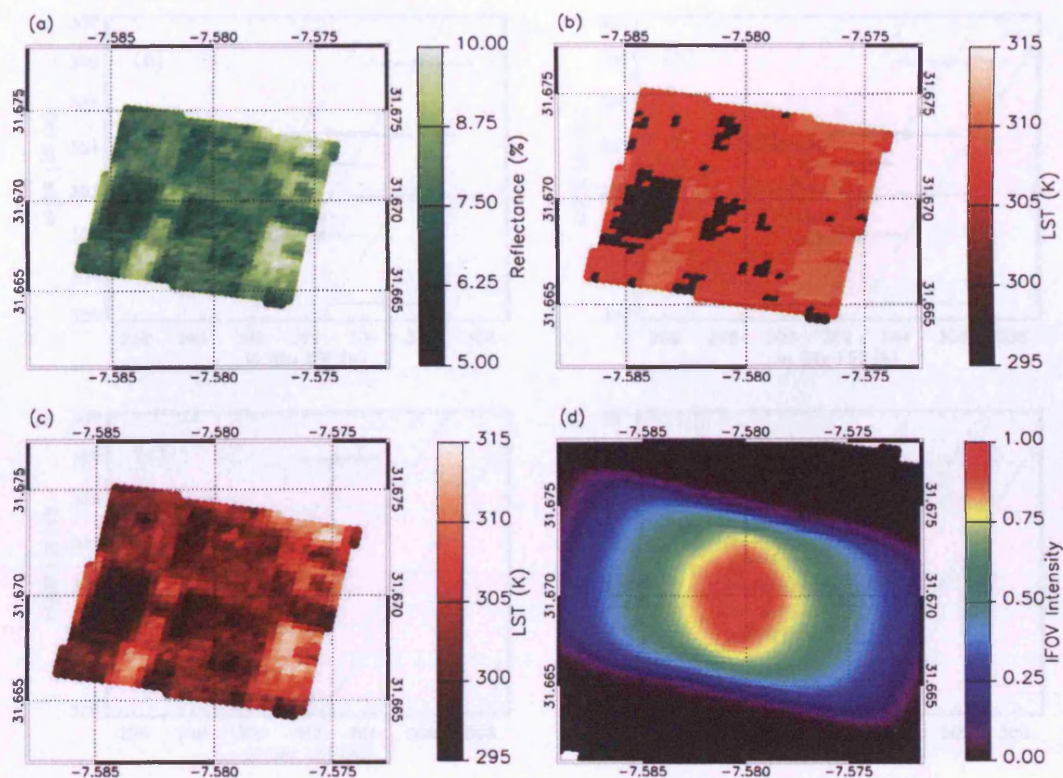


FIGURE 5.14. Example of the upscaling methodologies used in the study for one AATSR pixel over the field site. (a) shows the Landsat channel 1 reflectances for Landsat pixels falling within the nominal 1 km AATSR pixel size, (b) shows the ‘retrieved Landsat LSTs’ using weighted-mean method, (c) shows the ‘retrieved Landsat LSTs’ using the regression method and (d) shows the AATSR 11 μm IFOV weighting for this AATSR pixel.

Table 5.6. Calculated biases and standard deviations for the comparison of the four sets of derived in situ LSTs with the corresponding AATSR LSTs. Results are shown for all pixels and the eight well-correlated pixels (see Section 5.6).

In Situ LST	All Pixels		Eight Pixels	
	Bias (K)	StDev (K)	Bias (K)	StDev (K)
Weighted-mean method (no IFOV weighting)	0.60	2.70	0.69	1.13
Weighted-mean method (with IFOV weighting)	0.61	2.66	0.59	0.84
Regression method (no IFOV weighting)	3.08	1.99	3.10	0.69
Regression method (with IFOV weighting)	3.08	2.05	3.06	0.77

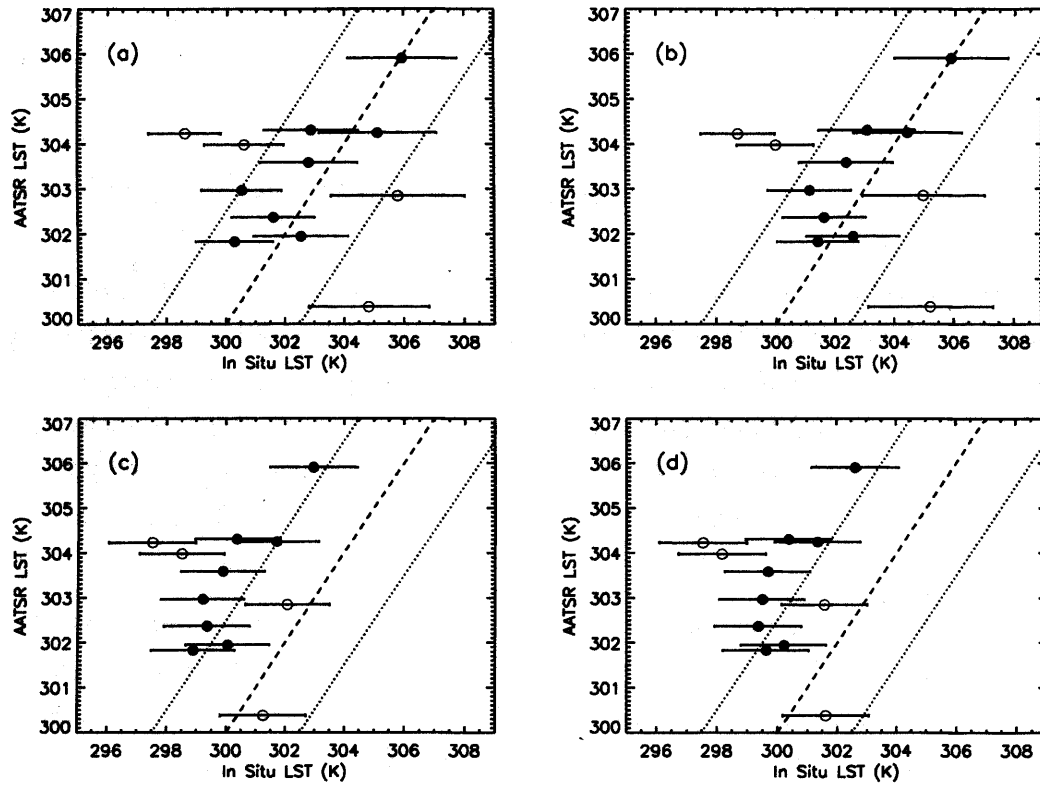


FIGURE 5.15. AATSR vs in situ LSTs for 12 pixels over the WATERMED site for (a) in situ LSTs derived using the weighted-mean method, (b) in situ LSTs derived using the weighted-mean method, with additional weighting from the true IFOV of the AATSR applied, (c) in situ LSTs derived using the regression method and (d) in situ LSTs derived using the regression method, with the AATSR IFOV weighting applied. In each graph, matchups represented by open circles correspond to AATSR LSTs that are flagged as having an Envisat blanking pulse associated with the measurements (see Section 5.6 for explanation).

outliers. Possible explanations for higher biases observed for these four pixels will be discussed in Section 5.6. For both methodologies, there is only a negligible change in the overall bias and standard deviation of the results when the true IFOV of the AATSR is considered. However, when we look at the results on a pixel-to-pixel basis, the change in LST is more than 0.1 K for nine of the twelve pixels (standard deviation is 0.57 K and 0.37 K for method 1 and 2, respectively). This is a significant finding, as it implies that considering the true IFOV of the AATSR could be important where there is sub-pixel variation of LST (or SST).

The major difference between the results obtained using method 1 and method 2 is in

the magnitude of the bias, although they are in agreement within the error estimates. This difference in bias, together with other potential sources of bias in the results, is discussed in Section 5.6

5.6 Discussion: Sources of Bias

The results of the validation exercise using in situ data obtained from both methodologies suggest that the AATSR is yielding an LST that is too warm. From the results of the sensitivity study carried out Chapter 3, this is expected for biome-12 mid-latitude retrievals. For a surface-air temperature difference of 10 K (inferred from ECMWF 1.125° gridded data (ECMWF 1995) appropriate for this field site), we would expect a warm bias of approximately 0.6 K, which agrees very well with the results from the weighted-mean method.

Another source of bias that should be considered is an incorrect classification of the field site within the AATSR LST algorithm. Currently, the site is classified as biome 12 (broadleaf trees with winter wheat). Table 5.7 shows the bias and standard deviations calculated using both the weighted mean and regression methods (considering the true IFOV of the AATSR). The results show that the best agreement with the in situ data is achieved by using the coefficients for biome 8 (broadleaf shrubs with groundcover), which yields a bias of -0.11 and 2.37 K for the weighted-mean and regression methods, respectively. Following this, the results for biome 12 provide the best results. The standard deviations are similar (within approximately 0.1 K) for all biomes.

In Section 5.5 we saw how the regression method yields a bias that is approximately 2.5 K warmer than for the weighted-mean method. Both methods are likely to be subject to errors in the bias as a result of the assumptions made in each case. However, it is likely that the weighted-mean method, where more assumptions are made and the methodology is more simplistic, is the largest source of the difference in the observed bias. This is also supported by the lower standard deviation obtained for the differences between AATSR and in situ LSTs for the regression method. As an example, let us consider the Landsat pixels classified as vegetation. Figure 5.16 shows a histogram of the Landsat channel 1 reflectances corresponding to the twelve AATSR pixels (considering the pixels as 1 km in size). According to these data, more than 40% of the total Landsat pixels are classified as vegetation, with almost 80% of these having a reflectance above the mean reflectance corresponding to the vegetation measurement site (B27). All of these Landsat pixels have been assigned the same LST of 296.64 K, despite the fact that the proportion of

Table 5.7. Calculated biases and standard deviations for the comparison of the four sets of derived in situ LSTs with the corresponding AATSR LSTs.

LST Biome #	Weighted-mean		Regression	
	Bias (K)	StDev (K)	Bias (K)	StDev (K)
1	5.19	2.77	7.66	2.17
2	2.49	2.73	4.96	2.12
3	2.50	2.73	4.97	2.12
4	0.89	2.66	3.36	2.05
5	0.92	2.67	3.39	2.06
6	1.18	2.69	3.65	2.09
7	0.78	2.68	3.25	2.07
8	-0.11	2.64	2.37	2.02
9	0.69	2.67	3.16	2.06
10	0.95	2.66	3.43	2.05
11	0.89	2.70	3.36	2.09
12	0.61	2.66	3.08	2.05
13	0.89	2.66	3.36	2.05

soil for most of the Landsat pixels of this classification is higher than that of the typical measurement surface in B27. This will result in most of the pixels classed as ‘vegetation’ having an LST that is too low, leading to an overall LST that is cold-biased.

Although the regression method allows more flexibility in terms of the ‘retrieved’ Landsat LSTs (i.e. the LSTs are not one of three values, as for the weighted mean method), this method does assume a linear relationship between the blue-visible reflectances and LST. From Figure 5.9 this does not seem an unreasonable assumption. However, there is a considerable amount of scatter in these data and at high reflectances, the relationship could be interpreted as non-linear. If this is the case, a polynomial equation would probably provide more accurate representation of the relationship between reflectance and in situ LST. Unfortunately, due to the limited number of in situ point observations of LST, it is not possible to perform this for this study.

Methodologies aside, there are other aspects of the observed biases that require further investigation. In Section 5.5, four pixels were identified as outlying data points (indicated by the open circles in Figure 5.15). Interestingly, the AATSR data for these four pixels were obtained in the presence of an Envisat blanking pulse, whilst the other

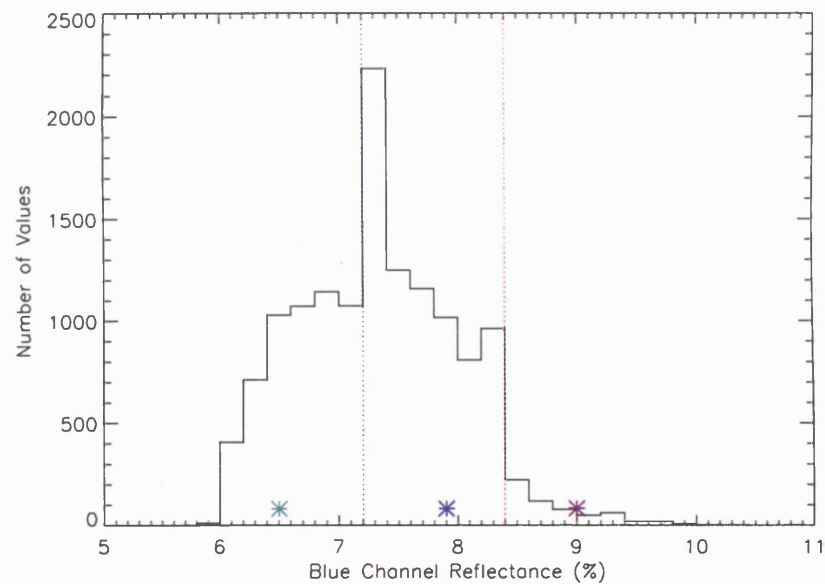


FIGURE 5.16. Histogram showing the distribution of Landsat channel 1 reflectances for the twelve AATSR pixels over the WATERMED field site. The blue dotted line shows the vegetation-mixed and the red dotted line, the mixed-bare soil classification boundaries used for the regression method. The green, blue and purple asterisks show the mean Landsat reflectance corresponding to the vegetation, mixed and bare soil surfaces, used in the regression method.

eight pixels were not. The presence of a blanking pulse in the AATSR data is flagged in the confidence word associated with each pixel, and indicates that either the Radar Altimeter-2 (RA-2) and/or the Advanced Synthetic Aperture Radar (ASAR), also on-board the Envisat satellite, were operating at the time when the AATSR pixel was being integrated. However, no evidence has ever been found to suggest that the presence of a blanking pulse affects the quality of ATSR-1/2 data (Mutlow 2000), so it seems unlikely that this could be the cause of the anomalies observed in these AATSR data.

A more likely explanation is in the derivation of the in situ LST or AATSR LST for these pixels. Figure 5.17a shows the AATSR–in situ LST differences as a function of the proportion of vegetation (using the weighted-mean method). The correlation is calculated to be 0.72, which suggests there is a relationship between these two parameters. In terms of the AATSR LST product, the results given in Chapter 3, which describe the sensitivity of the retrieved AATSR LST to errors in the emissivity assumed in the retrieval coefficients, cannot explain the observed biases. Even if we consider the extremes of a fully vegetated surface and a completely unvegetated surface, this would only result in a

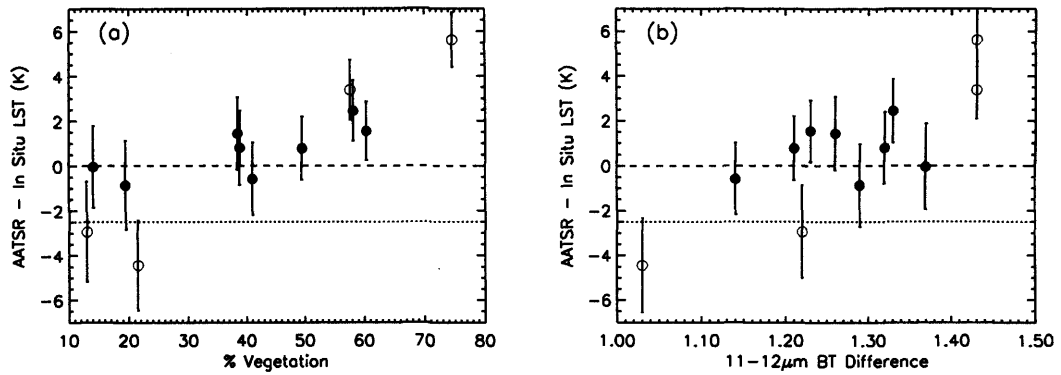


FIGURE 5.17. LST difference plotted as a function of (a) proportion of vegetation within each AATSR pixel, as determined by the weighted-mean method and (b) the 11–12 μm BT difference. In each graph, matchups represented by open circles correspond to AATSR LSTs that are flagged as having an Envisat blanking pulse associated with the measurements (see Section 5.6 for explanation).

change in bias of less than 2 K; in this experiment, we are seeing extremes of 4 or 5 K.

Figure 5.17b shows the AATSR–in situ LST differences as a function of the 11–12 μm difference, which is an indication of the variation of atmospheric water vapour and emissivity over the site. For emissivity, the results given in Chapter 3 suggest that the variation in the 11–12 μm BT difference due to emissivity should be no more than 0.1 K (for the maximum 11–12 μm emissivity difference of 0.015). Therefore, the remaining variation in the 11–12 μm BT difference of approximately 0.3 K must be due to the atmosphere. This variation, could, for example, be due to a change in total column water vapour of several % over the site, or a change in atmospheric temperature of 1% or less. Again, the results in Chapter 3 indicate that changes in atmospheric temperature or water vapour of this magnitude would only result in a change in the bias of the retrieved LST of less than 1 K.

Having excluded the AATSR LST product as a source of the extreme biases observed in the four outlying pixels, we must assume that it is the in situ LSTs that are incorrect. In addition to the assumptions and limitations of the methodologies (Section 5.4.2.1), there are two possible causes of the outliers. Firstly, inaccuracies in the AATSR geolocation may result in the wrong Landsat pixels being used to classify the AATSR pixel. Secondly, a change in the land use (e.g. harvesting) between the AATSR overpass (05/03/03) and acquisition of the Landsat data (15/03/03) could result in the wrong in situ LSTs being assigned to the Landsat pixels. Problems with the AATSR geolocation

are unlikely to be the cause, as the errors in the nadir-view geolocation are estimated to be much less than 100 m (Chapter 2). Furthermore, we would expect to see randomisation in the eight well-correlated data points if this were at fault. A change in land use is a possible cause, although no major harvesting event was observed to take place between these two dates. One other possible consideration is that large volumes of water may have been present at times during the campaign. The fields were often irrigated and extremely muddy during the fieldwork, which may have altered the visible properties of the surface, thus affecting their classification. The use of additional coincident high-resolution satellite data could resolve this issue.

Excluding these four outlying pixels, we find that the biases are largely unchanged, but the standard deviations are reduced significantly, as expected. The revised statistics are shown in Table 5.6, where the maximum standard deviation is now observed to be 1.13 K (obtained using the weighted-mean method with no additional IFOV weighting).

5.7 Conclusions

LSTs, derived using the operational AATSR LST retrieval algorithm, have been compared to in situ LST data corresponding to twelve AATSR pixels over the WATERMED site in Morocco. The AATSR data were obtained from the overpass occurring at 10:53 am GMT on 05 March 2003.

Point observations of LST were obtained over three surface regimes, classified as bare soil, mixed vegetation and soil, or vegetation. These LST data were derived from measurements of radiometric temperature, made along linear transects over each surfaces within ± 15 minutes from the time of the AATSR overpass. The measurements were corrected for emissivity effects using in situ emissivity and downwelling atmospheric radiance data. While the thermal emissivity of the site was found to vary by 1% or less, the radiometric temperatures deviated by more than 20 K, with the largest standard deviation obtained over the mixed vegetation and soil regime (standard deviation 5.41 K). In contrast, the bare soil regime was found to be the most radiometrically stable surface (standard deviation of 1.44 K). The standard deviation of the vegetated surface is calculated to be 2.52 K. As expected, the LST of the vegetated surface regime was found to be the coolest ($LST = 295.64 \pm 1.37$ K), as the vegetation actively transpires, keeping itself cool. The LST of the bare soil, and mixed vegetation and bare soil surfaces were found to be quite similar, at 309.10 ± 1.49 K and 307.25 ± 2.66 K, respectively.

As the site is heterogeneous in terms of LST on the the sub-pixel scale, an innovative

method was required in order to upscale the in situ data to the spatial scale of the satellite. Two methodologies were employed in this study. Both methods utilise 30-m blue-visible Landsat ETM+ data to estimate the variability of LST over the site, as LST demonstrates a strong dependence on the proportion of vegetation. For the first method, hereafter referred to as the weighted-mean method, each Landsat pixel has been categorised as either bare soil, mixed vegetation and soil, or vegetation. A representative 1-km in situ LST was then calculated from the mean of the in situ LSTs obtained over each of these surfaces, weighted by the proportion of each surface within each 1-km pixel. For the second method, hereafter referred to as the regression method, a linear equation was formulated from the in situ data and the Landsat reflectances corresponding to the measurement surfaces, to describe the relationship between reflectance and LST. The 30-m reflectances were then used to 'retrieve' an LST for each Landsat pixel, which were then averaged over the area covered by each AATSR pixel on the ground.

The results indicate that the AATSR retrieval algorithm is yielding an LST that is too warm over this site. For the weighted-mean method, this warm bias of 0.6 K agrees well with the bias predicted in Chapter 3 for a mid-latitude LST retrieval within this biome. A higher bias of approximately 3.1 K is obtained using the regression method. Despite this higher bias, the lower standard deviation of the regression method (2.0 K compared with 2.7 K for the weighted-mean method) suggests that this technique is providing a better estimate of the in situ pixel-to-pixel variation of LST. Moreover, the crude assumption within the weighted-mean method that the LST corresponding to each Landsat pixel must be one of three values, is likely to cause the results to be biased.

Despite their differences, both methods yield eight pixels that are well-correlated in terms of AATSR and in situ LST, and four outliers. The source of these four outliers requires further investigation. However, investigations within the framework of this study indicate that the bias cannot originate fully from the AATSR LST retrieval algorithm (assumptions about the atmosphere or emissivity), and is unlikely to be related to uncertainties in the AATSR geolocation. Interestingly, all four outliers correspond to AATSR pixels with Envisat blanking pulses (the other eight pixels do not have blanking pulses). However, no evidence has ever been found to suggest that the presence of a blanking pulse affects the quality of ATSR-1/2 data (Mutlow 2000), so it seems unlikely that this could be the cause of the anomalies observed in these AATSR data. Other than being an artefact of the methodologies used in this study, the most likely explanation is that the visible and thermal properties of the areas covered by these AATSR pixels has changed between the dates of the AATSR (05 March 2003) and Landsat (15 March 2003) overpasses. Additional high-resolution satellite imagery is required to determine if this is the

case. Excluding these outlying pixels reduces the standard deviation of the results by more than a factor of 2 (maximum 1.13 K).

Lastly, the impact of the true IFOV of the AATSR has been considered in this study. LSTs derived using both methodologies have also been calculated using the 11 μm IFOV weighting appropriate for the across track position of the AATSR observations in this study; similar results (within 0.1 K) are obtained using the 12 μm IFOV. The overall bias and standard deviation of the comparison with the AATSR LSTs shows negligible change. However, differences of several tenths of a degree on a pixel-to-pixel basis (standard deviation 0.57 K and 0.37 K for the weighted-mean and regression methods, respectively) are observed between the in situ LSTs obtained assuming a uniform 1×1 km IFOV and the true IFOV. These results demonstrate that the true IFOV of the AATSR could be an important consideration where there is sub-pixel variability of LST or SST.

This experiment has demonstrated the difficulties involved in validation of satellite LSTs over a site that is heterogeneous in terms of LST over the scale of the satellite pixel. For a homogeneous site, the problem of comparing in situ point observations with LSTs derived from satellite data is very much smaller. However, such land sites are few and far between, so developing a viable upscaling methodology that can be used over heterogeneous land surfaces is very desirable. For both methods employed in this study, a better approximation could have been made of the relationship between visible reflectance and LST if additional in situ point LST data were available that corresponded to more values within the range of reflectances over the site. This would have enabled improved results. An even better adaptation of the methodologies employed in this study, would have been to utilise temporally coincident high-resolution (e.g. 30 m) thermal imagery to assess the spatial distribution of temperature over the site at the time of the AATSR overpass. However, no such data were available for this study.

The results of this study are also limited in the sense that they provide only a 'snapshot' of the performance of the AATSR LST retrievals. The results of the SST validation experiment presented in Chapter 4 have shown the importance of continuous validation, to identify both seasonal effects, and to increase the statistical significance of the results. However, this experiment has been very useful in characterising the inherent problems associated with LST validation in general, and the potential to carry out validation over heterogeneous land sites.

Chapter 6

Conclusions and Future Work

6.1 Summary of Conclusions

The focus of this thesis has been an investigation into the accuracy of SST and LST retrievals from the AATSR, which was launched onboard ESA's Envisat satellite in March 2002. This work has been carried out through the combination of a theoretical sensitivity study and the results of in situ validation experiments. Both theoretical and empirical studies are intrinsically linked; we can only understand the validation results fully through the sensitivity study, but only the validation results can provide a truly direct assessment of the accuracy of the retrievals.

The AATSR (and ATSR-2) is currently the most accurate and precise operational space-borne radiometer. The instrument makes measurements of the TOA BTs and reflectances corresponding to seven spectral channels, three of which are in the thermal infrared at 3.7, 11 and 12 μm . Data from these channels are used to derive global SSTs and LSTs at 1 km (or greater) spatial resolution (although the 3.7 μm channel is not used for LST or daytime SST retrievals). Uniquely, the (A)ATSR instrument also has the ability to make measurements at both nadir and approximately 55° from zenith in the along-track direction, which provides additional information about atmospheric effects. This along-track view, together with its radiometric accuracy, means that the (A)ATSR has the potential to provide satellite-derived SSTs and LSTs that are superior to those produced by any other existing satellite sensors. At the time of writing, data from this forward view are not used in the operational LST retrieval scheme.

The sensitivity study reported in Chapter 3 has demonstrated that the most consistent SST retrievals are those that include the 3.7 μm channel (N3, D3). This is due

to the fact that this channel has a much lower sensitivity to surface emissivity, and to atmospheric temperature, water vapour and aerosol (excluding marine aerosol), which have been shown to be the main components of the atmosphere that affect the (A)ATSR channels. As the three-channel retrievals are weighted heavily in favour of 3.7 μm channel, these SSTs also demonstrate a much lower sensitivity to these parameters than the two-channel SSTs (N2, D2).

Although the AATSR thermal channels have been chosen such that the effects of the atmosphere are as small as possible, the sensitivity of the 11 and 12 μm channels to the atmosphere is still high, compared with that of the 3.7 μm channel. However, the additional information provided by the forward view appears to improve significantly the stability of the SST retrieval, although atmospheric extremes, for example very high levels of water vapour, may still introduce biases in the D2 retrievals of several tenths of a K. The two-channel retrievals are also much more sensitive than the three-channel retrievals to the emissivity of the sea surface. The results of this study suggest that biases of up to 0.3 K could be introduced into the mid- and polar-latitude SSTs if a constant emissivity is assumed. The effect is smaller in the tropics due to the high levels of water vapour attenuating changes in the at-surface BTs.

These findings are reflected in the results of the validation experiment described in Chapter 4, where AATSR SSTs have been compared with in situ SSTs derived from thermal observations made by the M-AERI during 2003. However, it should be remembered that these results are confined to the Caribbean, and may not be representative of the global performance of the SST retrievals. Considering all 99 cloud-free matchups (25 two-channel, 74 three-channel), the standard deviation of the three channel matchups is found to be less than 0.30 K, with overall biases of 0.10 K or less. The two-channel retrievals perform significantly worse; even the D2 SSTs have a bias and standard deviation of 0.16 K and 0.38 K, respectively.

Through both the sensitivity study and the SST validation experiment, the relationship between the corresponding dual and nadir SSTs is a point of interest. For the majority of the SST validation matchups, the nadir-view SSTs (N2, N3) are warmer than the equivalent dual-view SSTs (D2, D3). This is consistent with the results of the sensitivity study, where we find that the two- and three-channel D-Ns (dual-nadir SST differences) are typically negative. Although the D-N demonstrates some sensitivity to atmospheric water vapour and temperature, and surface emissivity, it is mineral dust aerosol that is seen to have the largest effect. Radiative transfer simulations yield that, although the TOA BTs are depressed in all channels in both views in the presence of aerosol, the relative weighting of the retrieval coefficients will result in a decrease in the nadir-view

SSTs, and an increase in the dual-view SSTs. This culminates in an overall increase in the D-N, which is already in use by others in the (A)ATSR field as a tracer for the transport of Saharan dust across the Atlantic.

Over the Caribbean, which is affected by Saharan dust from time to time, the dependence of the D-N on aerosol has been shown through correlation with MODIS aerosol optical depth. As the model results predict, the AATSR dual-view SSTs obtained in the presence of heavy tropospheric aerosol loading are warm biased, and the nadir-view SSTs, cold biased. Once these aerosol-contaminated data are excluded, the statistics imply that the performance of all the SST retrievals is better under aerosol-free conditions. However, there is a warm bias in the AATSR nadir-view retrievals that is of some concern. For N3, this bias is calculated to be +0.14 K. For N2, this bias of +0.57 K is comparable to the predicted bias of approximately +0.7 K in the model results for the mid-latitude and tropical atmospheres. This indicates that the nadir coefficients, in particular those for N2, are not optimal over this geographical region.

For LST, the sensitivity study of Chapter 3 demonstrates that the performance of the algorithm for biome 12 is very similar to the SST N2 algorithm. This is perhaps not surprising, since both retrievals use only the traditional split-window channels. The implications of the instability of this retrieval for LST are greater than for SST, due to more extreme variations of surface emissivity and the atmosphere over land. In addition, the sensitivity study shows that the surface-air temperature difference also has a bearing on the accuracy of the SST/LST algorithms. While this is probably insignificant over the oceans, the surface-air temperature difference can vary by several K over land. As we have seen for SST, the inclusion of data from the 3.7 μm channel and/or the forward view could improve the performance of the algorithm. In the case of the latter, further complications are then raised due to the angular variation of the emissivity of land surfaces. Including the 3.7 μm channel at night, however, could be extremely beneficial for LST, as this channel is not as sensitive to variations in emissivity as the split-window channels.

In Chapter 5 of this thesis, AATSR LSTs for twelve pixels (from a single daytime orbit) over the WATERMED field site in Morocco were compared with equivalent in situ data. As the site is heterogeneous in terms of LST on the spatial scale of the AATSR, an innovative method was required to upscale the in situ data in order to compare the two data sets. Two such methods were developed, which utilised high-resolution visible reflectances from LANDSAT ETM+ to estimate the thermal variation of LST over the site (as LST has been shown to have a strong dependence on the proportion of vegetation at this location). Both methods suggest that the AATSR LSTs are warm-biased compared

with the in situ data by at least 0.6 K. However, the results of this study are limited in that they provide only a ‘snapshot’ of the performance of the AATSR LST retrievals over this site. As seen from the validation of SSTs in Chapter 4, outliers in the agreement between satellite and in situ data may occur, and there may be seasonal variation of bias in the satellite data. Such features can only be identified through long-term validation where the number of matchups is high (e.g. at least several months with several matchups per month).

Despite the limitations of the results of this experiment, the exercise has been very useful in identifying the problems associated with LST validation, and exploring the possibilities of validation over heterogeneous sites. Homogeneous sites that are traditionally used for LST validation are few and far between, thus it is desirable to develop a method that can be employed over heterogeneous land surfaces. The findings of this study suggest that this may be possible for situations where many (ideally, many more than three) in situ point LST data are available, allowing the variation of LST over the site to be characterised fully.

Another important finding that resulted from this experiment is the impact of the true IFOV of the AATSR thermal channels. A common misconception is that the 1-km SST/LST data are an average of the SST/LST over that 1-km square. In reality, the IFOV extends beyond 1-km square (particularly in the forward view), where the sensitivity diminishes away from the central region of the pixel. For the twelve pixels considered in the validation experiment over the WATERMED field site, considering the true IFOV (instead of a homogeneous 1-km square for each pixel) results in differences of several tenths of a K on a pixel-to-pixel basis. This could have important implications for regions where there is sub-pixel variability of LST or SST.

6.2 Recommendations for Future Work

Considering the results presented in this thesis, there is much scope for further work. These recommendations are summarised below.

One of the principal aspects of this work that could be investigated further is on the effects of tropospheric aerosols on the AATSR TOA BTs. The effects of transported mineral dust aerosol, for example, in the infrared has been observed by several researchers (including this thesis). However, as the process of simulating accurately the effects of Saharan dust on the AATSR TOA BTs is extremely complex, due to the variability of the transported dust characteristics and uncertainties in the refractive indices, there is

currently very little information available on theoretical model results. Based on these results, together with the observational data, a correction for affected SST data, or even new retrieval coefficients that are tropospheric-aerosol robust, could be derived.

Continuing along these lines, it would also be useful to extend the validation record, using in situ data from the M-AERI, to include data from 2004 and 2005. This would enable the statistical significance of the results presented in Chapter 4 to be improved, and any further seasonal trends identified. Fortunately, this extended validation is already underway at the University of Leicester, using the AATSR validation software developed within the context of this PhD work.

The results of the sensitivity study have shown that the traditional split-window SST/LST retrieval algorithm is very sensitive to variations in surface emissivity and atmospheric conditions. Under many conditions, both the SST N2 and LST retrievals (for biome 12) are subject to high biases. For SST, this is not critical, as the dual-view and N3 retrievals have been shown to provide more accurate SSTs. However, for LST, the two-channel algorithm is the only available retrieval, so these biases need addressing as a matter of urgency if the AATSR is to provide a viable product. The possibility of including data from the $3.7\ \mu\text{m}$ channel (and possibly the forward view) could be investigated. The product may also benefit from utilising separate day/night coefficients to account for the differing surface-air temperature differences, which also affect the sensitivity of the retrievals.

Through the WATERMED experiment (Chapter 5), it is clear that LST validation over heterogeneous sites is extremely complex. The results of this study suggest that heterogeneous validation is possible, but a much better categorisation of the LST variability over such sites is required, for example, by utilising more radiometers. It would be very interesting and useful to extend the study in this way, which would provide the opportunity to improve upon the upscaling methodologies (from point LSTs to the spatial scale of the satellite) developed here. Furthermore, the SST validation experiment reported within this thesis highlights the need for continuous validation, as opposed to discrete measurement campaigns, such as the WATERMED experiment. Performing such an experiment would enable a true assessment of the performance of the product over this site to be carried out.

In Chapter 1, the potential to combine LSTs derived from polar-orbiting and geostationary sensors was highlighted. A combination data set of this type would provide LST data with the temporal and spatial resolution required for a number of applications. Some existing studies have attempted to address this issue, but the process is still in its early stages. Developing such a methodology could provide one of the most useful ap-

plications for LSTs derived from polar-orbiting sensors. With its unrivalled radiometric accuracy, the AATSR could become the standard against which the geostationary LSTs are measured. However, as demonstrated in this thesis, thorough validation, which will involve the further development of techniques for upscaling point in situ observations, is essential if this is to be possible.

ACKNOWLEDGEMENTS FOR PROVISION OF DATA AND FUNDING

This work was funded by a NERC studentship at the University of Leicester, UK. The WATERMED project is funded by the European Union (WATERMED, project ICA3-ct-1999-00015, EAGLE, project SST3-CT-2003-502057) and the Ministerio de Ciencia y Tecnologia (project REN2001-3105/CLI) for their financial support. Data were collected as part of this project in collaboration with the University of Valencia.

The AATSR data used in this study were provided by ESA. The AATSR is a nationally provided payload instrument on ESAs Envisat satellite and is funded by the UK Department of Environment, Food and Rural Affairs (DEFRA), in support of their programme in climate prediction and research, with additional contributions from Natural Environment Research Council (NERC), UK, & CSIRO, Australia. AATSR data support was also provided by Rutherford Appleton Laboratories, UK.

The M-AERI was developed with funding from the National Aeronautic and Space Administration (NASA). The data were made available for this study by RSMAS, University of Miami.

The Landsat ETM data published in this paper were obtained in the capacity of the WATERMED project, distributed by EROS data centre distributed active archive centre (EDC-DAAC) located at the US Geological Survey's EROS data centre in Sioux Falls, South Dakota, U.S.A.

Bibliography

- Ackerman, S., Strabala, K., Menzel, P., Frey, R., Moeller, C., Gumley, L., Baum, B., Seeman, S. W. & Zhang, H. (2002), 'Discriminating Clear Sky from Cloud with MODIS', *Algorithm Theoretical Basis Document (MOD35)* .
- Aires, F., Prigent, C. & Rossow, W. B. (2004), 'Temporal interpolation of global surface skin temperature diurnal cycle over land under clear and cloudy conditions', *Journal of Geophysical Research* **109**, doi: 10.1029/2003D003527.
- Alexander, M. & Scott, J. (2002), 'The influence of ENSO on air-sea interaction in the Atlantic', *Geophysical Research Letters* **29**(14), 10.1029/2001GL014347.
- Allen, M. R., Mutlow, C. T., Blumberg, G. M. C., Christy, J. R., McNider, R. T. & Llewellyn-Jones, D. T. (1994), 'Global Change Detection', *Nature* **370**, 24–25.
- Andersen, O. B., Knudsen, P. & Beckley, B. (2002), 'Monitoring sea level and sea surface temperature trends from ERS satellites', *Physics and Chemistry of the Earth* **27**, 1413–1417.
- Arimoto, R., Duce, R. A., Ray, B. J., Jr., W. G. E., Cullen, J. D. & Merrill, J. T. (1995), 'Trace elements in the atmosphere over the North Atlantic', *Journal of Geophysical Research* **100**(D1), 1199–1213.
- ASTER Spectral Library (1999), *Reproduced from the ASTER Spectral Library through the courtesy of the Jet Propulsion Laboratory, California Institute of Technology, Pasadena California. Copyright © 1999. California Institute of Technology. All Rights Reserved.*
- Barton, I. J. (2004), 'Global water vapor analyses over the oceans using Along Track Scanning Radiometer infrared data', *Journal of Geophysical Research* **109**(D2), doi:10.1029/2002JD002856.

- Barton, I. J., Minnett, P. J., Maillet, K. A., Donlon, C. J., Hook, S. J., Jessup, A. T. & Nightingale, T. J. (2004), 'The Miami2001 Infrared Radiometer Calibration and Intercomparison Part II: Shipboard Results', *Journal of Atmospheric and Ocean Technology* **21**(2), 268–283.
- Barton, I. J., Prata, A. J. & Cecket, R. P. (1995), 'Validation of the ATSR in Australian Waters', *Journal of Atmospheric and Oceanic Technology* **12**, 290–300.
- Barton, I. & Pearce, A. (2003), Validation of satellite-derived sea surface temperatures from AATSR data, in 'Proceedings of the MAVT workshop, Frascati, Italy', ESA.
- Becker, F. & Li, Z. (1990), 'Towards a local split window method over land surfaces', *International Journal of Remote Sensing* **11**(3), 369–393.
- Bell, M. J., Forbes, R. M. & Hines, A. (2000), 'Assessment of the FOAM global data assimilation system for real-time operational ocean forecasting', *Journal of Marine Systems* **25**, 1–22.
- Bertie, J. E. & Lan, Z. D. (1996), 'Infrared intensities of liquids XX: The intensity of the OH stretching band of liquid water revisited, and the best current values of the optical constants of H₂O(1) at 25° C between 15,000 and 1 cm⁻¹', *Applied Spectroscopy* **50**(8), 1047–1057.
- Brown, S. J., Harris, A. R. & Mason, I. M. (1997), 'New aerosol robust sea surface temperature algorithms for the along-track scanning radiometer', *Journal of Geophysical Research* **102**(C13), 27,973–27,989.
- Carlson, T. N. & Prospero, J. M. (1972), 'The large-scale movement of saharan air outbreaks over the northern equatorial Atlantic', *Journal of Applied Meteorology* **11**, 283–297.
- Caselles, V. & Sobrino, J. A. (1989), 'Determination of frosts in orange groves from NOAA-9 AVHRR data', *Remote Sensing of Environment* **29**(2), 135–146.
- Casey, K. S. & Cornillon, P. (2001), 'Global and Regional Sea Surface Temperature Trends', *Journal of Climate* **14**, 3801–3917.
- Challenor, P. C., Cipollini, P., Cromwell, D., Hill, K. L., Quartly, G. D. & Robinson, I. S. (2000), 'Propagation characteristics of extratropical planetary waves observed in the ATSR global sea surface temperature record', *Journal of Geophysical Research* **105**(C9), 21,927–21,945.

- CIMEL Electronique (2001), *CIMEL CE312 Thermal-Infrared Radiometer User Manual version 2.0*.
- Coll, C., Caselles, V., Galve, J. M., Valor, E., Niclòs, R., Sàncas, J. M. & Rivas, R. (2005), 'Ground measurements for the validation of land surface temperatures from AATSR and MODIS data', *Remote Sensing of Environment* **97**, 288–300.
- Conaway, J. & van Bavel, C. H. M. (1967), 'Evaporation from a wet surface calculated from radiometrically determined surface temperatures', *Journal of Applied Meteorology* **6**, 650–655.
- Dana, R. W. (1969), 'Measurement of 8–14 μm emissivity of igneous rocks and mineral surfaces', *NASA Science Report NSG-632, Goddard Space Flight Center, Greenbelt, MD*.
- Dash, P., Göttsche, F., Olesen, F. & Fischer, H. (2002), 'Review article: Land surface temperature and emissivity estimation from passive sensor data: theory and practice-current trends', *International Journal of Remote Sensing* **23**(13), 2563–2594.
- Deschamps, P. Y. & Phulpin, T. (1980), 'Atmospheric correction of infrared measurements of sea surface temperature using channels at 3.7, 11 and 12 μm ', *Boundary Layer Meteorology* **18**, 131–143.
- Diaz, J. P., Arbelo, M. & Exposito, F. J. (2001), 'Relationship between errors in AVHRR-derived sea surface temperature and the TOMS Aerosol Index', *Geophysical Research Letters* **28**(10), 1989–1992.
- Donlon, C. J., Castro, S. L. & Kay, A. (1999), 'Aircraft validation of ERS-1 ATSR and NOAA-14 AVHRR sea surface temperature measurements', *International Journal of Remote Sensing* **20**(18), 3503–3513.
- Donlon, C. J., Minnett, P. J., Gentemann, C., Nightingale, T. J., Barton, I. J., Ward, B. & Murray, J. (2002), 'Towards improved validation of satellite sea surface skin temperature measurements for climate research', *Journal of Climate* **15**(4), 353–369.
- Donlon, C. J. & Robinson, I. S. (1997), 'Observations of the oceanic thermal skin in the Atlantic Ocean', *Journal of Geophysical Research* **102**(C8), 18,585–18,606.
- Donlon, C. J. & Robinson, I. S. (1998), 'Radiometric validation of ERS-1 along-Track Scanning Radiometer Average Sea Surface Temperature in the Atlantic Ocean', *Journal of Atmospheric and Oceanic Technology* **15**, 647–660.

- Dorman, J. L. & Sellers, P. J. (1989), 'A global climatology of albedo, roughness length and stomatal resistance for atmospheric general circulation models as represented by the simple biosphere model (SiB)', *Journal of Applied Meteorology* **28**, 833–855.
- Dundas, R. M. (1991), The use of ATSR data to measure the radiative properties of aerosol particles, PhD thesis, University of Leicester.
- Dunion, J. P. & Veldon, C. S. (2003), 'The Impact of the Saharan Air Layer on Atlantic Tropical Cyclone Activity', *Bulletin of the American Meteorological Society* **85**, 353–365.
- ECMWF (1995), *The description of the ECMWF/WCRP level III-A global atmospheric data archive*.
- Edwards, D. P. (1992), GENLN2 - A general line-by-line atmospheric transmittance and radiance model, Technical report, NCAR/TN-361 STR National Center for Atmospheric Research, Boulder, Colorado.
- ESA (2002a), 'AATSR Overpass Tool'.
- ESA (2002b), 'The AATSR Products User Guide'.
- Forrester, T. N. & Challenor, P. (1995), 'Validation of ATSR sea surface temperatures in the Faeroes region', *International Journal of Remote Sensing* **16**(15), 2741–2753.
- Fowler, J. B. (1995), 'A third generation water bath based blackbody source', *Journal of Research of the National Institute of Standards and Technology* **100**, 591–599.
- Friedman, D. (1969), 'Infrared characteristics of Ocean Water (1.5–15 μm)', *Journal of Applied Optics* **8**(10), 2073–2078.
- Good, S. A. (2004), Effects on AATSR SST retrievals of error and bias in the measurement of radiances and conversion to brightness temperature, Technical report, University of Leicester.
- Good, S. A., Corlett, G. K., Noyes, E. J., Remedios, J. J. & Llewellyn-Jones, D. T. (2006), 'Cloud-contamination in AATSR SST retrievals', *Remote Sensing of Environment* submitted November 2005.
- Hale, G. M. & Querry, M. R. (1973), 'Optical constants of water in the 200 nm to 200 μm wavelength region', *Applied Optics* **12**, 555–563.

- Hanafin, J. A. & Minnett, P. J. (2005), 'Infrared-emissivity measurements of a wind-roughened sea surface', *Applied Optics* **44**, 398–411.
- Harris, A. R., Brown, S. J. & Mason, I. (1994), 'The effect of windspeed on sea surface temperature retrieval from space', *Geophysical Research Letters* **21**(16), 1715–1718.
- Harris, A. R., Saunders, M. A., Foot, J. S., Smith, K. F. & Mutlow, C. T. (1995), 'Improved sea surface temperature measurements from space', *Geophysical Research Letters* **22**(16), 2159–2162.
- Harrison, D. L. & Jones, C. P. (1993), 'A user appraisal of ATSR near-real-time products', *Proceedings of the First ERS-1 Symposium, Cannes, France, 1992 SP-359*, 791–795.
- Hess, M., Koepke, P. & Schult, I. (1998), 'Optical Properties of Aerosols and Clouds: The Software Package OPAC', *Bulletin of the American Meteorological Society* **79**(5), 831–844.
- Hill, K. L., Robinson, I. S. & Cipollini, P. (2000), 'Propagation characteristics of extratropical planetary waves observed in the ATSR global sea surface temperature record', *Journal of Geophysical Research* **105**(C9), 21,927–21,945.
- Jin, M. & Dickinson, R. E. (1999), 'Interpolation of surface radiative temperature measured from polar orbiting satellites to a diurnal cycle 1. Without clouds', *Journal of Geophysical Research* **104**(D2), 2105–2116.
- Jones, M. S., Saunders, M. A. & Guymer, T. H. (1996), 'Global remnant cloud contamination in the along-track scanning radiometer data: Source and removal', *Journal of Geophysical Research* **101**(C5), 12,141–12,147.
- K. Y. Kondratyev (1969), *Radiation in the Atmosphere*, Academic Press, New York, San Francisco, London.
- Kaufman, Y. J. & Tanré, D. (1998), 'Algorithm for remote sensing of tropospheric aerosol from MODIS', *Algorithm Theoretical Basis Document*.
- Kearns, E. J., Hanafin, J. A., Evans, R. H., Minnett, P. J. & Brown, O. B. (2000), 'An independent assessment of Pathfinder AVHRR sea surface temperature accuracy using the Marine Atmosphere Emitted Radiance Interferometer (MAERI)', *Bulletin of the American Meteorological Society* **81**(7), 1525–1536.

- Knieszys, F. X., Abreu, L. W., Anderson, G. P., Chetwynd, J. H., Shettle, E. P., Berk, A., Bernstein, L. S., Robertson, D. C., Rothman, P. A. L. S., Selby, J. E. A., Gallery, W. O., & Clough, S. A. (1996), The MODTRAN 2/3 report and LOWTRAN 7 model, Technical Report 4, Phillips Lab., Geophys. Directorate, PL/GPOS, Hanscom AFB, MA 01731, Contract F19628-91-C-0132.
- Lambin, E. F. & Ehrlich, D. (1996), 'The surface temperature-vegetation index space for land cover and land-cover change analysis', *International Journal of Remote Sensing* **17**(3), 463–487.
- Lawrence, S., Llewellyn-Jones, D. T. & Smith, S. J. (2004), 'The measurement of climate change using data from the Advanced Very-High Resolution and Along-Track Scanning Radiometers', *Journal of Geophysical Research* **109**(C8), doi:10.1029/2003JC002104.
- Li, X., Pichel, E., Maturi, E., Clemente-Colón, P. & Sapper, J. (2001), 'Deriving the operational nonlinear multichannel sea surface temperature algorithm coefficients for NOAA-15 AVHRR/3', *International Journal of Remote Sensing* **22**(4), 699–704.
- Llewellyn-Jones, D., Edwards, M. C., Mutlow, C. T., Birks, A. R., Barton, I. J. & Tait, H. (2001), 'AATSR: Global-Change and Surface-Temperature Measurements from Envisat', *ESA bulletin, February 2001* **105**, 11–21.
- Mason, G. (1991), Test and calibration of the Along Track Scanning Radiometer, A Satellite-Borne Infrared Radiometer Designed to Measure Sea Surface Temperature, PhD thesis, University of Oxford.
- Masuda, K., Takashima, T. & Takayama, Y. (1988), 'Emissivity of Pure and Sea Waters for the Model Sea Surface in the Infrared Window Regions', *Remote Sensing of Environment* **24**, 313–329.
- McMillin, L. M. (1984), 'Theory and Validation of the Multiple Window Sea Surface Temperature Technique', *Journal of Geophysical Research* **89**, 3655–3661.
- Merchant, C. J. & Harris, A. R. (1999), 'Toward the elimination of bias in satellite retrievals of sea surface temperature, 2. Comparison with in situ measurements', *Journal of Geophysical Research* **104**(C10), 23,579–23,590.
- Merchant, C. J., Harris, A. R., Murray, M. J. & A. M. Zvody, A. M. (1999), 'Toward the elimination of bias in satellite retrievals of sea surface temperature, 1. Theory, modelling and interalgorithm comparison', *Journal of Geophysical Research* **104**(C10), 23,565–23,578.

- Minnett, P. (1986), 'A numerical study of the effects of anomalous North Atlantic atmospheric conditions on the infrared measurement of sea surface temperature from space', *Journal of Geophysical Research* **91**(C7), 8509–8521.
- Minnett, P. J. (1990), 'The regional optimisation of infrared measurements of sea-surface temperature from space', *Journal of Geophysical Research* **95**, 13,497–413,510.
- Minnett, P. J. (1991), 'Consequences of sea surface temperature variability on the validation and applications of satellite measurements', *Journal of Geophysical Research* **96**(C10), 18,475–18,489.
- Minnett, P. J. (2003), 'Radiometric measurements of the sea-surface skin temperature - the competing roles of the diurnal thermocline and the cool skin', *International Journal of Remote Sensing* **24**, 5033–5047.
- Minnett, P. J., Knuteson, R. O., Best, F. A., Osborne, B. J., Hanafin, J. A. & Brown, O. B. (2001), 'The Marine-Atmospheric Emitted Radiance Interferometer: A High-Accuracy Seagoing Infrared Spectroradiometer', *Journal of Atmospheric and Oceanic Technology* **18**, 994–1013.
- Murray, M. J., Allen, M. R., Merchant, C. J., Harris, A. R. & Donlon, C. J. (2000), 'Direct observations of Skin-Bulk SST variability', *Geophysical Research Letters* **27**(8), 1171–1174.
- Mutlow, C. J. (2000), ATSR images: Frequently Asked Questions, in 'http://www.atsr.rl.ac.uk/documentation/docs/imagefaq/faq.pdf, Draft issue 1.0'.
- Mutlow, C. T., Závody, A. M., Barton, I. J. & Llewellyn-Jones, D. T. (1994), 'Sea surface temperature measurements by the along-track scanning radiometer on the ERS 1 satellite: Early results', *Journal of Geophysical Research* **99**(C11), 22,575–22,588.
- Newman, S. M., Smith, J. A., Glew, M. D., Rogers, S. M. & Taylor, J. P. (2005), 'Temperature and salinity dependence of sea surface emissivity in the thermal infrared', *Quarterly Journal of the Royal Meteorological Society* **610**(B), 2539–2557.
- Nightingale, T. J. & Birks, A. R. (2004), AATSR Algorithm Verification: Comparison of AATSR and ATSR-2 Data, Technical report, Rutherford Appleton Laboratory, Contract Report to Estec.
- Nightingale, T. & Llewellyn-Jones, D. T. (2003), SCIPRO - Validation of ATSR-2 and AATSR with SISTeR, in 'Proceedings of the MAVT workshop, Frascati, Italy', ESA.

- O'Carroll, A. G., Watts, J. G., Horrocks, L. A., Saunders, R. W. & Rayner, N. A. (2005), 'Validation of the AATSR meteo product sea-surface temperature', *Journal of Atmospheric and Oceanic Technology* - in press .
- Ouzounov, D. & Freund, F. (2004), 'Mid-infrared emission prior to strong earthquakes analyzed by remote sensing data', *Advances in Space Research* **33**, 268–273.
- Parkes, I. M., Sheasby, T. N., Llewellyn-Jones, D. T., Nightingale, T. J., Závody, A. M., Mutlow, C. T., Yokoyama, R., Tamba, S. & Donlon, C. J. (2000), 'The Mutsu Bay Experiment: validation of ATSR-1 and ATSR-2 sea surface temperature', *International Journal of Remote Sensing* **21**(18), 3445–3460.
- Pierangelo, C., Chédin, A., Heilliette, S., Jacquinet-Husson, N. & Armante, R. (2004), 'Dust altitude and infrared optical depth from AIRS', *Atmospheric Chemistry and Physics Discussions* **4**, 3333–3358.
- Prata, A. (2002a), 'Land surface temperature measurement from space: AATSR algorithm theoretical basis document', *Contract Report to ESA, CSIRO Atmospheric Research, Aspendale, Victoria, Australia* .
- Prata, A. (2002b), Land Surface Temperature Measurement from Space: Global surface temperature simulations for the AATSR, Technical report, CSIRO Atmospheric Research, Australia.
- Prata, A. J. (1994), 'Land surface temperatures derived from the advanced very high resolution radiometer and the along-track scanning radiometer 2. Experimental results and validation of AVHRR algorithms', *Journal of Geophysical Research* **99**(D6), 13,025–13,058.
- Prata, A. J. & Cecket, R. P. (1999), 'An Assessment of the Accuracy of Land Surface Temperature Determination from the GMS-5 VISSR', *Remote Sensing of Environment* **67**, 1–14.
- Prospero, J. M. & Carlson, T. N. (1972), 'Vertical and areal distribution of Saharan dust over the western equatorial North Atlantic Ocean', *Journal of Geophysical Research* **77**, 5255–5265.
- Querry, M. R., Holland, W. E., Waring, R. C., Earls, L. M. & Querry, M. D. (1977), 'Relative Reflectance and Complex Refractive Index in the Infrared for Saline Environmental Waters', *Journal of Geophysical Research* **82**(9), 1425–1433.

- Remedios, J. J. (1999), 'MIPAS atmospheric data sets designed for use with Oxford RFM (download from http://www-atm.physics.ox.ac.uk/RFM/rfm_downloads.html#atm)'.
- Reutter, H., Olesen, F.-S. & Fischer, H. (1996), Determination of Land Surface Temperatures from AVHRR and METEOSAT Data, Environment, final report, Insitut für Meteorologie und Klimaforschung.
- Rhoads, J., Dubayah, R., Lettenmaier, D., O'Donnell, G. & Lakshmi, V. (2001), 'Validation of land surface models using satellite-derived surface temperature', *Journal of Geophysical Research* **106**(D17), 20,085–20,099.
- Rice, J. P., Butler, J. J., Johnson, B. C., Minnett, P. J., Maillet, K. A., Nightingale, T. J., Hook, S. J., Abtahi, A., Donlon, C. J. & Barton, I. J. (2004), 'The Miami2001 Infrared Radiometer Calibration and Intercomparison: 1. Laboratory Characterization of Blackbody Targets', *Journal of Atmospheric and Oceanic Technology* **21**, 258–267.
- Rice, J. P. & Johnson, B. C. (1998), 'The NIST EOS Thermal-Infrared Transfer Radiometer', *Metrologia* **35**, 505–509.
- Rothman, L., Barbe, A., Benner, D. C. & et al (2003), 'The HITRAN molecular spectroscopic database: edition of 2000 including updates through 2001', *Journal of Quantitative Spectroscopy and Radiative Transfer* **82**, 5–44.
- Rubio, E., Caselles, V. & Badenas, C. (1997), 'Emissivity measurements of several soils and vegetation types in the 8-14 μm wave band: analysis of two field methods', *Remote Sensing of Environment* **59**, 490–521.
- Saunders, R. W. (1986), 'An automated scheme for the removal of cloud contamination from AVHRR radiances over Western Europe', *International Journal of Remote Sensing* **7**, 867–886.
- Saunders, R. W. & Kriebel, K. T. (1988), 'An improved method for detecting clear sky and cloudy sky radiances from AVHRR data', *International Journal of Remote Sensing* **9**, 123–150.
- Schäädlich, S., Göttsche, F. M. & Olesen, F.-S. (2001), 'Influence of land parameters and atmosphere on Meteosat brightness temperatures and generation of land surface temperature maps by temporally and spatially interpolating atmospheric correction', *Remote Sensing of Environment* **75**, 39–46.

- Schluessel, P., Emery, W. J., Grassl, H. & Mammen, T. (1990), 'On the bulk skin temperature difference and its impact on satellite remote sensing of sea surface temperature', *Journal of Geophysical Research* **95**, 13,341–13,356.
- Smith, A. H., Saunders, R. W. & Závody, A. M. (1994), 'The validation of ATSR using aircraft radiometer data over the tropical Atlantic', *Journal of Atmospheric and Oceanic Technology* **11**, 789–800.
- Smith, D. L. (2004), AATSR Infra-Red Radiometric Calibration Report, Technical report, Rutherford Appleton Laboratory, document PO-TN-RAL-AT-0537, Issue 1.
- Smith, D. L., Delderfield, J., Drummond, D., Edwards, T., Mutlow, C. T., Read, P. D. & Toplis, G. M. (2001), 'Calibration of the AATSR Instrument', *Advances in Space Research* **28**(1), 31–39.
- Smith, W. L., Knuteson, R. O., Revercomb, H. E., Feltz, W., Howell, H. B., Menze, W. P., Nalli, N. R., Brown, O., Brown, J., Minnett, P. & McKeown, W. (1996), 'Observations of the Infrared Radiative Properties of the Ocean - Implications for the Measurement of Sea Surface Temperature via Satellite Remote Sensing', *Bulletin of the American Meteorological Society* **77**(1), 41–51.
- Snyder, W. C., Wan, Z., Zhang, Y. & Feng, Y.-Z. (1998), 'Classification-based emissivity for land surface temperature measurement from space', *International Journal of Remote Sensing* **19**(14), 2753–2774.
- Sobrino, J. A. & Raissouni, N. (2000), 'Toward remote sensing methods for land cover dynamic monitoring: application to Morocco', *International Journal of Remote Sensing* **21**(2), 353–366.
- Sobrino, J., Raissouni, N., Oliso, A., Hasager, C., Berlaïd, M. A., Rahman, S. A. & Chehbouni, A. (2001), 'WATEREMD - WATer use Efficiency in natural vegetation and agricultural areas by Remote sensing in the MEDiterranean basin', *IGARSS, IEEE (2001) Intern. Geosc. and Rem. Sens. Symp., Univ of New south Wales, Sydney, Australia 9-13 July*.
- Sobrino, J. S. & Caselles, V. (1993), 'A field method for measuring the thermal infrared emissivity', *ISPRS Journal of Photogrammetry and Remote Sensing* **48**, 24–31.
- Sobrino, J. S. & Cuenca, J. (1999), 'Angular variation of thermal infrared emissivity for some natural surfaces from experimental measurements', *Applied Optics* **38**(18), 24–31.

- Susskind, J., Rosenfield, J. & Reuter, D. (1984), 'An accurate radiative transfer model for use in the direct physical inversion of HIRS2 and MSU temperature sounding data', *Journal of Geophysical Research* **89**, 4677–4697.
- Sutherland, R. A. (1986), 'Broadband and spectral emissivities (2-18 μm) of some natural soils and vegetation', *Journal of Atmospheric and Oceanic Technology* **3**, 199–202.
- Thomas, T., Turner, J. & Symon, C. J. (1993), 'A Comparison of ATSR and Shipboard SST Measurements along Transects between the UK and the Antarctic', *Proceedings of the 1st ERS-1 Symposium, Cannes, 1992 SP-359*, 801–805.
- Vazquez-Cuervo, J., Armstrong, E. M. & Harris, A. (2004), 'The effect of aerosols and clouds on the retrieval of infrared sea surface temperature', *Journal of Climate* **17**, 3921–3933.
- Wan, Z. (1999), 'MODIS Land-Surface Temperature', *Algorithm Theoretical Basis Document v3.3*.
- Wan, Z., Zhang, Y. & Zhang, Q. (2004), 'Quality assessment and validation of the MODIS global land surface temperature', *International Journal of Remote Sensing* **25**(1), 261–274.
- Wan, Z., Zhang, Y., Zhang, Q. & Li, Z. (2002), 'Validation of the land-surface temperature products retrieved from Terra Moderate Resolution Imaging Spectroradiometer data', *Remote Sensing of Environment* **83**, 163–180.
- Watts, P. D., Allen, M. R. & Nightingale, T. J. (1996), 'Wind speed effects on sea surface emission and reflection for the Along Track Scanning Radiometer', *Journal of Atmospheric and Oceanic Technology* **13**, 126–141.
- World Meteorological Organization, ed. (1985), *World Climate Research Program, Scientific plan for the Tropical Ocean and Global Atmosphere Programme*, Vol. 107, WCRP Publications Series.
- Závody, A. M., Mutlow, C. T. & Llewellyn-Jones, D. T. (1995), 'A radiative transfer model for sea surface temperature retrieval for the along-track scanning radiometer', *Journal of Geophysical Research* **100**(C1), 937–952.
- Závody, A. M., Mutlow, C. T. & Llewellyn-Jones, D. T. (2000), 'Cloud-clearing over the ocean in the processing of data from the along-track scanning radiometer (ATSR)', *Journal of Atmospheric and Oceanic Technology* **17**(5), 595–615.

Závody, A. M., Mutlow, C. T., Llewellyn-Jones, D. T. & Barton, I. J. (1994), 'Quantitative remote Sensing in the 11 μm wavelength region using ATSR', *Proceedings Second ERS-1 Symposium - Space at the Service of our Environment, Hamburg, Germany, 11-14 October 1993* ESA SP-361 (January 1994), 829–833.